Photoassociation of ultracold RbYb in an optical lattice - a quest towards absolute ground state molecules

Inaugural-Dissertation

zur

Erlangung des Doktorgrades der

Mathematisch-Naturwissenschaftlichen Fakultät

der Heinrich-Heine-Universität Düsseldorf

vorgelegt von

Bastian Pollklesener

aus Wuppertal

Düsseldorf, August 2023

Aus dem Institut für Experimentalphysik
der Heinrich-Heine-Universität Düsseldorf

Gedruckt mit der Genehmigung der
Mathematisch-Naturwissenschaftlichen Fakultät der
Heinrich-Heine-Universität Düsseldorf

Tag der mündlichen Prüfung: 29.09.2023

Referent:	Prof. Dr. Axel Görlitz
Koreferent:	Prof. Dr. Philip Kollmannsberger

Summary

The main endeavor of this thesis was to advance the setup of a new molecule experiment pioneered by T. Franzen [1] and perform photoassociation (PA) spectroscopy in ultracold mixtures of Rubidium (Rb) and Ytterbium (Yb) in optical lattices in order to find ways to produce ground state RbYb molecules. Diatomic molecules consisting of an alkali metal and a two-electron atom such as the RbYb molecule have a paramagnetic ground state that allows the manipulation with electric and magnetic fields because they posses an electric and magnetic dipole moment. Additionally, the interactions between and properties of ultracold polar molecules are interesting for studies of quantum phenomena such as ultracold chemistry [2]–[4], precision measurements [5] and quantum computing [6]–[8].

The new apparatus is divided into three segments of stainless steel chambers. Two of them are called 'production chambers', in which ultracold clouds of rubidium (Rb) and ytterbium (Yb) are prepared in low-pressure environments ($1 \cdot 10^{-11}$ mbar) and cooled to temperatures of µK. A third chamber is called the 'science chamber', where they are brought together using high-power optical dipole traps (ODTs). In order to provide the laser light for these optical traps, the development of home-built laser systems, especially high power fiber lasers and amplifiers at 1064 nm, has been a key element of my thesis. Their successful implementation enabled long distance transport over 45 cm in the ODTs between the 'production' vacuum chambers and the 'science' chamber, which made the simultaneous preparation of Rb and Yb atom clouds possible. This allows us to simultaneously load each atomic species under ideal conditions and enables easy re-configurations of the science chamber without disturbing the production setups, which was lacking in the retired apparatus formerly developed in this group [9]–[14]. Within the scope of this thesis Bose-Einstein condensation was individually achieved for each atomic species in crossed optical dipole traps (XODTs).

In order to produce high density mixtures of the isotopes ^{87}Rb and ^{170}Yb in a combined optical trap a complex experimental sequence needed to be designed and optimised. By utilizing a vertical lattice, Rb atoms could be elevated to connect the two crossed optical dipole traps for the two species and eventually join Yb and Rb atoms in the same trap potential. After improvements of this experimental sequence (compared to [1]) the machine is able to repeatedly create an ultracold mixture of $5 \cdot 10^5$ Rb and $9 \cdot 10^4$ Yb atoms with temperatures of $T_{\mathrm{Rb}} = 5.3\,\mu\mathrm{K}$ and $T_{\mathrm{Yb}} = 1\,\mu\mathrm{K}$ in a XODT. Beyond that, the setup and loading of an even more complex final optical trap - a three dimensional optical lattice - was an essential part of the progress in this thesis. This new trap opens up the possibility for a variety of advanced experimental studies. Following the preparation of ultracold gas mixtures, this work focused on photoassociation under various trapping conditions.

The first step of photoassociation is 1-photon-spectroscopy, where unbound atom pairs of

Rb and Yb are converted to electronically excited RbYb molecules. This photoassociation spectroscopy is conducted to map the potential energy curves of excited molecular states and extract information about the interaction between atoms, for example their scattering lengths [15]. Important theoretical work on the potential energy curves of the RbYb system was performed by Sorensen et al. [16] in 2009, by Tohme et al. [17] in 2013 and later by Shundalau et al. [18] in 2017. Previous results of spectroscopy close to the Rb D1 line measured transitions to the electronically excited $^2\Pi_{1/2}$ state in ^{87}Rb^{176}Yb reaching a binding energy of $E_\mathrm{B} = -h \cdot 2.2\,\mathrm{THz}$ for the vibrational level $\Delta\mathrm{v} = -28$ [19].

In this work a tunable and stable laser system at 556 nm was used for spectroscopy near the $^1S_0 \rightarrow {}^3P_1$ intercombination transition of Yb. Compared to former measurements close to the Rb D1 line, spectroscopy conducted close to the narrow intercombination line allows for higher resolution and reaches weakly bound states close to the atomic threshold due a much smaller natural linewidth of $\Gamma = 2\pi \cdot 181\,\mathrm{kHz}$. Here an extensive search for 1-photon resonances to more excited molecule potentials near the [Rb] $5\mathrm{s}\,{}^2S_{\frac{1}{2}}$ + [Yb] $6\mathrm{s}\,6\mathrm{p}\,{}^3P_1$-asymptote in a mixture of ^{87}Rb, $|F = 1, m_F = -1\rangle$ and ^{170}Yb atoms spanning a frequency range of $0.1 - 11\,\mathrm{GHz}$ was performed during the preceding thesis of Tobias Franzen [1] and was partly repeated within the scope of this thesis.

As a result of the extensive scan we detected the first pair of 1-photon resonances near the intercombination line of Yb and investigated their relevant shifts to determine their binding energies at $E_{\mathrm{B}_1} = -h \cdot 3057.2(3)\,\mathrm{MHz}$ and $E_{\mathrm{B}_2} = -h \cdot 3074.3(3)\,\mathrm{MHz}$. Using Zeeman shifts a characterisation of the detected transitions including attempts at line assignment were made. After these first results (published in [20]) this thesis focused on the improvements of photoassociation rates in various trap configurations aiming at tighter confinement. This effort resulted in an improvement of the photoassociation rate by a factor of ten to $K_{\text{PA-XODT}} = 5(2) \cdot 10^{-13}\,\mathrm{cm}^3/\mathrm{s}$ in a crossed optical dipole trap. In a 2D optical lattice the rate could be further increased to $K_{\text{PA-2D}} = 8.5(1.3) \cdot 10^{-13}\,\mathrm{cm}^3/\mathrm{s}$, while a 3D lattice achieved comparable values at $K_{\text{PA-3D}} = 1.0(2) \cdot 10^{-12}\,\mathrm{cm}^3/\mathrm{s}$. This enhancement is a significant step (compared to the value reported in [1] and [20]) as it facilitates the detection of previously unobserved weaker PA resonances. Furthermore experimental studies in optical lattices benefit from increased PA rates to enable the all-optical production of molecules in the ground state with free-bound STIRAP [21], [22].

Following the discovery of 1-photon PA lines, we utilized the stronger transition found at $-3.057\,\mathrm{GHz}$ to perform 2-photon spectroscopy. Thanks to the linewidth of the single photon resonance with $\Gamma = 3.0(3)\,\mathrm{MHz}$, and the stability and coherence of the photons provided by the PA laser system, the two least bound vibrational states of the ground state molecular potential could be measured with high accuracy. With an analysis of the Zeeman, intensity and thermal line shifts their binding energies are determined to $E_\mathrm{B}(\Delta\nu' = -1) = h{\cdot}101.9(1)\,\mathrm{MHz}$ and $E_\mathrm{B}(\Delta\nu' = -2) = h{\cdot}1011.1(1)\,\mathrm{MHz}$. Using dark resonance spectroscopy the Rabi frequencies of both free-bound and bound-bound transitions could be estimated to $\Omega_{\mathrm{FB}} \approx 2\pi \cdot 1\,\mathrm{kHz}$ and $\Omega_{\mathrm{BB}} \approx 2\pi \cdot 1\,\mathrm{MHz}$.

Based on the results concerning photoassociation of RbYb at the intercombination line of Yb, I have developed concepts for an improvement of the experimental setup. This

includes a capillary oven design, a new laser system with higher power for the Yb Zeeman slower and a bichromatic trap design, that are currently under construction. Furthermore I propose to reduce the apparatus to two vacuum chambers to eliminate the necessity to transport Yb. With these improvements we should be able to enhance the phase space density of our dual species mixture to increase the PA rate in photoassociation experiments even further and create conditions for double degeneracy in the Rb-Yb mixture. Moreover, calculations of Mott Insulator transitions in this thesis propose how to prepare both atomic species in a dual Mott Insulator state in the 3D optical lattice as this promises to be the best conditions for efficient production of vibrational ground state molecules [23], [24].

In a dual Mott Insulator, magnetic Feshbach resonances or 'stimulated Raman adiabatic passages' (STIRAP) are the prospective tools to convert atoms to ground state molecules. While magnetic Feshbach resonances have not been found in the Rb-Yb system in a previous experiment [14], they are definitely worth a second investigation under improved conditions following the predictions in [25], as they have been found in the very similar RbSr [26], CsYb [27] and LiYb [28] systems. In this regard the 'science' vacuum chamber may soon be equipped with additional strong magnetic field coils for the creation and finally manipulation of ground state RbYb molecules.

The other possibility for the creation of ground state molecules is so-called STIRAP, which is the all-optical way to transfer a pair of atoms to a weakly bound vibrational state if magnetic Feshbach resonances prove to be ineffective. Here the magnitude of Rabi frequencies Ω_{FB} and Ω_{BB} determined with our 2-photon dark resonance spectroscopy play a vital role. To obtain large Rabi frequencies and therefore drive an efficient STIRAP sequence the wave function overlap of an unbound scattering state and a bound excited state needs to be as large as possible, a condition that can be achieved in a dual Mott-insulator. Admittedly, free-bound STIRAP in a heteronuclear molecule has not been reported yet and up until now was only realized for Sr_2 molecules in an optical lattice [29], [30]. However, the results in Sr_2 demonstrates the feasibility of this approach for the future. Furthermore STIRAP is already a widely successful tool to bring previously associated weakly bound molecules into the absolute ground state [31].

Zusammenfassung

Das Hauptanliegen dieser Arbeit war es, ein neues Molekülexperiment dessen Aufbau von T. Franzen [1] begonnen wurde, zu erweitern und Photoassoziations-Spektroskopie (PA) in ultrakalten Mischungen von Rubidium (Rb) und Ytterbium (Yb) durchzuführen um neue Wege zur Herstellung von RbYb-Molekülen im Grundzustand zu finden. Zweiatomige Moleküle bestehend aus einem Alkalimetall und einem Zweielektronen-Atom wie das RbYb Molekül, haben einen paramagnetischen Grundzustand, der die Manipulation mit elektrischen und magnetischen Feldern ermöglicht, da sie ein elektrisches und magnetisches Dipolmoment besitzen. Darüber hinaus sind die Wechselwirkungen zwischen und die Eigenschaften von ultrakalten polaren Molekülen für die Erforschung von Quantenphänomenen wie der ultrakalten Chemie [2]–[4], Präzisionsmessungen [5] und Quantencomputern [6]–[8] interessant.

Die neue Apparatur ist in drei Segmente von Vakuumkammern unterteilt. Zwei davon werden als "Produktionskammern" bezeichnet, in denen ultrakalte Gase aus Rubidium (Rb) und Ytterbium (Yb) im Hochvakuum ($1 \cdot 10^{-11}$ mbar) erzeugt und auf Temperaturen von µK abgekühlt werden. In einer dritten Kammer, der so genannten "Wissenschaftskammer", werden sie mit Hilfe von optischen Dipolfallen (ODTs) hoher Leistung zusammengeführt. Um das Laserlicht für diese optischen Fallen bereitzustellen, war die Entwicklung von selbstgebauten Lasersystemen, insbesondere Hochleistungs-Faserlasern und Verstärkern bei 1064 nm, ein wesentlicher Teil meiner Arbeit. Ihre erfolgreiche Implementierung ermöglicht einen Langstreckentransport in den ODTs über 45 cm zwischen den "Produktions"-Vakuumkammern und der "Wissenschaftskammer", wodurch die gleichzeitige Präparation von Rb- und Yb-Atomwolken möglich ist. Dadurch können wir jede der beiden Atomsorten unter idealen Bedingungen gleichzeitig kühlen und laden sowie die Wissenschaftskammer leicht umkonfigurieren, ohne die Produktionsaufbauten zu stören, was bei dem früher in dieser Gruppe entwickelten, inzwischen ausrangierten Experiment nicht möglich war [9]–[14]. Im Rahmen dieser Arbeit wurde die Bose-Einstein-Kondensation für jede Atomsorte einzeln in gekreuzten optischen Dipolfallen (XODTs) erreicht.

Um Mischungen der Isotope ^{87}Rb und ^{170}Yb bei hoher Dichte in einer kombinierten optischen Falle zu erzeugen, musste eine komplexe Versuchssequenz entworfen und optimiert werden. Durch die Verwendung eines vertikalen optischen Gitters konnten Rb-Atome angehoben werden, um zwei gekreuzte optische Dipolfallen für beide Atomsorten zu verbinden und schließlich Rb-Atome mit Yb-Atomen im selben Fallenpotential zu vereinigen. Nach Verbesserungen dieses Versuchsablaufs (im Vergleich zu [1]) ist die Maschine in der Lage, zuverlässig eine ultrakalte Mischung aus $5 \cdot 10^5$ Rb- und $9 \cdot 10^4$ Yb-Atomen mit Temperaturen von $T_{\mathrm{Rb}} = 5.3\,\mu\mathrm{K}$ und $T_{\mathrm{Yb}} = 1\,\mu\mathrm{K}$ in einer XODT zu erzeugen. Darüber hinaus war der Aufbau und die Beladung einer noch komplexeren optischen Falle - eines drei-

dimensionalen optischen Gitters - ein wesentlicher Teil des Fortschritts in meiner Arbeit. Diese neue Falle eröffnet die Möglichkeit für eine Vielzahl von fortgeschrittenen experimentellen Studien. Nach der Herstellung von ultrakalten Gasgemischen konzentrierte sich diese Arbeit auf die Photoassoziation unter verschiedenen Fallenbedingungen.

Der erste Schritt der Photoassoziation ist die 1-Photonen-Spektroskopie, bei der ungebundene Atompaare von Rb und Yb in elektronisch angeregte RbYb-Moleküle umgewandelt werden. Diese Photoassoziationsspektroskopie wird durchgeführt, um die molekularen Potentialkurven der angeregten Molekülzustände zu bestimmen und Informationen über die Wechselwirkung zwischen den Atomen, wie z.B. die Streulängen [15], zu gewinnen. Wertvolle theoretische Arbeiten zu den Energiepotentialkurven des RbYb-Moleküls wurden von Sorensen [16] in 2009, von Tohme [17] in 2013 und später von Shundalau [18] im Jahr 2017 veröffentlicht. Frühere PA-Spektroskopie an der D1-Linie von Rb zum elektronisch angeregten $^2\Pi_{1/2}$ Molekülzustand an ^{87}Rb^{176}Yb erreichten eine Bindungsenergie von $E_\mathrm{B} = -h \cdot 2.2\,\mathrm{THz}$ für das Vibrationsniveau $\Delta \mathrm{v} = -28$.

Zur Durchführung der PA-Experimente im Rahmen dieser Arbeit wurde ein durchstimmbares und präzises Lasersystem bei 556 nm für die anschließende Spektroskopie in der Nähe des $^1S_0 \rightarrow {}^3P_1$ Interkombinationsübergangs von Yb verwendet. Im Vergleich zu früheren Messungen in der Nähe der D1-Linie von Rb ermöglicht die Spektroskopie in der Nähe der schmalen Interkombinationslinie eine höhere Auflösung und erreicht schwach gebundene Zustände in der Nähe der atomaren Schwelle aufgrund einer viel kleineren natürlichen Linienbreite von $\Gamma = 2\pi \cdot 181\,\mathrm{kHz}$. Eine umfangreiche Suche nach 1-Photonen-Resonanzen zu Molekülpotentialen nahe der $[\mathrm{Rb}]\,5\mathrm{s}\,{}^2S_{\frac{1}{2}} + [\mathrm{Yb}]\,6\mathrm{s}\,6\mathrm{p}\,{}^3P_1$-Asymptote in einem Gemisch aus ^{87}Rb, $|F = 1, m_F = -1\rangle$ und ^{170}Yb Atomen über einen Frequenzbereich von $0.1 - 11\,\mathrm{GHz}$ wurde bereits in der vorangegangenen Arbeit von Tobias Franzen [1] durchgeführt und im Rahmen dieser Arbeit teilweise wiederholt.

Als Ergebnis der umfangreichen Suche entdeckten wir das erste Paar von 1-Photonen-Resonanzen in der Nähe der Interkombinationslinie von Yb und untersuchten ihre relevanten Verschiebungen, um ihre Bindungsenergien bei $E_{\mathrm{B}_1} = -h \cdot 3057.2(3)\,\mathrm{MHz}$ und $E_{\mathrm{B}_2} = -h \cdot 3074.3(3)\,\mathrm{MHz}$ zu bestimmen. Anhand der beobachteten Zeeman-Verschiebungen wurde eine Charakterisierung der entdeckten Übergänge einschließlich Versuchen zur Linienzuordnung unternommen. Nach diesen ersten Ergebnissen (veröffentlicht in [20]) konzentrierte sich diese Arbeit auf die Verbesserung der Photoassoziationsraten in verschiedenen Fallenkonfigurationen mit engerem Einschluss der Atome. Diese Bemühungen führten zu einer Verbesserung der Photoassoziationsrate um einen Faktor zehn auf $K_{\text{PA-XODT}} = 5(2) \cdot 10^{-13}\,\mathrm{cm}^3/\mathrm{s}$ in einer gekreuzten optischen Dipolfalle. In einem optischen 2D-Gitter konnte die Rate weiter auf $K_{\text{PA-2D}} = 8.5(1.3) \cdot 10^{-13}\,\mathrm{cm}^3/\mathrm{s}$ gesteigert werden, während ein 3D-Gitter ähnliche Werte mit $K_{\text{PA-3D}} = 1.0(2) \cdot 10^{-12}\,\mathrm{cm}^3/\mathrm{s}$ erreichte. Diese Verbesserung ist ein bedeutender Schritt (im Vergleich zu den in [1] und [20] erreichten Werten), da sie den zukünftigen Nachweis von bisher nicht beobachteten schwächeren PA-Resonanzen erleichtern sollte. Darüber hinaus profitieren experimentelle Messungen in optischen Gittern von erhöhten PA-Raten, um die rein optische Produktion von Molekülen im Grundzustand mit "free-bound STIRAP" [21], [22] zu ermöglichen.

Nach der Entdeckung der 1-Photonen-PA-Linien wurde der stärkere Übergang bei $-3.057\,\mathrm{GHz}$ zur Durchfühung der 2-Photonen-Spektroskopie genutzt. Dank der schmalen gemessenen Linienbreite der Einzelphotonenresonanz von $\Gamma = 3.0(3)\,\mathrm{MHz}$, sowie der Stabilität und Kohärenz der Photonen des PA-Lasersystems konnten die beiden am wenigsten gebundenen Vibrationszustände des Grundzustand-Molekülpotenzials mit hoher Genauigkeit gemessen werden. Mit einer Analyse der Zeeman-, Intensitäts- und thermischen Linienverschiebungen konnten ihre Bindungsenergien zu $E_\mathrm{B}(\Delta\nu' = -1) = h \cdot 101.9(1)\,\mathrm{MHz}$ und $E_\mathrm{B}(\Delta\nu' = -2) = h \cdot 1011.1(1)\,\mathrm{MHz}$ ermittelt werden. Mit Hilfe von Dunkelresonanzspektroskopie konnten im Anschluss die Rabi-Frequenzen der Übergänge vom thermischen Streuzustand zum elektronisch angeregten Molekülzustand (free-bound) und der Übergänge vom angeregten Molekülzustand zu den beobachteten Vibrationsniveaus des Molekülgrundzustandes (bound-bound) zu $\Omega_\mathrm{FB} \approx 2\pi \cdot 1\,\mathrm{kHz}$ und $\Omega_\mathrm{BB} \approx 2\pi \cdot 1\,\mathrm{MHz}$ abgeschätzt werden.

Ausgehend von den Ergebnissen zur Photoassoziation von RbYb an der Interkombinationslinie von Yb habe ich Konzepte für eine Verbesserung des Versuchsaufbaus entwickelt. Dazu gehören ein Kapillarofen, ein neues Lasersystem mit höherer Leistung für den Yb-Zeeman-Slower und ein bichromatisches Fallendesign. Teilweise werden diese Verbesserungen derzeit bereits in der Apparatur implementiert. Außerdem schlage ich vor, die Apparatur mittelfristig auf zwei Vakuumkammern zu reduzieren, um die Notwendigkeit des Yb-Transports zu beseitigen. Mit diesen Verbesserungen sollten wir in der Lage sein, die Phasenraumdichte unserer Rb-Yb Mischungen zu erhöhen, um die PA-Rate in Photoassoziationsexperimenten noch weiter zu erhöhen und die Voraussetzungen für ein doppeltes Bose-Einstein-Kondensat aus Rb and Yb zu schaffen. Darüber hinaus wird in dieser Arbeit anhand von Berechnungen von Mott-Isolator-Übergängen vorgeschlagen, wie beide Atomspezies in einem dualen Mott-Isolator-Zustand im optischen 3D-Gitter präpariert werden können, da dies die besten Bedingungen für eine effiziente Produktion von Grundzustandsmolekülen zu sein verspricht [23], [24].

In einem dualen Mott-Isolator Zustand sind magnetische Feshbach-Resonanzen oder "stimulierte adiabatische Raman-Passagen" (STIRAP) die potenziellen Werkzeuge, um Atome in Grundzustandsmoleküle umzuwandeln. Obwohl magnetische Feshbach-Resonanzen im Rb-Yb-System in einer früheren Untersuchungen [14] nicht gefunden wurden, sind sie definitiv eine erneute Untersuchung unter verbesserten experimentellen Bedingungen nach den Vorhersagen in [25] wert, da sie in den sehr ähnlichen Systemen wie RbSr [26], CsYb [27] und LiYb [28] gefunden wurden. In diesem Zusammenhang könnte die "Wissenschafts"-Vakuumkammer bald mit zusätzlichen starken Magnetfeldspulen für die Erzeugung und schließlich Manipulation von RbYb-Molekülen im Grundzustand ausgestattet werden.

STIRAP ist die rein optische Alternative, um ein Atompaar in einen schwach gebundenen molekularen Vibrationszustand zu versetzen, wenn sich magnetische Feshbach-Resonanzen als unwirksam erweisen. Dabei spielt die Größe der Rabi-Frequenzen Ω_FB und Ω_BB, die mit Hilfe der Dunkelresonanzspektroskopie in dieser Arbeit ermittelt wurden, eine entscheidende Rolle. Um große Rabi-Frequenzen zu erhalten und somit eine effiziente STIRAP-Sequenz zu betreiben, muss der Überlapp der Wellenfunktionen eines ungebunde-

nen Streuzustands und eines gebundenen angeregten Molekülzustands so groß wie möglich sein, eine Bedingung, die in einem dualen Mott-Isolator erreicht werden kann. Allerdings wurde über "free-bound" STIRAP in einem heteronuklearen Molekül bisher noch nicht berichtet und lediglich für Sr_2-Moleküle in einem optischen Gitter realisiert [29], [30]. Dennoch zeigen die Ergebnisse mit Sr_2 die Machbarkeit dieser Idee. Darüber hinaus ist STIRAP ein sehr erfolgreiches Instrument, um zuvor assoziierte, schwach gebundene Moleküle in den absoluten Grundzustand zu transferieren [31].

Contents

Summary iii

Zusammenfassung vii

1. Introduction 1
- 1.1. Motivation . . . 1
- 1.2. Cooling and making molecules . . . 3
- 1.3. Why RbYb molecules ? . . . 5
- 1.4. Previous work on RbYb molecules . . . 5
- 1.5. Thesis outline . . . 6

2. Theory of atoms and molecules 9
- 2.1. Colliding Atoms . . . 9
  - 2.1.1. Elastic collisions . . . 9
  - 2.1.2. Inelastic collisions . . . 11
- 2.2. Isotope selection . . . 12
- 2.3. Molecular Physics . . . 16
  - 2.3.1. Angular momentum coupling in molecules . . . 16
  - 2.3.2. Molecular potentials . . . 17
  - 2.3.3. Vibration . . . 20
  - 2.3.4. Rotation . . . 23
- 2.4. Atom-light interaction . . . 24
- 2.5. Photoassociation . . . 25
  - 2.5.1. Saturated photoassociation rate . . . 27
- 2.6. 2-Photon Photoassociation . . . 29
- 2.7. Theory of optical traps . . . 32
  - 2.7.1. Optical dipole trap . . . 32
  - 2.7.2. Optical lattice . . . 34

3. Experimental apparatus 43
- 3.1. Three vacuum chambers . . . 43
  - 3.1.1. Atomic oven for Rb and Yb . . . 44
  - 3.1.2. Production chambers . . . 46
  - 3.1.3. The science chamber . . . 47
- 3.2. Piezoelectric cantilever shutter . . . 48
- 3.3. Rubidium laser system . . . 50
  - 3.3.1. Rubidium spectroscopy . . . 52

3.3.2. Repumpers . . . 52
3.3.3. The Rubidium MOT . . . 52
3.3.4. Imaging Rubidium . . . 55
3.3.5. Rubidium Tweezer . . . 55
3.4. Ytterbium laser system . . . 57
3.4.1. The blue system . . . 57
3.4.2. The green system . . . 59
3.4.3. Intercombination line MOT . . . 60
3.4.4. 30 W fiber amplifier . . . 66
3.4.5. Ytterbium Tweezer . . . 70
3.5. Lattice laser system . . . 73
3.6. The 532 nm laser system . . . 76
3.7. A new fiber laser for optical traps . . . 79
3.8. Photoassociation laser system . . . 83
3.9. Science chamber . . . 86
3.9.1. Crossed optical dipole traps . . . 86
3.9.2. Optical Lattice . . . 88
3.9.3. Verdi beam . . . 90
3.9.4. PA beam . . . 91
3.9.5. Imaging . . . 91
3.10. Microwaves . . . 93
3.11. Experiment Control and Data Analysis . . . 95
3.11.1. From Atticus to Cicero - operating complex machinery . . . 95
3.11.2. Collecting Images . . . 96
3.11.3. Analysing Images . . . 97

4. Preparation of an ultracold mixture 101
4.1. Rubidium . . . 103
4.1.1. The magneto optical trap . . . 103
4.1.2. Magnetic trap and microwave evaporation . . . 104
4.1.3. Optical tweezer and transport of atoms . . . 106
4.1.4. Crossed optical dipole trap and evaporation to a BEC . . . 109
4.1.5. Hyperfine state manipulaton via microwave . . . 111
4.2. Ytterbium . . . 115
4.2.1. Yb MOT . . . 115
4.2.2. Tweezer and transport . . . 119
4.2.3. Crossed optical dipole trap evaporation to a BEC . . . 120
4.3. Optical lattice . . . 122
4.3.1. Shaking and pulsing of a 1D lattice . . . 123
4.3.2. Loading and release of a ^{87}Rb-BEC . . . 125
4.4. Mixture in a combined trap . . . 126
4.4.1. Synchronized evaporation . . . 127
4.4.2. Lattice elevator loading and transport . . . 130

4.4.3. Merging sequence . . . 131
4.4.4. Final combined trap . . . 133

5. 1-Photon-Photoassociation 139
5.1. Introduction . . . 139
5.2. Photoassociation on the Yb intercombination line versus the D1 line of Rb . 139
5.3. Search for excited Molecules at the $^2S_{\frac{1}{2}}+^3P_1$ asymptote . . . 142
5.4. A single pair of photoassociation lines . . . 145
5.4.1. Zeeman shift . . . 145
5.4.2. Light shift . . . 147
5.4.3. Thermal shift . . . 147
5.4.4. Attempts at interpretation and line assignment . . . 148
5.4.5. Photoassociation rate . . . 159
5.4.6. Line strength . . . 161
5.4.7. Linewidth . . . 163
5.5. Photoassociation in a optical lattices . . . 167
5.5.1. Preparation in optical lattices . . . 167
5.5.2. 1-photon-PA in optical lattices . . . 167
5.5.3. Mott Insulator with an optical lattice . . . 171
5.5.4. Molecules in a Mott insulator . . . 172
5.6. Summary and Outlook . . . 173

6. 2-Photon-Photoassociation 175
6.1. Introduction to the RbYb ground state . . . 175
6.2. 2-photon-photoassociation with the intercombination line . . . 177
6.3. Shifts . . . 178
6.3.1. Zeeman shift . . . 178
6.3.2. Light shift . . . 179
6.3.3. Thermal shift . . . 179
6.4. Dark resonances . . . 179
6.5. Franck-Condon factors and Rabi frequencies . . . 181
6.6. Summary and future prospects . . . 183

7. Quest for the absolute ground state 185
7.1. Improving conditions for 1-photon PA near the intercombination line . . . 185
7.2. Balanced optical dipole traps . . . 188
7.2.1. Bichromatic traps . . . 188
7.2.2. Monochromatic traps . . . 189
7.3. Preparing vibrationally excited ground state molecules . . . 193
7.3.1. Guided decay . . . 193
7.3.2. Free-bound STIRAP . . . 194
7.4. The third photon - The next step towards absolute ground state molecules . 196

A. Appendix **201**
A.1. Hund's case (e) 201

Bibliography **203**

Danksagung **227**

Publications **229**

Eidesstattliche Erklärung **231**

1.

Introduction

This thesis is part of a research project on ultracold *Rubidium-Ytterbium* (RbYb) molecules in the Görlitz group at the Heinrich Heine University Düsseldorf. The focus of the research project is the creation and investigation of polar molecules in their rotational, vibrational and electronic ground state, in which they reveal interesting long range interactions. This introduction presents recent progress that has been made in the field of ultracold molecules and motivates fascinating applications to the RbYb molecule.

1.1. Motivation

Cold Atoms

The ability to cool atoms to extremely low temperatures approaching absolute zero (mK-µK) has opened up an important field in atomic physics. The first deceleration of atoms in a 'Zeeman slower' [32] and their subsequent trapping and cooling in the first magneto-optical trap (MOT) [33] by using lasers and magnetic fields enabled the study of cold atoms in a controlled environment. Subsequently more complex cooling techniques like polarisation gradient cooling [34] and Raman cooling [35] were invented. Together with the evaporative cooling technique, the temperature of a cold atom gas could even be reduced to the nK regime [36], which eventually led to the creation of the first 'Bose-Einstein-Condensates' (BECs) [37][38] which has meanwhile be achieved for many atomic species, in particular alkali metal, alkaline earth metal, and lanthanide atoms.

These quick advancements in laser cooling and the increasing ability to manipulate atoms facilitated the investigation of exciting new quantum phases and systems. Since the achievement of BEC and the Fermi degeneracy [39] it is now possible to observe phenomena of many body physics [40]. For example, exploring the behaviour of BECs in optical lattices created by laser light [41], the visualization of the quantum phase transition from a superfluid to a Mott insulator state [42], quantum droplets [43] and the interaction of diatomic mixtures [44] are especially notable. In addition to studying the fundamental properties of matter, laser cooling has lead to new precision experiments, like highly accurate optical lattice clocks [45], atomic fountain clocks [46] and the use of atom interferometers measuring the constant of gravity [47].

Cold Molecules

Turning the attention to cold molecules instead of atoms is the next big step as the rich internal structure of a molecule increases the complexity and is very interesting for physics as well as fundamental chemistry. A large number of combinations of alkali and alkaline-earth atoms can form bound molecular states that have become accessible with the technical progress of the field [48]. The diversity of the interactions between molecules is again most interesting in the ultracold quantum regime. This creates a new 'playground' for physicists and a new research field in molecular physics.

The great interest in ultracold polar molecules is mainly attributed to their dipole-dipole interaction resulting from a large electric dipole moment induced by charge separation [49]. Neutral atoms are mainly limited to short range interactions since they have only have a small magnetic dipole moment and an even smaller (and not yet detected) predicted electric dipole moment [50]. Depending on the complexity of the electron shell structure their magnetic dipole moments varies (Rb = $1\mu_B$, Cr = $6\mu_B$ and Dy = $10\mu_B$). Magnetic dipole interactions have been detected [51], [52], but they are only significant for a few elements and even for the most magnetic elements they are typically only of the order of the contact interaction. With molecules possessing a comparatively large electric dipole moment (of a few Debye) it is possible to use dipoles that interact with each other over longer distances extending the interaction length of a few Å in atomic mixtures to a distance of thousands of Å in optical lattices [53]–[55]. The properties of ultracold molecules enable the study of lattice spin models [56], the observation of quantum magnetism [57] and might even help to fully understand the theory of superconductivity [58]. Admittedly, the creation of such molecules and the observation of additional quantum phenomena introduced by their complex interactions remains a challenging task.

Other research areas could also profit from ultracold molecules, such as ultracold chemistry [2]–[4], precision measurements [5] and their prospective use for quantum computing [6]–[8].

Ultracold chemistry involves the study of chemical reactions at very low temperatures ($<$ 1 mK), which are largely unexplored. Observing these reactions in a controlled and precise manner becomes possible if the reactants are significantly slowed down and placed in their absolute ground state. An ensuing guided reaction provides insights in the fundamental mechanisms of collisions and reaction rates [59]. The possibility of repeating and easily changing the conditions of the process with quantum state preparation and external fields allows to tune reactions [4], [60]. It also offers the potential of inferring the behavior of higher temperature in detail, in order to develop more efficient methods of synthesis.

Precision measurements with molecules can test the fundamental units and forces in physics. The high spectral resolution achievable for ultracold molecules provides an ideal stage to test the smallest variations and search for extremely small interactions. Molecules are used to search for the electron electric dipole moment (eEDM) [61]–[64], the evolution of the fine structure constant [65] or the variation of the electron-to-proton mass ratio [66]. Even more complex molecules with more than two atoms such as ammonia have recently been cooled and show interesting prospects for future precision measurements [67].

Even before the Nobel prize in physics in 2022 was awarded for the '*Experiments with entangled photons, establishing the violation of Bell inequalities and pioneering quantum information science*' [68], quantum simulation and computation has attracted a lot of additional attention. Ultracold molecules are among the best candidates for the storage of qubits [69] or even as qudits [70]. One of the main advantages of using ultracold polar molecules for quantum computing is, that they can be made to interact with one another in a controlled and precise way via long range interactions using their large electric dipole moments. Another advantage is the (possibly) long coherence time duration allowing the qubits to be manipulated for longer a longer time [71].

1.2. Cooling and making molecules

There are generally two paths to produce cold molecules. The first is to use the well established cooling techniques known from atoms and apply them directly to molecules. While molecules are much harder to handle due to their multitude of transitions, a lot of progress has recently been made in the direct laser cooling of molecules [72]. Relevant criteria for such molecules are strong transitions that allow scattering of a large number of photons to slow the heavy molecule down and a relatively simple ground state hyperfine structure. One of the main challenges is to find quasi closed transitions to avoid decay into intermediate states, which require a high number of re-pump lasers. The accessibility of wavelengths and high intensity for the required lasers still limits the selection of molecules that can be cooled, although laser technology is catching up fast. Up until now, laser cooling below the Doppler limit [73] as well as confinement in magneto-optical, magnetic and optical traps is already possible as reported by recent experiments with CaF [73], SrF [74], YbF [64], YO [75] and SrOH [76] and has been proposed for several more. Even elastic collisions between ultracold ground-state CaF molecules have been observed recently [77], indicating that the direct laser cooling approach is catching up with the more conventional way of making molecules from ultracold atoms.

However, the greatest success of ultracold atom experiments is still prevalent in the creation of cold molecules. The RbYb molecule presented in this thesis is created by first individually cooling down its atomic constituents followed by their photoassociative assembly to molecules. The commonly used tools to create molecules from ultracold mixtures of atoms are magnetic Feshbach resonances [78] and photoassociation (optical Feshbach resonance) [79].

In magnetic Feshbach resonances, tuning of a magnetic field shifts a bound molecular state relative to the scattering state of free atoms. By ramping over a resonance, both states are energetically close for a short time allowing atoms to be turned into molecules and vice versa. The effectiveness of this process heavily depends on the applicable coupling mechanisms. For bi-alkali molecules magnetic Feshbach resonances are broad and widely successful due to their strong interaction via electron spins [80]. In the case of the RbYb molecule however an alkali atom (Rb) is paired with a closed-shell alkaline-earth atom (Yb). Here the dominating electron-spin coupling does not exist but alternative mecha-

nisms have been proposed to produce weaker resonances [25], [81], [82]. Fortunately other experiments with similar molecules recently reported Feshbach resonances in RbSr [26], CsYb [27] and LiYb [28] and urge us to also find them in RbYb. The observed resonances are however much narrower than in bialkali mixtures, which makes their application for molecule production challenging.

Photoassociation is the second route to converting atoms to molecules, which is the path we have so far pursued for RbYb. In 1-photon photoassociation a single photon can induce the optical coupling between the scattering state and an electronically excited molecular state if two atoms collide and absorb the photon during the collision. Subsequently, the excited molecule will either split up into a pair of single atoms or decay into bound molecular ground states with high vibrational quantum numbers. It typically can follow multiple decay channels into different vibrational ground state levels and is thus hard to track. However, a decay channel with a large Franck-Condon factor can provide a predominant selection of a single state. This easy method requiring only a single laser, a beneficial molecular structure and subsequent molecule detection was first presented in Cs_2 [83]. An extension of this principle is the use of a second photon in 2-photon photoassociation, which guides the decay into the desired ground state by coupling the electronically excited state to a specific vibrational ground state. If both lasers are used, the first can pump atoms into an intermediate excited molecular state and the second causes stimulated emission to dump them into the molecular ground state, as reported for the production of RbCs molecules [84]. Unfortunately, this process remains inefficient because of its incoherence and the decay of the intermediate state.

The transfer of molecules with a coherent process such as stimulated Raman adiabatic passage (STIRAP) [85] circumvents the necessity to populate an excited state and therefore increases the transfer efficiency [86], [87]. This method already helped many ultracold molecule experiments to reach the rovibronic ground state, proving its high transfer efficiency and robustness, with Rb_2 [88], KRb [89], Cs_2 [90], RbCs [31], [91] and NaK molecules [54]. However these experiments already start with previously associated weakly bound Feshbach molecules. Having no access to usable Feshbach resonances (as currently the case for the Rb-Yb system) forces experimenters to use free-bound transitions, which are much weaker due to the small wave function overlap with a scattering state. Nevertheless, the production of Sr_2 molecules in the electronic ground state using STIRAP on unbound atom pairs demonstrates the feasibility of this approach if no viable Feshbach resonances exist [29], [30]. This method can be extended to an all-optical production of ground state molecules from free atoms with two independent subsequent STIRAP sequences and a total of four laser fields [22]. An all optical creation of Sr_2 molecules in the absolute ground state has recently been achieved with the combination of a photoassociation pulse followed by spontaneous decay into a weakly bound molecule and a subsequent STIRAP process [92].

1.3. Why RbYb molecules ?

As already mentioned, most work on ultracold molecules focuses on alkali metals forming dimers. Their big advantage is the single valence electron, which makes them easy to cool with lasers in an easily accessible wavelength spectrum. However the molecule associated from alkali metals always has a diamagnetic ground state since the electron spins contributed the two atoms cancel each other. A pairing of an alkali metal and an atom with a closed electron shell like Yb or alkaline earth atoms such as Sr leaves the electron spin of the alkali atom unpaired. Therefore diatomic molecules with this specific combination not only have an electric but also a magnetic dipole moment in the absolute ground state. In the case of RbYb molecules we obtain a paramagnetic $^2\Sigma_{1/2}$ ground state, which allows the manipulation with electric and magnetic fields.

Since we are using the pathway of creating molecules from ultracold mixtures, it is advisable to pick elements that have previously been cooled to degeneracy. The Rb atom is among the most frequently used alkali metals and was the first one for which BEC was achieved [38], due to its advantageous scattering length and accessible laser cooling transitions. Yb on the other hand has a narrow linewidth intercombination transition that allows cooling to µKs and high resolution spectroscopy and has been successfully cooled to quantum degeneracy [93], [94].

With two Rb isotopes and seven Yb isotopes a lot of combinations allow the formation of bosonic and fermionic molecules in a Rb-Yb mixture. The choice of the ^{87}Rb isotope combined with the remaining options in Yb already covers a wide range of scattering lengths and interaction properties (see figure 2.3).

There is a hand full of experiments that work with similar diatomic mixtures, which come with some perks and downsides, like interesting mass discrepancies and molecular ground states but also face technical challenges in molecule production. Comparing and discussing their experiences and results is very helpful for the progress of research. To the best of the authors knowledge the research on open-shell ground state molecules is still limited to experiments on RbSr [95] in Amsterdam (Schreck group), CsYb [96] in Durham (Cornish group), LiYb [97], [98] in Seattle (Gupta group), LiEr in Kyoto (Takahashi group)[1] [99] and finally our experiment on RbYb in Düsseldorf (Görlitz group). An effort to produce RbYb molecules had also been started in Maryland (Porto group) [100] but has meanwhile been discontinued.

1.4. Previous work on RbYb molecules

There is already a lot of work conducted on RbYb molecules since the research at the Heinrich-Heine-University Düsseldorf began in 2004 [9]. Past experiments started with sympathetic cooling of Yb with Rb [10] and the investigation of thermalisation and interaction of different isotopes [12]. This lead to the finding of a remarkable isotope separation of ^{174}Yb and ^{87}Rb [101] and an extremely small interaction between ^{170}Yb and ^{87}Rb, which

[1] They also announced starting to work on ultracold triplespecies quantum gas mixtures of Yb, Er and Li.

suggested a large positive s-wave scattering for ^{174}Yb +^{87} Rb and a value close to zero for ^{170}Yb +^{87} Rb.

Long term efforts on studying the production and photoassociation spectroscopy of RbYb molecules along the D1 asymptote of Rb, yielded information on the binding energies of the electronically excited $^2\Pi_{1/2}$ state down to a binding energy of $E_b = h \cdot 2.2\,\mathrm{THz}$ [11], [14], [19], [102]. Moreover with 2-photon photoassociation spectroscopy the $^2\Sigma_{1/2}$ ground state was probed down to a binding energy of $E_b = h \cdot 58\,\mathrm{GHz}$ [13], [14], [19].

Growing knowledge of the (ground state) molecular potential curves allowed a calculation of all scattering lengths in the RbYb system [15]. Unfortunately, no magnetic Feshbach resonances were found during a search [14] for some of the predicted resonances suggested in [25]. However Autler-Townes spectroscopy was performed in a double species MOT to determine relative Franck–Condon factors of molecular transitions in RbYb for efficient future molecule production [103].

Important theoretical work on the potential energy curves of the RbYb system was performed by Sorensen et al. [16] in 2009, by Tohme et al. [17] in 2013 and later by Shundalau et al. [18] in 2017. Furthermore an optical cycle model suggesting transitions into the ground vibronic state for RbYb (and CsYb) was presented in [104]. Another approach to produce ground state molecules by picking alternative magnetic Feshbach resonances that utilise the ^{3}P manifold of Yb was recently proposed in [105].

There have also been other research groups that invested some time to study Rb and Yb interactions. Namely the group at the Joint Quantum Institute of the University of Maryland where degenerate Bose-Fermi mixtures were investigated [100] and the group at the University of Hamburg who spent a limited amount of time with a combination of Yb with Rb [106] but have since then been more interested in degenerate Yb mixtures with different isotopes.

1.5. Thesis outline

The goal of this thesis was to construct and develop a new RbYb molecule experiment pioneered by Franzen [1] and lead it towards the production of absolute ground state molecules. After retiring the old molecule experiment that was operated in Düsseldorf for more than ten years, a new machine was designed to improve on the shortcomings of its predecessor. The new apparatus features three vacuum chambers for individual trapping and cooling, easy reconfiguration and most of all improved optical access. The distance between the chambers is covered by long distance optical transport.

During this thesis the new experiment caught up and even surpassed its previous version in many aspects. It is now able to routinely prepare ultracold mixtures of Rb and Yb and proved its capabilities by individually achieving Bose-Einstein-condensation for each species. First successful photoassociation measurements utilizing the narrow intercombination line transition $^2\mathrm{S}_{1/2} +^3 \mathrm{P}_1$ [20] show the capabilities of high resolution spectroscopy. This could be the first step towards free-bound STIRAP in future attempts to create ground state molecules. Striving for enhanced photoassociation rates is kicked

of by the development of a 3D optical lattice and the first successful photoassociation experiments within this trap. This thesis marks the first step towards a mixed Mott insulator state on the way to efficiently produce long-lived ground state molecules via free-bound STIRAP [30].

This thesis is organised as follows, starting with this introduction and continues in chapter 2, where the theoretical background needed to understand the atomic and molecular physics relevant to this work is covered. Furthermore the second chapter deals with the method of photoassociation, the concept of optical traps in which our experiments are performed and motivates the choice of isotopes. In chapter 3, I describe the entire experimental apparatus from the vacuum system to the developed laser systems, microwaves, imaging technique and experiment control. Chapter 4 then explains the experimental sequence and how to operate the molecule machine. The preparation of Rb and Yb is individually explained, from loading MOTs with Zeeman slowers to the evaporation in crossed optical dipole traps to quantum degenerate gases. Next the 3D optical lattice and current techniques to join both atomic species to an ultracold mixture is discussed. Afterwards I present the experiments performed with 1-photon photoassociation in two different optical traps in chapter 5. During our extensive search covering more than 10 GHz in frequency a single pair of resonances to an excited molecular potential was discovered. This signal is evaluated in terms of line shifts and photoassociation rate. Moreover an attempt at molecular state assignment is made. Continuing with 2-photon photoassociation experiments in chapter 6, I present high precision spectroscopy of the least two bound molecular ground states. Additionally, we performed dark resonance spectroscopy on both states, which gives us estimates for the free-bound and bound-bound Rabi frequencies. In the end I will talk about the quest for the absolute ground state of RbYb molecules in chapter 7, where I suggest improvements to the machine and give an outlook into the future production of absolute ground state molecules including a dual Mott insulator state inside the optical lattice, possible magnetic Feshbach resonances and applications of STIRAP sequences. Finally, the results of this thesis are briefly summarized.

2.

Theory of atoms and molecules

This chapter explains the theoretical concepts needed to understand the relevant atomic and molecular physics for this thesis. Section 2.1 starts off with collisions between atoms and connects to section 2.2, where I discuss the scattering behaviour of all Rb and Yb isotope combinations motivate our specific selection of isotopes. In section 2.3 I briefly summarize angular momentum coupling in molecules and molecular potentials. Afterwards, section 2.5 and 2.6 explain the methods of 1-photon and 2-photon-photoassociation. Finally, section 2.7 introduces the theory of optical traps (ODT and 3D optical lattice), in which we perform the experiments of my thesis.

2.1. Colliding Atoms

Moving atoms, provided they are not identical fermions, will collide or 'scatter' once they meet another particle. Understanding scattering events is crucial for experiments with trapped ultracold atoms. They determine how and to what magnitude atoms inside a tightly confined space interact with each other. First 'elastic collisions' enable thermalisation and thus evaporative cooling in atomic samples (chapter 2.1.1). Secondly, three-body collisions, two-body spin relaxation or collisions with background gas can be summarised as 'inelastic collisions' (chapter 2.1.2). Furthermore the stability of a BEC and the miscibility of a two-species mixture depend on the famous 'scattering length' and thus the choice of isotopes for this experiment (chapter 2.2).

2.1.1. Elastic collisions

For elastic collisions the internal states and the total kinet,0, ic energy of the colliding bodies remains the same. In quantum gas experiments they are important for thermalisation in cold atom traps and the production of molecules via photoassociation or Feshbach resonances. Therefore it is helpful to learn about collisions in the quantum world. The following section is based on the references [107]–[109], where more details can be found.

Consider a collision of two quantum particles as an interaction of an incident wave with a potential $V(\vec{r})$. The incoming non-relativistic particle with wave vector $\vec{k} = \vec{p}/\hbar$ is scattered with the relative momentum $\vec{p}$ and energy E. This scattering process can be described with the time-independent Schrödinger equation.

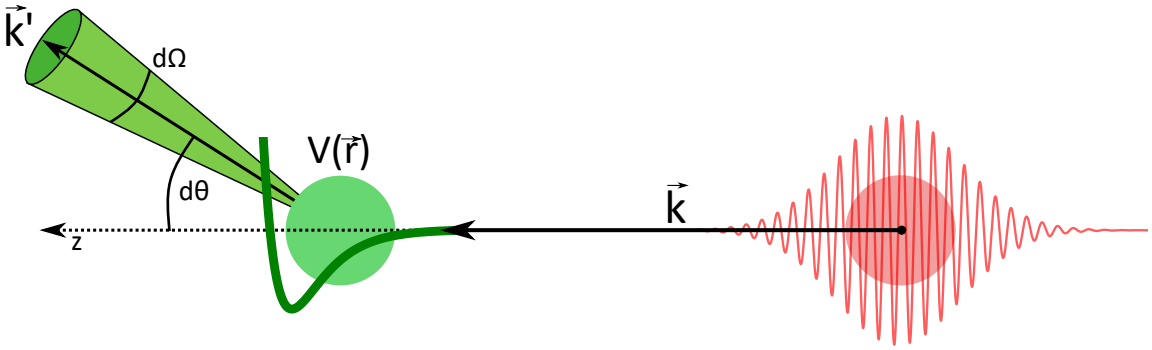

Figure 2.1.: Sketch of an elastic scattering process. The incident wave $\vec{k}$ is scattered by potential $V(\vec{r})$ and deflected in direction $\vec{k'}$ under the solid angle $d\Omega$.

$$\left(\frac{\hat{\vec{p}}^2}{2\mu} + V(\vec{r})\right)\Psi(\vec{r}) = E\Psi(\vec{r}) \tag{2.1}$$

The solution $\Psi(\vec{r})$ of this equation[1] consists of the incident wave Φ_{in} and the scattered wave Φ_{out}.

$$\Psi(\vec{r}) \propto \Phi_{\text{in}} + \Phi_{\text{out}} = e^{-i\vec{k}\vec{r}} + f(k,\theta)\frac{e^{ikr}}{r} \tag{2.2}$$

The scattering amplitude $f(k,\theta)$ depends on the energy and the angle of deflection θ. From it one can determine the differential and total scattering cross-section:

$$\frac{d\sigma(k,\theta)}{d\Omega} = |f(k,\theta)|^2 \qquad \text{and} \qquad \sigma(k) = \int |f(k,\theta)|^2 d\Omega \tag{2.3}$$

Here $d\Omega$ is the solid angle for the deflected wave and $\sigma(k)$ can be understood as the effective area in which particles experience a scattering event.

In order to find a solution to the scattering problem and an expression for the scattering amplitude the radial wavefunction is decomposed into partial waves with Legendre polynomials $P_l(\cos\theta)$, where l indicates the angular momentum involved in the collision.:

$$f(k,\theta) = \frac{1}{2ik}\sum_{l=0}^{\infty}(2l+1)(e^{2i\delta_l(k)} - 1)P_l(\cos\theta) \tag{2.4}$$

Here $\delta_l(k)$ is a phase shift that is picked up in a collision in the l'th partial wave. The cross section $\sigma_l(k)$ thus depends on the angular momentum l, which gives rise to the centrifugal barrier $\frac{\hbar^2 l(l+1)}{2m_\mu r^2}$ and changes the effective potential as illustrated in figure 2.2 [108].

The total cross section is

$$\sigma(k) = \sum_{l=0}^{\infty}\sigma_l(k) \qquad \text{with} \qquad \sigma_l(k) = \frac{4\pi}{k^2}(2l+1)\sin^2\delta_l(k) \tag{2.5}$$

[1] We assume that $V(\vec{r})$ is zero for large $|r|$.

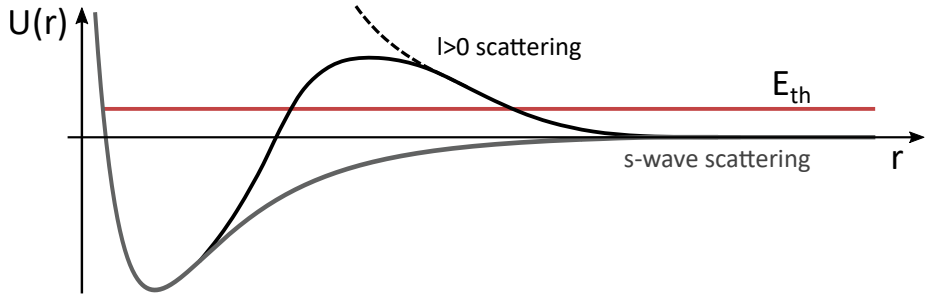

Figure 2.2.: Sketch of the centrifugal potential barrier for $l > 0$ scattering compared to s-wave scattering.

For quantum particles at the low energy limit ($k \to 0$) - where only s-wave scattering (l=0) is allowed - the expression simplifies to $\sigma(k) = 4\pi a^2$ for distinguishable particles and $\sigma(k) = 8\pi a^2$ for indistinguishable particles. The scattering length a is thereby defined as [108]:

$$a = -\lim_{k\to 0} \frac{\tan\delta_0(k)}{k} \tag{2.6}$$

The effective cross section (and thus the scattering length) determines the elastic collision rate per atom

$$\gamma_{el} = n\sigma\langle v_r\rangle_T \tag{2.7}$$

in a gas with density n and average relative thermal velocity $\langle v_r\rangle_T$ for temperatur T [110]. If it is sufficiently large, evaporative cooling down to a BEC (only for bosons) can be performed in a reasonable timescale.

2.1.2. Inelastic collisions

In inelastic collisions, the internal state of a particle can be changed by the scattering event. For ultracold atoms this typically results in a release of kinetic energy. Typical inelastic collisions in ultracold atom experiments are three-body recombination, spin relaxation or collisions with high energy particles from the background gas. All of these are so called 'bad' collisions since they are unwanted and lead to a loss of atoms in a trap [111]. Three-body collisions are of main interest for our experiment since they scale with the density squared.

A three-body recombination happens if three atoms collide and form a bound molecule with two atoms while the third atom carries away the released binding energy of the molecular state. The process leads to a loss of all three atoms as the trap depth is usually to shallow for the products. The three-body collision rate measures the thermal recombination per atom in [s^{-1}] and can be written as

$$\gamma_3 = K_3 n^2 \tag{2.8}$$

with K_3, the three-body constant in $[\mathrm{cm}^6\mathrm{s}^{-1}]$ [110], [112]. In an experiment with Rb and Yb, both single-species and mixed-species three-body collisions have to feature small K_3 values to avoid high trap losses. Ultimately, for high densities $> 10^{13}\,\mathrm{cm}^{-3}$ and ultracold temperatures $< 10\,\mu\mathrm{K}$ the elastic collision rate has to be much larger than the inelastic collision rate for every combination of possible reaction partners [2].

2.2. Isotope selection

This section discusses the practicability of different isotope combinations of Rb and Yb in our experiment based on their properties. Key aspects to look out for are the individual thermalisation rates for evaporative cooling of Rb and Yb samples, the miscibility of the isotopes when joining both quantum gases to an ultracold mixture and the suitability of RbYb molecules in a dual Mott insulator state (see section 2.7.2).

Scattering length

Before the isotope selection we first take a look at the scattering lengths in figure 2.3 and table 2.1. The figure showing the interspecies scattering lengths contains vertical lines indicating a pole where the scattering lengths diverge. This occurs when the least bound state of the scattering potential is crosses the threshold. An *ab initio* calculation for these scattering lengths is practically impossible without precise knowledge of the potential. Measurements of the least bound levels of molecule potentials via photoassociation are the best way to determine accurate values for a [15][114]. The more direct but way more complicated method is the observation of collision dynamics in a BEC, which can be used if photoassociation lines have yet to be found.

Coming back to the already determined values ([15] in 2011) in table 2.1 - large scattering lengths imply strong interaction due to a large effective cross-section $\sigma(k) \propto a^2$ and thus high collision rates. For large absolute values of the scattering length a big upside is the rapid thermalisation, which allows very fast evaporation times. Small values have the opposite effect. The sign of a scattering length indicates an attractive (negative sign) or repulsive (positive sign) interaction.

positive **a** : For large positive values the three-body constant scaling $K_3 \propto a^4/\mu$ [113] leads to a fast decay in high density gases[1]. Furthermore diatomic mixtures with large interspecies scattering lengths can become immiscible, which was demonstrated by a striking phase separation for ^{174}Yb and ^{87}Rb in [101].

negative **a** : For large negative values degenerate quantum gases are hard to achieve because they collapse beyond a relatively small critical atomnumber $N_{\max} = \sqrt{\frac{2\hbar}{m\omega_0 a^2}}$ due to their attractive interaction.

small **a** : Small scattering lengths combine the advantage of negligible three-body losses and good miscibility with the disadvantage of slower thermalisation rates.

[2] A scaling law for the three-body constant for large scattering lengths a is $K_3 \propto \frac{a^4}{\mu}$ [113]

[1] This is also the case for negative scattering lengths.

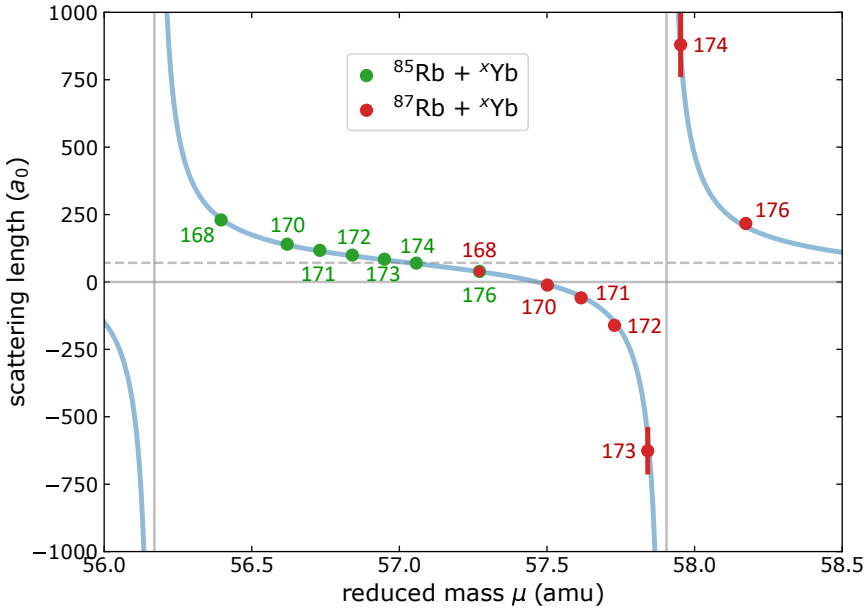

Figure 2.3.: Interspecies scattering lengths a of Rb-Yb pairs as a function of reduced mass μ. Data from [15] and dashed line giving the mean scattering length of Gribakin and Flambaum [115].

Fortunately magnetic Feshbach resonances are able to tune the scattering length to circumvent the mentioned problems [116].

Rubidium and Ytterbium

There are a total of 14 options to choose from two available rubidium and seven ytterbium isotopes. Starting with rubidium, both isotopes are bosons with nuclear spin. ^{85}Rb is the more abundant isotope with 72.17 % compared to ^{87}Rb with 27.87 %. More importantly they have completely different intraspecies scattering lengths. ^{85}Rb has a large negative value at $-400\,a_0$ and ^{87}Rb has a smaller positive length at $100\,a_0$. While the interspecies scattering values between ^{85}Rb and the Yb isotopes look promising for sympathetic cooling, they are all positive with similar size and thus offer less exciting interactions. The big problem with this Rb isotope though is the creation of a stable BEC. Although magnetic Feshbach resonances have been used to tune the scattering length of ^{85}Rb and make stable BECs possible [117], it is still an uncomfortable isotope to work with. The golden standard for a lot of quantum gas experiments thus is still ^{87}Rb. Its convenient scattering length and easy transitions for laser cooling enabled the first BECs [38]. Furthermore our science chamber is currently not equipped with the required bias fields and adapted microwave fields[2] for ^{87}Rb but some redesign would make a switch to the ^{85}Rb isotope feasible.

With the current choice of our ^{87}Rb isotope seven possible combinations with Yb remain. This element is about twice as heavy as Rubidium and has five bosonic and two fermionic isotopes. The bosons all have no nuclear spin while the fermions ^{171}Yb and ^{173}Yb have

[2]Different nuclear spin changes the hyperfine structure splitting.

$I = 1/2$ and $I = 5/2$ respectively. Generally having the free options between Bose-Bose, Fermi-Fermi or Bose-Fermi mixtures is a advantageous perk in experiments with Yb as showcased by interacting dual Mott insulators of bosons and fermions [118] and the study of novel quantum phases in a mixture of the two fermionic isotopes in the Takahashi group [119]. For us the hyperfine structure of fermionic Yb would increase the complexity of photoassociation spectra and controlled preparation of the spin mixture. While this does not rule out fermions entirely, it suggests to start with the simpler bosonic mixtures. The intraspecies scattering lengths of Yb are quite diverse but impossible to tune because the ground state of Yb has no magnetic structure. This rules out the use of magnetic and leaves optical Feshbach resonances [120], [121] as an uncomfortable option inducing unwanted trap losses. For this reason the choice of the Yb isotope becomes less negotiable. Table 2.1 features colored markers labeling the weaknesses of each option which are now discussed. Isotopes are generally favourable if their abundance is high, evaporation performs well, inelastic collision rates are small and miscibility with the other species is given.

Table 2.1.: Scattering lengths and three-body constants for Ytterbium isotopes [110]

Isotope	Abundance [125] [%]	Yb-Yb $[a_0]$	^{87}Rb^{X}Yb $[a_0]$	^{85}Rb^{X}Yb $[a_0]$	K_3^{YbYb} [113][122] $[cm^6 s^{-1}]$	K_3^{RbYb} [123][124] $[cm^6 s^{-1}]$
^{168}Yb ●	0.1	252	39	230	$1.4 \cdot 10^{-28}$	$4.3 \cdot 10^{-32}$
^{170}Yb ■	3.0	64	-11	140	$5.7 \cdot 10^{-31}$	$3.8 \cdot 10^{-34}$
^{171}Yb ★	14.3	-3	-59	117	$2.7 \cdot 10^{-36}$	$2.2 \cdot 10^{-31}$
^{172}Yb ◆ ▲	21.8	-599	-161	100	$4.3 \cdot 10^{-27}$	$1.2 \cdot 10^{-29}$
^{173}Yb ◆ ▲	16.1	-200	-626	84	$5.2 \cdot 10^{-29}$	$2.8 \cdot 10^{-27}$
^{174}Yb ▼ ◆	31.8	105	880	70	$4.0 \cdot 10^{-30}$	$1.1 \cdot 10^{-26}$
^{176}Yb ▲ ★	12.8	-24	217	39	$1.1 \cdot 10^{-32}$	$4.0 \cdot 10^{-29}$

● low abundance ■ small $a_{(\mathrm{Yb}\text{-}^{87}\mathrm{Rb})}$ ★ small $a_{(\mathrm{Yb\text{-}Yb})}$ ◆ K_3 too high ▲ collapsing/unstable ▼ not miscible with ^{87}Rb

● ^{168}Yb is simply ruled out because of its very low natural abundance of 0.1 %.

◆ ▲ ^{172}Yb has a large negative intraspecies scattering length and thus high inelastic loss rate K_3^{YbYb} leading to problems during evaporation or long hold times. Reaching quantum degeneracy is extremely difficult for this isotope.

◆ ▲ ^{173}Yb is a fermion and has a similar issue with a large negative scattering length with ^{87}Rb creating three-body losses.

▼ ◆ ^{174}Yb has the highest abundance and a favourable intraspecies scattering length. It has thereby been the most convenient isotope for the setup and calibration of the machine

until it meets ^{87}Rb. Due to the large positive scattering length ^{87}Rb and ^{174}Yb simply do not want to mix making photoassociation only possible at the interface.

▲ ★ ^{176}Yb already has a relatively small intraspecies scattering length which makes evaporation inefficient and slow. But once temperatures in the range of the optical traps are reached, a Ramsauer-Townsend minimum at 25 µK [114] is approached, which brings thermalisation to a hold. Furthermore it is also hard to condense.

★ ^{171}Yb has an even smaller intraspecies scattering length and needs to be cooled sympathetically. For this the scattering length with ^{87}Rb is actually suitable but requires an excellent overlap of both quantum gases to be effective. A bichromatic trap design to match the trap depth for both species is recommended for all isotope combinations but is even more critical in this case. Moreover this isotope is also a fermion.

■ ^{170}Yb is left and currently the chosen isotope. It's intraspecies scattering length is convenient for evaporation and features low three-body loss rates. Furthermore it is insensitive to the temperature of ^{87}Rb due to a very small interspecies scattering length and has good miscibility. The only downside of this weak interaction is the difficulty of thermalisation measurements and determination of overlap between both atom clouds. Finally the combination of a repulsive interaction for both species in the intraspecies case and an attractive interaction for the mixed case creates a favourable Mott-Insulator state for experiments in optical lattices.

Table 2.2.: Properties of the selected Rubidium and Ytterbium isotopes

property	symbol	^{87}Rb [126]	^{170}Yb
mass	m	86.909 u	169.935 u [127]
nuclear spin	I	3/2	0
abundance	η	27.83 %	3.04 % [127]
scattering length	a_{gg}	$98.98 \pm 0.04\, a_0$	$63.87 \pm 0.02\, a_0$ [128]
vapor pressure	P_v	$2 \cdot 10^{-3}$ torr (125°C)	$8 \cdot 10^{-2}$ torr (440°C) [129]

2.3. Molecular Physics

While molecular spectroscopy has been carried out for a long time, this field is still very active and partly unexplored. Even the study of relatively simple diatomic molecules is considerably more complex compared to single atoms. The interaction of two nearby atoms changes the well understood electronic structure. New quantum numbers need to be introduced because a molecule has the possibility to vibrate ν, rotate J and has a larger number of angular momenta involved. This leads to different couplings of angular momenta in molecules, which will be treated in the following chapter. More extensive literature about diatomic molecules can be looked up in [130]–[134].

2.3.1. Angular momentum coupling in molecules

Molecular states are composed of angular momentum coupled atomic states. Considering various ways on how these momenta can be assembled gives rise to Hund's coupling cases [135], [136]. The categorisation into such cases helps physicists understand molecular spectra and defines the so called 'good' quantum numbers to describe a molecular state. What eventually becomes a good quantum number depends on the dominant energy term of the interaction at hand. However it should be noted that this description works best in idealised situations and is not necessarily applicable to all systems which may have to be assigned to a mix of cases.

The angular momenta involved to compose the standard five Hund's cases (a) - (e) are the following:

- $\vec{L} = \vec{l_1} + \vec{l_2}$ the electronic orbital angular momentum.
- $\vec{S} = \vec{s}_1 + \vec{s}_2$ the electronic spin angular momentum.
- $\vec{J} = \vec{L} + \vec{S} + \vec{R}$ the total angular momentum.
- $\vec{N} = \vec{J}$ - $\vec{S}$ the total angular momentum excluding electron spin.
- $\vec{R} = \vec{N}$ - $\vec{L}$ the rotational angular momentum of the nuclei.

The choice of letters for the momenta is somewhat arbitrary and can therefore deviate from other literature. The selection of Hund's cases and the notation for molecular states mainly depends on the size of the molecule or rather the internuclear separation R. Tightly bound molecules with $R < 20\,a_0$ in a short range potential are assigned to case (a) or (b). In Hunds case (a) the orbital and spin momentum of each atom directly couples to the molecular axis. Since a diatomic molecule is linear, the projection of these angular momenta onto the internuclear axis is important. For the precession of the electronic orbital angular momentum $\vec{L}$ around the axis, the absolute value projection along the axis is labeled Λ. Likewise the projection of the electronic spin angular momentum $\vec{S}$ becomes Σ. The two projections Λ and Σ then couple together and form $\Omega = \Lambda + \Sigma$ as the projection of the total angular momentum along the axis. The molecular term symbol is then written as

$$^{2S+1}\Lambda^{\pm}_{\Omega,(g/u)} \tag{2.9}$$

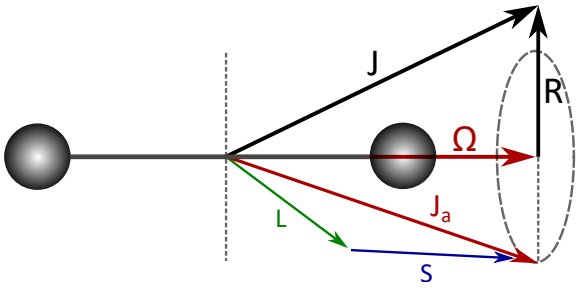

Figure 2.4.: Hunds case c).

with g/u indicating the parity and +/− the reflection symmetry of wavefunctions at a plane containing the internuclear axis. In analogy to the atomic notation of angular momentum, states with $\Lambda = 0, 1, 2, ...$ are assigned to the Greek letters Σ,Π,Δ etc.

In this thesis we will create long range RbYb molecules through photoassociation with $R > 40\,a_0$ and thus cannot apply the molecular notation for Hunds case (a) and (c) to any spectrum we find. For heavy atoms with many electrons this far apart, the electrostatic interactions are smaller because the electron clouds are well separated and not distorted. If the rotational constant of the molecule is small compared to the electric energy, also discussed in section 5.4.4, Hund's case (c) may be an appropriate choice.

Hund's case (c)

In Hund's case (c) the projections Λ and Σ are not defined and cease to be good quantum numbers because of a strong spin-orbit coupling. Figure 2.4 illustrates how instead the orbital angular momentum $\vec{L}$ and spin angular momentum $\vec{S}$ will couple and form $\vec{J}_a$, which precesses around the nuclear axis. Its projection onto the internuclear axis becomes Ω, which can have positive and negative sign $\pm\Omega$ and thus has a two fold degeneracy for a non-rotating molecule called Ω-doubling (5.4.4). The nuclear rotational angular momentum is now vectorially added ($\vec{J} = \vec{R} + \vec{\Omega}$) to Ω yielding the total angular momentum of the molecule $\vec{J}$.

The quantum numbers describing case (c) are $|n, J_a, J, \Omega, M_J\rangle$. The electronic states are characterised by Ω values as well as the total angular momentum of the molecule J. The molecular states for such molecules are labeled as

$$\Omega^{\pm}_{(g/u)} \tag{2.10}$$

Furthermore for values of $\Omega > 0$ we expect the states to be degenerate if the molecule has no rotation. We thus expect state splitting for molecules that rotate, which removes the Ω-doubling degeneracy of the molecular states with the rotational levels having relative energies of $E_J = BJ(J + 1)$ [131].

2.3.2. Molecular potentials

The RbYb molecules considered in this work are often called 'physicist molecules' to emphasize their weak coupling compared to ionic or covalent bonds. The electrostatic interactions

or Van der Waals force, holding our atoms together to form a diatomic molecule, depend on the distance of the nuclei. The molecular potentials discussed here are adiabatic energies as a function of the distance between the atoms cores in diatomic molecules forming molecular potential energy curves (PECs) that depend on the electron configuration of its constituents. It is important to note that the described potentials $V(\vec{r})$ only depend on the nuclear motion[1] in contrast to the description with Hunds cases, where the complete molecule with all electrons is described. As an example, figure 2.5 shows the comparison of model potentials, namely a Morse potential from Soerensen [16], a Lennard Jones potential produced from C_n coefficients of Münchow [137] and an ab initio perturbation theory potential curve from Shundalau et al. [18] of the $^2\Sigma_{1/2}$ ground state of RbYb.

Noticeably they all look different due to the fact that determining the shape of a molecule potential $V(\vec{r})$ (in 2.12 and 2.14) depending solely on nuclei distance is very challenging without sufficient experimental data[2]. In principle the Schrödinger equation

$$\left(-\frac{\hbar^2}{2\mu}\frac{\partial^2}{\partial r^2} + V(\vec{r}) + \frac{\hbar^2}{2\mu\vec{r}^2}(J(J+1))\right)\Psi(\vec{r}) = E\Psi(\vec{r}) \tag{2.11}$$

with the reduced mass μ and rotational quantum number[3] J, has to be solved in order to obtain eigenenergies $E < 0$, that give the binding energies of the molecule. However even the simplest molecules[4] can not be solved analytically and in the case of Rb and Yb, a plethora of 107 electrons contribute to the interaction potential $V(\vec{r})$. For this reason some approximations have to be made to simplify the calculations. The most prominent one in molecular dynamics is the Born Oppenheimer approximation. It assumes that the wavefunctions of electrons and the nuclei of a molecule can be treated separately, since the atoms core is much heavier and slower than electrons.

Ab-initio calculations - various methods are summarized in [134] - try to get as close to the real molecule as possible. However they have to use reasonable approximations to all components making up the Hamiltonian [138]. For this reason they are not always as accurate as an experimental physicist wants them to be. On one hand calculations are important for guidance in photoassociation experiments and help to understand the molecule. On the other hand, experimental results on binding energies is valuable feedback to theorist and helps them to tune their potential curves to more accurately predict the molecule.

Typically these potentials are handled in two parts: the short range and the long range region of the potential. In the next subsections we treat two approaches that represent good approximations for each region before we return and use one of them to find the vibrational states near the dissociation energy.

[1] In the Born-Oppenheimer approximation nuclei and electrons are treated separately.

[2] Note that the Lennard Jones potential was actually used to reproduce experimental data in a very limited range and thus cannot be expected to fit at other internuclear separations.

[3] Despite the confusing notation, the total angular momentum and the rotational quantum number are not equal.

[4] except H_2^+

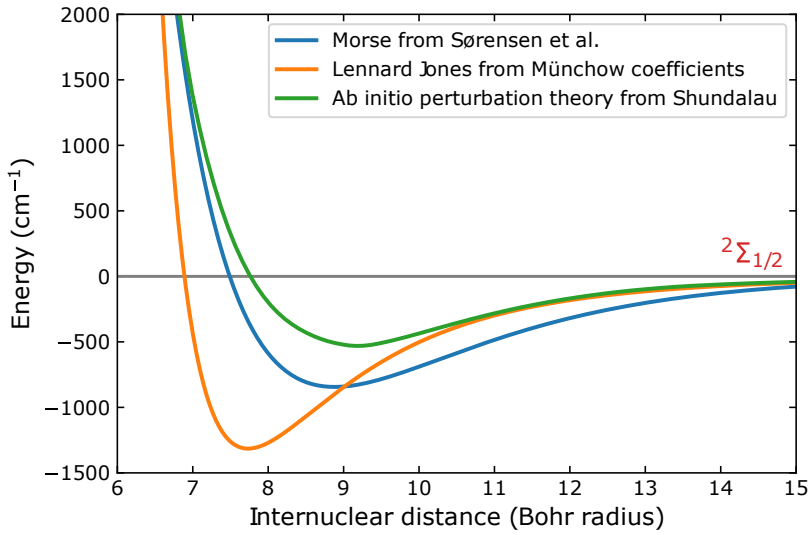

Figure 2.5.: Comparison of model energy curves of the $^2\Sigma_{1/2}$ ground state of the RbYb molecule. The Morse potential from Soerensen [16] is similar to the ab-initio calculations from Shundalau [18] in the short range, while the Lennard-Jones potential curve from Münchow [13] matches well in the long range part of the potential.

Short range: Morse potential

If the molecule has a 'small' bond length[5] and is therefore in the short range region, the Morse potential [139] is a well established approach to fit the potential curve. It can be expressed as

$$V(r) = D_E \cdot \left(1 - e^{-\omega_E \sqrt{\mu/2D_E}\,(r-r_E)}\right)^2 \tag{2.12}$$

with the potential depth D_E, the harmonic oscillation frequency ω_E and equilibrium distance r_E. Solving the Schrödinger equation shows that the spacing of binding energies for vibrational levels,

$$E_\nu = \hbar\omega_E \left(\nu + \frac{1}{2}\right) - x_E \hbar\omega_E \left(\nu + \frac{1}{2}\right)^2 + \ldots \tag{2.13}$$

in such anharmonic potentials, discussed in section 2.3.3, decreases with increasing vibrational quantum number ν, with the anharmonicity constant $x_E = \hbar\omega_E/4D_E$. The deeply bound states of a molecule are well represented in this model such that Morse parameters are often included in the publications performed with more complex ab-initio calculations.

Long range: Lennard Jones potential

If the molecule falls into the long range category, where the potential curve asymptotically approaches the atomic energy levels, it is common to use a power law to write the potential.

[5] Keep in mind that short internuclear distances are still large bond lengths for a chemist.

The interaction potential in this case is written as a sum of the dominant forces described with C_n terms

$$V(r) = E_D + \sum_n \frac{C_n}{r^n}, \tag{2.14}$$

where E_D is the dissociation limit. The attractive Van-der-Waals force gives the essential term for the long range tail of the potential curve. For hetero-nuclear molecules it gives rise to the term $-C_6/r^6$ and stems from the induced dipole moment in both atoms. The C_6 coefficient is a number that can be calculated with theoretical methods. However the uncertainty of the static polarizabilities limits the accuracy of the coefficient predictions [140][6]. We will later see (chapter 5.2) that even small changes to the long range potential complicate the location of the binding energies in our experiment. The repulsive force originating from a nearby atom changing the electronic wavefunctions is often described with $n > 6$, for example $n = 12$ in a Lennard-Jones type potential [141]. More terms like C_8 and C_{10} are occasionally included to further tune the potential curve and adapt it to published experimental results.

Finally a comparison of the classical short and long range potentials with a more complex ab-initio perturbation theory calculation from M. Shundalau [18] in figure 2.5 demonstrates how each approach fits relatively well into its dedicated region. Combined versions are thus regularly used to allow a description of a wider internuclear distance r.

2.3.3. Vibration

Molecules are more complex than atoms since they can vibrate and rotate, hence have additional degrees of freedom. In the following we will first concentrate on vibrating molecules. The vibrational states of a molecule can be calculated numerically by solving the Schrödinger equation for any given potential energy curve. The vibrational wavefunction yields the probability density of finding a molecule at a certain internuclear distance corresponding to a vibrational level. Their shape and amplitudes compared to wavefunctions in different molecular potentials give rise to the wavefunction overlap (i.e. the Franck-Condon factor) that describes the strength of optical transitions (see section 2.5). Solving the Schrödinger equation in 2.11 for a Lennard-Jones type potential $V(r)$ returns the vibrational levels and wavefunctions presented in figure 2.6. The accuracy of the eigenstates and their energies relies of course in the accuracy of the potential derived from measurements or theoretical predictions.

The number of nodes of a wavefunction is equal to the vibrational quantum number ν. For the deepest bound states the potential can be approximated by a harmonic oscillator, while the wavefunction for higher states extends further outside due to the increasing anharmonicity of the potential. The probability to find a molecule with internuclear distance r in a given state is proportional to the square of the absolute value of the wavefunction $|\Phi(r)|^2$. Since the wavefunctions have the highest amplitude just inside the classical outer

[6] The uncertainty of the Yb static scalar $^3P_1$ polarizability determines accuracy of the C6 predictions for the potential in our photoassociation experiments [140].

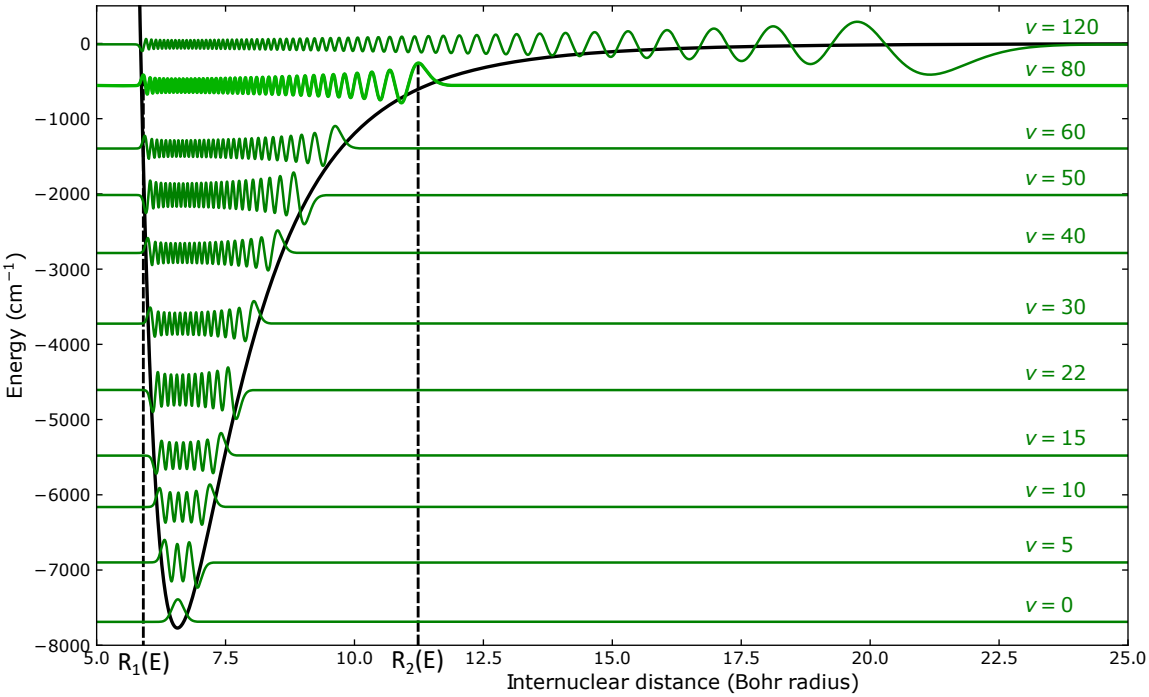

Figure 2.6.: Vibrational wavefunctions in a Lennard-Jones type potential without rotational component. Here $R_1(E)$ and $R_2(E)$ are the inner and outer classical turning points of the potential corresponding to the $\nu = 80$ vibrational level.

turning point (R_2(E) in figure 2.6) of the potential, the size of the molecule is usually described by this point.

The quantum number ν is counted upwards starting with $\nu = 0$ in the lowest level without vibration. Since the number of bound vibrational states is often unknown, if the potential is unexplored but used for photoassociation experiments, it is impossible to assign the correct number. Therefore the new reference is the dissociation threshold. The alternative way of counting starts with the least bound state at $\Delta\nu = -1$. The negative value is chosen to prevent confusion.

The relevant vibrational levels in this thesis are very close to the dissociation threshold. If some of these energies and their distance to each other are measured, the Leroy Bernstein formula [142][143] offers information about the long range potential and helps to quickly calculate the next vibrational energies.

In the next segment I will derive the formula following Ref. [131]. The starting point is the WKB (Wentzel–Kramers–Brillouin) quantization condition for the eigenvalues of a Lennard-Jones type potential $V(r)$, in which the wavefunction is modeled with an expanded exponential function and a slowly changing amplitude or phase resulting in

$$\nu + \frac{1}{2} = \frac{\sqrt{2\mu}}{\pi\hbar} \int_{R_1(E)}^{R_2(E)} \sqrt{E(\nu) - V(r)}dr \tag{2.15}$$

Here, $E(\nu)$ is the energy of level ν, μ the reduced mass and $R_1(E)$ and $R_2(E)$ are the

inner and outer classical turning points of the potential. If we differentiate the formula with respect to $E(\nu)$ we get

$$\frac{d\nu}{dE(\nu)} = \frac{\sqrt{2\mu}}{2\pi\hbar}\int_{R_1(E)}^{R_2(E)} \frac{1}{\sqrt{E(\nu)-V(r)}}dr \tag{2.16}$$

The integral will be almost unchanged if the potential $V(r)$ is replaced with an $-C_n/r^n$ function that is accurate at the outer turning point $R_2(E)$, which is close to the dissociation threshold D_E [144].

$$\frac{d\nu}{dE(\nu)} \approx \frac{\sqrt{2\mu}}{2\pi\hbar}\int_{0}^{R_2(E)} \frac{1}{\sqrt{E(\nu)+C_n/r^n}}dr \tag{2.17}$$

We can now substitute $y = R_2(E)/r$ and obtain

$$\frac{d\nu}{dE(\nu)} \approx \frac{\sqrt{2\mu}}{2\pi\hbar}\frac{C_n^{1/n}}{E(\nu)^{(n+2)/2n}}\int_{0}^{1} \frac{1}{\sqrt{(y^n-1)}}dy \tag{2.18}$$

with the integral solved with Gamma function $\Gamma(n) = (n-1)!$

$$\int_{0}^{1} \frac{1}{\sqrt{(y^n-1)}}dy = \frac{\sqrt{\pi}}{n}\frac{\Gamma(\frac{1}{2}+\frac{1}{n})}{\Gamma(1+\frac{1}{n})} \tag{2.19}$$

After integrating and rearranging we get the final Leroy-Bernstein formula [131]

$$E_v = D_E - \left((\nu_D-\nu)\cdot\sqrt{\frac{\pi}{2\mu}}\cdot\frac{\Gamma(1+1(n)}{\Gamma(1/2+1/n)}\cdot\frac{\hbar(n-2)}{(-C_n)^{1/n}}\right)^{\frac{2n}{n-2}} \tag{2.20}$$

where ν_D is the non-integral effective value of ν at the dissociation limit and describes the fractional vibrational level at the dissociation energy D_E.

Mass scaling

Changing the isotope of either atom in a diatomic molecule alters the reduced mass μ. Since the nuclei are assumed to be infinitely heavy compared to electrons in the Born-Oppenheimer approximation, the interaction potential should not be influenced by this. However changing the mass of an atom attached to another affects the vibrational motion[7]. Therefore the vibrational energy levels are expected to shift slightly depending on the total mass of the atoms involved. In heavy atoms such as Yb the mass scaling effect is smaller since the relative change in mass is smaller. From equation 2.20 we see how the energy depends on the reduced mass. The fractional vibration value ν_D also scales with the square root of the reduced mass [145].

$$\nu_D = \sqrt{\mu}\frac{\sqrt{8}}{h}\int_{0}^{R_2}\sqrt{-V(r)}dr \tag{2.21}$$

[7] Also rotation is affected but to a smaller degree.

Deviations from the Born-Oppenheimer approximation beyond the ordinary mass scaling are more apparent in lighter elements and can break down the assumption. For heavy atoms such as Rb and Yb, the Zeeman effect, Stark effect and temperature of the atomic mixture have been found to dominate the shift of the detected transition (see chapter 5), which is relevant for the correction of positions for levels and Feshbach resonances [146].

2.3.4. Rotation

The remaining degree of freedom is the rotation of the molecule. For a diatomic molecule the rotational axis is simply perpendicular to the molecular axis and passes through the center of mass. In the Schrodinger equation 2.11 the energy contribution is already included. The energy is quantized with the rotational quantum number J to

$$E_{\mathrm{rot}} = B_\nu \cdot J(J+1). \tag{2.22}$$

We can neglect higher order terms, which would lead to a centrifugal distortion of the molecule, because in cold atom experiments only the lowest J numbers are populated. The rotational constant B_ν depends on the moment of inertia of the molecule and can be derived analog to a classical rigid rotor.

$$B_\nu = \frac{\hbar^2}{2\mu {r_{\mathrm{eff}}}^2} \tag{2.23}$$

This is here expressed with the reduced mass μ and the effective bond length r_{eff} of the molecule.

2.4. Atom-light interaction

To understand the coupling and population of states (also relevant to the vibrational states in molecular potentials discussed in section 2.3.3) with light the concept of atom-photon interaction [147] needs to be explained. In this section I discuss the Rabi frequency, which is relevant for the method of photoassociation in sections 2.5 and 2.6 and later on estimates of Franck-Condon factors in section 6.5.

To analyse the evolution in an atomic system with levels $|1\rangle$ and $|2\rangle$ and enegies $\hbar\omega_1$ and $\hbar\omega_2$ driven with a resonant laser field $\vec{E}_L = \epsilon\vec{E}_0 \cdot \cos\left(\omega_L t - \vec{k}_L\vec{r}\right)$ one has to solve the Schrödinger equation

$$i\hbar\frac{\partial}{\partial t}\Psi(\vec{r},t) = \hat{H}\Psi(\vec{r},t) \quad \text{with} \quad \Psi(\vec{r},t) = c_0(t)e^{-i\omega_0 t}\psi_0(\vec{r}) + c_1(t)e^{-i\omega_1 t}\psi_1(\vec{r}) \tag{2.24}$$

as the general solution of the wavefunction of a two level atom. For the time dependent coefficients $c_0(t)$ and $c_1(t)$ we get two equations

$$\begin{aligned}\dot{c}_0(t) &= i\frac{\vec{d_{01}}\cdot\vec{\epsilon}E_0}{\hbar}e^{-i\omega_{10}t}\cos(\omega_L t)c_1(t)\\ \dot{c}_1(t) &= i\frac{\vec{d_{10}}\cdot\vec{\epsilon}E_0}{\hbar}e^{i\omega_{10}t}\cos(\omega_L t)c_0(t)\end{aligned} \tag{2.25}$$

which includes the atomic transitions frequency $\omega_{10} = \omega_1 - \omega_0$ and the resonant Rabi frequency [147]

$$\Omega_0 = \frac{\vec{\epsilon}E_0}{\hbar}\cdot\langle 1|\,\vec{d}\,|2\rangle \tag{2.26}$$

with the dipole operator $\vec{d}$ and the states characterizing the transition dipole moment. If the laser field is not resonant with the transition and has a detuning $\delta = \omega_L - \omega_{10}$, the generalized Rabi frequency is described with

$$\Omega = \sqrt{\delta^2 + {\Omega_0}^2} \tag{2.27}$$

The population of a state thus depends on the intensity I of the driving laser field and the dipole matrix element, which also describes the coupling strength between the states. This coupling can also be written as a lifetime or rather a spontaneous emission rate, leading to an alternative formula for the Rabi frequency.

$$\Omega_0 = \gamma_{\rm at}\sqrt{\frac{I}{2I_{\rm sat}}} \qquad \text{, with} \quad I_{\rm sat} = \frac{\hbar{\omega_{\rm at}}^3\gamma_{\rm at}}{12\pi c^2} \tag{2.28}$$

For Ω_0 the atomic Rabi frequency with the natural linewidth $\gamma_{\rm at}$ and the atomic saturation intensity $I_{\rm sat}$.

2.5. Photoassociation

Photoassociation (PA) is a promising technique for the creation of weakly bound molecules and is often used for the spectroscopy of molecular potentials. The ingredients for PA experiments are ultracold atoms and a photon of specific frequency that bridges the energy gap between the free collisional state and a bound electronically exited molecular state. In this simplified picture two colliding atoms absorb the incoming photon to form the molecule in an excited state, which either subsequently breaks up into two atoms with enough kinetic energy to leave the trap or decays into a molecular ground state. Both cases are typically not detected and thus lead to an observable loss of reaction partners.

$$\mathrm{A} + \mathrm{B} + \nu_{\mathrm{L}} \rightarrow [\mathrm{AB}]^* \tag{2.29}$$

The following theoretical description is based on the detailed treatment in [79] and the extended application to the intercombination transition in Yb [148]. The production of these weakly bound molecules relies on the coupling between a free scattered state and a bound state. The photoassociation rate coefficient for this event is given by [148]

$$K(I, \Delta, \vec{p}_c, \vec{p}_r) = \frac{\hbar\pi}{k_r \mu} \sum_{e,g} (2l+1) \cdot \frac{\Gamma_{\mathrm{pe}} \cdot \Gamma_{\mathrm{eg}}(I, \epsilon_r)}{\left[\delta_{\mathrm{FB}}(\Delta, I, \vec{p}_c, \vec{p}_r)\right]^2 + \left[\hbar\Gamma_{\mathrm{tot}}(I, \epsilon_r)/2\right]^2} \tag{2.30}$$

and depends on the light intensity I, the detuning to the atomic resonance Δ, the motion $\vec{p}_c$ of the center of mass and $\vec{p}_r$, the relative motion of the particles. In an experiment the momentum distribution of all reaction partners is characterized by the temperature of a thermal cloud of ultracold atoms. Therefore, the thermal distribution has to be averaged. The formula contains k_r and ϵ_r as the wavenumber and kinetic energy of the relative motion, μ as the reduced mass and the partial wave l. The partial wave l is only relevant for collision energies, which are large enough so that higher partial waves play a role and is thus $l = 0$ in our case. δ_{FB} is the detuning to the PA resonance including all line shifting effects [1].

The linewidth Γ_{tot} of a PA resonance is a sum,

$$\Gamma_{\mathrm{tot}}(I, \epsilon_r) = \Gamma_{\mathrm{pe}} + \sum_g \Gamma_{\mathrm{eg}}(I, \epsilon_r), \tag{2.31}$$

where Γ_{eg} is the light induced rate of molecules returning from excited state 'e' to ground state 'g' and Γ_{pe} contains all other possible decay channels of the exited state such as predisassociation or radiative decay. For molecular states close to disassociation Γ_{pe} could be assumed to be the natural linewidth of the exited atomic state. However since predisassociation can enter into the observed linewidth this is not guaranteed [105]. Even if radiative decay is the dominant process, strong coupling to electronic molecular ground states may induce widths larger than the atomic linewidth. The light stimulated width can be evaluated further with Fermis golden rule,

[1] $\delta_{\mathrm{FB}} = \Delta + \epsilon_D - \epsilon_r - \Delta_e - E_e(I, \epsilon_r) - E_{\mathrm{rec,mol}}$ with Doppler shift, energy of the scattering state, recoil shift and AC stark shift.

$$\Gamma_{\mathrm{eg}}(I,\epsilon_r) = \frac{2\pi}{\hbar} \cdot |\langle \Psi_e | \hat{V}_{\mathrm{laser}}(I) | \Psi_g(\epsilon_r) \rangle|^2 \rho(\hbar\omega), \tag{2.32}$$

depending linearly on the light intensity I and the optical coupling between both states via the laser field operator $\hat{V}_{\mathrm{laser}}$, with the density of photon states $\rho(\hbar\omega)$. For a sufficiently low light intensity, 1-photon scattering is expected to have Lorentzian line-shapes [149]. In the cases of transitions to very weakly bound states and the assumption that the transition dipole moment stays constant between vibrational states, we are able to separate the matrix element into two parts [148]. First the electronic component and secondly a part given by the Franck-Condon factor, which describes the overlap between the wavefunctions of states 'e' and 'g'. This approach allows us to rewrite the formula as

$$\Gamma_{\mathrm{eg}}(I,\epsilon_r) = \Gamma_A \frac{3}{4\pi} \frac{I {\lambda_A}^3}{c} f_{\mathrm{eg}}^{\mathrm{rot}} f_{\mathrm{eg}}^{\mathrm{FC}}(\epsilon_r) \tag{2.33}$$

with the atomic decay width Γ_A and wavelength λ_A. The rotational line strength factor $f_{\mathrm{eg}}^{\mathrm{rot}}$, which depends on the angular momenta of the states involved, and the free-bound Franck-Condon factor $f_{\mathrm{eg}}^{\mathrm{FC}}(\epsilon_r)$. This last term depends on the temperature of the atomic cloud because the energy distribution of the scattering state changes the overlap integral

$$f_{\mathrm{eg}}^{\mathrm{FC}}(\epsilon_r) = \left| \int_0^\infty \Phi_e(r) \Phi_g(r;\epsilon_r) dr \right|^2 \tag{2.34}$$

between the vibrational wavefunctions of the excited state Φ_e and the free wavefunction ground state Φ_g.

The effective photoassociation rate is reduced, broadened and shifted to lower detunings because of the collisional energy [150]. This encourages us to perform PA at ultracold temperatures to maximise the signal amplitude since the predicted rates close to intercombination transitions are small to begin with [22].

Figure 2.7 shows the principle of 1-photon photoassociation spectroscopy in the experiment (5). The laser field ω with intensity I creates a coupling with Rabi frequency Ω_{FB} between a free scattering state $|g\rangle$ and excited molecular state $|e\rangle$. When scanning the laser frequency over a resonance ($\delta_{\mathrm{FB}} = 0$) the atom number (in state $|g\rangle$) is expected to decline in a Lorentzian shape as electronically excited molecules are created and not detected in the experiment.

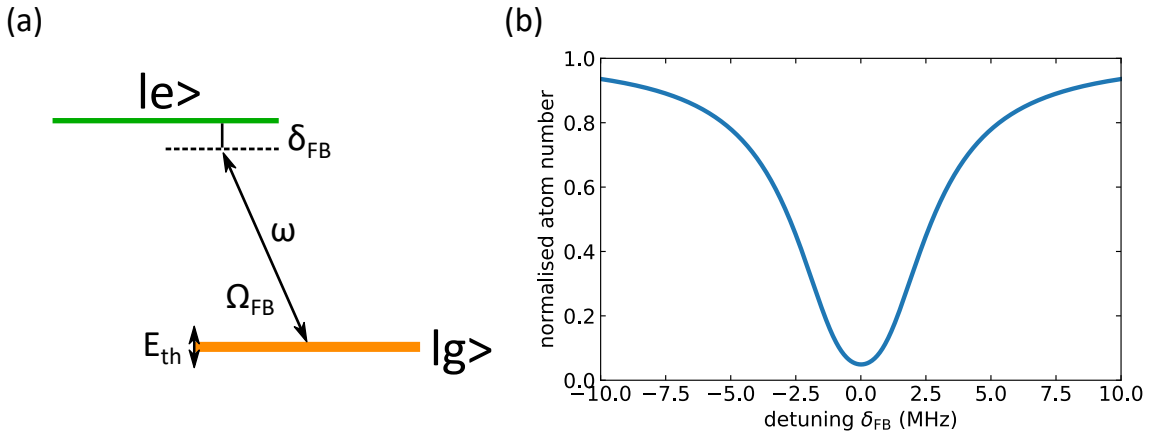

Figure 2.7.: (a) Two level scheme for 1-photon PA with light field ω and Rabi frequency Ω_{FB} coupling the (coloured) states. δ_{FB} denotes the photon detuning from the transition between free scattering state $|g\rangle$ and the excited molecular state $|e\rangle$. The thermal energy E_{th} shifts the free scattering state. In segment (b) the expected Lorentzian 1-photon PA signal shows a reduced normalised atomnumber if the detuning δ_{FB} is small and thus close to a resonance, creating electronically excited molecules that are undetected.

2.5.1. Saturated photoassociation rate

In order to get a feeling for the expected photoassociation rate in the experiment, the saturated rate can be calculated with some assumptions. In the following we will consider the case of PA at the intercombination line of Yb which is the relevant case for this thesis. The first assumption is that we can measure the line on resonance and neglect any shifts with $\Delta_{\mathrm{FB}} = 0$. Furthermore the natural decay of the exited state is approximated by the natural linewidth of the atomic state $\Gamma_{\mathrm{pe}} = \Gamma_{\mathrm{nat}} = 2\pi{\cdot}181\,\mathrm{kHz}$ and predissociation assumed to not enter into the detection rate. The remaining light induced decay Γ_{eg} according to [79] is

$$\Gamma_{\mathrm{eg}}(I,\epsilon_r) = \frac{4\pi^2 I}{\hbar c}\cdot\left|\langle e|\,\vec{d}\cdot\vec{e}\,|g\rangle\right|^2 = \frac{4\pi^2 I}{\hbar c}\cdot\mathbf{M} \tag{2.35}$$

with molecular dipole moment $\vec{d}$, polarization of the light field $\vec{e}$ and dipole matrix element $\mathbf{M}$. The resonant PA rate coefficient can then be written as (see [11] or [79] for more details)

$$K_{\mathrm{res}}(I) = \frac{\hbar\pi}{k_r\mu}\cdot\frac{\Gamma_{\mathrm{nat}}\cdot\Gamma_{\mathrm{eg}}(I,\epsilon_r)}{0+\left[(\Gamma_{\mathrm{nat}}+\Gamma_{\mathrm{eg}}(I,\epsilon_r))/2\right]^2} = \frac{\hbar\pi}{k_r\mu}\cdot 4\frac{I_{\mathrm{opt}}\cdot I}{(I_{\mathrm{opt}}+I)^2} \tag{2.36}$$

with I the light intensity and I_{opt} the optimal intensity yielding the highest PA rate. Since the second fraction of equation 2.36 can at best be equal to one, the maximum amplitude is simply given by the first term.

$$K_{\mathrm{max}} = \frac{\hbar\pi}{k_r\mu} = \frac{\hbar^2\pi}{\sqrt{k_B T_{\mathrm{eff}}\mu^3}} \quad \text{with} \quad k_r = \frac{\sqrt{2E\mu}}{\hbar}\,, \quad E = \frac{1}{2}k_B T_{\mathrm{eff}} \tag{2.37}$$

For a typical effective temperature in our experiment of

$$T_{\text{eff}} = \frac{m_{\text{Yb}} T_{\text{Rb}} + m_{\text{Rb}} T_{\text{Yb}}}{m_{\text{Yb}} + m_{\text{Rb}}} = 3.6\,\mu\text{K} \tag{2.38}$$

with $T_{\text{Rb}} = 5\,\mu\text{K}$ and $T_{\text{Yb}} = 1\,\mu\text{K}$, the saturated PA rate can be calculated. In this case the normalized rate is $K_{\text{max}} = 1.7^{-10}\,\text{cm}^3/\text{s}$ per Yb atom per Rb density. This would mean that we get a rate of $r_{\text{max}} \sim 1700\,\frac{1}{\text{s}}$ per Yb atom, with $r_{\text{max}} = K_{\text{max}} \cdot \rho_{\text{Rb}}$ in a Rb density of $10^{13}\,\text{cm}^3$.

Unfortunately the expected PA rate in our experiment can be estimated to be orders of magnitudes smaller then K_{max}. The reason for this is the weak coupling between the excited state and the free ground state given by the transition dipole moments (TDMs) as has been observed in similar systems [151] and also confirmed by theoretical predictions in [18][22]. Due to a small TDM the PA laser intensity I_{opt} needed to reach the maximum PA rate is very high[2]. At such high intensities the excessive atom loss from photon scattering close to the atomic line directly negates the advantages of a maximised PA rate as Yb atoms are quickly removed from the trap. There are however proposals to enhance the PA rate by nonresonant-light control of shape resonances [152] which might open up new possibilities in the future.

[2]The optimal intensity to reach saturation in the PA rate can be estimated to $\approx 2{\cdot}10^7\,\text{W/m}^2$. Comparing the saturated PA rate with the measured PA rate in chapter 5, would yield a required power of $\approx 0.5\,\text{W}$ for the PA laser beam.

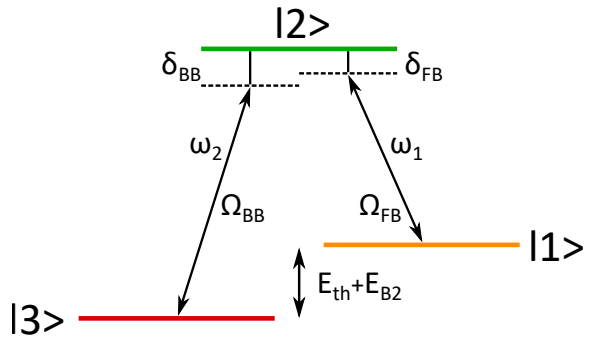

Figure 2.8.: Three level Λ type scheme for 2-photon PA with light fields ω_1 and ω_2 coupling the (colored) states. δ_{FB} denotes the detuning from the free scattering state $|1\rangle$ and excited molecular state $|2\rangle$, while δ_{BB} is the detuning from $|2\rangle$ to the bound ground state level $|3\rangle$. State $|1\rangle$ and $|3\rangle$ are separated by the sum of the thermal energy E_{th} and the binding energy E_{B2}.

2.6. 2-Photon Photoassociation

An extension of 1-photon PA spectroscopy is the two-color spectroscopy also known as 2-photon photoassociation (2-PA), which is visualised in figure 2.8 [153]. First reports on 2-PA with $^7Li_2$ molecules were already published in 1995 [154]. The previous description merely probed the association of single atoms from a thermal scattering state $|1\rangle$ to bound molecules in state $|2\rangle$ via a single laser field with angular frequency ω_1. Introducing a second photon of frequency ω_2 couples this intermediate state $|2\rangle$ to a molecular ground state level $|3\rangle$. This constitutes a three level system, in which the couplings of the laser fields are expressed with the Rabi frequencies Ω_{FB} for free-bound and Ω_{BB} for bound-bound transitions. If the laser frequencies don't match the transition frequency they are detuned by δ_{BB} and δ_{FB}. In an alternative representation the two-photon detuning is given by $\Delta_{2\gamma} = \delta_{\mathrm{FB}} - \delta_{\mathrm{BB}}$ and can be used together with the single photon detuning δ_{FB}. Furthermore the energy difference between the scattering state $|1\rangle$ and the bound state $|3\rangle$ is equal to the binding energy of the vibrational level E_{B2} plus the thermal energy E_{th}.

In a 2-level system coherence is shown in the oscillating population between the states known as Rabi flopping. The evolution of a driven 3-level system reveals new interesting effects like Autler-Townes splitting [155], dark states [156] and electromagnetically induced transparency EIT [157] [158]. All these phenomena depend on the Rabi frequencies, detunings, decay rate Γ of the exited state and effective decay rate Γ_{eff} including decoherence of the dark state.

The first application to spectroscopy is to leave the first photon on resonance with $\delta_{\mathrm{FB}} = 0$, while the frequency of the second photon is scanned. If the scanned frequency is near a bound-bound transition, state $|2\rangle$ is AC-Stark shifted out of resonance for the first photon. For $\Omega_{\mathrm{BB}} >> \Omega_{\mathrm{FB}}$ this shift is large enough to completely prevent 1-PA photoassociation. For low intensities of the bound-bound laser field the Stark shift becomes negligibly small. If however the relative linewidth between both lasers is equally small ($\Omega_{\mathrm{BB}} < \Gamma_{\mathrm{eff}}$) the problem has to be treated based on quantum interference between paths

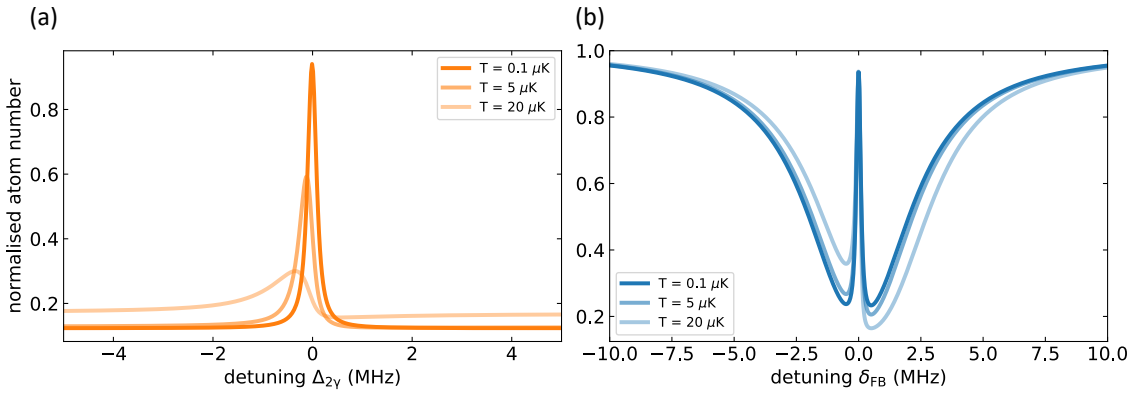

Figure 2.9.: Atom loss rate (equation 2.39) visualised for the two experimentally relevant cases. In (a) δ_{FB} is set to zero, producing a Lorentzian curve that shows the expected increase in atom number during a scan across a 2-photon resonance. In (b) the bound-bound laser is set to this resonance and a dark resonance (EIT shape) appears when δ_{FB} is scanned across a 1-photon PA resonance. Increasing the thermal energy from 0.1 µK to 5 µK or 20 µK smears out the collisional state $|1\rangle$ and averaging the fit function 2.39 over the thermal Boltzmann distribution reduces the linewidth of the 2-photon resonance and creates a distortion of the dark resonance.

$|1\rangle \rightarrow |2\rangle$ and $|1\rangle \rightarrow |2\rangle \rightarrow |3\rangle \rightarrow |2\rangle$ (or higher orders). If both lasers are on resonance destructive interference between paths prevents the population of state $|2\rangle$ [158]. In both cases the binding energies for state $|3\rangle$ can be determined through an increasing number of atoms.

The second variant is to leave the second photon on resonance $\delta_{\mathrm{BB}} = 0$, while this time the frequency of the first photon is scanned. In this case the number of atoms is expected to decrease as the detuning δ_{FB} approaches zero, as was already established in 1-photon PA (2.5). In the 2-photon case however a sharp peak at resonance appears due to the EIT created by the resonant second photon. The physics responsible for the cancellation of the 1-PA line in EIT is identical to that involved in the formation of a dark-state and coherent population trapping [147].

The loss of atoms is introduced by coupling a three-level system to photoassociation laser fields, which leads to the population of excited molecular bound states and their following decay. For $\Omega_{\mathrm{BB}} >> \Omega_{\mathrm{FB}}$ - which is easily fulfilled due to a large disparity in FCFs between bound-bound and free-bound transitions in molecules - the master equation derived in [158], was analytically solved for a lambda type three level system and can now be written as [159]

$$\frac{\dot{N}}{N} = \frac{{\Omega_{\mathrm{FB}}}^2 \left[4\Gamma {\Delta_{2\gamma}}^2 + \Gamma_{\mathrm{eff}}({\Omega_{\mathrm{BB}}}^2 + \Gamma_{\mathrm{eff}}\Gamma)\right]}{\left|{\Omega_{\mathrm{BB}}}^2 + (\Gamma + 2i\delta_{\mathrm{FB}})(\Gamma_{\mathrm{eff}} + 2i\Delta_{2\gamma})\right|^2} \tag{2.39}$$

where Γ is the decay rate of the excited state $|2\rangle$ and Γ_{eff} the effective decay rate including the decoherence of the dark state. In figure 2.9 the equation is visualised for both presented cases. For the first case in segment (a), δ_{FB} is set to zero, effectively reducing the

curve to a Lorentzian. In segment (b) the condition $\delta_{\mathrm{FB}} = -\Delta_{2\gamma}$ puts the bound-bound laser on resonance, producing the dark resonance or EIT shape. The equation is used to fit the data observed in the experiment in the 2-PA chapter 6. Of course the thermal energy in the atomic mixture of the experiment smears out the collisional state $|1\rangle$. Therefore equation 2.39 has to be averaged over the thermal Boltzmann distribution, which reduces the linewidth of the 2-photon resonance (a) and creates a distortion of the dark resonance (b). The extracted values of the Raabi frequencies give important information of possible applications with stimulated Raman Adiabatic Passages (STIRAP) to form molecules [86][87]. More about experimental results can be found in chapter 6.4 and an outlook on STIRAP is presented in chapter 7.3.2.

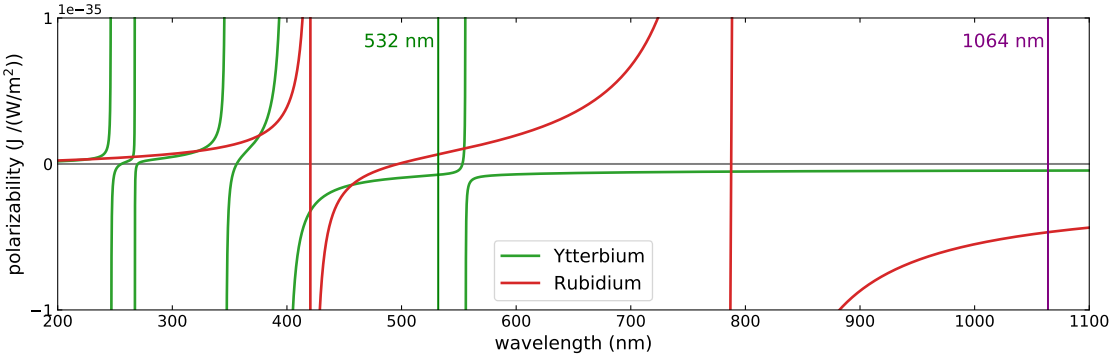

Figure 2.10.: Polarizability of Ytterbium (green) and Rubidium (red) depending on the wavelength of the light field (taken from reference [1]). The relevant trap wavelengths are marked by the vertical lines.

2.7. Theory of optical traps

In order to carry out the experiments in this thesis, the atoms are held and transported in optical dipole traps (ODTs). These traps are routinely used tools to produce and manipulate atomic clouds in the µK regime. Most recently arrays of many micro dipole traps have even used to control the configuration of particles as atomic qubits in quantum computer research [160] [161].

2.7.1. Optical dipole trap

This chapter introduces the conservative interaction of atoms with a light field and mostly follows the extensive treatment in [162]. The light field of a laser has an electric field $\vec{E}$ which induces a dipole moment in the atom $\vec{d}$. This results in an interaction between the electric field and dipole moment. This effect, known as the AC-Stark or Autler-Townes effect [147][163], shifts the atomic energy depending on the intensity of the light field and the distance to transitions. It also gives rise to the ability to trap atoms or molecules in intensity gradients of far detuned light fields called optical dipole traps [164].

The atoms induced dipole moment

$$\vec{d} = \alpha(\omega_L)\vec{E} \tag{2.40}$$

depends on the complex atomic polarizability $\alpha(\omega_L)$ and in turn on the frequency ω_L of the driving field $\vec{E}$. This leads to a dipole potential by time averaging $\langle ... \rangle$ over fast oscillations. The potential can thus be expressed as the product of the real part of the polarizability and the intensity $I(\vec{r}) = 2\epsilon_0 c|\vec{E}|^2$ and is given by

$$V_{\mathrm{dip}}(\vec{r}) = -\frac{1}{2}\langle \vec{d} \cdot \vec{E} \rangle = -\frac{1}{2\epsilon_0 c}\mathrm{Re}(\alpha(\omega_L))I(\vec{r}) \tag{2.41}$$

The spontaneous scattering rate in contrast is proportional to the imaginary part of the polarizability and the laser intensity.

$$\Gamma_{\mathrm{sc}} = \frac{1}{\hbar\epsilon_0 c}\mathrm{Im}(\alpha(\omega_L))I(\vec{r}) \tag{2.42}$$

The polarizability itself can be calculated by Lorentz's model of a classical damped oscillator [162]. In this derivation damping is introduced by the dipole radiation and resulting energy loss of the oscillation electron. The wavelength dependent polarizability can be expressed as

$$\alpha(\omega_L) = 6\pi\epsilon_0 c^3 \frac{\gamma/{\omega_0}^2}{{\omega_0}^2 - \omega_L - i(\omega^3/{\omega_0}^2)}\gamma \tag{2.43}$$

with γ the spontaneous decay rate of the exited state and ω_0 the atomic transition frequency. The semi-classical approach which considers the atom as a two-level quantum system interacting with the classical radiation field arrives at the same result, but the damping rate is replaced by the dipole matrix element between the states $\gamma = \frac{{\omega_0}^3}{3\pi\epsilon_0\hbar c^3}|\langle e|\mu|g\rangle|^2$. The calculation of the frequency-dependent polarizability for Rb and Yb atoms presented in figure 2.10 is based on the transitions collected from [165].

The complete dipole potential and the scattering rate for an atom can now be computed by summing over all transitions. With the help of equation 2.43 the dipole potential and scattering rate for a single transition can be written as

$$V_{\mathrm{dip}}(\vec{r}) = -\frac{3\pi c^2}{2{\omega_0}^3}\left(\frac{\gamma}{\omega_0 - \omega_L} + \frac{\gamma}{\omega_0 + \omega_L}\right) I(\vec{r}) \approx \frac{3\pi c^2}{2{\omega_0}^3}\frac{\gamma}{\Delta} I(\vec{r}) \tag{2.44}$$

$$\Gamma_{\mathrm{sc}}(\vec{r}) = \frac{3\pi c^2}{2\hbar{\omega_0}^3}\left(\frac{\omega_L}{\omega_0}\right)^3\left(\frac{\gamma}{\omega_0 - \omega_L} + \frac{\gamma}{\omega_0 + \omega_L}\right)^2 I(\vec{r}) \approx \frac{3\pi c^2}{2\hbar{\omega_0}^3}\left(\frac{\gamma}{\Delta}\right)^2 I(\vec{r}) \tag{2.45}$$

where $\Delta = \omega - \omega_0$ is the detuning of the laser field from the atomic transition. For the term on the right side of both equations the rotating wave approximation was applied. This only holds for small detuning $|\Delta| << \omega_0$ and is thus only applicable near resonance.

Two essential point can be inferred from the last formulas. First the sign of the potential depends on the detuning Δ. For a blue detuning ($\Delta > 0$) the potential is repulsive, while red detuning ($\Delta < 0$) creates an attractive potential. Common optical dipole traps in experiments with ultracold gases thus use red detuned laser fields with high power to trap atoms or molecules in this potential. High powers or high intensities are desirable to collect particles because the trap depth scales with intensity $I(\vec{r})$. The scattering rate however also scales with the intensity of the laser beam and causes trap loss due to the recoil of scattered photons. Since the potential scales with I/Δ and the scattering rate scales with I/Δ^2 the scattering events can still be minimized for large detunings. Nevertheless there is a persisting heating effect of rare scattering events from far off-resonant trap photons. The remaining heating rate in the optical trap is

$$T_{\mathrm{heat}} = \frac{2}{3}\frac{E_R}{k_B}\Gamma_{\mathrm{sc}} \qquad \text{with} \qquad E_R = \frac{\hbar^2 k^2}{2m} \tag{2.46}$$

being the recoil energy of a scattered photon[1].

[1]For the maximum intensity of a typical dipole trap with 10 W at 1064 nm and a radial beam waist of 50 µm, 16.3 photons (Yb) / 29.2 photons (Rb) are scattered per second. The resulting heating rates are 0.54 µK/s for Yb and 1.89 µK/s for Rb.

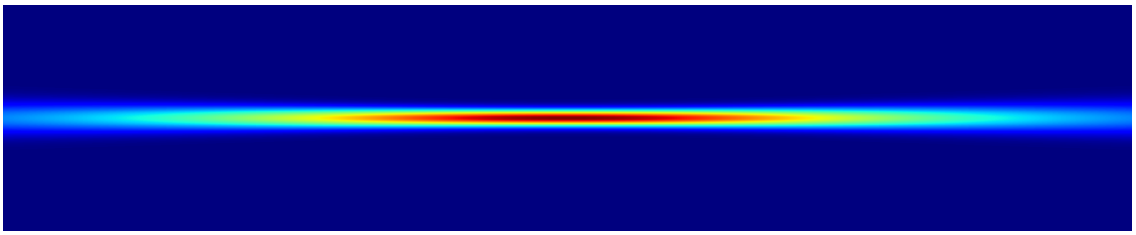

Figure 2.11.: Intensity distribution of a focused Gaussian laser beam.

Optical dipole traps with Gaussian beams

All optical dipole traps in this experiment are realised with red detuned beams assumed to be of Gaussian shape, which are formed by focusing a collimated beam with a lens into the vacuum chamber. Such a laser beam propagating in the z-direction is characterised by its wavelength λ and beamwaist ω_0 and follows a shape

$$w(z) = \omega_0 \sqrt{1 + \left(\frac{z}{z_r}\right)^2} \tag{2.47}$$

with the Rayleigh range $z_R = \pi {\omega_0}^2/\lambda$. The intensity of the beam depends on the radial and axial distance r, z from the focal point with

$$I(r,z) = \frac{2P}{\pi w(z)^2} \cdot e^{-2r^2/w(z)^2} \tag{2.48}$$

and the maximum $I_0 = \frac{2P}{\pi \omega_0^2}$ for $r, z = 0$. The harmonic approximation

$$V(r,z) = -V_0 \left[1 - 2\left(\frac{r}{\omega_0}\right)^2 - \left(\frac{z}{z_R}\right)^2\right] \tag{2.49}$$

to a cylindrical symmetric dipole trap [166] leads to the trapping frequencies $\omega_r = \sqrt{4V_0/m{\omega_0}^2}$ and $\omega_z = \sqrt{4V_0/m{z_R}^2}$.

2.7.2. Optical lattice

This chapter discusses the concept of optical lattices and is oriented on the work in [167][166]. Optical lattices are periodic potentials formed by two or more laser beams. The beams interfere and thus create recurring potential wells where atoms can be trapped similar to a ordinary ODT. For two counter-propagating laser beams the spacing a between these wells or the periodicity of the standing light wave is dictated by the wavelength of the trap light is given by

$$a = \frac{\lambda_L}{2} = \frac{\pi}{k} \tag{2.50}$$

Depending on the detuning one can either trap particles in the intensity minima ($\Delta > 0$) or maxima ($\Delta < 0$) of the lattice[2].

[2]In our case of a 1064 nm lattice the light is red detuned, which traps atoms in the intensity maxima.

1D lattice potential

The potential of a one dimensional lattice consisting of a retro reflected Gaussian beam along the z-axis can be written as

$$V(r,z) = -V_{\text{lat}} \cdot e^{-2r^2/{\omega_0}^2} \cdot \sin^2(kz) \approx -V_{\text{lat}} \left(1 - 2\frac{r^2}{{\omega_0}^2}\right) \cdot \sin^2(kz), \tag{2.51}$$

where k is the wave vector, ω_0 is the combined beam waist and V_{lat} is the maximum potential depth. The depth of this potential is four times larger than an ODT beam without reflection due to the interference of the standing wave of the optical lattice. For a far detuned lattice, in which the detuning is large compared to the excited state fine structure, the lattice depth can be estimated to be [166]

$$V_{\text{lat}} = 4 \cdot V_0 \approx 4 \cdot \frac{3\pi c^2}{2{\omega_0}^3} \frac{\gamma}{\Delta} \frac{2P}{\pi\omega_0^2} \tag{2.52}$$

It should be noted that the lattice depth is commonly given in units of single photon recoil energies E_R.

3D lattice potential

In our experiment the final trap is a cubic lattice, which consists of three almost orthogonal pairs of retro reflected laser beams. Different frequencies and polarization are used for each pair to avoid interference effects between them. The potential resulting due to the overlap of the three 1D lattices with directions x, y, z is

$$\begin{aligned} V(x,y,z) = &-V_x \cdot \exp\left(-2\frac{y^2+z^2}{{\omega_x}^2}\right) \sin^2(kx) \\ &-V_y \cdot \exp\left(-2\frac{x^2+z^2}{{\omega_y}^2}\right) \sin^2(ky) \\ &-V_z \cdot \exp\left(-2\frac{x^2+y^2}{{\omega_z}^2}\right) \sin^2(kz) \end{aligned} \tag{2.53}$$

with Gaussian shaped $1/e^2$ radii $\omega_x, \omega_y, \omega_z$ and V_x, V_y, V_{lz} as the individual potential depths of the superimposed 1D lattices. In the case of a 'deep' lattice, meaning that the depth of the potential within a single lattice site is sufficiently large to be approximated by a harmonic potential, the trapping frequency on a single lattice site can be written as

$$\omega_{\text{lat}} = \sqrt{\frac{2V_{\text{lat}}k^2}{m}} \qquad \text{or} \qquad \hbar\omega_{\text{lat}} = 2\sqrt{V_{\text{lat}}E_R} \tag{2.54}$$

However this formula is only valid in the center as the lattice depth becomes more shallow with increasing distance from the centre of the Gaussian beams. For this reason the trap frequencies get reduced, which in turn results in a change of the vibrational energies of an atom trapped at a single lattice site $E_{\text{level}} = n \cdot \hbar/2(\omega_x + \omega_y + \omega_z)$. In the case of an isotropic lattice with $V_{x,y,z} = V_{\text{lat}}$, $\omega_{x,y,z} = \omega_0$ and $r^2 = x^2 + y^2 + z^2$ the confinement is given by [166]

$$V_{\text{ext}}(r) = E_R \left(2\frac{V_{\text{lat}}}{E_R} - \sqrt{\frac{V_{\text{lat}}}{E_R}}\right) \frac{2r^2}{{\omega_0}^2} \tag{2.55}$$

Bloch bands and Wannier functions

The physics of particles moving through the periodic potential of a lattice is described by Bloch's theorem. It assumes that such a particle has a wave function of the form [168]

$$\Phi_q(x) = u_q^{(n)}(x)e^{iqx} \tag{2.56}$$

with the function $u_q^{(n)}(x)$ being periodic with a periodicity a and the quasi-momentum q. These Bloch functions are solutions of the Schrödinger equation and a product of a plain wave e^{iqx} and the periodic function. Inserting them in the Hamiltonian gives us a Schrödinger equation for $u_q^{(n)}(x)$:

$$\left[\frac{(\hat{p}+q)^2}{2m} + V(x)\right] u_q^{(n)}(x) = E_q^{(n)} u_q^{(n)}(x) \tag{2.57}$$

The lattice potential $V(x) = \sum_r V_r e^{2irkx}$ and functions $u_q^{(n)}(x) = \sum_l c_l^{(n,q)} e^{2ilkx}$ have the same periodicity and can thus be written as Fourier sums. The potential and kinetic energy terms then become [167]

$$V(x)u_q^{(n)}(x) = \sum_l \sum_r V_r e^{2i(r+l)kx} c_l^{(n,q)} \tag{2.58}$$

$$\frac{(\hat{p}+q)^2}{2m} u_q^{(n)}(x) = \sum_l \frac{(2\hbar kl+q)^2}{2m} c_l^{(n,q)} e^{2ilkx} \tag{2.59}$$

For an optical lattice, where $V(x) = V_{\text{lat}} \cdot \sin^2(kx) = -\frac{1}{4}V_{\text{lat}}(e^{2ikx} + e^{-2ikx} + 2)$ only three components of the Fourier sum $\sum_r$ are not zero. For $r = \pm 1$ the component evaluates to $-1/4V_{\text{lat}}$ and for $r = 0$ to $V_{\text{lat}}/2$. Now equation 2.57 can be written in a simplified matrix form

$$\sum_l H_{l,l'} \cdot c_l^{(n,q)} = E_q^{(n)} c_l^{(n,q)} \quad \text{with } H_{l,l'} = \begin{pmatrix} (2+q/\hbar k)^2 E_R & -1/4V_{\text{lat}} & 0 & \cdots \\ -1/4V_{\text{lat}} & (4+q/\hbar k)^2 E_R & -1/4V_{\text{lat}} & \cdots \\ 0 & -1/4V_{\text{lat}} & (6+q/\hbar k)^2 E_R & \cdots \\ \vdots & \vdots & \vdots & \ddots \end{pmatrix} \tag{2.60}$$

From here the band structure of the first Brillouin zone from $-\hbar k$ to $\hbar k$ for different optical lattice depths can be calculated and is plotted in figure 2.12. The Eigenvalues $E_q^{(n)}$ of H show the energies in the n^{th} band for different quasi momenta. Through the associated eigenvectors[3] $c^{(n,q)}$ the corresponding Bloch functions are determined with $u_q^{(n)}(x)$ and formula 2.56.

In order to understand the localisation of atoms in the lattice one has to look at Wannier functions [169]. They are an orthogonal and normalized sum of wave functions multiplied with the Bloch functions for the n^{th} energy band [170],

$$W_n(x - x_i) = \frac{1}{\sqrt{M}} \sum_q e^{-iqx_i} \cdot \Phi_{n,q(x)} \tag{2.61}$$

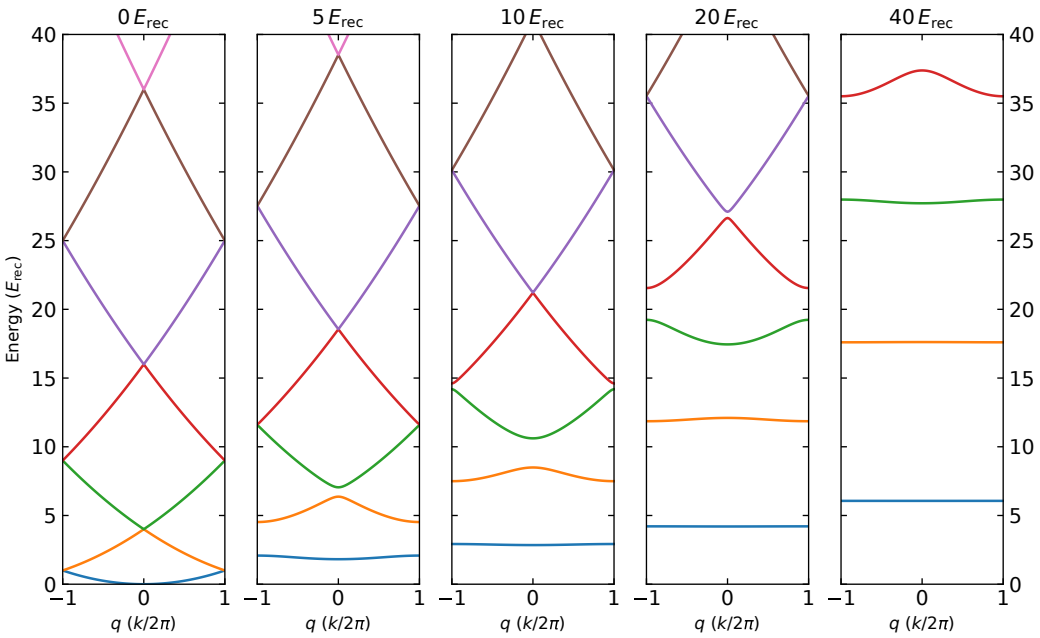

Figure 2.12.: Band structure of an optical lattice with different potential depths $V_{\text{lat}} = 0, 5, 10, 20, 40$ in recoil energies. In the absence of a potential (left) the particle can move freely mapped onto the first Brillouin zone. With deeper lattices (to the right) band gaps emerge until the energy levels become completely flat and are separated by $\hbar\omega$.

where M denotes the total number of lattice sites and x_i the position within the i^{th} lattice site. In figure 2.13 the Wannier functions and the square of its absolute value are plotted for different lattice depths in the 0^{th} (left) and 1^{st} (right) band. At low lattice depths the localised Wannier functions reach into the adjacent lattice sites. Wannier functions of adjacent lattice sites create an overlap with this function. The squared Wannier function beneath gives a measure for the corresponding probability density of the atom. Its tails suggests a probability for the atom to be located at the neighbouring lattice sites, which relates to the tunnelling rate at low lattice depths. For higher lattice depths the localisation of the atom in the original lattice site increases and the probability density on adjacent lattice sites becomes negligibly small. Two overlapping Wannier functions of neighboring sites i and j can help with the calculation of the tunneling matrix element [166]

$$J = \int W_n(x - x_i) \left(-\frac{\hbar^2}{2m} \frac{\partial^2}{\partial x^2} + V(x) \right) W_n(x - x_j) dx \tag{2.62}$$

,which can alternatively be expressed by the width of the lowest energy band [171] via

$$J = \frac{E^{(0)}_{q=0} - E^{(0)}_{q=\hbar k}}{4} \tag{2.63}$$

In the special case of a deep sinusoidal lattice ($V_{\text{lat}} >> E_R$) the nearest-neighbour tunneling parameter for the lowest band can be approximated with [172]

[3] For large $|l|$ the values for $c^{(n,q)}$ become negligibly small and can be discarded if the lower energy bands are considered.

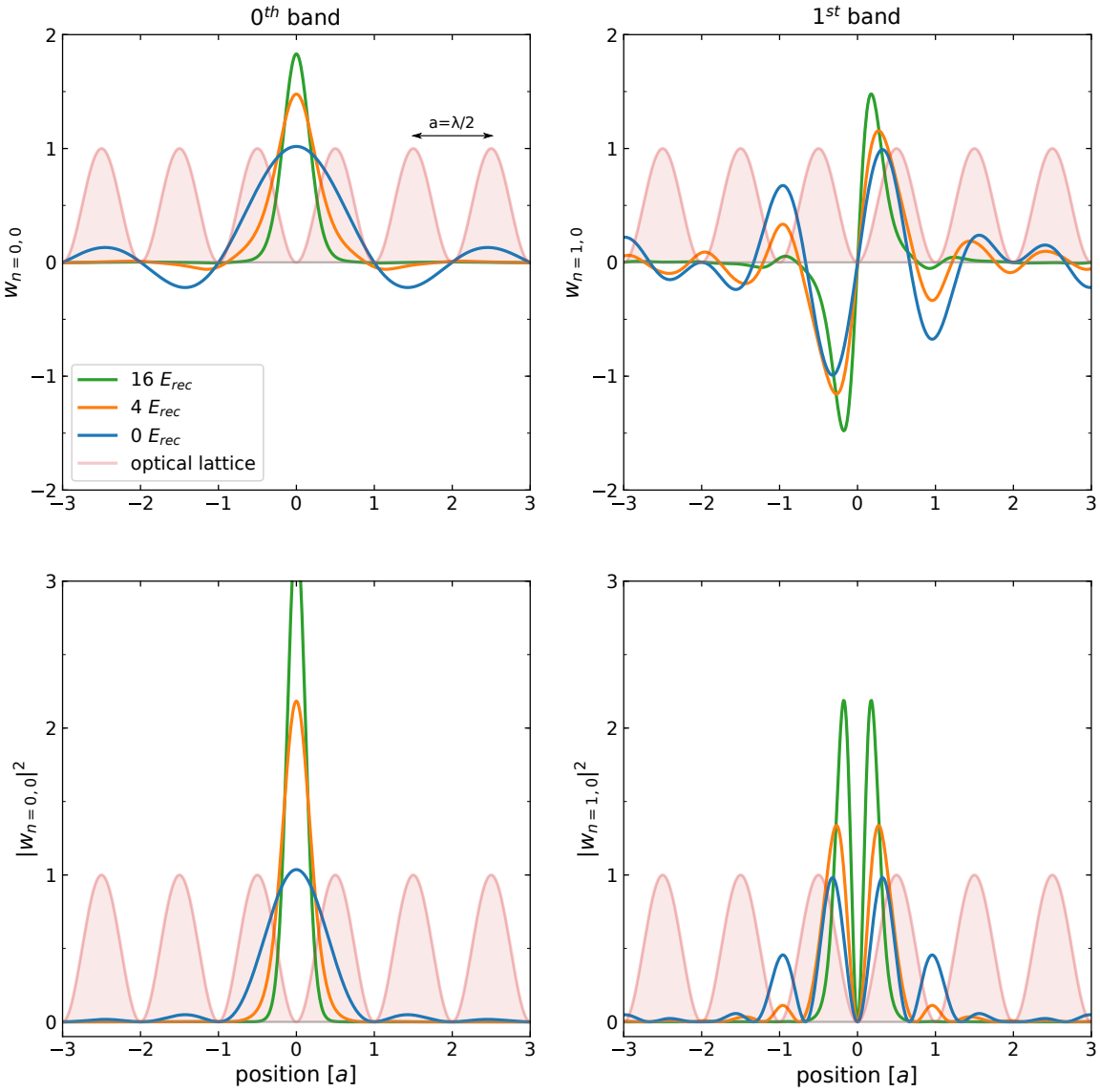

Figure 2.13.: Wannier functions and the square of their absolute values for the 0^{th} and 1^{st} band of an optical lattice depending on the position (x-axis) along the lattice potential in units of the lattice spacing. Different lattice depths (0,4,16 E_R) and the normalized optical lattice potential are displayed in different colours.

$$J \approx \frac{4}{\sqrt{\pi}} \left(\frac{V_0}{E_r}\right)^{3/4} \mathrm{e}^{-2\sqrt{\frac{V_0}{E_r}}} \tag{2.64}$$

In the upcoming chapter this term will determine the transition from atoms hopping into adjacent lattice sites to isolated states without interaction.

Lattice interactions and Mott Insulator

Until now we have only considered how non-interacting atoms can be described in our lattice. However if atoms share a potential-well they will attract or repel each other. An interaction energy term needs to be added to the kinetic 'hopping' energy to accomplish a full picture. It can be calculated with an integral over the Wannier functions of particles and interaction amplitude g, which depends on the dimensionality of the lattice and the s-wave scattering length a [173].

$$U = g \int |W(\mathbf{r})|^4 d\mathbf{r} \quad \text{with} \quad g = \frac{4\pi\hbar^2 a}{2m} \quad (3D) \tag{2.65}$$

This on-site interaction energy can also be approximated with a harmonic oscillator approach. In it, the Wannier function around a lattice site is estimated by the ground state of the harmonic oscillator [174] yielding for the interaction energy

$$U \approx \sqrt{\frac{8}{\pi}} k_L a E_R \left(\frac{V_{\mathrm{lat}}}{E_R}\right)^{3/4} \tag{2.66}$$

For the tight-binding limit of the ground state in an optical lattice we can finally write the complete Bose-Hubbard Hamiltonian

$$H = J \sum_{i,j} (\hat{b}_i^\dagger \hat{b}_j + \hat{b}_j^\dagger \hat{b}_i) + \frac{U}{2} \sum_i \hat{n}_i(\hat{n}_i - 1) \tag{2.67}$$

with creation and annihilation operators $\hat{b}_i^\dagger \hat{b}_j$ at sites i and j to describe the tunneling of atoms from site j to i and the atom counting operator $\hat{n}_i = \hat{b}_i^\dagger \hat{b}_i$.

In figure 2.14 the tunneling strengths J and the on-site interaction strengths U for different isotopic combinations (^{87}Rb+^{170}Yb, ^{170}Yb+^{170}Yb, ^{87}Rb+^{87}Rb) are plotted. The approximations from equation 2.64 and 2.66 are included in green dashed lines. With increasing lattice depth, tunneling for the lowest band is already strongly suppressed at $20\,E_R$, while the interaction energy between particles growths stronger. The interaction for ^{87}Rb+^{87}Rb and ^{170}Yb+^{170}Yb is repulsive, while ^{87}Rb+^{170}Yb pairings are favourable in lattice sites due to the small negative scattering length. This is very interesting for the preparation of molecule production in 3D optical lattices in a mixed Mott insulator state [175], [176]. Furthermore the tuning of the ratio between J and U gives rise to a quantum phase transition from a conducting 'superfluid' state to a insulating state. So called Mott insulator transitions in optical lattices in quantum degenerate atomic ensembles were proposed by Jaksch et al. [177] and have since been experimentally demonstrated in many experiments [42], [178], [179]. They occur during the transition from shallow to deep

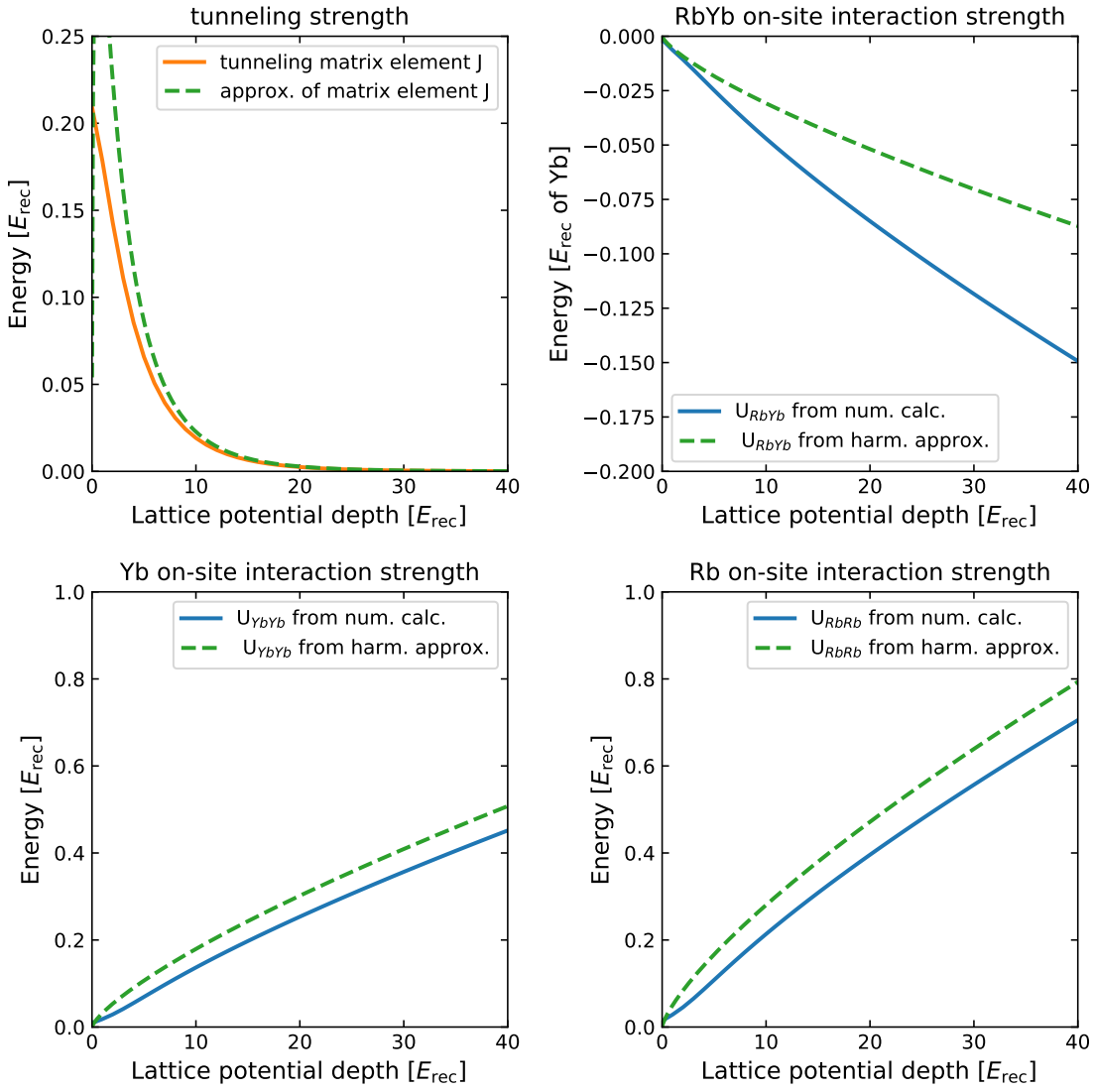

Figure 2.14.: The top left panel displays the tunneling strength J (independent of atomic species) in the ground state band of our 3D lattice. The three surrounding figures show the interaction energies of all possible diatomic pairings within a single lattice site indicating a repulsive interaction for homo-nuclear and attractive interaction for the hetero-nuclear ^{87}Rb+^{170}Yb pairing. (This figure presents all plots as a function of lattice potential depth in recoil energies E_{rec}.)

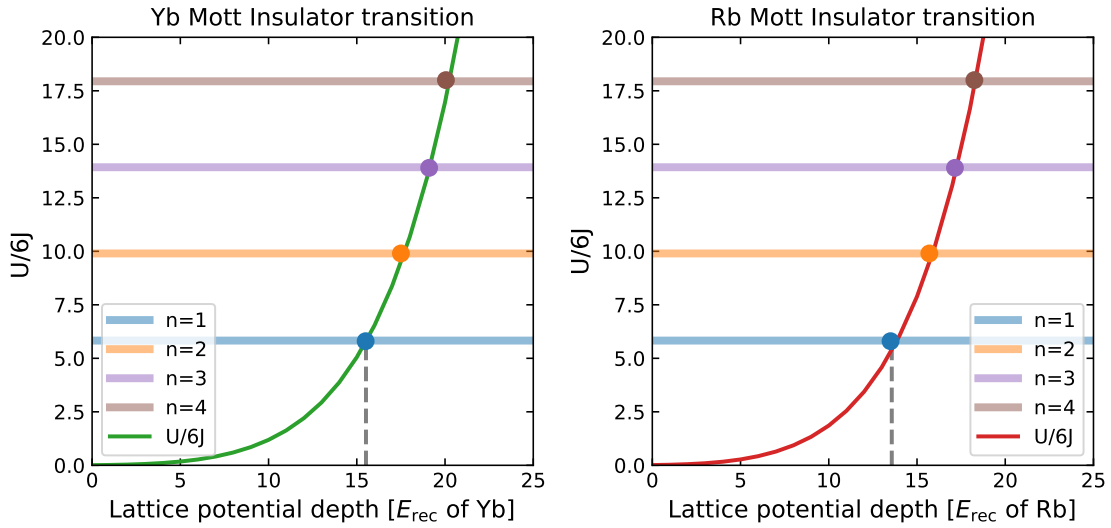

Figure 2.15.: Mott insulator transitions for full lattice fillings with either only ^{87}Rb or ^{170}Yb. The superfluid (SF) to Mott insulator (MI) transitions for $n = 1, 2, 3, 4$ are indicated at the crossings with the critical $U/6J$ ratios. For $n = 1$ the dashed vertical line shows the lattice depth at the lowest phase transition. Again this figure presents the plots as a function of lattice potential depth in recoil energies corresponding to the trapped species.

lattices or vice versa. In the shallow lattice the wave functions of individual particles are delocalized over the lattice ($J >> U$). Furthermore the occupation of a lattice site is not well defined in the superfluid state. In the insulating state particles are fixed and their wave functions are restricted to single lattice sites leading to the loss of coherence ($J << U$). The position of a phase transition is characterised by the critical ratio [166]

$$(U/J)_c = z \cdot 5.8 \tag{2.68}$$

with $z = 6$ for a 3D lattice and $n = 1$ atom per lattice site. For fillings of $n = 2, 3, 4$ the ratios for a phase transition are $U/6J = 9.9, 13.9, 17.9$. When the lattice potential depth is increased the ratio $U/6J$ changes as plotted by the parabolic curves. The superfluid (SF) to Mott insulator (MI) transitions are calculated for Rb and Yb and different lattice fillings n in the bottom of figure 2.15.

3.

Experimental apparatus

Note to the reader: While completely new components like a capillary oven (section 3.1.1), piezoelectric shutters (section 3.2) and new high power laser systems (section 3.7 and section 3.6) have been added to the experimental apparatus, a lot of topics of the experimental setup in this thesis were already treated in the previous work by T. Franzen [1]. Nonetheless, these topics are still covered for completeness, contain some additional details or shorten parts that have been discussed extensively in the thesis of T. Franzen.

This chapter gives a complete overview of the experimental apparatus used for this work. It mostly consists of the vacuum chambers, optical systems and electronics that are used to operate the 'molecule machine'. The setup of this new apparatus began before this thesis as described in [1] and is yet to be completed. However a lot of progress has been made and crucial systems are now running error free for years.

The experiment is set up in a way that separates most laser systems from the actual experimental optical table via optical fibers. This protects them against vibrations when working around the experimental table and avoids illuminating atoms with stray light. Additionally the fibers decouple the laser setup from the experiment and thus reduce the impact of laser issues on the alignment of the experiment. For clarity we will call the separated laser systems to be in the *laser room* and the setup around the vacuum system *science table*.

In this chapter, we start with an overview of the vacuum system (chapter 3.1) before we explain the optical systems (chapters 3.3, 3.4, 3.5, 3.6 and 3.7) which are used for trapping and cooling atoms and those which are used for molecular spectroscopy (chapter 3.8).

3.1. Three vacuum chambers

The whole vacuum assembly is divided into two so called *production chambers*, in which the respective atomic species are prepared, and a *science chamber* where they are brought together using a pair of optical tweezers. This separation allows us to independently optimize the conditions for the production of cold samples of *Rb* and *Yb* in the *production chambers*, without restricting the possibilities for experiments in the *science chamber*. The predecessor experiment struggled with the limitations of combined production of these atomic clouds and optical access in a joined vacuum chamber [9]–[12], [14]. This issue is now eliminated by choosing three vacuum chambers with individual configurations for

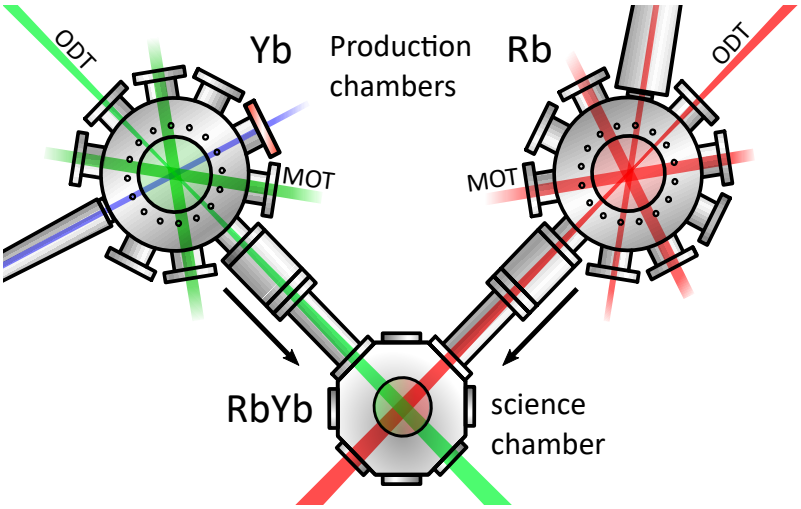

Figure 3.1.: Overview of the vacuum setup of the experiment. Two production chambers each with attached Zeeman slower and oven are designed to prepare Rb (right) and Yb (left) separately. Optical transport into a shared science chamber is possible via optical dipole traps (ODTs), where both species can be mixed or also studied individually. The highlighted window (in red at Yb production chamber) is heated to 230 °C to prevent coating with Yb from the atom beam.

magnetic coils and the possibility to load atoms simultaneously. Furthermore it is also possible to vent each vacuum chamber individually for upgrades without breaking the vacuum in the rest of the system by using pneumatic gate valves that can be closed in such cases. In figure 3.1 a sketch of the vacuum system is shown. Each production chamber (left: Yb right: Rb) is connected to a Zeeman slower and an atomic oven. The science chamber in the middle is connected by differential pumping tubes along the indicated optical dipole trap (ODT) laser beams to enable optical transport. In the science chamber the laser beams can be overlapped to from a combined trap.

3.1.1. Atomic oven for Rb and Yb

The sources of atoms are atomic ovens that are heated to 125 °C (Rb) and 420 °C (Yb). They are both connected to a Zeeman slower and ion pumps, while viewports offer monitoring of the beam fluorescence. Both oven systems remained unchanged from the description in [1] until the old Yb oven was replaced by a new self-build capillary version[1].

A new capillay oven for Yb

The new self-made design of the capillary oven shown in figure 3.2 has been thoroughly tested in [180]. It is inspired by different cold atom experiments that already use these types of designs [181]–[183]. First results show a reduced angle of exit of Yb atoms that is limited

[1] The lifetime of the used Yb ovens depend on the filling and operating temperature (≈ 2 years). The novel self-build capillary oven replaced the old one once it ran out of atoms.

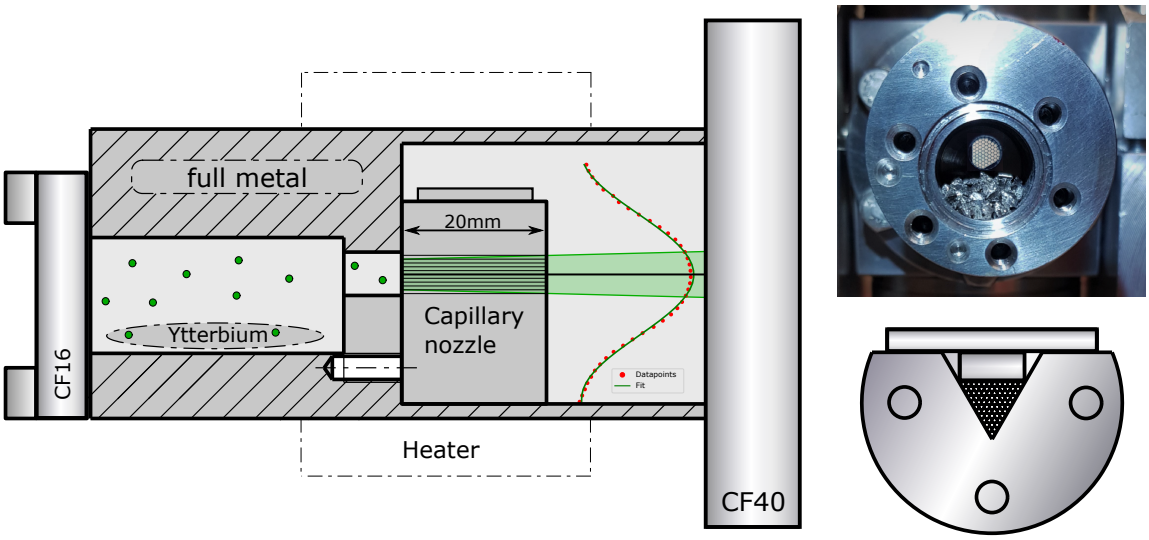

Figure 3.2.: The new capillary oven design features a triangular stack of 78 capillaries, which create a collimated beam of atoms. The oven is heated by a heating element that is positioned at the center of the capillary array to avoid blockage of the steel tubes. The photo on the right side shows that the reservoir is filled from the backside and situated below the capillary nozzle.

by the dimensions of the capillary steel tubes (MicroGroup Stainless Steel 304H22XX). The tube specifications are: 20 mm length; 0.590 ± 0.015 mm inner diameter; 0.715 ± 0.010 mm outer diameter. The underlying concept is creating a more collimated beam of atoms instead of wasting 99% of atoms that leave a simple nozzle at large angles and never arrive in the production chamber and thus increases the lifetime of an oven. In a regime of molecular flow the flux in a single tube can be described by [184].

$$I(\theta) = \frac{\mathrm{d}N}{\mathrm{d}t} = \frac{n\bar{\nu}}{4\pi}\mathrm{d}A cos(\theta)\mathrm{d}\omega = \frac{n\bar{\nu}}{4\pi}Aj(\theta)\mathrm{d}\omega \tag{3.1}$$

if the Knudsen number $K = \lambda/L$ is larger than one[2]. Here, A is the cross section of the tube, $\bar{\nu}$ the average particle velocity and $j(\theta)$ the angular distribution of the flux. For the determination of $j(\theta)$ we have to distinguish between atoms that travel though the capillary without wall collisions $\theta < \arctan(\frac{2r}{L})$ and those that hit the wall at least once $\theta \geqslant \arctan(\frac{2r}{L})$ [184]. In figure 3.2 the angular distribution of the flux is illustrated (not to scale) by the inserted curve. The angle at which the atom flux intensity $I(\theta)$ is reduced to $1/e$ was determined to be $\theta = 1.6(8)^\circ$. The combined nozzle array made of 78 capillaries is created by stacking and clamping them together in a triangle shape, see figure 3.2 (bottom right side). The required vapor pressure is reached by heating a reservoir of metal Yb chunks with a heater element. The metal chunks rest on a lower level compared to the capillary nozzle and the heating element is positioned at the center of the capillary array in order to keep the tubes at a higher temperature than the rest of the oven and thus

[2]This only holds for low densities and negligible collision rates between atoms. If this is not the case we enter an intermediate regime that has to be used to calculate the angular distribution.[181]

avoid blockage of the steel tubes with either Yb or other impurities from the reservoir. For maintenance the oven is easily accessible by a CF16 flange on the backside.

The old Yb oven

In contrast to the new oven design, the previously used version used two collimating holes to create a collimated beam - one at the position of the capillary array and one inside the CF40 flange connection further downstream.

The used isotope ^{170}Yb has low abundance and forces us to use a relatively high vapor pressure and high flux since the oven is filled with a natural mixture of Yb isotopes. This led to multiple issues due to Yb atoms (or other substances) from the oven depositing on a mirror inside the vacuum chamber - and once this was removed - a window indicated in red in figure 3.1. We and similarly other groups [185] observed a thickening grayish layer on surfaces facing the Yb oven that reduced the available intensity of our slower beam. As a countermeasure the production chamber was opened under nitrogen atmosphere with a glove bag and a new Quartz viewport (Allectra 110-VQPZ-C40-UV) has been installed. It is currently heated to 230 °C prolonging the duration until the next window change is necessary due to degrading performance. Side-measurements, where the removed window with Yb coating was heated, showed a partial desorption and significant improvement in transmission that supports this approach.

3.1.2. Production chambers

Pressure: $1,0 \cdot 10^{-11}$ mbar

The production chambers stretch over two levels on our science table as illustrated in figure 3.3. On level one they are both equipped with eight viewports - for lasers and imaging - and are each attached to the science chamber and to individual Zeeman slowers[3]. The viewports of the Rubidium production chamber are all equipped with broadband anti-reflection (AR) coatings for wavelengths from 550 nm to 1100 nm (*Lesker* DUV C3). For the Ytterbium chamber only the window opposing the connection to the science chamber has this coating. All other viewports are covered with DUV C2 broadband coatings ranging from 425 nm to 760 nm, which are still quite transparent at 400 nm. Watercooled magnetic coils are used to generate the MOT field gradients for both production chambers and in addition a quadrupole field for the magnetic trap in the case for Rb. Each upper coil is placed inside a recessed flange close to the center of the chamber to increase the available field gradient. The lower coils are placed below the viewports on the outside of the chamber to ensure optical access and offer a good cross-section for pumping. Three bias coils mounted on the MOT viewports per chamber are used to shift the magnetic field zero in each desired axis. The cylindrical shape is extended down to level two, where the ion pumps and titanium sublimation (TiSub) pumps are located. The ion pumps for all chambers are continuously operating and the titanium sublimation pumps are fired sporadically to increase their pump rate. A microwave antenna, laser outputs, optics and

[3]The Slowers are not included in picture 3.3.

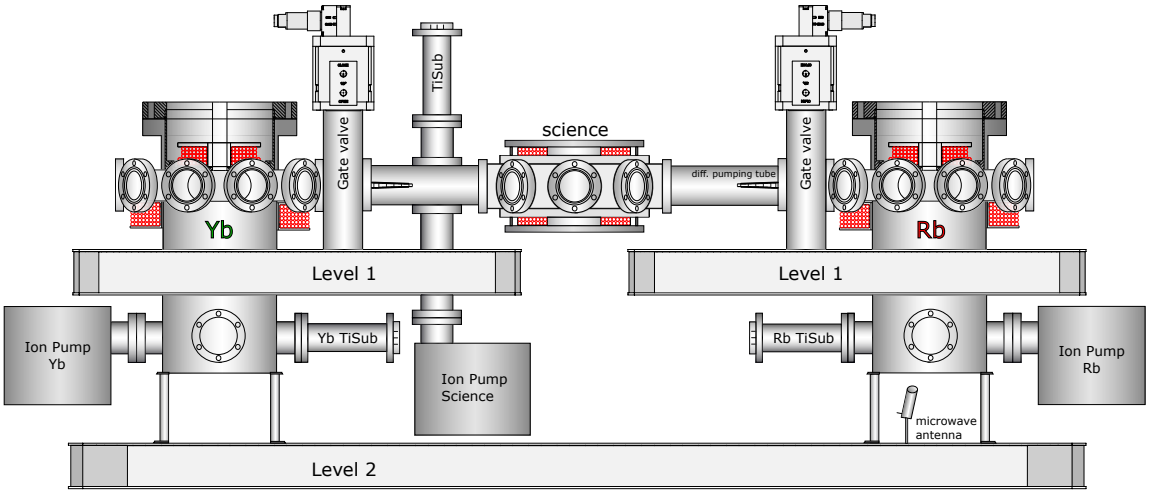

Figure 3.3.: Vacuum system on two levels. To the left (Yb) and the right (Rb) are the production chambers, which sandwich the science chamber in the middle. Pumping equipment is mostly situated on level 2. The magnetic field coils for the quadupole fields in each chamber are marked in red. Note that orientation of components and scales are not correct for better visibility.

AOM drivers are placed below to free up space on level one and provide vertical beams for the system.

3.1.3. The science chamber

Pressure: $< 1,0 \cdot 10^{-11}$ mbar

The science chamber is located in between both production chambers. They are connected via differential pumping tubes (length: 150 mm, diameters: 14 mm and 8 mm) to enable even better vacuum for experiments in the main chamber. The previously mentioned pneumatic gate valves can isolate the science chamber for future upgrades. For now the science chamber is an empty spherical octagon (Kimball MCF600-SphOct-F2C8). Due to the connection to the other chambers, six horizontal and two vertical viewports remain for imaging and trap beams. The viewports are mostly uncoated because their use was not determined in the beginning of construction. The ports along the axis of the differential pumping tubes and production chambers however have a broadband coating (*Lesker* DUV C3). This coating has good anti-reflection (AR) properties from 550 nm – 1100 nm as well as at 532 nm[4]. For magnetic field control, two identical coils are mounted, on top and bottom, on the outside along the vertical axis. All pressures are readings of our ion pump controllers which agree with lifetime measurements in optical dipole and quadruple traps [186].

[4]ODT's at 1064nm and 532nm have been operated through these viewports.

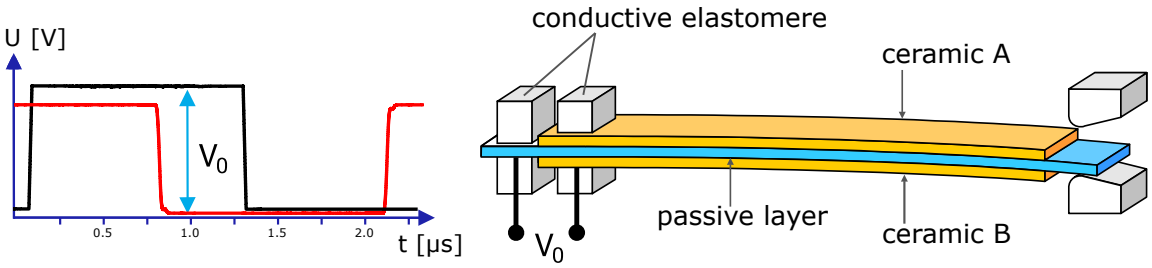

Figure 3.4.: Sketch of a piezoelectric cantilever element modified from [188]. A high voltage V_0, applied to a passive layer and ceramic A or B, can alternately bend the element upwards (A) and downwards (B).

3.2. Piezoelectric cantilever shutter

Mechanical shutters are frequently used devices in all cold atom laboratories. The requirement to fully extinguish even nanowatts of resonant light surpasses the capabilities of acousto-optic modulators (AOM) and often requires a physical stop for those photons. Furthermore AOMs deform the shape of laser beams at high laser intensities and are thus not suitable in such cases. For quite a while, small audio speakers [187] have been used to raise and lower a sandpaper disk in order to block or let a laser beam pass through a hole in its center. These types of shutters are typically slow as they have a fall/rise time of milliseconds. This makes a combination of AOM's and these shutters necessary if the experimenter wants to act fast [1] and at the same time properly block all light. Other disadvantages of speaker shutters are their limited lifetime (some live years, some live weeks) and the vibration that impacts laser stability. In practice it is a nuisance to find and replace (half-)broken mechanical shutters and we thus started to replace them with a new piezoelectric cantilever design.

The new solution is a bending piezo element that can be moved into the laser path by applying a high voltage to a trimorph piezo ceramic, see figure 3.4. The design is inspired by [189] and the piezo elements used are Type1/Type2/Type5 benders from *Johnson Matthey Piezo Products*. They are about 50 mm long and can reach a total deflection of ~ 2 mm. The deflection is proportional to the applied voltage, however in this application it is practical to choose 230 V. This Voltage V_0 is applied to ceramic A and B to get the maximum deflection limited by plastic nobs at each end to minimize jitters.

Figure 3.5 shows a picture of the housing and the attached wires with a piezo element. We use a simple TTL (transistor–transistor logic) trigger signal send to a high voltage driver to activate the motion of the bender and reach a fall time of 24 ± 2 µs for the extinction of a focused beam of 90 µm at 532 nm. This is of course only an example of a case, in which the fall time was optimised, and is not representative for all employed piezo shutters. Nevertheless it proves that by simple timing of the trigger delay an optical dipole trap (ODT) can be switched off in less than 30 µs for time of flight measurements (tof), as is the case for our 532 nm laser beam.

[1] Rise/Fall Time of AOM's is usually on the order of tens or hundreds of nanoseconds.

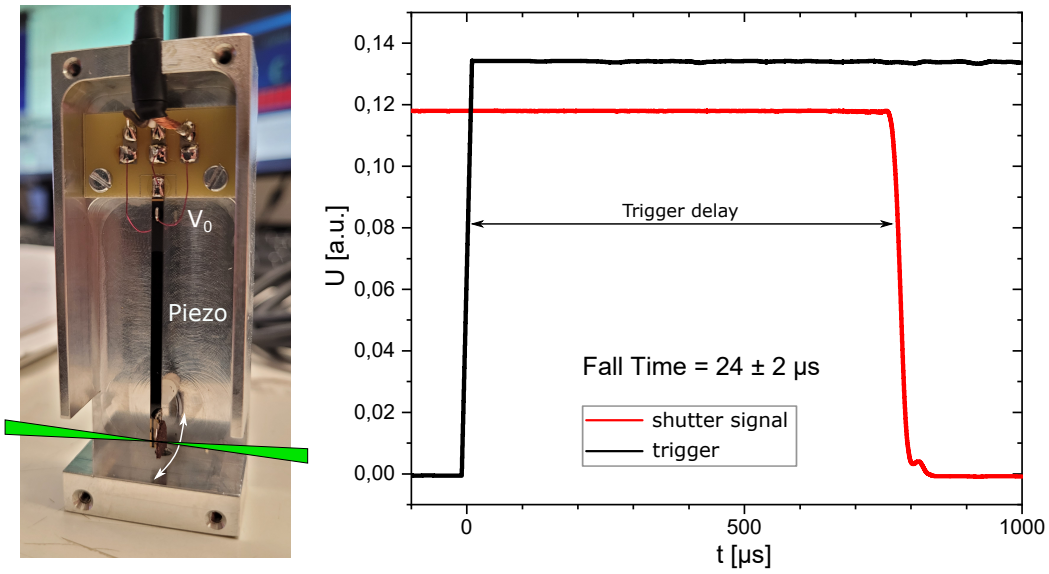

Figure 3.5.: The left shows the final design of our new piezo shutters with a 'virtual' laser beam. The aluminum housing can be closed and is grounded by connecting it to the optical table. On the right a measurement of the trigger delay (800 µs) and shutter signal (measured with a fast photodiode) shows a fall time of 24 $\pm$ 2 µs.

Since the conversion to the new shutter design, we have not noticed any failures or deterioration of the shutter quality. In some cases however the plastic nobs need some adjustment to avoid jitters of the piezo or vibration due to the bender hitting the nob.

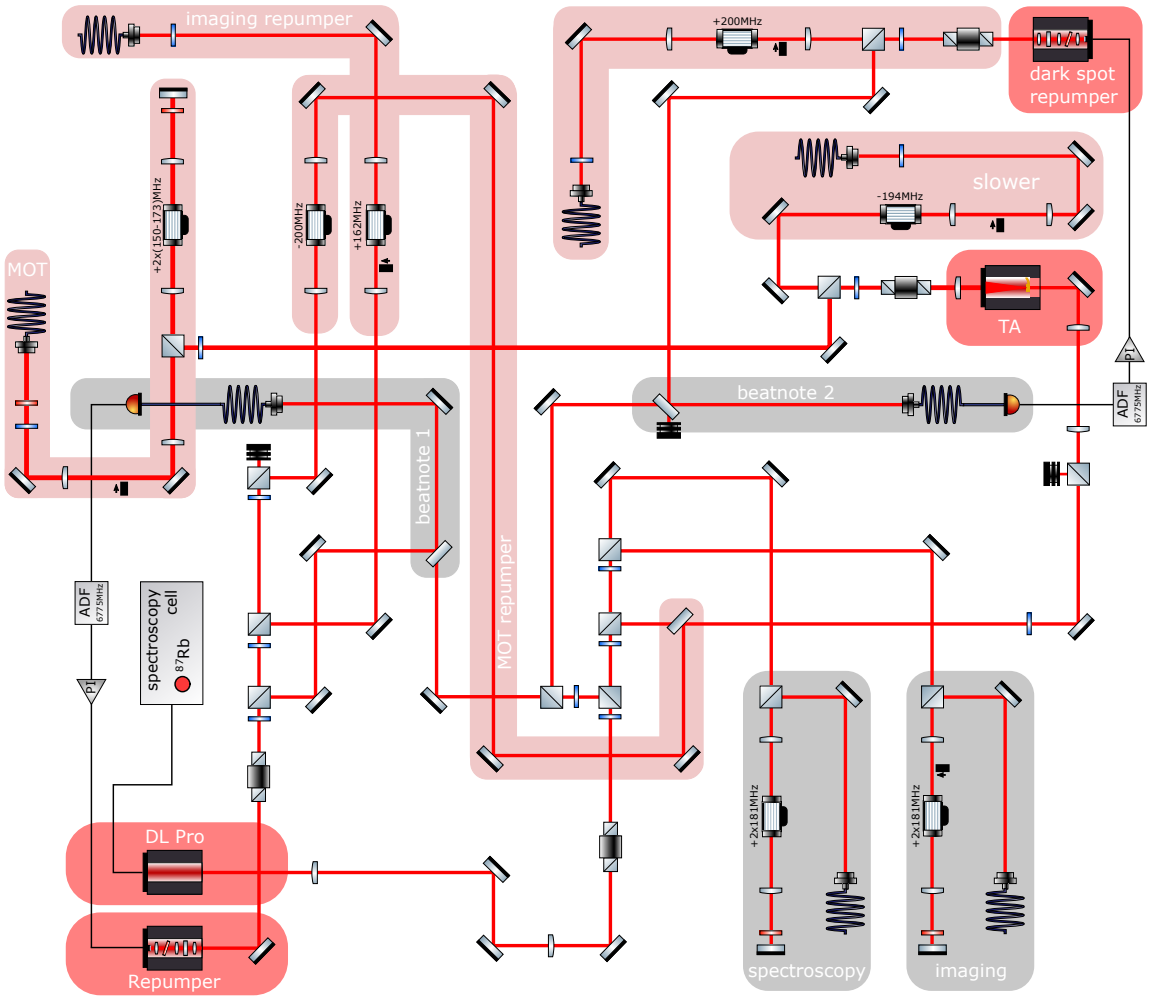

Figure 3.6.: Schematic diagram of the Rubidium laser system, containing the spectroscopy cell, the master laser (DL Pro), two repumper lasers and the tapered amplifier. Aside from that, beam paths, AOM's, shutters, fibers couplings and beatnote locks are shown and labeled accordingly.

3.3. Rubidium laser system

The Rb laser system takes the essential role in the process of loading and cooling Rubidium atoms in its production chamber as well as providing imaging light. With the complex setup of optical components presented in figure 3.6 we can prepare and time all needed beams and adjust frequencies, while the assemblies shown in figure 3.9 and figure 3.10 deliver them to the atoms. This chapter is divided into several parts ranging from the frequency stabilisation of 780 nm light to the realisation of a Rb magneto-optical trap (MOT) and a optical dipole trap (ODT).

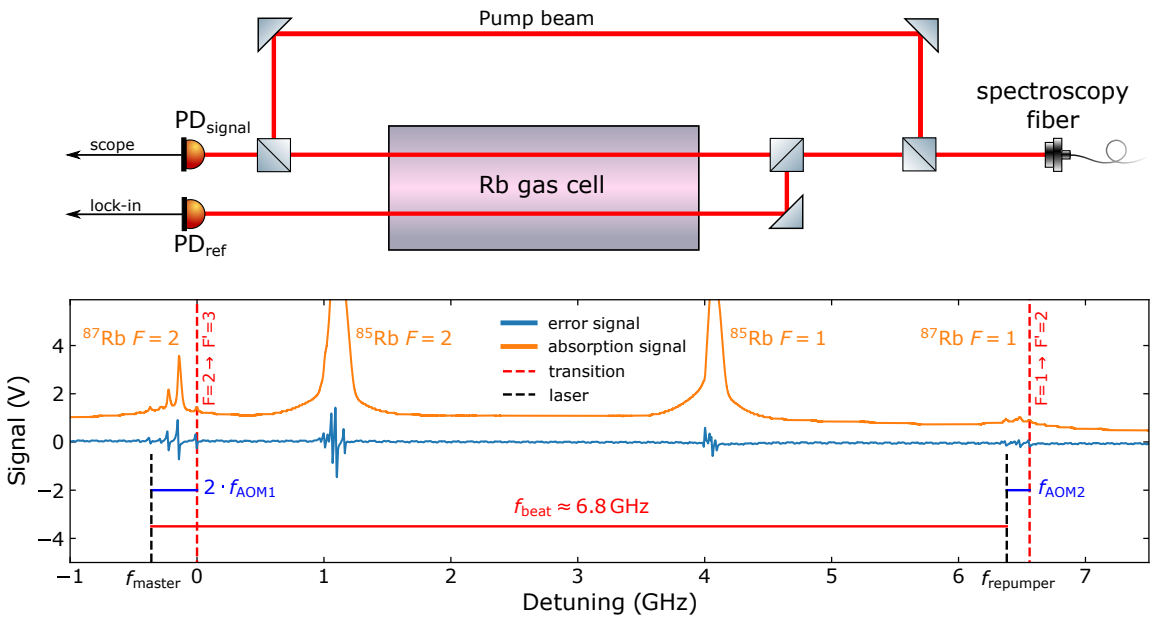

Figure 3.7.: The top panel sketches the spectroscopy Rb gas cell with pump and probe beams, which eventually produces an absorption (yellow) and error signal (blue) of a Doppler-free Rb spectroscopy. In the bottom panel (taken from [1]) these are plotted together with the MOT (F = 2 → F' = 3) and repump transition (F = 2 → F' = 2) in dashed red lines. The beat frequency of 6.8 GHz and the AOM detunings are shown underneath. The actual frequencies of the master laser and repumper are drawn in black dashed lines. (adapted from [1])

3.3.1. Rubidium spectroscopy

Cooling of our ^{87}Rb atoms is done with light driving the $^2S_{1/2} \rightarrow {}^2P_{3/2}$ (F = 2 → F' = 3) transition at 780, 250 nm, also known as the D2 line of Rb. It has a linewidth of $\gamma = 2\pi \cdot 6.06\,\text{MHz}$ [126] and can reach a Doppler temperature of 146 µK [190]. In order to induce this cooling process a frequency stabilised laser is required. We use a commercial grating stabilized *Toptica DL Pro* that is locked, 360 MHz red detuned, to a saturated absorption spectroscopy signal, shown in figure 3.7. The frequency shift for MOT operation is realized with a double pass AOM ($2 \cdot 180\,\text{MHz}$).

In figure 3.6 the beam path of the spectroscopy light is depicted. Light for the spectroscopy module is coupled into a polarisation maintaining optical fiber and afterwards split into a pump and two probe beams. The resulting signal of an overlapping probe beam with the pump beam is compared to the second probe beam that serves as a reference. The laser can then be stabilized to the error signal of a Doppler free spectroscopy signal.

3.3.2. Repumpers

In the level diagram 3.8, relevant hyperfine states and transitions for ^{87}Rb are shown. In order to close the cooling cycle of Rb, atoms accumulating in the F = 1 state have to be pumped back into the F' = 2 state. Due to the fact that a few Rb atoms take the off-resonant transition to the excited state, namely the F = 2 → F' = 2 transition and a following decay to the F = 1 state, a 'repumper' at 780, 236 nm has to be employed. State preparation also requires the Rb atoms to be repumped for imaging at the D2 line.

As a result we use repump lasers that are stabilized to a frequency offset of 6.8 GHz to the DL Pro via beatnote locks. The beatnote locking technique is extensively treated in [1]. The repumping lasers are self-built external cavity diode laser (ECDL) systems that produce about ∼ 35 mW of output power. We use *Sharp GH0781JA2C* diodes in a narrow band interference filter setup [191], which requires low maintenance until the laser diodes need to be replaced.

3.3.3. The Rubidium MOT

The mentioned locked lasers are sufficient to operate a magneto optical trap (MOT) for Rb. However, some more key ingredients like a magnetic field, a 'dark spot repumper' and a slower beam need to be added to the already mentioned repumping light and red detuned MOT light for full operation of our experiment. All these light fields need to be switchable with shutters and/or AOM's, frequency shifted by AOM's and coupled into fibers in the lasersystem (see figure 3.6) and guided through the vacuum chamber presented in figure 3.9.

Slower and MOT beams

We use ∼ 50 mW of the master laser light and split it into multiple beams for spectroscopy, imaging and beatnote locking. About 20 mW is left over as the main seed signal for

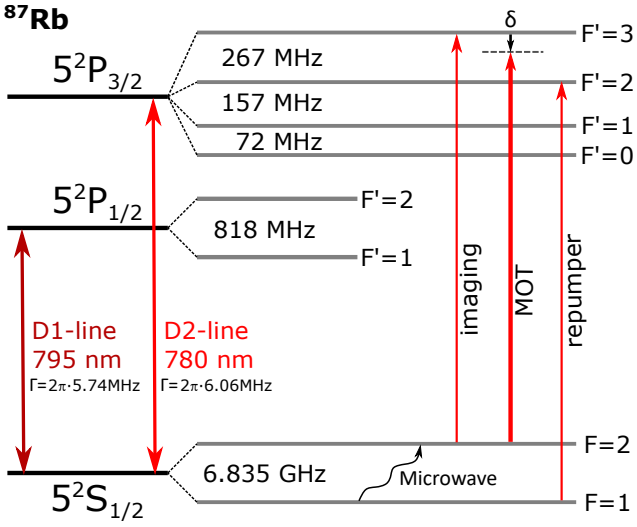

Figure 3.8.: Energy level diagram of ^{87}Rb with hyperfine structure and transitions used for the Rb MOT. Energy values and linewidth taken from [126].

a tapered amplifier (*TA from Coherent formerly DILAS TA-0780-1000*). The amplified light ($\sim 600\,\mathrm{mW}$) is then divided and subsequently fiber coupled to a fiber for the slower beam (20 mW) and for the MOT beam. The ends of both fibers are located on the science table and coupled out with achromatic doublets to create large collimated beams. Their powers can be read out with photodiodes for fiber coupling or power stabilisation[1]. The slower beam polarisation is linearised by a $\lambda/2$ wave plate and a polarisation cleaning cube. Afterwards the beam is polarised with a $\lambda/4$ wave plate, directed through the Zeeman slower and focused onto the Rb oven nozzle. The MOT beam (60 mW) is split into six beams of equal power, which create three pairs of counter-propagating beams with σ^+ and σ^- polarisation. In figure 3.9 the path of each beam is sketched, as it is routed across two levels of the science table by many mirrors, wave plates and polarisation cubes. Six beams instead of three retro-reflected beams (compared to the Yb MOT in section 3.4.3) are used because of the high optical density that is reached in this MOT. The detuning of MOT and Slower light can be adjusted by changing the frequency of their respective AOM's on the laser table.

Repumping a MOT

Repump light is incorporated into the MOT in two different ways. The first and simple solution is taking light from a repump laser and combining it with the master signal as an additional seed ($\sim 2\,\mathrm{mW}$) for the TA. This creates the advantage to always have repump signal in all MOT beams with perfect overlap because it comes from the same single mode fiber. However to increase the peak density in a otherwise density limited MOT a second repumper called the 'dark spot repumper' is used. (It is the second laser that is stabilized with beatnote 2, see figure 3.6). This laser beam is fiber coupled and afterwards shaped into a doughnut form by a circular gold layer on an AR-coated glass substrate[2]. It passes

[1] Currently not in use because is was not necessary due to an already stable power output.

[2] Initially for the dark spot MOT, an additional depumper beam was reflected of the backside of the coating surface to travel inside the dark region of the doughnut beam. It was eliminated as it sadly did not

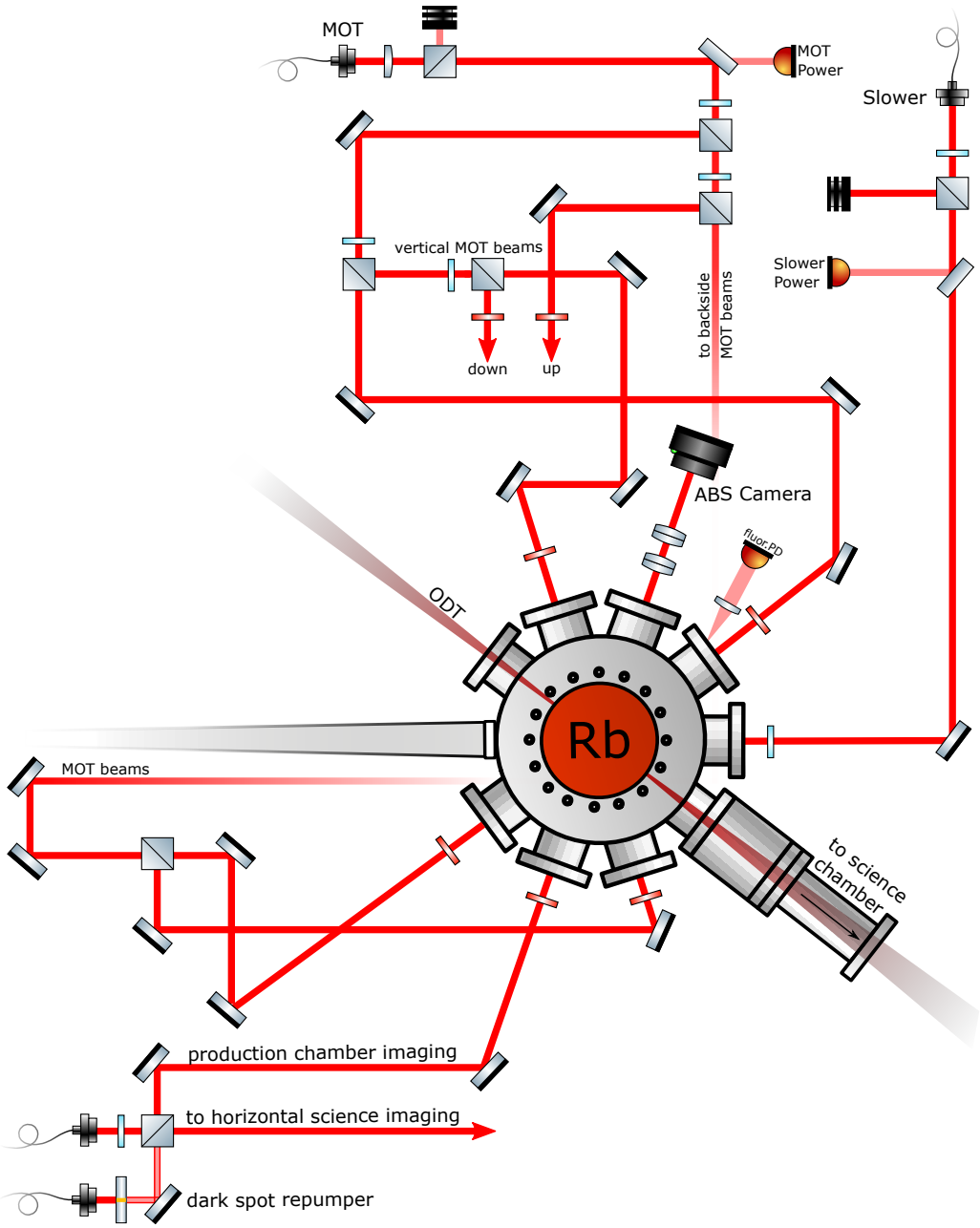

Figure 3.9.: Setup of the optical components and beams used for cooling and imaging in the Rb production chamber. The path of all six MOT beams, the dark spot repumper, the slower and the imaging beams is sketched out. The ODT beam for the optical transport is also indicated with a focus in the center of the vacuum chamber.

trough a polarisation cube and overlaps with the imaging light for Rb. Since we only have a single dark spot beam, we do not illuminate the entire trap volume around the dark region in the center. Fortunately this is not needed because atoms move trough the entire trapping region. Therefore we can choose the direction of the beam freely as long as we overlap the dark region with the center of the magneto-optical trap. To have more control and an easier adjustment we choose the imaging path as we can simply check the beam alignment on the camera that is usually used in the imaging system.

3.3.4. Imaging Rubidium

The imaging system of Rb shines resonant light onto a cloud of cold Rb atoms and then onto a camera chip and thereby creates an absorption picture. For more information on the imaging systems read section 3.9.5.

The light gets delivered to the vacuum ports by a single mode fiber and includes two wavelengths. Imaging repumping light ($\sim 500\,\mu W$) and imaging light ($\sim 50\,\mu W$) is combined by a fused fiber coupler, which provides spatial overlap. Resonant imaging light is prepared by taking light ($\sim 2\,mW$) from the master laser and copying the double pass AOM configuration of the spectroscopy beam path. If the same AOM frequencies are used, the fiber coupled light signal is automatically resonant with the imaging transition. For the imaging repumping light a beam from our repumper laser is split off, shifted by an AOM (+162 MHz) and finally fiber coupled. In order to image the Rb atoms and determine their atom number we prepare them in the F = 2 state. This is accomplished by using a repumping light pulse $\sim 0.8\,ms$ (800 µs pulse duration) before the exposure of the camera. This works similarly to all repumping techniques employed in the MOT as it ensures all atoms to interact with the ensuing imaging pulse (400 µs pulse duration).

On the science table a coupler collimates the imaging beam. Afterwards it is divided into two beams by a polarisation cleaning cube, which also serves as the input for the dark spot repumper beam. The reflected beam is guided through the production chamber onto the camera, while the transmitted beam is used for imaging in the science chamber. Quarter wave-plates and magnetic bias fields in the imaging axis are used for Rb imaging to ensure a well-controlled imaging polarisation (typically σ_+ or σ_-). This leads to the largest possible cross section and delivers the most reliable measurements in atoms number and density.

3.3.5. Rubidium Tweezer

The Rb tweezer system shown in figure 3.10, provides up to 30 W of 1064 nm light for the optical dipole trap, which traps and transports Rb atoms to the science chamber.

We use a commercial *Nufern NUA-1064-PB-0050-D0* fiber amplifier with a nominal power of 50 W. It is seeded by 14 mW of a spectrally multimode *IPG PYL-20M-LP* fiber laser[3]. Since the fiber to free space output of the *Nufern* does not come with isolation

increase the MOT density.

[3]This seed laser is also used as the seed in our Yb Tweezer system.

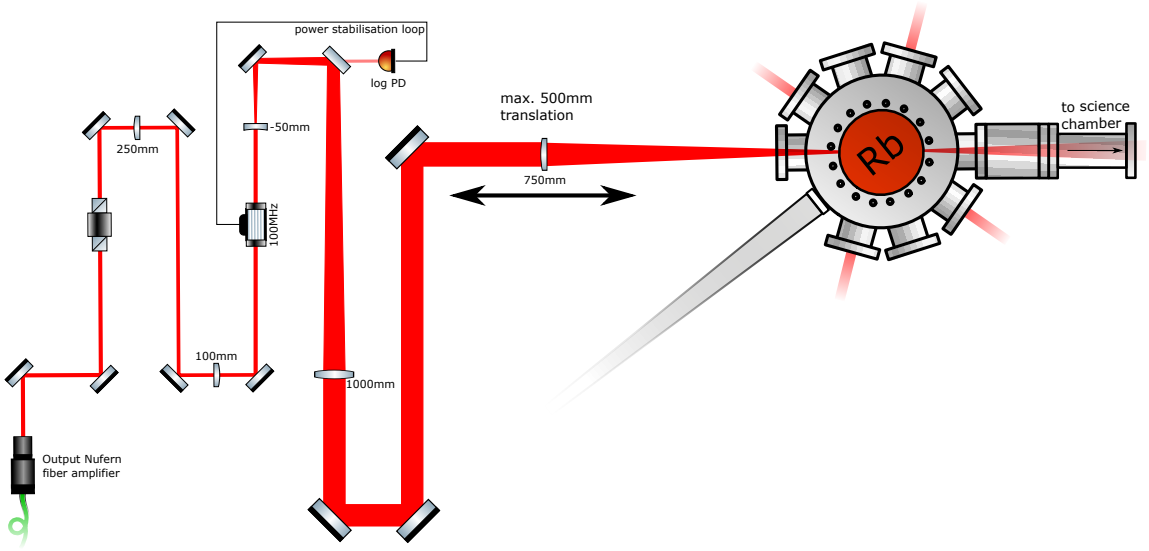

Figure 3.10.: Visualisation of the Rb tweezer system, which prepares the ODT beam for optical transport. The power stabilisation loop with the logarithmic photodiode and the AOM is shown. The beam shaping telescope to increase the beam diameter and its final focusing lens with indicated translation is sketched as well.

a free space isolator (*Thorlabs IO-5-1064-VHP*) is used[4]. The beam size is reduced by a telescope (250 mm/100 mm) to reach high efficiency in the first order diffraction of a *Crystal Technology 3110-191* AOM ($\sim$ 90%). The power of this beam is controlled by adjusting the radio frequency power injected into the AOM. This is done by changing the input of the associated AOM driver with a control voltage. The power gets stabilized via a logarithmic photodiode signal which records the transmission of a mirror behind the AOM. Furthermore the AOM is used for the fast switch off of the optical trap[5]. Finally the beam is magnified with a (−50 mm/1000 mm) telescope before being focused to a beam waist of 40 µm by a 750 mm lens. This lens is mounted on a *Aerotech ABL1500* air-bearing translation stage, which can move the lens and thus its focal spot axially over a distance of 500 mm. Atoms loaded in the Rb tweezer (ODT) can be transported in this focus to a desired position in the science chamber.

[4] [1] and [192] report substantial loss of isolation in this (TGG based) isolator. However, together with the back-reflection interlock of the amplifier, it is still sufficient for our purpose.

[5] In the Ytterium tweezer setup the AOM is also changed/modulated in frequency.

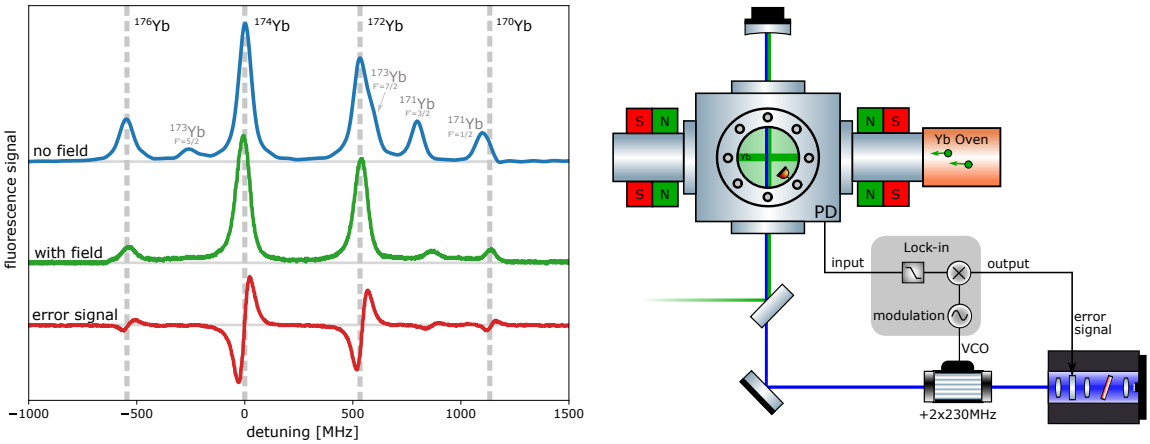

Figure 3.11.: On the left side of the picture a fluorescence spectroscopy signal of Yb with (green) and without (blue) magnetic field is presented. The error signal (red) belongs to the signal with field. The signals are presented with arbitrary offset for better visibility. The right section shows the spectroscopy system, which creates the recorded signal. It includes the spectroscopy vacuum chamber with oven and attached magnets, the master laser, the AOM, the photodiode and a sketch for the lock-in circuit. (adapted from [1])

3.4. Ytterbium laser system

The Ytterbium laser system has to fulfill the same duties as the Rubidium laser system. Loading and cooling of Yb atoms is also done in a MOT in its distinct production chamber, while a similar ODT transports Yb atoms to the same destination - the common science chamber. All beams and frequencies for the Yb MOT as well as imaging light are provided by laser systems with two different wavelengths, named after their colour - the 'blue' (in figure 3.12) and 'green' (in figure 3.16) system. In addition to presenting the laser setup this chapter explains how the MOT is actively position stabilized and thereafter loaded into an optical tweezer.

3.4.1. The blue system

The blue lasersystem, shown in figure 3.12, provides the Zeeman slower beam and the Yb imaging light for the experiment. It is operated at 398.9 nm on the $^1S_0 \rightarrow {}^1P_1$ transition of Yb. This transition is especially useful for fast cooling and imaging due to its large linewidth of $\Gamma = 2\pi \cdot 29\,\mathrm{MHz}$ and a Doppler temperature of 0.69 mK [193], see figure 3.13.

Spectroscopy

Deceleration of atoms in a Zeeman slower and absorption imaging requires a frequency stabilized laser. We use a self-built interference filter based external cavity diode laser system [191], [194] with a AR coated *Nichia NDUA116T* diode as the 'master' laser, that was constructed in [195]. It is frequency stabilized by a fluorescence spectroscopy signal, which is depicted in figure 3.11. A collimated atomic beam in a small spectroscopy

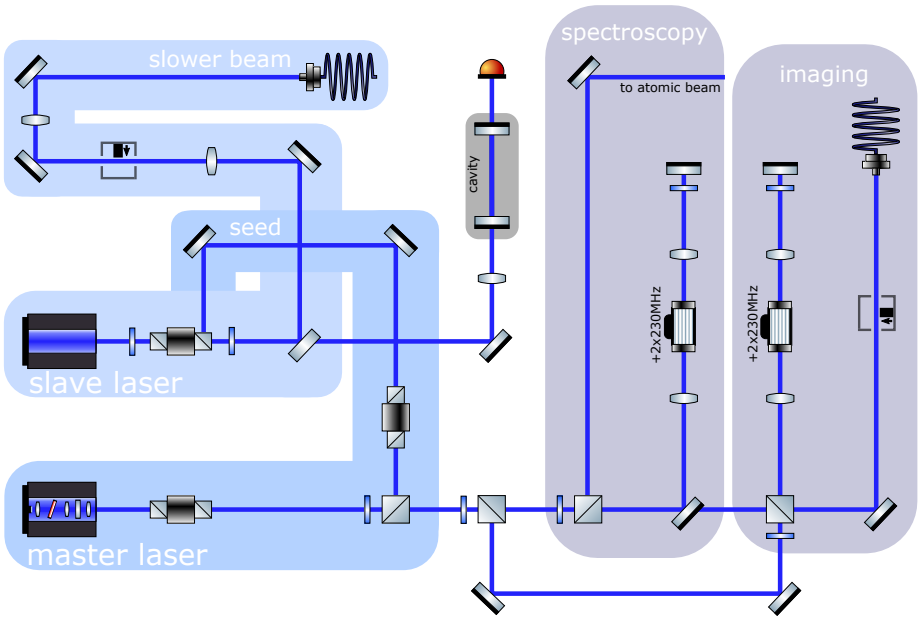

Figure 3.12.: Sketch of the blue laser system at 399 nm, which provides light for the Yb Zeeman slower. It contains a master-slave laser configuration and delivers imaging light to the experiment.

vacuum chamber is orthogonally intersect with the laser beam. The concave mirror on top of the chamber reflects the laser beam to effectively double the fluorescence signal and cancel Doppler shifts. The photodiode that collects all fluorescence light is located in the plane perpendicular to the plane of the image. It is worth noting that the polarisation of the laser needs to be orthogonal to this axis based on the characteristics of the Hertzian dipole in order to detect light. A second concave mirror along the axis on the backside of the chamber is used to collect and reflect more photons back to the photodiode which would be otherwise lost - enhancing the spectroscopy signal even further. Due to a low natural abundance of ^{170}Yb this is necessary to create a sufficiently large error signal. We stabilise the laser frequency by adjusting the external cavity length with a ring piezo element and can modulate the signal at a frequency of $\sim 10\,\mathrm{Hz}$ using a double pass AOM ($+2 \cdot 230\,\mathrm{MHz}$). The error signal is generated by demodulating the photodiode signal with a lock-in amplifier. In figure 3.11 this fluorescence signal is recorded in two variants. The blue line shows a signal without and the green line a signal in presence of a magnetic field. In order to split, for example the bosonic ^{170}Yb from the fermionic ^{171}Yb isotope signal, a pair of permanent neodym magnets have been attached to the sides of the chamber. This spreads the fermionic lines over a large frequency and leaves the bosons untouched.

On a side note, a green laser beam traveling though the chamber is also included in the sketch. Previously for frequency stabilisation of the green laser described in chapter 3.4.3, a two colour spectroscopy was used. Here the small depletion of the signal in a locked state was used to stabilise the frequency doubled 1112 nm laser.

Master and Slave laser

The stabilized 'master' laser seeds a so called 'slave' laser. In figure 3.12, this master-slave configuration is shown. A *Nichia NDV4313* laserdiode is injected with $\sim 750\,\mu W$ of seed light from the master laser. This forces the slave laser to copy its spectral characteristics, changing from a 401 nm multimode signal to the masterlasers wavelength and operating single mode with 40 mW. The injection quality can be monitored by a cavitiy signal that uses a small portion of this light. In order to prevent feedback back to the master and to the slave laser itself, three isolators are employed.

Slower and imaging light

Since the spectroscopy beam is frequency shifted by the AOM ($+2\cdot230\,MHz$), all blue lasers are red detuned with respect to the atomic resonance. The slower beam ($\sim 30\,mW$) for the Zeeman slower is hence directly fiber coupled and switched on/off with a piezo shutter. Due to observed degradation of beam quality and fiber coupling of a simple single mode fiber, it was replaced by a new fiber with coreless endcaps (*SMC-E-360Si-2.3-NA012-3-APC.EC-0-1000 Schäfter+Kirchhoff*). The high powers on both facets (especially input side) were leading to damaged fiber ends that needed regular polishing, which is now not necessary anymore. On the experiment side of the fiber, seen in figure 3.14, the light is coupled out with an achromatic doublet to ensure a large collimated beam. Since the fiber is not polarisation maintaining a $\lambda/4$ wave plate is used to correct rotation by the fiber. The beam is then sent through the heated window[1] ($230\,^\circ C$), the Zeeman slower and focused to the nozzle of the Yb oven.

The imaging light needs a frequency shift of $+2\cdot230\,MHz$ to be tuned back into resonance. Therefore the beam has an similar setup which includes an additional piezo shutter to extinguish stray light. Fast switch off is still realised with the AOM. We shine $\sim 50\,\mu W$ of light onto a cloud of cold Yb atoms and afterwards on a camera chip, which creates an absorption image. The imaging pulse used is typically 300 µs long and needs no other previous state preparation as for Rb.

3.4.2. The green system

The green lasersystem, shown in figure 3.16, generates the light for the intercombination line (green) MOT. It is operated at 555.8 nm on the narrow $^1S_0 \rightarrow {}^3P_1$ intercombination transition of Yb. This transition is especially useful for loading cold MOTs due to its small linewidth of $\Gamma = 2\pi \cdot 182\,kHz$ and Doppler temperature of $4.4\,\mu K$ [106], see figure 3.13.

1112 nm fiber amplifier

Light at a wavelength of 556 nm is created by frequency doubling infrared light at 1112 nm. In the previous work [1] a custom fiber amplifier at this wavelength with an output power

[1] This vacuum window is heated to minimise the Yb layer depositing on its surface.

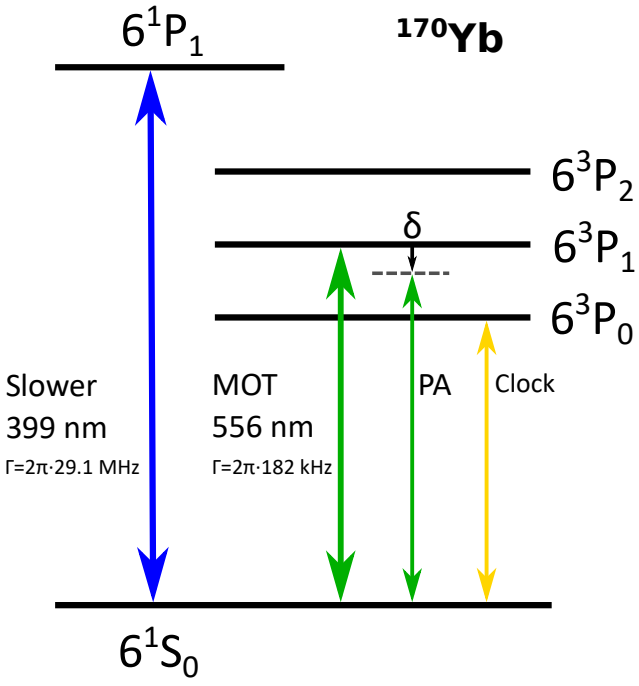

Figure 3.13.: Energy level diagram of ^{170}Yb with transitions used for the Yb Slower, MOT and photoassociation. Linewidths are taken from [106].

of 500 mW was build and published [196]. Since this amplifier and the theory behind it is covered in detail in [1], it will only be touched briefly in this section.

In the center of figure 3.16, the fiber amplifier is shown. As a seed source, a DFB fiber laser module was rescued from an old fiber laser system (*Koheras Boostik*). For the pump source at 1064 nm, a commercial laser module (*BKTel MFL-1370*), providing up to 5 W of power is used. Wavelength division multiplexers (WDM's, *Lightcomm HPWDM-X-1*2-1064/1112*) can combine seed and pump light and send it to the 22 m long active fiber (*Fibercore DF1100*). The fiber is heated to 75 °C in order to increase the absorption cross section at the pump wavelength. The fiber output is divided into the monitor output and the main output, which is connected to the polarization controller and the PPLN (periodically poled lithium niobate) SHG (single harmonic generation) module (*NTT Electronics WH-0556-000-A-B-C*).

It is important to note that the amplifier has to be protected from backreflections especially at a gain maximum of Yb doped fibers at 1080 nm. This is done by monitoring of backward propagating light on photo diodes combined with an electronic interlock system and fiber isolators. Due to the design and the unconventional pump wavelength, amplified spontaneous emission (ASE) and stimulated Brillouin scattering (SBS) barely occur in this setup.

3.4.3. Intercombination line MOT

The origin of 200 mW 'green' (556 nm) MOT light is a fiber-coupled frequency doubling crystal (PPLN SHG module). For the right conditions in temperature ($\sim$ 52.5 °C) and polarisation the maximum conversion efficiency is reached. The linewidth of the light is on the order of several 10 kHz.

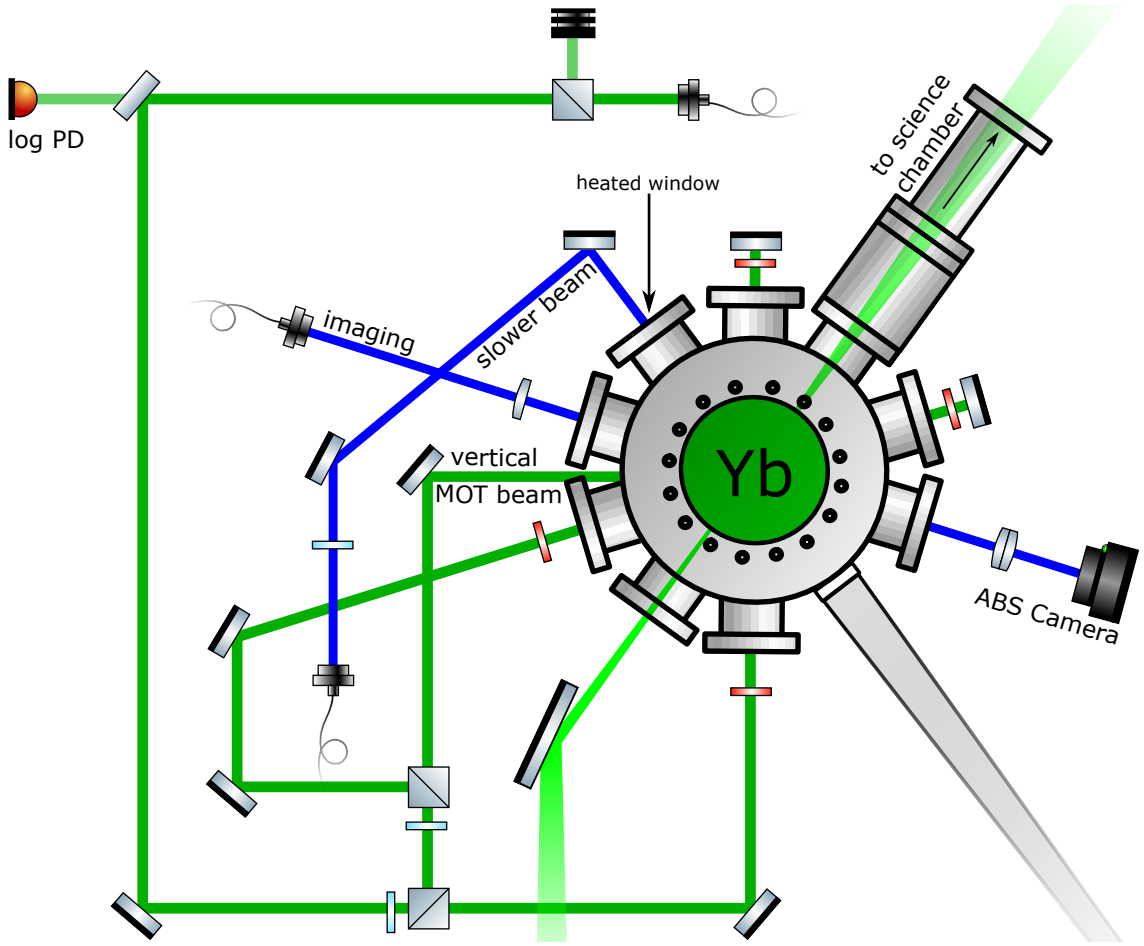

Figure 3.14.: Setup of the optical components and beams for cooling and imaging around the Yb production chamber. The path of the retro-reflected MOT beams, the slower and the imaging beam is sketched out. The ODT beam for optical transport is also indicated with a focus in the center of the vacuum chamber.

Behind the PPLN crystal the free space laser beam at 556 nm is collimated and shifted in frequency by an AOM. This AOM is utilized for fast switching of the beam and to change the detuning in the MOT. A piezo shutter is also positioned close to the AOM to properly extinguish stray light, since already nanowatts of resonant light can affect the lifetime of a loaded ODT. An ensemble of waveplates compensates polarization rotation of the light propagating in the fiber that leads the the science table. Power stabilisation of the MOT light is realised by a logarithmic photodiode that measures the transmission through a mirror behind the fiber output. The AOM acts as an adjuster for the coupled MOT power in order to reach and control low intensities in the cooling sequence of the MOT.

On the side of the science table (figure 3.14) this beam is again collimated by a self built collimator with an achromatic doublet for reduced spherical aberration. The light with faulty polarisation is discarded using a PBS cube. The remaining power ($\sim 30\,\mathrm{mW}$) is then split into three separate MOT beams. After of each beam has passed through the vacuum chamber, it gets retro reflected with good overlap of the incident beam. Quarter waveplates before entry and reentry into the chamber generate circular polarisation. In contrast to the Rb MOT, the low optical density allows us to work with only three retro-reflected beams instead of six in this MOT setup[2]. The used beams are $\sim 15\,\mathrm{mm}$ in diameter and the horizontal pairs have roughly equal power. The vertical beam however has about half the power as it is particularly important for the temperature and position of the final MOT during the loading step of the tweezer presented in sections 4.2.1 to 4.2.2 [3].

Frequency stabilisation of an intercombination line MOT

The laser frequency used for a narrow linewidth Yb MOT has great influence on its position since it highly depends on the laser detuning. It is especially sensitive along the vertical axis of the trap region, which poses a crucial point for the transfer into a tightly focused ODT. Therefore much effort was invested into an active position stabilisation of the Yb cloud using a *Raspberry Pi* camera, which compensates the long term drift of a Zerodur reference cavity. Our method was published in [197] and is described here in condensed form.

The Zerodur cavity

The laser described in 3.4.2 is locked to a reference cavity via the Pound-Drever-Hall method [198]. The cavity is set up with a Zerodur spacer (length: 105 mm) with a (low) thermal expansion coefficient (CTE) of $0 \pm 0.100 \times 10^{-6}\,\mathrm{K}^{-1}$ and low loss mirrors with a reflectivity of $\mathrm{R} = 0.99995$ at 1112 nm ($r = -250\,\mathrm{mm}$). This should in theory give a finesse

[2] It is technically possible to operate higher optical density MOTs with reflected beams, but I suspect it is more cumbersome to align.

[3] During the setup of the Yb MOT a lot of different power distributions, positions and sizes in MOT beams were tested. While some of them were ideal for loading a MOT, they were not compatible with a compressed MOT and vice versa. The distribution described in the text is a rule of thumb and usually never the reason of 'Why is there no MOT?'.

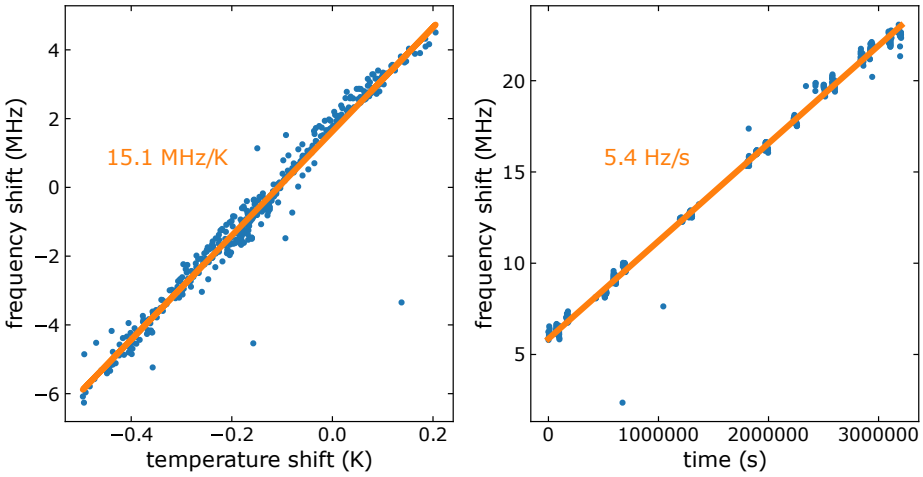

Figure 3.15.: Drifts of the Zerodur cavity used for the frequency stabilisation of the intercombination line MOT, taken from [1]. The left graph shows the frequency shift of 15.1 MHz/K due to temperature changes of the cavity. On the right side the aging effect of the Zerodur spacer with stable temperature, which effectively results in a shrinking of the cavity length, was determined to be 5.4 Hz/s (0.5 MHz/24h).

of $\mathcal{F} = 60.000$. It is placed inside a vacuum chamber with a pressure of $\sim 10^{-7}$ mbar and mounted on a temperature stabilized copper block. These measures improve the stability of the cavity, which is still sensitive to temperature changes. The level of stability, which is needed to reproduce a loading sequence of an ODT from the cold Yb MOT can be estimated to be 50 kHz, since the vertical displacement of the center of the cloud should not be larger then 10 µm (see figure 3.17). This is smaller than the linewidth of the MOT transition but still larger than the expected cavity linewidth of 25 kHz.

This implies that the temperature stability has to be around ± 1 mK corresponding to a cavity length change of only a few pm. On the left plot in figure 3.15 the actual reaction (15.1 MHz/K) of the cavity to temperature shifts is shown. Due to variations in the ambient temperature of the laboratory that couple to the cavity spacer via radiation and limitations of the temperature control loop, our stability requirements are not fully reached. Additional to this issue we observe an anticipated aging effect of our cavity, which effectively means that our spacer is shrinking over time. In the right plot of figure 3.15 we can see that this effect was determined to be 5.4 Hz/s (0.5 MHz/24h) or a shrinkage of $\frac{\Delta l}{l} = -3 \cdot 10^{-7}$/a. The following sections discuss the consequences of this drifting cavity and presents a solution to this problem. Furthermore we can note that a cavity spacer with a CTE that is orders of magnitude smaller and a professional mounting of cavity mirrors could make this solution obsolete. Currently the cavity mirrors are fixed to the spacer with glue eligible for vacuum, which can contribute to the change in cavity length. Mounting mirrors without glue is possible with optical contact bonding. Such specialized cavities, called ultra low expansion (ULE) cavities, are commercially available but are somewhat costly.

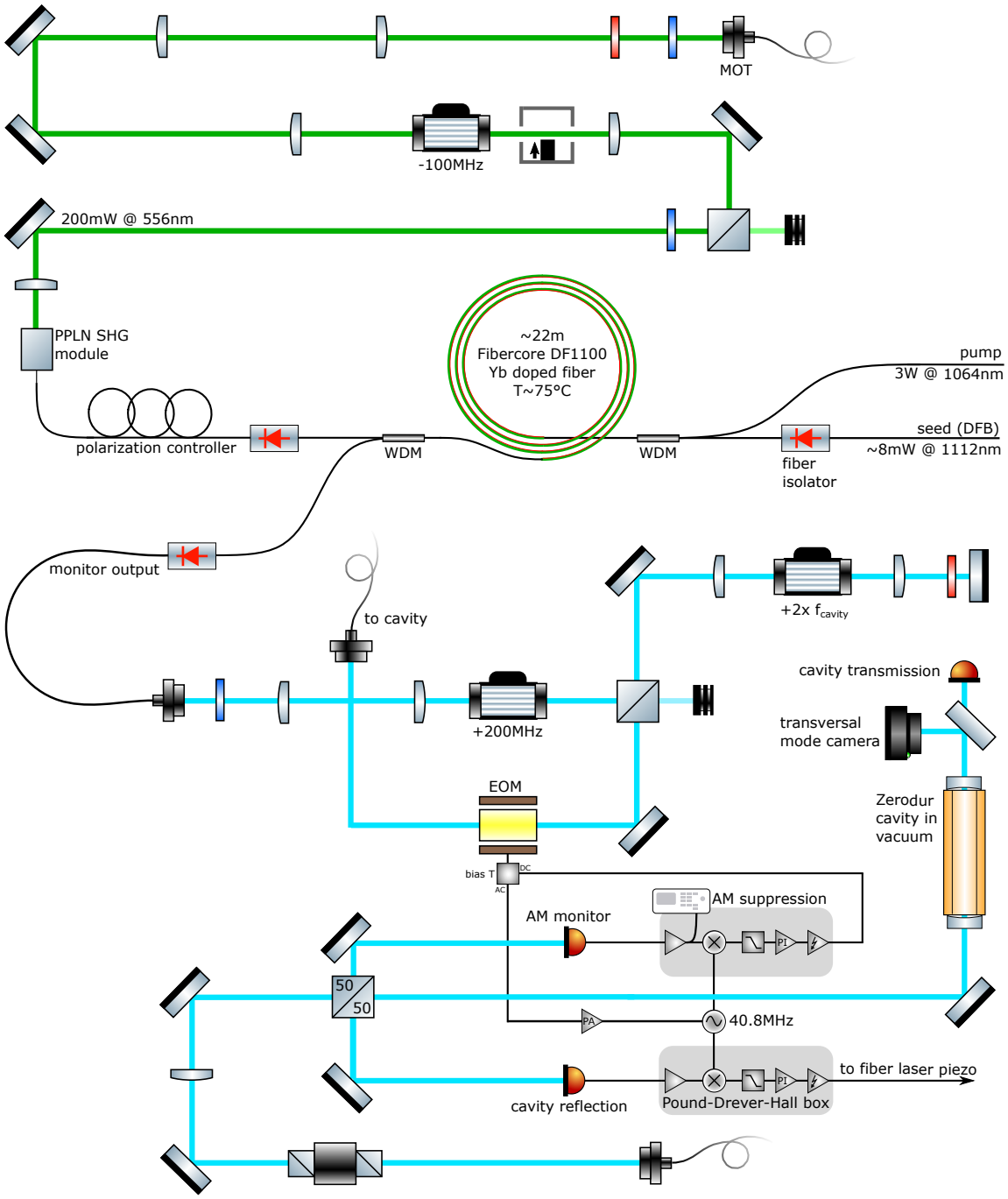

Figure 3.16.: The 1112 nm/556 nm laser system includes the self-build fiber amplifier at 1112 nm, its frequency stabilisation system with a Pound-Drever-Hall lock to a Zerodur cavity and frequency doubling to 556 nm light to provide MOT beams. A highly simplified sketch of the fiber amplifier, that was published in [196] and is explained in detail in [1], can be found in the center of the image. Its output (green) is frequency doubled (PPLN SHG module) and fiber coupled. Below, the monitor output of the amplifier (turquoise) is used to stabilize the MOT frequency by utilising the Zerodur cavity, AOM's, and an EOM to modulate sidebands.

Short term stabilisation with a cavity lock

As a start the experimental components that are used for the lock are explained. The bottom part of figure 3.16 illustrates the setup for frequency stabilisation of the MOT laser with a cavity lock. The reflection of the cavity is used to create the error signal to utilise the Pound-Drever-Hall (PDH) method. In order to distinguish the large number of infrared lasers in the image we use turquoise colour for the monitor output of the 1112 nm amp.

First of all the polarisation and the size of the free space laser beam are adjusted with a $\lambda/2$ plate and a telescope to get good mode-matching for all following AOM's and the electro-optic modulator (EOM). We use a self-build free space EOM to add 40.8 MHz sidebands to our PDH signal. The EOM has a z-cut lithium niobate crystal that is connected to an RF amplifier. The AOM's are used to compensate the long term frequency shifts of the cavity that were discussed in the previous section 3.4.3 and will be important for the next section. The first AOM adds merely an additional frequency shift of +200 MHz, which became necessary because the second AOM's frequency range was not large enough. The frequency of the second AOM is constantly changed due to drift of the cavity and will force us to change the lock point by a free spectral range (FSR) of the Zerodur cavity eventually. A short fiber is used to separate this section from the cavity to avoid misalignment. Since the EOM creates a residual amplitude modulation (RAM) due to ethalon effects caused by the flat surfaces of the crystal, a intensity stabilization of the beam is needed. Before the light is finally coupled into the cavity, it is split by a 50/50 cube and half of its power is sent to the amplitude modulation (AM) monitor photo diode. A servo loop for AM suppression is employed, which changes the bias voltage of the crystal by combining its signal with the RF modulation with a bias-T [199]. To avoid the bias voltage loop falling out of lock due to thermal drifts, an automatic inverter flips the polarity to move to a better locking point with zero RAM, when the output limits are approached.

The signal transmitted through the cavity can be observed by a transversal mode camera. Here a rear view camera originally intended for cars has been utilized to observe the cavity modes, which simplifies the search for a cavity mode and shows that we lock to a TEM_{00} mode. Finally the frequency is stabilized on short time scales with the PDH lock by acting on the fiber laser piezo. The result of this lock can be observed in the red curve in figure 3.17, where the position of a Yb MOT slowly drifted 300 µm in an hour.

Long term stabilisation with a Rasberry Pi

The issue of the drifting cavity, presented in the previous sections, prevents the long term stability of the Yb MOT position. For narrow-linewidth MOTs the position of the trap center is determined by the magnetic field and effective detuning including the position-dependent Zeeman shift of the laser due to the gravitational sag. At small laser intensities a changing laser frequency has the strongest influence on the MOT position [197]. As a consequence we implemented another feedback loop into the system. We use pictures of atom clouds taken by a camera connected to a *Rasberry Pi* to actively correct their position by changing the laser frequency [197].

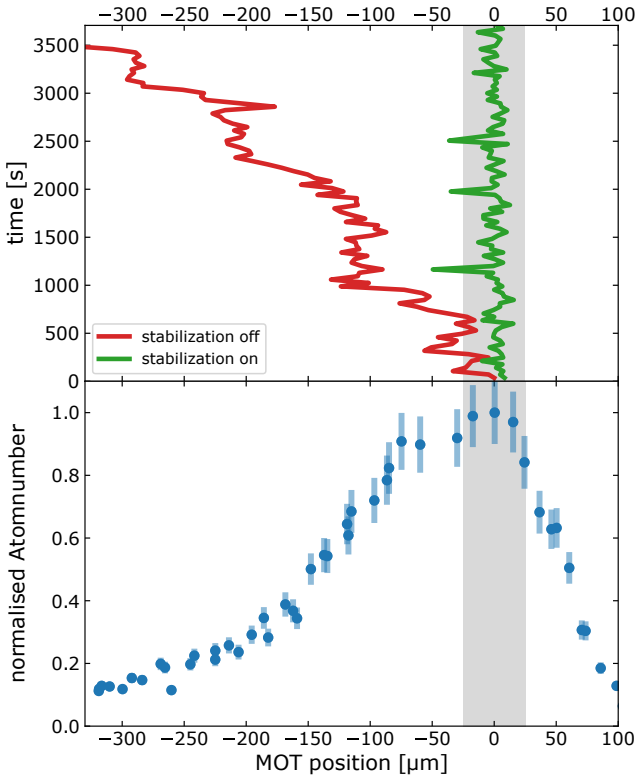

Figure 3.17.: The top panel shows the position of the compressed Yb MOT over time, with (green) and without (red) active position stabilization. The plot below displays the normalised atomnumber after a completed transfer into the Yb tweezer depending on the final vertical MOT position.

First, the *Rasberry Pi* receives a picture of a fluorescent MOT during its cooling and compression process, where it is highly sensitive to frequency changes. Then the center of gravity of the recorded fluorescence of the atom cloud is calculated and compared to a set position value. The required frequency shift is proportional to the displacement from this position. It is calculated and applied to the direct digital synthesizer (DDS) driving the AOM frequency. This yields a fast correction of the overlap with the ODT within one loading cycle. The difference to the set value can be used for the next cycle. Here a weighted drift rate can be used to predict a good frequency for the next shot, which effectively represents a slow PI controller. A second picture after the adjustment is taken to confirm the corrected position.

The green curve in figure 3.15 shows how the long term stabilisation with this technique keeps the MOT position within 50 µm of the set point, which enables a stable tweezer loading from a narrow linewidth Yb MOT. The plot below displays the normalised atomnumber in the tweezer after a completed transfer and clearly shows that the experiment is reproducible if the stabilization keeps the MOT withing the gray region.

3.4.4. 30 W fiber amplifier

High power fiber lasers and amplifiers are commonly used to produce focused light for ODT's. Due to an unfortunate failure of a commercial 532 nm fiber laser, previously used for the Yb tweezer, a new solution had to be found. The quest for a high power laser beam to create a new ODT for Yb is thus presented in this chapter.

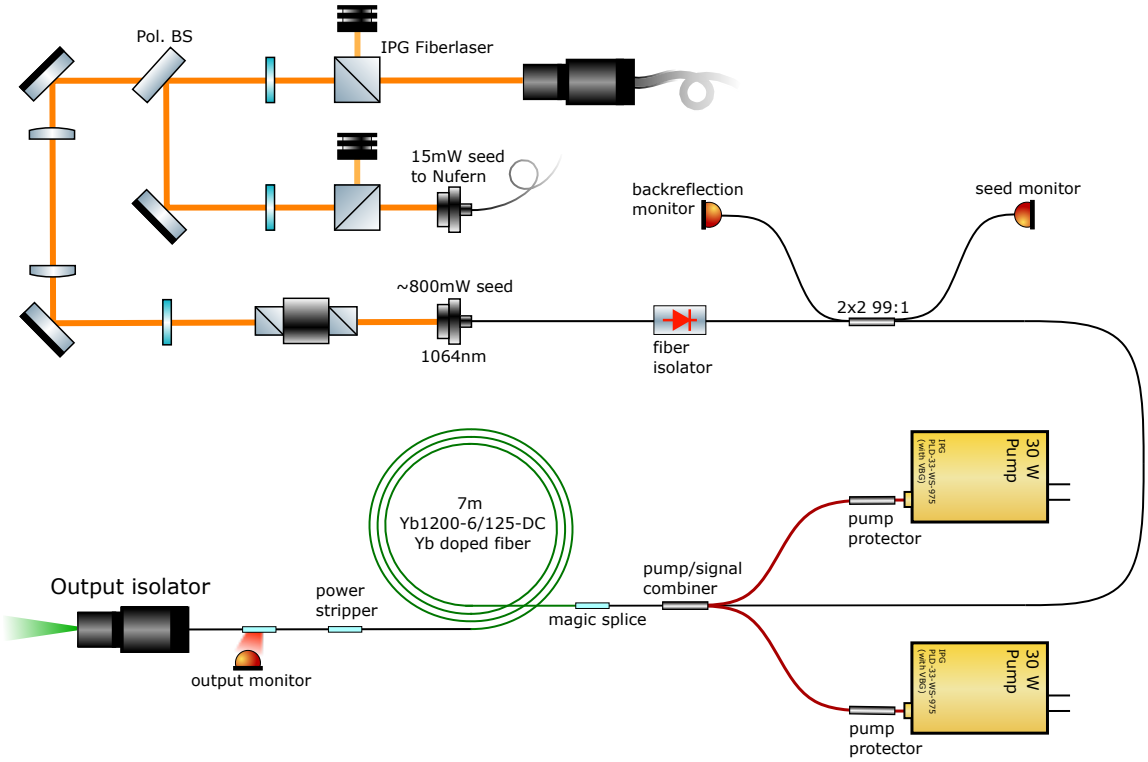

Figure 3.18.: Schematic diagram of the high power fiber amplifier system. The spectrally multimode fiberlaser ($IPGPYL-20M-LP$) provides seed light (orange) for both fiber amplifiers in the experiment that constitute the optical tweezers. The self-build Yb-doped fiber amplifier generates 30 W output power at 1064 nm for the Yb ODT.

Since only parts of the previously used commercial system were found to malfunction, the pump diodes and a fiber isolator could be salvaged for the new system. This new fiber amplifier is a self-build system at 1064 nm with 30 W output power. It amplifies a spectrally multimode fiberlaser ($IPG - PYL - 20M - LP$) that provides $\sim$ 800 mW of seed light.

In figure 3.18 the setup for the seed light (top) and the fiber amplifier (bottom) is shown. Seed light from this laser is used for both high power fiber amplifiers in this experiment. Therefore a polarising beam splitter is used to create two seed beams. In order to prevent harmful power variations, the laser needs to be switched on about an hour before the amplifier as the polarisation of the seed laser rotates during its warm up. The polarisation of the seed light (especially for the Nufern) is also carefully prepared by PBS cubes and waveplates. For the Yb fiber amplifier we use an additional free space isolator to prevent back-reflections.

Before the setup of the amplifier is discussed, the principle of amplification in doped fiber amplifiers (DFAs) is explained here.

These amplifiers use a so called 'active fiber', which is a fiber that is doped with ions (in our case Yb ions), as a gain medium. Ions inside the fiber core will absorb photons from a 'pump' source and decay by stimulated emission at the wavelength of a 'signal' source. For an Yb-doped fiber amplifier (YDFA) the absoption cross section peaks at 975 nm, which gives the most practical pump wavelength. Fiber-coupled diode lasers at this wavelength are readily available even up to hundreds of Watts with build-in wavelength stabilisation. However also other wavelengths can be used in different pump designs [196].

This 'signal' source is often referred to as the 'seed', whose presence is vital for the survival of the amplifier. Without a seed, ions choose a favourable decay channel in the emission spectrum with a large cross section, which leads to self amplification or short term lasing with a power spike that quickly destroys the amplifier. Even with sufficient seed signal, another effect called amplified spontaneous emission (ASE) plays an important part in DFA's. ASE is essentially the noise signal in fiber amplifiers with a spectrum that follows the gain medium. To keep it and other damaging effects in check, photodiodes with interlock systems are commonly used. Higher power and broad linewidth seed signals are also potent means to protect the amplifier from backwards lasing due to SBS (stimulated Brillouin scattering). Common signal wavelengths can be 1064 nm (Nd:YAG), 1047 nm (Nd:YLF) or 1083 nm (spectroscopic measurements [200]) but are possible for a wide range in the gain spectrum.

As previously stated, our home built amplifier uses a high power multimode 1064 nm seed signal, that reduces the tendency of the amplifier to self-pulsing or ASE. Nevertheless a fiber isolator is used first in the setup to prevent any optical feedback to the IPG fiber laser. Next a fused coupler (2x2 99:1) splits off one percent of the seed light to monitor it via a photodiode. If the amount of light is insufficient the amplifier cannot be turned on or will be shut down by interlock electronics. The shutdown is always realised by a fast switch off of all pump sources. The second port of the fused coupler monitors the back-reflection signal of the amplifier.

A pump-signal combiner can multiplex the signal and two multimode pumps into a single

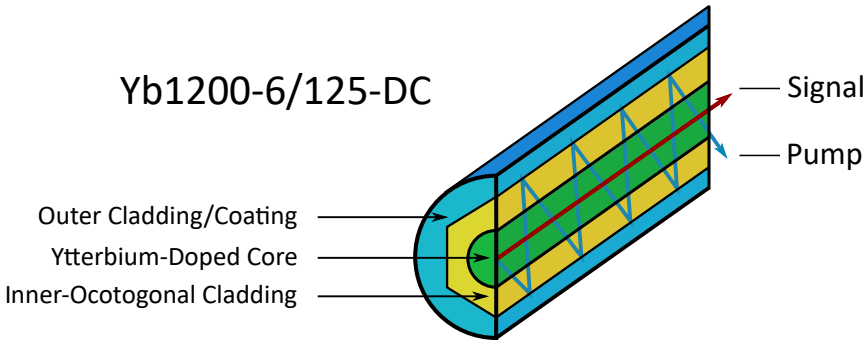

Figure 3.19.: Cross section of a Yb1200-6/125DC fiber with Yb doped fiber core in the center (green), inner octagonal cladding around the core (yellow) and an outer cladding (blue). The signal wavelength is propagating in the core while the inner cladding functions as a waveguide for the pump wavelength.

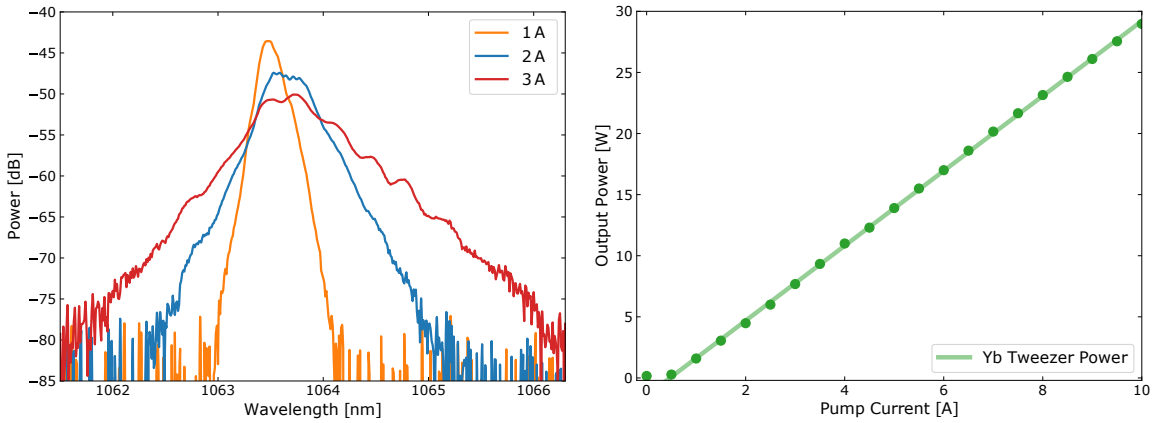

Figure 3.20.: The left shows the spectrum of the seed signal (IPG fiber laser) for the fiber amplifier at different pump currents of the IPG. On the left the output power of the amplifier is plotted for different pump currents of its pump diodes.

double clad fiber (DCF). Such a fiber has a structure consisting of three layers of optical material. The inner-most layer called core is surrounded by the inner cladding, which is surrounded by the outer cladding. The three layers have different refractive indices, which allows to keep the signal wavelength inside the core and the pump wavelength inside the core and the inner cladding. This fiber is connected to 7 m of the Yb doped fiber *Yb1200-6/125-DC* with a splice. The splice is labeled 'magic' splice in the figure because our concept to retain the pump light in the cladding worked surprisingly well. This is not a given as the coating of the fiber itself is removed during the splice preparation. The splice thus needs to be encased by special epoxy (*Norland NOA 1369*) and cured under scotch tape (or nitrogen atmosphere) with UV light. The refractive index of the epoxy has to match outer cladding of the double clad fiber to ensure total reflection of the pump light.

The pump light inside the active DCF, depending on the length of the doped fiber, will be almost completely absorbed. The signal wavelength will be amplified and travel in its

core. All remaining pump light can be removed by a 'power stripper'. This is a splice, which does the complete opposite to the 'magic splice'. It uses an epoxy (*Norland NOA 86H*) with a refractive index similar to the fiber cladding and removes its guiding feature in order to allow the residual pump light to leave the fiber.

The output power of the laser is monitored by a photodiode, which is glued to a splice and detects stray light. This is a cheap and useful tool at high powers, where fused couplers are costly and likely to fail. Finally the signal wavelength is released as a laser beam by a fiber to free space outcoupler with included isolator. The characteristic spectrum of the multimode seed fiber laser (IPG) is adopted by the fiber amplifier and shown in figure 3.20 together with the output power. It is important to note that a current of $\sim 1\,\mathrm{A}$ is selected for the (IPG) seed fiber laser because of observed broadening effects of the spectrum at higher currents. The 'features' of this spectrum will be thoroughly discussed in upcoming sections that deal with the optical transport of atoms in ODT's.

3.4.5. Ytterbium Tweezer

The Yb tweezer system described in section 3.4.4 provides 30 W of 1064 nm light for the optical dipole trap, which traps and transports Yb atoms to the science chamber. To enable proper differentiation between multiple traps at infrared wavelengths such as 1064 nm the laser beam in this case is colored green in figure 3.21.

In this setup the high power laser beam is first collimated by a 200 mm lens[4]. Afterwards an AOM (*Gooch/Housego 3080-198*) is used to ramp the power of the laser beam. The adjustment of the radio frequency power in the crystal of the AOM is done by varying the experiment control voltage connected to its driver. A power stabilisation loop is implemented with a logarithmic photodiode detecting a small amount of transmitted light behind a mirror. The AOM is also used for fast switching of the optical trap and is especially designed for high optical power densities. With previous AOMs, changing beam shapes and astigmatism in the focus of the ODT beam was a recurring issue. Since the transport of Yb atoms in ODTs is found to be highly sensitive to the quality of the focus, any changes of the wavefront due to e.g. thermal effects in the AOM are detrimental for the experiment. Although the issue may not be fully resolved the trap did not need adjustment for months after swapping to the new AOM. Another neat purpose of the AOM is the ability to shape the laser beam along the horizontal axis by mixing a modulation signal to the +80 MHz frequency. The trap shape can be modified because the angle of deflection of the first order diffraction is changed by a frequency $\pm\Delta f$. This modulation frequency is fast compared to the trap frequency, which leads to an enlarged time-averaged horizontal trap size at the focus[5]. This means that Yb atoms do not see a fast sweeping laser beam but an time-averaged potential. In figure 3.21 the trap shaping function is shown. The time spent at a frequency different from the center frequency is displayed on the right. The used waveform function is designed to create a harmonic trapping potential

[4]The optics of the output of the fiber amplifier were manually removed because the beam diameter was too large.

[5]This only works if the AOM is not positioned in a focus itself.

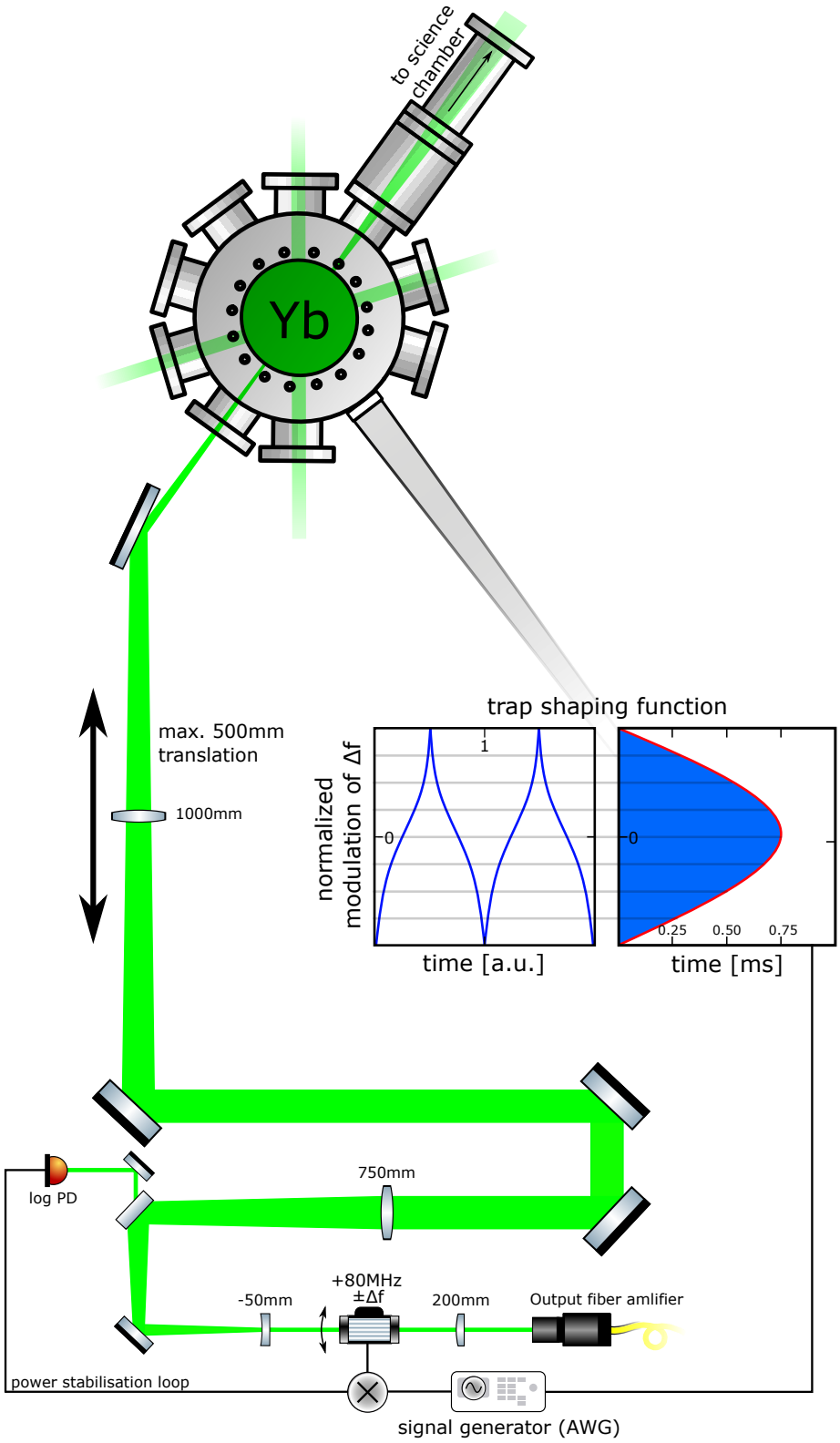

Figure 3.21.: Illustration of the Yb tweezer system, which prepares the ODT beam for optical transport. The power stabilisation loop with a logarithmic photodiode and the AOM is shown. The trap shaping function, displayed in the inset graph, increases the horizontal trap size at the focus by creating a time-averaged harmonic potential.

by remaining close to the center wavelength for a longer time [201]. We use an arbitrary waveform generator (AWG) to create this waveform with adjustable modulation frequency and peak to peak voltage (the amplitude can also be changed by the experiment control).

The following optical elements are very similar to the Rb tweezer setup (see chapter 3.3.5). A telescope (−50 mm and 750 mm lens) is used to increase the beam diameter. A set of mirrors align the laser beam along another *Aerotech ABL1500* air-bearing translation stage, which can move the final lens (1000 mm) and its focal spot over a distance of 500 mm. Finally the transport of Yb atoms into the science chamber can be carried out.

3.5. Lattice laser system

This chapter presents the lattice laser system shown in figure 3.22, which provides light for three perpendicular and retro-reflected optical lattice beams. The system uses a *Innolight Mephisto* Nd:Yag non-planar ring oscillator (NPRO) as seed light for a self-build fiber amplifier. The narrow linewidth (spectral linewidth $< 3\,\mathrm{kHz}$), low noise ($< -140\,\mathrm{dB/Hz}$) and frequency stability ($\sim 1\,\mathrm{MHz/min}$) of this laser is well suited for optical lattices. However it is more challenging to amplify a narrow kHz-wide signal than a multimode GHz-wide signal due to stimulated brillouin scattering (SBS) [202]. This nonlinear effect is frequently encountered in narrow-band fiber amplifiers and has to be monitored closely if long active fibers and high pump powers are used.

Before the seed light is fiber coupled to the amplifier, it has to pass an optical isolator to avoid back reflections and a waveplate to control its polarisation. Again, the infrared light at 1064 nm is visualised in figure 3.22 with a different color - this time yellow. The following fiber amplifier was built in the scope of [203]. First, an additional fiber isolator protects the seed laser from parasitic lasing. Fused couplers (99:1 and 90:10) are used to monitor SBS, back reflection, seed power and output power[1] of the amplifier. About $\sim 100\,\mathrm{mW}$ of power is used as the seed signal, which is combined with the pump light in a pump-signal-combiner. For the pump light, two different diodes are used - the first is a 15 W diode with volume bragg grating (VBG) - the second is a 9 W diode without it[2]. The VBG stabilises the pump diode to 975 nm. The spectrum of an unstabilised pumpdiode shifts with temperature, hence this pumpdiode is mounted on a temperature controlled Peltier element.

The splice from pump-signal combiner to 7 m active fiber is a commercial splice that was removed from an otherwise broken fiber amplifier. The residual pump light, which was not absorbed by traveling through the active fiber, is dumped in a power stripper. Due to a mismatch in fiber core diameters in this system, the splice functioning as a mode field adapter (MFA) at this point is sub-optimal[3]. The watercooled splice links a 6 µm core size to a 10 µm core required for the fiber isolator output and is thus a 'home-built MFA'. Finally more isolation is needed in form of a water-cooled[4] fiber isolator (*DK Photonics* max. 20 W) and fiber to free space isolator (*DK Photonics* Outcoupler). This is crucial because the light of the optical lattice beams will eventually be retro-reflected back towards the fiber amplifier.

The output power of the described system is about 6 W. It is limited by the SBS signal, which is plotted in the right panel in figure 3.23.

The third part of the lattice laser system is the distribution unit which splits the output of the fiber amplifier into three beams of equal power. Wave-plates and PBS cubes divide the

[1] On this photodiode the AC signal is monitored to shutdown pumpdiodes in case of pulsing.

[2] The reason for this is purely historic, see [203]. In principle pump diodes with VBG are favourable because no temperature control is needed.

[3] MFA splices are hard to perform with unspecialised equipment since the diameter of the glass has to gradually change without defects. I advise to buy MFA parts if needed because the splices are hard to get right with standard splicers.

[4] Thermal effects impacted the transmission of the isolator.

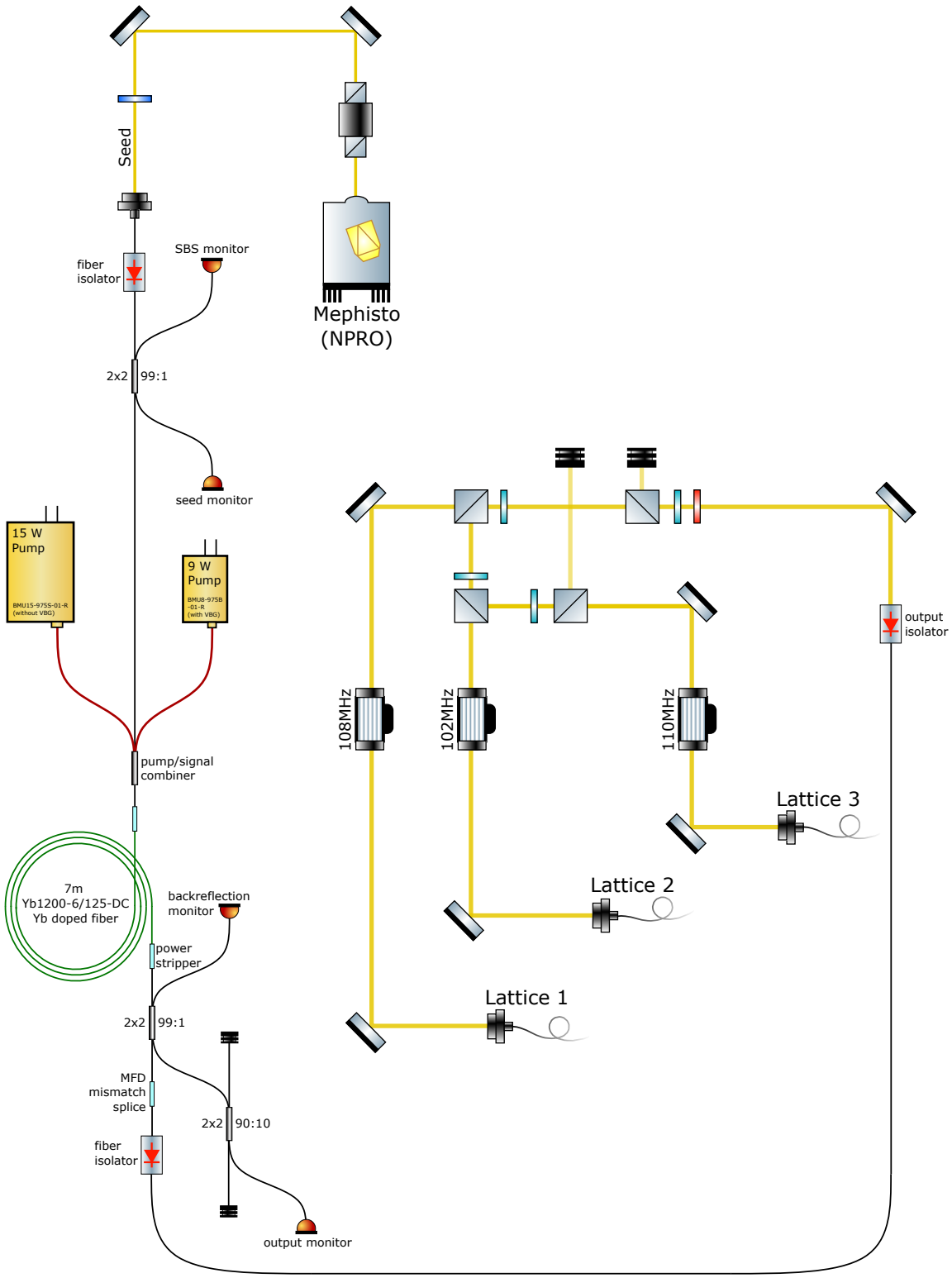

Figure 3.22.: The Lattice laser system includes a *Innolight Mephisto* Nd:Yag as the seed laser for a self-built narrow linewidth fiber amplifier and a free space beam distribution unit for the three optical lattice beams.

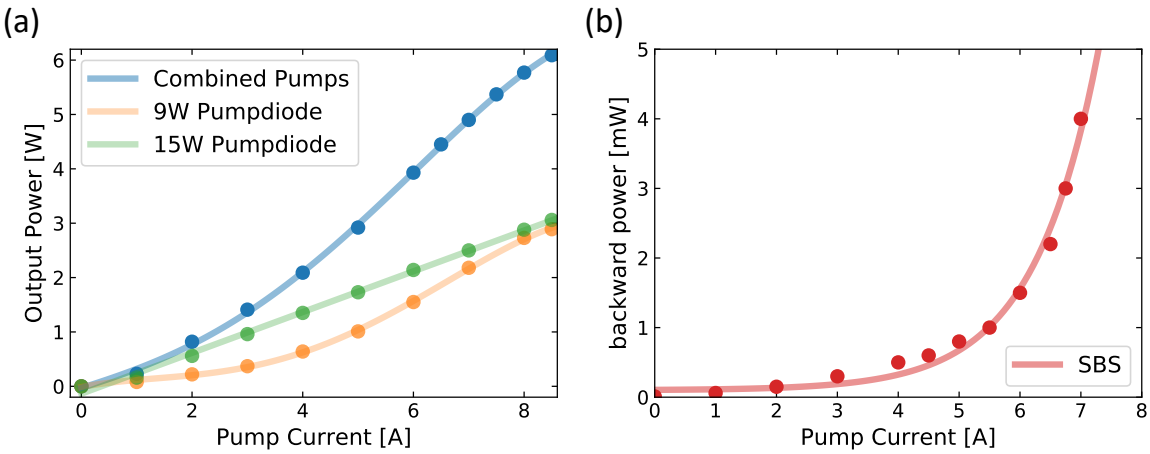

Figure 3.23.: In segment (a) the output power of the lattice fiber amplifier is plotted for different pump currents of each individual (15 W green and 9 W yellow) or both combined pump diodes (blue). In (b) the exponentially growing backward power signal caused by SBS in the amplifier is shown for increasing pump currents.

laser beam and clean its polarisation. AOMs of different frequencies (102 MHz, 108 MHz and 110 MHz) are used for each lattice path. They shift the ligth in the three arms of the lattice to different frequencies to impede beating of the lattice beams close to trap frequencies. Additionally they are also used to individually ramp the power levels and quickly switch beams on and off. Finally, the first order diffraction is fiber coupled into three fibers that are labeled Lattice 1, Lattice 2 and Lattice 3. They lead to the science chamber, which is presented in 3.9.

In order to stabilise all three lattice powers, photodiodes and power stabilisation loops are implemented. This is necessary because the polarisation of the fiber amplifier was found to slowly rotate over time (minutes) and change the power distribution.

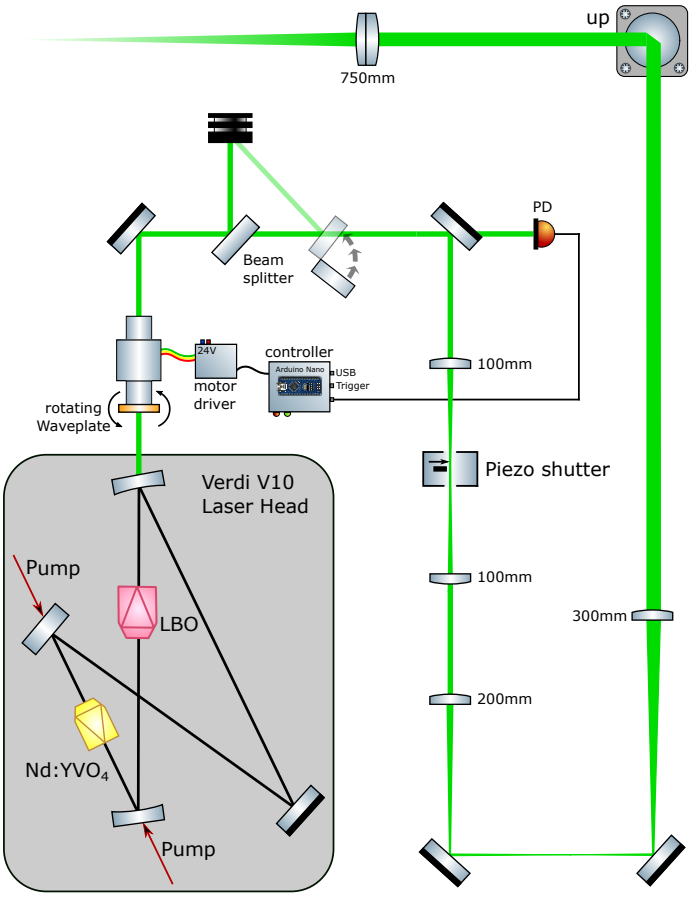

Figure 3.24.: The laser system at 532 nm uses the commercial, high power *Verdi V10 Coherent* laser. Power control is realised with a $\lambda/2$ wave plate, which is rotated by a Arduino controlled stepper motor and a polarising wave plate. The switch-off of the beam is carried out by a combination of a fast piezo shutter and a slow mechanical flip mount.

3.6. The 532 nm laser system

The laser system at 532 nm adds an extra laser beam to the final optical trap of this experiment. Its focus is superimposed on a crossed optical dipole trap (1064 nm) and can be used to tune the large potential depth difference between Rb and Yb atoms [204]. Since a wavelength of 532 nm is repulsive for Rb and attractive for Yb it can create a bichromatic trap that balances the potential difference for both species and increase the overlap density for photo-association experiments. In chapter 7.2 the application of this trap, including a visualisation of the trap depth, is discussed in more detail.

Light with this frequency is commonly produced by frequency doubling of a 1064 nm source. In our system a commercial, high power *Verdi V10 Coherent* laser is placed below the science chamber on the lower level of the science table. In figure 3.24 the laser head of this system is shown. A neodymium-doped yttrium orthovanadate (Nd:YVO_4) crystal absorbs pump light and emits 1064 nm photons into a bow-tie cavity. The frequency doubling in this cavity is realised with a lithiumtriborate (LBO) crystal ($\sim$ 148 °C). An

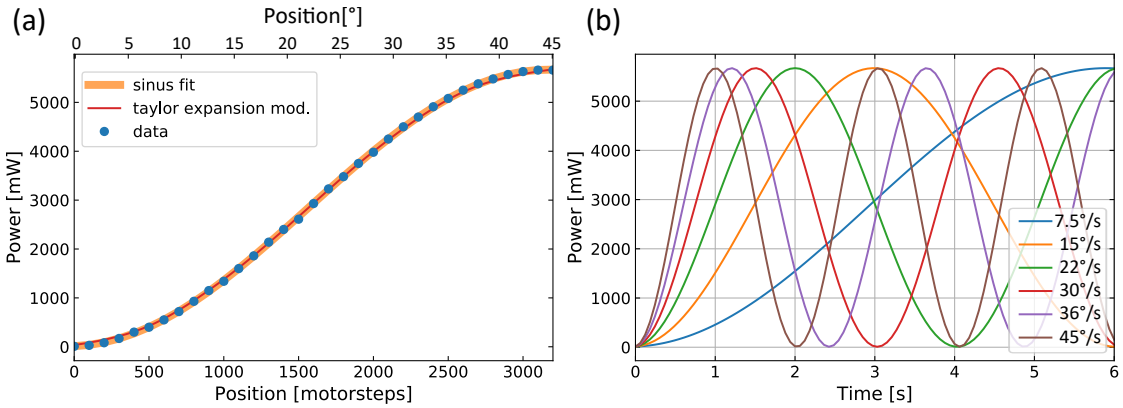

Figure 3.25.: (a) shows the rotation of the waveplate for power ramping of the 532 nm laser. The transmission of light through a PBS plate is measured for different motor-steps or rotationangles up to $45\,^{circ}$. A sinusoidal fit was approximated with a Taylor expansion for the implementation into the experiment control. (b) shows six different motor velocities that are available for the rotation of the waveplate with a simulation of the different modes that can be currently used for power ramps in the experiment. This limits possible ramp times or power functions due to the constant waveplate speed.

output mirror transmits up to 10 W of 532 nm light out of the laser head. The power of this laser beam depends on carefully adjusted parameters (mostly temperatures) of the pump diodes, etalon, Nd:YVO_4 and LBO crystal.

We have found that AOM crystals or PBS cubes are susceptible to thermal effects from high powers at a wavelength of 532 nm and distort the beam profile in the focus. Therefore the power of the laser beam is changed with a waveplate and a polarising plate beamsplitter (*Thorlabs* PBSW-532) instead. The vertical polarisation of the Verdi is rotated by the $\lambda/2$ waveplate to control the power transmitted by the polarising beamsplitter. We use a hollow axle stepper motor to rotate the waveplate. The driver for the motor is controlled via RS232 signals from an *Arduino Nano*, which is connected to the experiment control (USB). The waveplate position can be calibrated with a photo diode that detects light behind a mirror. A calibration script, that can be triggered via experiment control, automatically searches for the smallest photodiode signal by rotating the waveplate back and forth. This zero-position is saved and used as a reference for all power ramps. In the left panel of figure 3.25 the power of the laser beam is plotted for positions of the stepper motor and translated rotation in angles. For this graph a power of about 7 W (on the Verdi Display with 28.0 A) was chosen[1]. Since the Cicero program of the experiment control can not work with sinusoidal functions a sinus fit could not be used in the power calibration. Thus a taylor expansion is used to convert motor positions into powers.

The driver of the stepper motor has only six different velocity modes as presented in segment (b) in figure 3.25. These motor speeds can be set via RS232 commands before the rotation is executed. At the moment this limits the possible evaporation ramps that

[1]It should be noted that the real power output of the laser is always overestimated in the displayed value.

can be realised with these commands because there are only six possible ramp times to a specific set power. The corresponding curves are calculated and displayed on the right in figure 3.25. A power stabilisation loop with a photodiode enabling linear power ramps can and should be implemented in the code of the waveplate controller in the near future.

Once the desired power is achieved the beam can be prepared and focused into the science chamber. First a telescope is used to create a focus at the position of a piezo shutter (see figure 3.24). It was optimised to extinguish the light as fast as possible and reached a time of $24 \pm 2\,\mu s$ for a beam size of $90\,\mu m$. A rapid switch off for time of flight measurements is required in the absence of an AOM that usually fulfills this task. Due to the high power density in the focus a mirror piece is glued on the cantilever piezo to reflect the beam into a beam dump. Since even this mirror can not withstand a long exposure to the beam an additional shutter in front is implemented. This shutter is a mirror that is moved into the beam by a mechanical flip mount (*Thorlabs* MFF101), which is much slower due to the reaction and travel time of the motor. The slow shutter needs to be pre-triggered and closes approximately 0.5 s after the piezo shutter to avoid any damage on the first mirror. After the shutter the beam diameter is increased by a 200 mm/300 mm telescope and elevated to the upper level of the science table. Finally the laser is focused to a beam size of $\sim 100\,\mu m$ by a 750 mm achromatic lens to intersect in the focus of a crossed ODT.

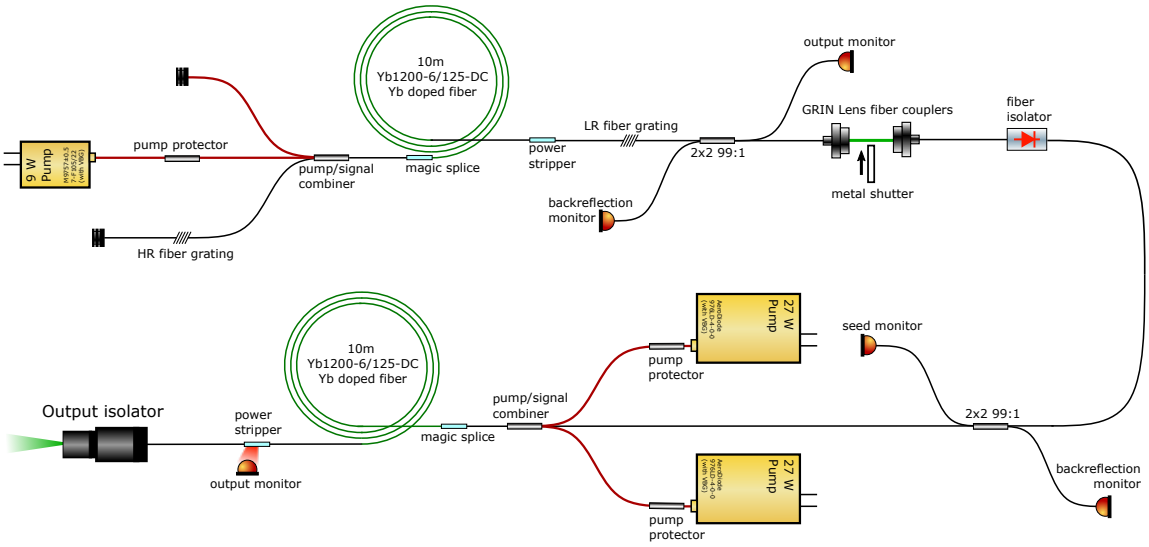

Figure 3.26.: Sketch of the self-built fiber laser and fiber amplifier system with 30 W output power. The fiber laser is realised with fiber bragg gratings and provides the amplifier with seed light. A mechanical shutter between a pair of GRIN lenses can separate laser and amplifier whenever the laser is pulsing. The amplifier is similar to the previous one shown in figure 3.18.

3.7. A new fiber laser for optical traps

Fiber lasers like fiber amplifiers (see section 3.4.4) use doped fibers as the gain medium. Commonly a pair of fiber bragg gratings (FBG) is spliced to either side of it or are directly included in the doped fiber to create a resonator [205]. Other forms of fiber lasers can be realised as a ring laser via fused couplers, fiber loops and optical circulators [206]. However the linear setup is the most commonly used version. These lasers can serve in a wide range of applications as pulsed or cw lasers. Numerous different wavelengths and powers are available from plenty of commercial suppliers.

To be able to replace failing fiber laser systems in our laboratory and stay within an affordable price range, the skill to splice commercial fiber components had to be learned. In all self-build fiber amplifier projects (see sections 3.4.4 and 3.5) this was already achieved. For a fiber laser however a clear distinction is the absence of a seed signal and the possibility to have short lasing pulses instead of continues light emission that we want to achieve. While a lot of researchers want their fiber lasers to create ultra short nanosecond pulses instead of cw-light, pulsing can be a source for high peak powers that destroys fiber components. Many reasons can lead to pulsing of a fiber laser including the cavity being too long, the length of the doped fiber[1] and mode competition or reflections within the cavity [207]. Especially in the turn-on phase a cw-fiber laser is prone to pulse formation because

[1]The end of the active fiber is the weakly pumped region and it can be responsible for signal re-absorption along the fiber length. It thereby can cause random pulsing due to a 'saturable absorption effect' that is also observed in Q-switched lasers [207].

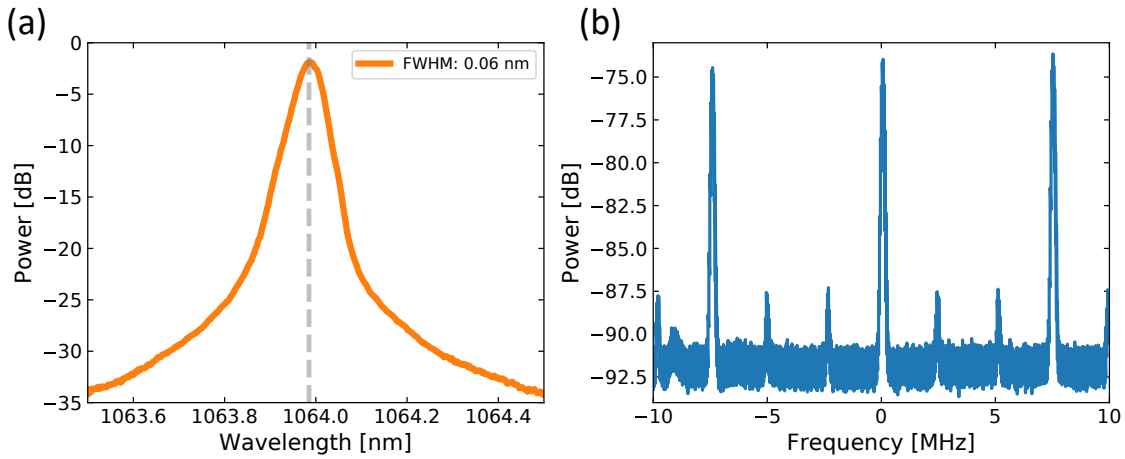

Figure 3.27.: Recorded spectra of the fiber laser in continuous wave mode at $\sim 1\,\mathrm{W}$. (a) shows the optical spectrum with a center wavelength of 1064 nm recorded with an optical spectrum analyser. (b) presents the rf-spectrum recorded with a fast photo diode revealing a mode spacing of 7.5 MHz.

the laser is in a transient state and is still stabilizing. In the following a new fiber laser combined with a fiber amplifier is presented (see figure 3.26). A system like this can be used in all optical trapping experiments and can be scaled in power with the appropriate fiber components.

The fiber laser uses a pump-signal combiner to feed pump light into the gain medium (see top of figure 3.26). A 9 W pump diode (*PhotonTec Berlin (VBG)*) at 975 nm is used. For the gain fiber 10 m of *Yb1200-6/125-DC* Yb doped fiber is choosen. In the 'magic' splice (see section 3.4.4) the 6/130 µm output fiber of the combiner is spliced to the 6/125 µm gain fiber with octagonal cladding. Afterwards the splice is re-coated with special epoxy (*Norland NOA 1369*) and needs to be cured under scotch tape with UV light because oxygen inhibits the curing process of the epoxy. The refractive index of the epoxy has to match the refractive index of the outer cladding of the double clad fiber to ensure total reflection of the pump light. The pump light is absorbed by the 'active' fiber up to a small percentage, which gets blocked in the 'power stripper'. This power stripper uses an epoxy (*Norland NOA 86H*) with a refractive index similar to the one of the inner fiber cladding in order to be transparent for the pump light and thus removes its guiding feature. Now the excited Yb ions in the gain fiber can emit photons with different frequencies/wavelengths within the large gain bandwidth. Due to strongly broadened laser transitions in glasses a wide wavelength tuning range can be achieved with e.g. fiber bragg gratings (FBG). In our fiber laser a wavelength of 1064 nm is realised with a pair of gratings with center wavelengths at $1064 \pm 0.5\,\mathrm{nm}$[2]. In figure 3.27 (a) the spectrum with a FWHM of 0.06 nm is recorded with an optical spectrum analyser. The first bragg grating (OC) (Bandwidth: $0.1 \pm 0.05\,\mathrm{nm}$, HI1060 fiber) is placed behind the 'power stripper' and reflects $20 \pm 3\%$ of the light back through the active fiber to the pump-signal combiner. Here the input signal

[2]Both gratings are matched much closer than $\pm 0.5\,\mathrm{nm}$ in their center wavelength as a pair.

fiber is used as a 'mirror' by splicing the second bragg grating (Bandwidth: 0.4 ± 0.1 nm, HI1060 fiber) to this fiber end. This grating has a very high reflectivity of $> 99\%$ within its bandwidth at 1064 nm and transmits all other wavelengths that are dumped afterwards.

The two fiber gratings create the laser resonator, which forces a linewidth smaller than the bandwidth (0.1 nm) of the low reflection (OC) grating. The output of this grating is divided by a (99:1) fused coupler to monitor the back reflection into the laser and its pulse behaviour via photo diodes. If strong pulsing of the laser is detected an interlock system switches off the pump diode.

The spectrum of the laser is recorded with a fast photodiode in the right plot of figure 3.27. A longitudinal mode spacing of 7.5 MHz can be observed. The main mode spacing suggests a cavity length of $\sim$ 13.8 m, which matches well with the used fiber length in between the FBGs. In between there are small peaks with 2.5 MHz spacing and significantly less power, which might be coming from higher modes.

The link of fiber laser and amplifier is realised with a pair of gradient-index (GRIN) lenses (*Thorlabs 50-1064*). They have a gap of about 1 cm, where a free space beam can be blocked by a metal shutter. The shutter blocks the laser in idle position or when the laser is pulsing at low pump currents. Once the laser is turned on and reaches a continuous wave lasing, the shutter is automatically removed from the beam path with an electromagnet built from a relay. This mainly protects the fiber isolator on the amplifier input from pulse powers during the turn on/off stage of the fiber laser[3].

Due to pulsing, the characterisation of the fiber laser output power is limited and since this was done in a completed system with shutter, powers during the pulse region could not be measured. In figure 3.28, segment (a) shows output powers for very low signal and pump currents above 2 A. For currents higher than 3 A the output power reaches more than 600 mW, which is twice the damage thresh hold for the GRIN lenses and is thus also not recorded. The linear behaviour of the output power is outlined as well as the power of the pump diodes (from datasheets). The pulse and cw region are separated by a gray transition area, where the pulsing amplitude decreases. The 'shutter-line' represents the opening of the shutter under safe conditions.

The second part of the system is a self-build fiber amplifier. Since this amplifier is very similar to the one presented in chapter 3.4.4 only their differences are explained here. One of these differences is the spectrum of the seed laser used in this setup. In this case the laser is more susceptible to self pulsing at low intensities, which can also destroy fiber amplifiers. As a precaution a minimum of 500 mW seed power is selected to be required to turn on the pump diodes (*PhotonTec Berlin* M976 27W VBG) of the amplifier. Furthermore the back reflection of the amplifier is closely monitored. Another difference is the detection of the output power at the end of the power stripper by a photo diode. This avoids the use of a second splice just to monitor leaking light but is tricky to align. The photodiode should not detect much stray light and thus needs to be shielded from the rest of the fibers and is positioned at the end of the re-coated splice.

[3] A simple splice between fiber laser output and fiber isolator resulted in the destruction of the inbound grin lens of a fiber isolator when turning on the laser.

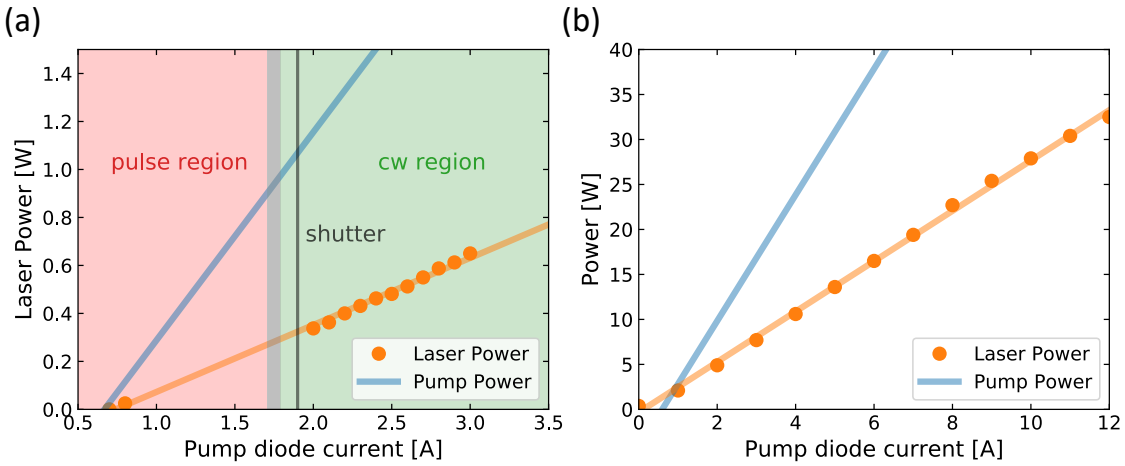

Figure 3.28.: Power diagrams for fiber laser and fiber amplifier, which are both measured at the collimated fiber output of the system. The fiber laser power is simply measured with switched-off amplifier. (a) the fiber laser output is divided into a 'pulse' and 'cw' region. The broad gray line indicates the transition from pulsing to cw, while the narrow line represents the opening/closing of the shutter. (b) shows the output power of the amplifier (complete system). In both graphs the pump power is not directly measured but inferred from the data sheet for the used pump diode currents.

Finally the fiber laser and amplifier system is capable of producing 30 W of 1064 nm light shown in the current-power graph in segment (b) of figure 3.28 and is currently used as the second beam in a crossed ODT for Yb.

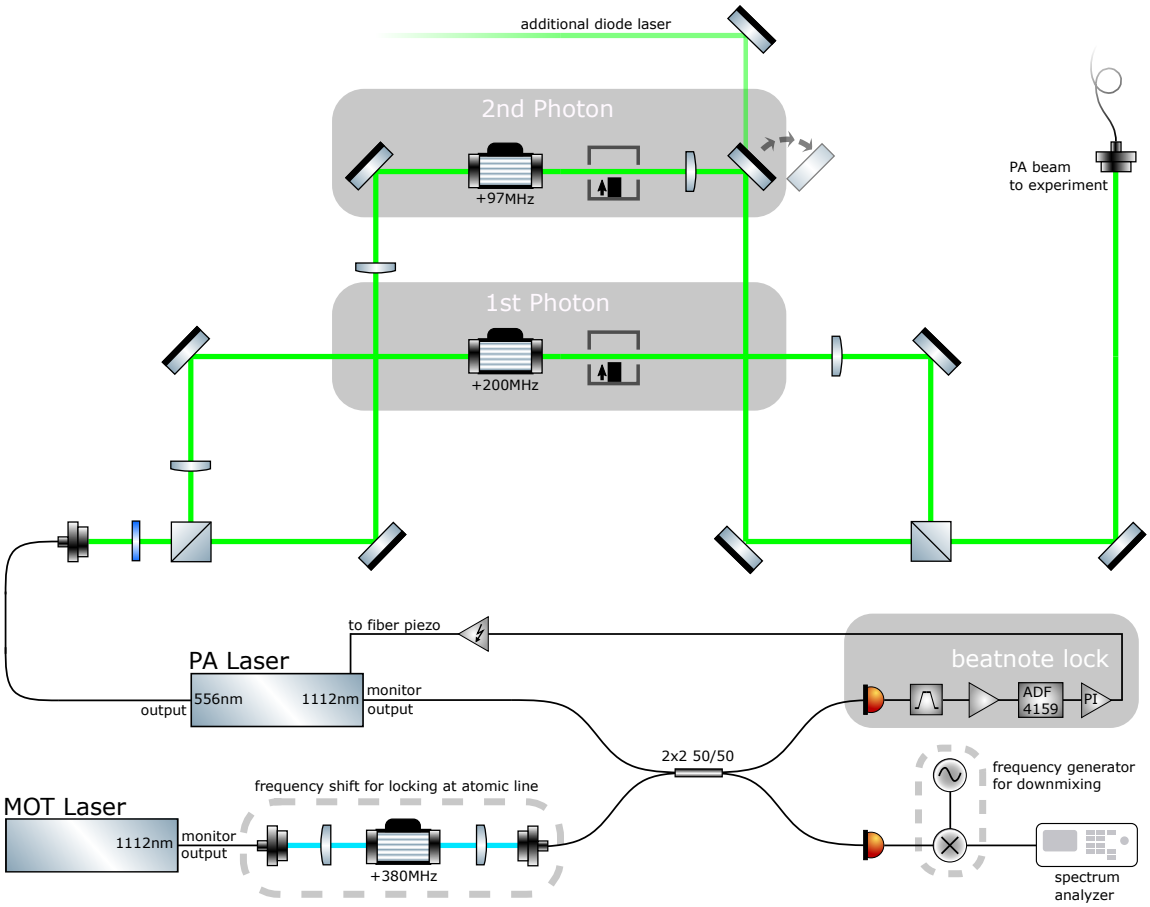

Figure 3.29.: Sketch of the photoassociation laser system adapted from [1]. The system provides the first photon for a free-bound and a possible second photon for a bound-bound molecule transition. The beams are overlapped (possible additional diode laser path included), fiber coupled and delivered to the science table. The frequency stabilisation in the infrared (1112 nm) is realised with a beatnote setup between the commercial *NKT Koheras BASIK* module and the Yb MOT laser.

3.8. Photoassociation laser system

Until now, the described laser systems were used for the preparation and handling of ultracold atoms. The photoassociation (PA) laser system is designed to provide photons, which excite the atoms to weakly bound molecules. For this process - frequency, power and timing are crucial parameters that need to be controlled. The setup described in this section and its beatnote lock system has been assembled in the scope of [208] and was used and refined during [1] and this work.

First the light is generated by a commercial *Menlo*-Laser consisting of a *NKT Koheras BASIK* module, amplified by a pre-AMP and converted via a second harmonic generation (SHG) PPLN device at 555.8 nm [1] [209]. This laser comes with a PM output fiber and

[1] This system once provided about 20 mW but has degraded below 1 mW in power over time and needed

is outcoupled as a free space beam on the laser optical table. Subsequently it is divided into two paths with variable power levels labelled as the 1st photon and the 2nd photon in figure 3.29.

1st Photon

The 1st photon is required to drive the free-bound transition to form highly excited molecules. For this the PA laser needs to be tuned close to the $^2S_{1/2}$ + $^3P_1$ asymptote of the molecular potential discussed in chapter 2.3.2 . PA light is only needed at the end of the experimental cycle for short times. For this reason an AOM and a piezo shutter is used for fast and complete switch on/off of the 1st photon. The light can then coupled into a fiber that leads to the science table.

The most crucial element for PA light (1st and 2nd photon) is the frequency stabilisation and detuning with respect to the atomic transition of Yb. A beatnote lock between the MOT and the PA laser is an ideal tool for this because the MOT laser is already stabilised to the $^1S_0 \rightarrow ^3P_1$ transition. Furthermore they are close enough in frequency (search range for PA lines is about 10 GHz). For this both infrared monitor outputs are combined in a fused fiber coupler (50:50). One of its fibers is connected to a photodiode and a spectrum analyzer that can be used to observe the quality and frequency of the beatnote signal. For frequencies larger than 3 GHz a frequency generator is used for down-mixing because of the limited bandwidth of the rf-analyzer. The other fiber output is simply plugged to a 'small formfactor pluggable' (1300 nm SFP+) module (*Finisar FTLF1429P3BCE*). As explained in detail in [1], this module features a high bandwidth (> 12 GHz) InGaAs detector and limiting amplifier. In contrast to the beatnote modules used in the Rb laser system, this solution can work with even smaller signal strengths and is less prone to fluctuations due to polarisation changes. The module generates a beat signal that is already amplified to −6 dBm. It is mounted on a custom board containing filters, Arduino controller and SMA connectors. One of them is connected to an rf-amplifier (*Mini Circuits ZX60-123LN-S+*, for 0.5−12 GHz) and filters[2]. Due to signal noise on the pump laser of the MOT laser we see multiple peaks with a 10 MHz spacing on the beatnote signal, which disturb our frequency lock. In an effort to surpress these side-peaks and improve the lock, different bandpass filters have to be used for selected scan ranges. A synthesizer chip on a ADF4159 board generates a reference frequency and error signal proportional to a computed frequency error. The error signal is then transferred to the fiber piezo of the PA laser as a voltage and the frequency of the laser is adjusted when the stretcher piezo elongates the fiber length.

With the described locking scheme the 1-photon photoassociation experiments can be carried out from 0.5 to ∼ 14 Ghz detuning with respect to the dissociation threshold with minor interruptions due to filter exchanges. For a scan below 500 MHz we are limited by the

to be checked for defective parts. After various repairs including new temperature controllers of the active fiber in the 'Amp' and 'SHG' module and a replacement of the pump diode in the seed module we have achieved 9.5 mW output power.

[2]Filters have to be changed depending on beatnote frequency

minimum frequency of the synthesizer chip. Therefore carefully choosen AOM detunings have been used to realise measurements very close to the atomic line.

2nd Photon

The 2nd PA photon is required to drive the bound-bound transition and bring molecules into a vibrational level of the ground state potential. For this the detuning of both PA photons must equal the binding energy plus the thermal energy of the scattering state. Therefore the 2nd photon always needs to be blue detuned to the 1st photon. In figure 3.29 this detuning is realised with AOMs. The compelling advantage of using only AOMs for the main (1st) photon and auxiliary (2nd) photon is the good coherence and small relative linewidth. However if the binding energy of the selected state is larger than a couple hundred MHz (only the most weakly bound state of ^{87}Rb^{170}Yb $\Delta\nu' = -1$ with $E_b = h \cdot 103\,\mathrm{MHz}$ is withing range[15]), AOMs alone can not span this frequency difference. In this case an EOM or a different light source has to be used.

In an effort to reach the next bound level ($\Delta\nu' = -2$ with $E_b = h \cdot 1.02\,\mathrm{GHz}$ [15]) a home built phase modulator (EOM) with a z-cut lithium niobate crystal was installed. The work of T. Franzen [1] gives a detailed description of how he optimised the conditions for sideband generation in a so called 'split ring resonator' [210]. In short, a hollow cylinder around the crystal acts as a resonator for the input signal. It can be frequency tuned by sticking 'small bits' of magnetic or dielectric material into the cylinder. In the final setup $\sim 20\,\%$ of the carrier signal was converted into the first sideband with a drive power of $\sim 1\,\mathrm{W}$ and a tunability of about 60 MHz at 1.02 GHz. It is worth noting that the third sideband at $3 \cdot 1.02\,\mathrm{GHz}$ is very close to the atomic line (see chapter 5) and can have severe impact even at low powers.

The third level at 3.67 GHz could not be accessed with this method since the used one-photon transition at 3.05 GHz interferes with the atomic transition and we would need to drive 3rd order sidebands on the EOM. Hence experiments with a separate diode laser system need to be carried out to detect all other bound levels. Up until now the diode laser system, set up in the scope of a bachelor thesis [211], served as an independent narrow linewidth source at 1112 nm for the 2nd photon but could not detect additional transitions as already discussed in [1].

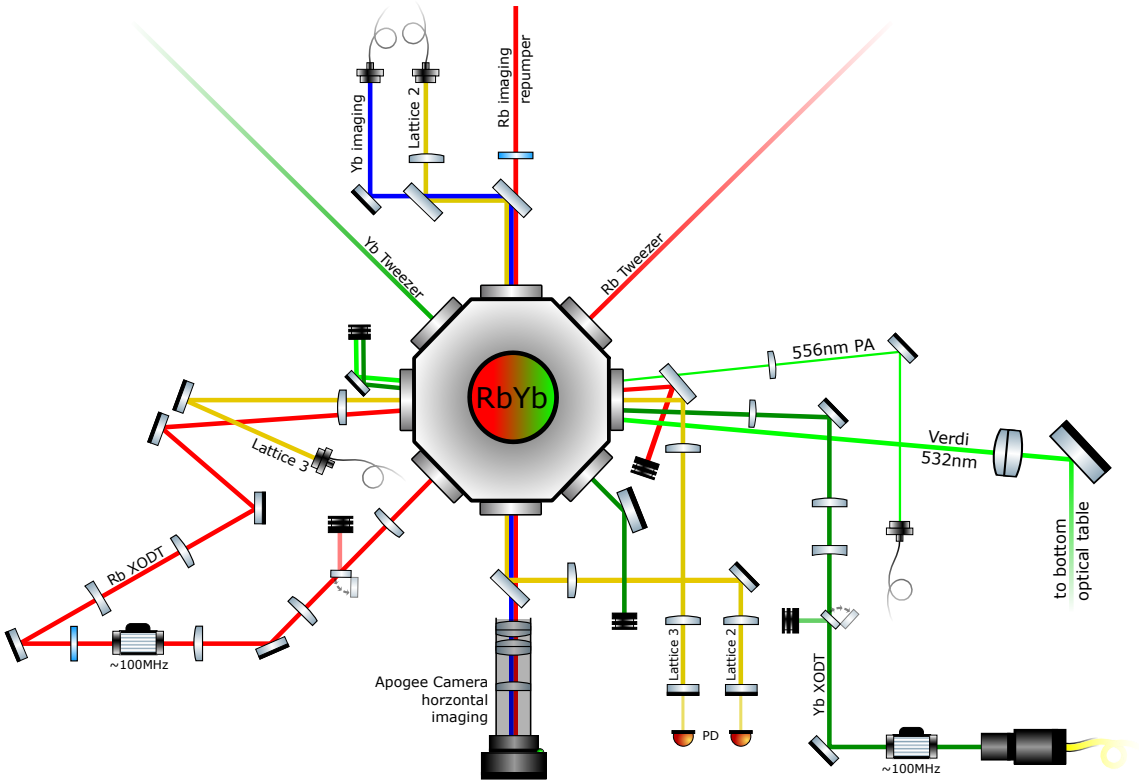

Figure 3.30.: Outline of the bird-eye view of the setup around the science chamber. Laser beams and optical components form optical traps and perform photoassociation experiments in the center of the vacuum chamber. A horizontal imaging system (Apogee) is capable of imaging both Rb and Yb atoms. Note that the colours do not always represent the correct wavelength of trapping light but match with all previous laser system sketches.

3.9. Science chamber

In the 'science chamber' numerous laser beams intersect in the center of the vacuum chamber. The current configuration of optical traps, lattice beams, PA beam and imaging systems is sketched in figure 3.30. This image gives a rough view of the experiment in a birds-eye perspective and leaves out the vacuum parts of both production chambers. In the following sections all components that form crossed optical dipole traps, vertical (see figure 3.31) and horizontal absorption imaging systems and the three dimensional lattice are presented. Furthermore the 532 nm (Verdi) beam for trap balancing and the PA beam needed for photoassociation experiments will also be discussed.

3.9.1. Crossed optical dipole traps

The crossed optical dipole traps (XODT) for each atomic species are constructed with two intersecting laser beams. Since both species arrive in optical tweezers as already mentioned in sections 3.3.5 and 3.4.5, one of those laser beams is already available. Due to the large difference in trap depths for Rb and Yb, the foci of the tweezer beams are adjusted to

different heights in the center of the vacuum chamber. Attempts to evaporate a crossed optical dipole trap composed of both tweezer beams (at the same height) have shown a complete loss of Yb atoms due to collisions with hot Rb atoms and were thus quickly discarded.

Rubidium XODT

The crossed ODT for Rb is formed by folding the tweezer beam to intersect with itself. The resulting optical trap is positioned below the Yb trap center. During the transport of atoms, the folded beam is blocked to avoid any crossing[1]. In addition to that, an unblocked beam would not be collimated by the first lens (300 mm) behind the chamber and thus exceed the aperture of the following AOM. Hence a motorized flip-mirror is used to reflect the beam into a beam dump. Due to a lack of space on the upper level on the science table, a razor-blade based beam-block with water cooling is used. Once the transport is completed the mirror is moved away from the beam, which is then guided through an AOM (3110-125 Crystal Technology) operating at around 100 MHz. The AOM is utilized to control the power of the crossing beam, shift the frequency of the light to prevent interference and shift the horizontal position of the trap center. Shifting the trap center is realised by tuning the AOM frequency to change the deflection angle of the first order and hereby shifting the intersection point of both beams. Due to the small active aperture of the AOM, a telescope is used to reduce the beam diameter in front of the AOM and increase the beam diameter behind it. Another crucial optical element in the setup is the $\lambda/2$ waveplate, which rotates the polarisation of the crossing beam by 90°. The polarisation of the XODT beams need to be orthogonal to each other to avoid interference effects. The reason for this is the multimode spectrum and mode spacing, which is induced by the IPG seed laser and is featured in both the incoming and the crossing beam[2].

Finally the folded beam is focused to a beam waist of $\sim$ 100 µm at the intersection with the tweezer beam with a 200 mm lens and is eventually absorbed by another beam block. The remaining power is about 40 % of the tweezer beam (which has a beam waist of 50 µm) and creates a dimple trap potential, which confines atoms and raises the density of Rb atoms.

Ytterbium XODT

The crossed ODT for Yb is formed with its respective optical tweezer and the fiber laser presented in chapter 3.7. An additional laser avoids multiple restrictions of the folding method presented in the case for Rb. First of all it increases the available power in the crossing beam and enables independent power ramps for both beams. Secondly it features

[1] Interference effects can induce ripples in the crossed ODT potential because both beams have the same mode spacing.

[2] While the frequency shift of the crossing beam is specifically chosen to be in between the 4 MHz mode spacing of the IPG seed laser, orthogonal polarisation further reduced the problematic interference effects and improved the lifetime of a Rb BEC in the trap and made shifting the trap center via the AOM frequency possible.

a different mode spacing and is thus much less likely to induce interference. Since both light sources are not polarisation maintaining the utilization of a $\lambda/2$ waveplate would be futile.

The setup for the crossing beam is similar to the Rb version in the previous section. It includes an AOM (3110-191 Crystal Technology) operating around 100 MHz for power control, switch off and horizontal shifting of the beam. The beam block is identical to the one for the Rb crossed ODT but is used slightly differently. Given that no interference issues have been observed the crossing beam can be left unblocked during the Yb transport but is usually blocked whenever the trap is not needed to avoid any off resonant scattering. The rest of the setup includes a (−50 mm/100 mm) telescope which increases the beam diameter three-fold. Finally the crossing beam is focused to a beam waist of 100 µm with a 250 mm lens and eventually absorbed by another beam block. Together with the tweezer beam with a beam waist of 40 µm a dimple trap [212] for the evaporation of Yb atoms is assembled.

3.9.2. Optical Lattice

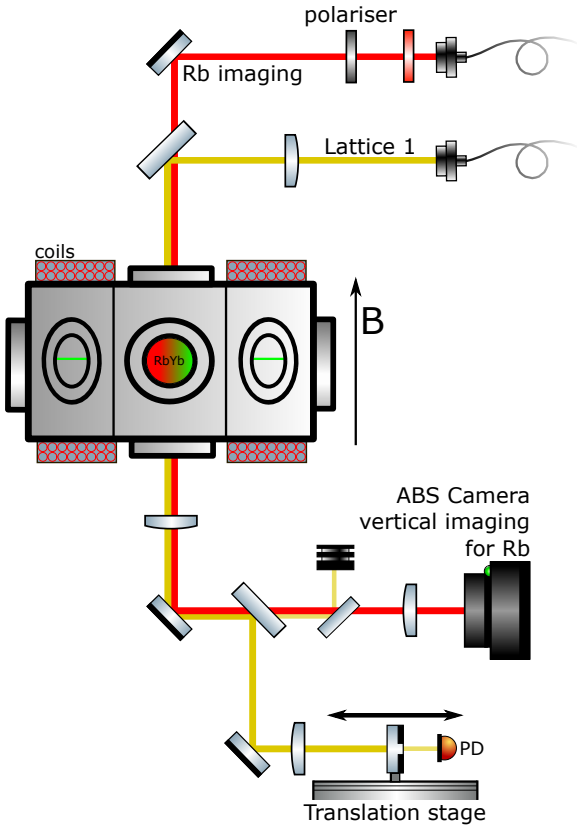

Figure 3.31.: Outline of the side-view of the science chamber and optical components for the vertical optical lattice. The vertical port is used for Rb imaging and an optical lattice (Lattice 1 also known as lattice elevator). A pair of coils on top and underneath the chamber generate a magnetic offset field.

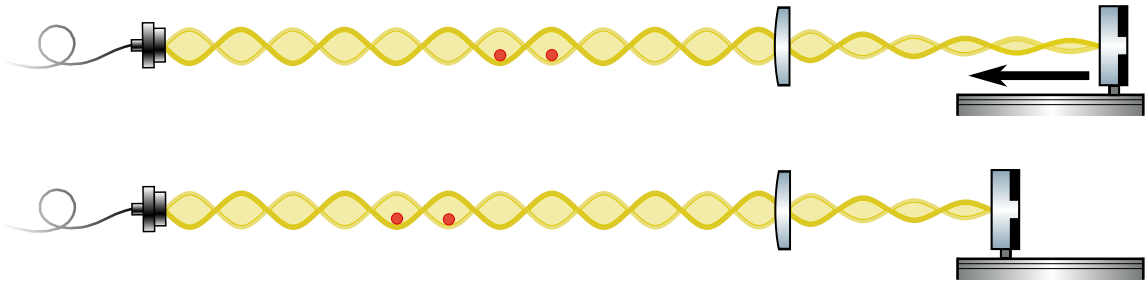

Figure 3.32.: Lattice elevator (Lattice 1). Atoms (red) trapped inside the antinodes of the standing wave are transported if the mirror is moved by the translation stage. Note that this picture excluded focusing lenses for the lattice and is not to scale.

The optical lattice system was initially developed in [186][203]. It is intended as the final optical trap for molecule experiments. It is displayed in three yellow retro-reflected laserbeams in figure 3.30 for the horizontal plane and figure 3.31 for the vertical axis. All beams intersect in the trap center of the Yb crossed ODT to form a three dimensional optical lattice.

Light for the three beams originates from the lattice laser system described in chapter 3.5 and the beams are numbered with 1,2 and 3 at the fiber collimators. Polarisation maintaining fibers (*PM980-XP Thorlabs*) bring the light to the science table to allow for orthogonal polarisations of the three beams and thus minimize interference effects between lattice beams. For the collimators we use a home-built version that consists of an aspheric lens (*C220-TMD-C Thorlabs*) mounted inside a lens tube. The collimated beams have a calculated beam diameter of 3.5 mm.

Lattice 1

The vertical lattice, also referred to as lattice 1, is coupled out above the vacuum chamber. Figure 3.31 illustrates how the beam is aligned through the vacuum chamber. The optical components are mounted on top or underneath the chamber on small breadboards or the optical table. A 200 mm lens is used to focus the beam in the center of the chamber. Underneath it another 200 mm lens re-collimates it and sends it towards the retro-reflector. Since the lattice path overlaps with the vertical imaging beam for Rb, a set of two mirrors is used to fully deflect all infrared light from the CCD *ABS UK-1117* camera. In the lattice path a 100 mm lens and is used to focus the beam on the surface of the retro-reflective mirror (cat-eye configuration).

Such a cat-eye configuration is used for all lattice beams to reduce sensitivity to misalignment of these mirrors. The light is sent back and forms an optical standing wave. Photodiodes behind the optical fiber in the lattice laser system (see figure 3.22) are utilized to monitor the alignment of the backreflection.

Furthermore the vertical optical lattice potential is used to transport Rb atoms upwards to the plane of the Yb crossed ODT and finally capture them in a combined optical trap. In figure 3.32 this process is sketched in two steps. We use a motorised linear translation stage

(*Thorlabs DDSM100*) to move the mounted retro-reflecting mirror. The travel range of 100 mm is primarily used for alignment since the transport distance is only about 1 mm. For a better understanding, only the fiber coupler and the 100 mm focusing lens are included in the picture. If the mirror is translated towards the science chamber, the antinodes of the standing wave move along. A Rb atom cloud, which is trapped in the antinodes of a one dimensional optical lattice follows this motion. For movement without extreme acceleration this process induces no heating or trap loss due to high trap frequencies in the optical lattice. It is important to note that the displacement of the mirror without moving the focusing lens causes a misalignment of the reflected focus position. However for small translations we see no negative influence of this effect as the power coupled back into the lattice fiber does not significantly change with the position of the translation stage.

Lattice 2

Lattice 2 is aligned along the horizontal imaging axis and thus overlaps with the Rb and Yb imaging beam. In order to merge them properly, the first mirror combines lattice and Yb imaging beam (HR 1064 nm/HT 400 nm) while the second one (HR 1064 nm/HT 780 nm) combines all three beams[3]. A lack of space due to the placement of the imaging optics forces us to use a 300 mm focusing lens for this lattice beam. On the camera side of the chamber it is split off by a high reflectivity mirror for infrared light (HR 1064 nm/HT $400 - 700$ nm), send though a 200 mm re-collimation lens and is finally back-reflected.

Lattice 3

Lattice 3 shares the window port with the crossing beam of the Rb ODT. Due to the limited space around the vacuum chamber especially along this axis it uses the same focusing lens of 200 mm. Due to the close proximity of ≈ 2 mm of both beams passing through the lens, potential astigmatism is kept to a minimum. After leaving the vacuum chamber, the beam is collimated by a 250 mm lens and focused by a 100 mm lens onto the 'cat-eye' mirror.

The lattice beams are focused to calculated beam waists of 77 µm for lattice 1 and 3 and 116 µm for lattice 2. The real values can deviate from these due to imperfect alignment of the incoming and back-reflected focus positions. Furthermore having only partial overlap can decrease the resulting potential depth of the standing waves. To balance any differences in potential depth between lattices, a power stabilisation is implemented for every lattice arm. Photodiodes behind the back-reflecting mirrors detect residual light and the power in each beam can be changed with the respective AOM. How the potential depth is measured is elaborated in chapter 4.3.

3.9.3. Verdi beam

The 532 nm Verdi beam from the laser system presented in chapter 3.6 can be added to the Yb crossed ODT as a balancing beam. It is arriving on the upper level of the science table via a periscope and gets focused in the science chamber by a 750 mm achromat. The beam

[3]The mirror is not designed to reflect light around 400 nm and thus looses some of it in transmission.

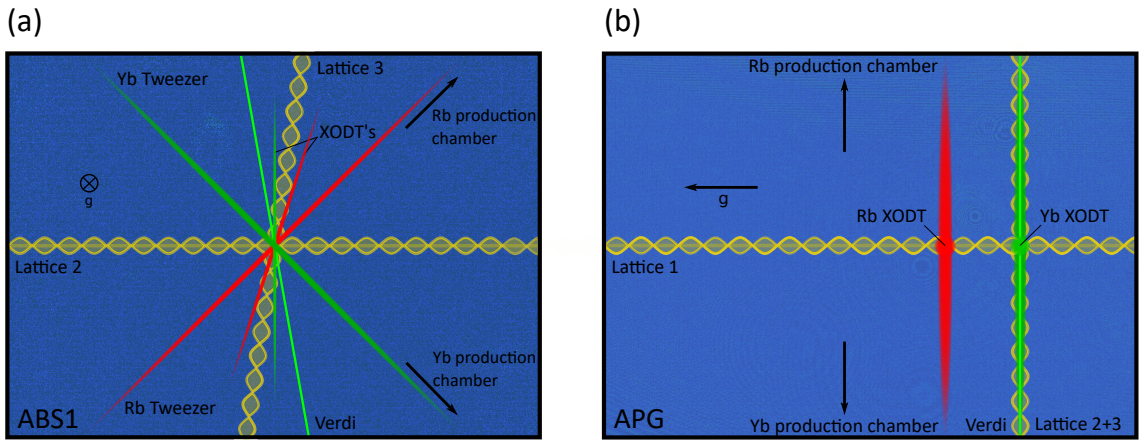

Figure 3.33.: Sketches to represent the orientation of optical traps in the in the science chamber. (a) shows the vertical view of the ABS1, while (b) presents the side-view of the Apogee camera. For visibility, the optical lattices are drawn in yellow standing waves, optical dipole traps for Rb are coloured red and traps for Yb in green. The Verdi beam is included in bright green.

is propagating almost parallel to the Yb ODT crossing beam. We use a slightly different angle to guide it through the outer sides of the windows of the vacuum chamber. After exiting, the beam is deflected into a beam block.

3.9.4. PA beam

The photoassociation light which is prepared, with the laser system in chapter 3.8, arrives at the science table in a single mode fiber. It is collimated with a fiber coupler and focussed onto the atoms with a 300 mm lens. Waveplates and a PBS cube can be used to adjust the polarisation of the light but are not included in figure 3.30. Together with a magnetic bias field, produced by the coils above and underneath the vacuum chamber, either π or a mix of σ_+ and σ_+ polarisation can be selected. Before entering the chamber and eventually exciting atoms, the photons have to pass through an IR mirror due to the restricted space on the table. This reduces the intensity of the beam slightly but has no substantial impact on the beam quality. The beam waist at the focus has a measured value of $\sim 110\,\mu$m.

3.9.5. Imaging

The principle of our (absorption) imaging systems is based on a large beam of resonant light radiating the atoms in the vacuum chamber. Sensitive cameras set up behind the chamber can detect this light or images of atom clouds absorbing it (see section 3.11.2). The imaging system for the science chamber features two different fields of view. It is currently possible to image either Rb or Yb atoms on a camera along the horizontal axis. Additionally Rb atoms can be observed along the vertical axis on a second camera. This enables us to simultaneously image both atomic species independently.

Horizontal imaging

The horizontal imaging system is included in figure 3.30. Here, single mode fibers transfer Rb and Yb imaging light to the science table. The light fields are combined with a dichroic mirror and sent through the vacuum chamber for absorption imaging. Before hitting the camera chip, both wavelengths have to pass a lens system. This lens array is specially designed to prevent chromatic aberration for visible light. We use two consecutive achromatic doublets (N-BK7 and SF5, *Edmund Optics 49-366* VIS-NIR) with a broadband AR coating at 400 nm and 780 nm. A final N-BK7 singlet 500 mm lens on the camera side is used to adjust the residual focal shift after the doublets.

The camera is a cooled CCD chip from *Apogee Ascent A285* (APG) with an effective pixel size of 7.2 µm x 7.2 µm. The field of view is about 10 mm x 7.5 mm, which gives us a 1360x1024 pixel resolution. Compared to simple CCD chips, this version has a lower read out noise due to cooling of the chip. On the right side of figure 3.33, a sketch for the field of view for the APG camera is shown. The optical traps are sketched in their estimated positions and are not to scale. We utilize the longer axis of the camera to increase our field of view along the vertical axis to image atoms in long time-of-flight (TOF) measurements. Thus TOF measurements of up to 30 ms for both species are possible. The trap centers of both crossed ODTs are consequently positioned in the upper part of the chip.

Vertical imaging

The vertical imaging system is included in figure 3.31. As already mentioned, it is merely used for Rb imaging but can occasionally be modified for Yb imaging when trapping beams have to be aligned[4]. Part of the imaging light for Rb is split off by a fused coupler to provide additional light for the science chamber without switching the fiber coupler port. We use a waveplate and a linear polariser to fix the polarisation of the light. Afterwards the imaging beam is overlapped with the vertical lattice and sent through the chamber. It is then separated from the infrared light before hitting the camera chip (by a dichroic mirror).

For the vertical imaging system we use an ordinary industrial CCD *ABS UK-1117* camera (ABS). The chip size is a little smaller with 8 mm x 6 mm. A pixel size of 8 µm x 8 µm results in a picture with 768x567 pixels. On the left side of figure 3.33 the sketch for the field of view of the ABS camera is presented. Similar to the right side, the optical traps are only presented for visualisation/orientation and are not to scale.

[4]Plugging the Yb imaging fiber to the vertical fiber coupler port and removing the polariser can be used to determine the rough position of optical taps for Yb. All optical elements and the adjustment of the camera however are bad for blue light.

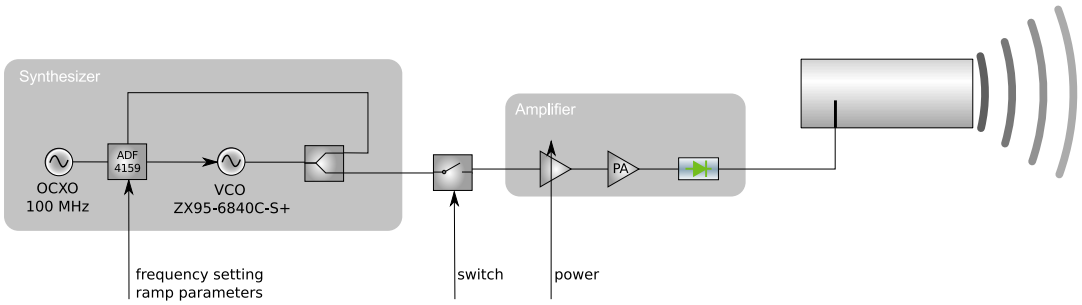

Figure 3.34.: Microwave setup for Rb taken from [1]. The synthesizer frequency can be phase locked to a reference and adjusted with experiment controls. An amplifier increases the signal strength and a self-built antenna emits the signal towards Rb atoms to drive the 6.8 GHz hyperfine transition.

3.10. Microwaves

This chapter presents the setup of two self-built microwave systems at 6.8 GHz. The design concept and its implementation is thoroughly described in [1] and [213]. Both microwave signals are used to manipulate Rb atoms during the experiment. The first setup is installed at the Rb production chamber, while the second system is used at the science chamber.

The microwaves can drive the 6.835 GHz transition between the hyperfine states in the groundstate of Rb. The first mircowave utilizes this to efficiently evaporate Rb in a quadrupole trap. The second is used for the controlled preparation of Zeeman (m_f) and hyperfine (F) states. This allows us to do spectroscopic measurements with different molecular states in photoassociation experiments with Yb. The complete setup with synthesizer, amplifier and antenna is sketched in figure 4.3.

Synthesizer

The synthesizer is equipped with a voltage controlled oscillator (VOC *Minicircuits* ZX95-6840-S+) as a signal source. The ADF 4159 chip[1] on an evaluation board can read/set frequencies and ramp parameters given by the experiment control and adjust the VCO accordingly with a tuning voltage. This is realised by phase locking (PLL) the VCO to an external crystal oscillator. In the first microwave a temperature compensated crystal (TCXO) is already included on the evaluation board and delivers a reference with sufficient frequency stability for its application[2]. The microwave built for manipulation of the atoms in the science chamber [213] is equipped with an external oven controlled oscillator (OCXO ECOC-2522-100.000-5-G-C). It creates a more stable reference frequency at 100 MHz($\pm$10.0 ppb), which enables precise measurements (in kHz steps) with higher

[1] Direct Modulation/Fast Waveform Generating, 13 GHz, Fractional-N Frequency Synthesizer

[2] The exact frequency ramp and stability in the evaporation of the magnetic trap of Rb is not important, since it is slowly ramped over 100 MHz.

resolution.

The output signal of the synthesizer is connected to a microwave switch (HMC1118 *Analog Devices*). It disconnects the synthesizer from the amplifier to provide a quick switch-off function. This is especially necessary when working with short microwave pulses, since the amplifier takes about 2 ms to extinguish the signal when turned off. With this switch a fast attenuation of 48 dBm in 200 ns can be realised.

Amplifier and Antenna

The amplifier is an old rescued part from a communication satellite system (*Terrasat* Microwave ED-0278-4). Due to a lack of documentation of this module, it was analysed [213] and found to include an analog gain control, (slow) digital muting input and an integrated microwave isolator. The output power can be tuned with an input voltage via the experiment control and provides up to 6 W. A self made microwave antenna is attached to the output of the amplifier. The concept for this sawed-off waveguide type horn antenna is treated in [214] and a helpful calculator for our antenna was found on websites [215] for local WLAN networks. Our antenna is a copper tube with one open end for the emission of the signal in a 40° angle. The signal is fed into the tube via a metal stub with $\lambda/4$ length. It is placed at a distance of $\lambda/4$ from the closed end and $\lambda/2$ from the open end of the waveguide. In an effort to match the resonance frequency of the antenna to the signal frequency and minimize the back reflection into the amplifier, three metal screws are used. The screws are simply attached on the opposite side of the feed as adjustable elements, which tune the resonance of the waveguide.

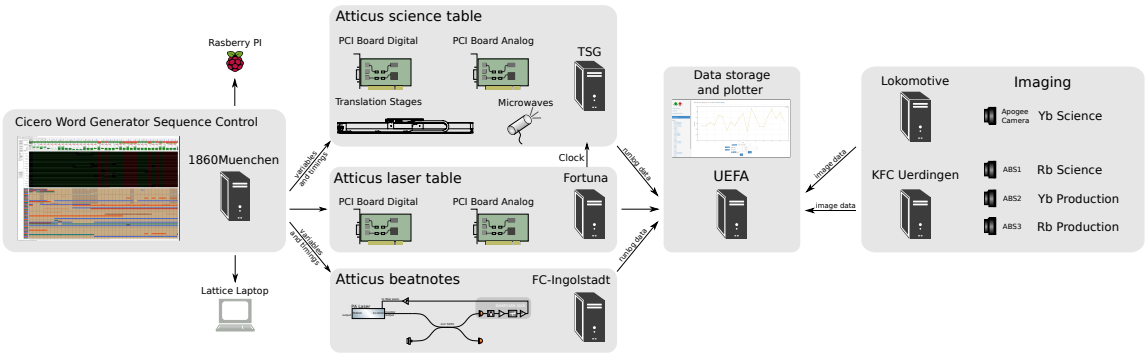

Figure 3.35.: Overview of the experiment control with computers for Atticus servers, Cicero sequence control, imaging and data analysis.

3.11. Experiment Control and Data Analysis

Experiments with ultracold atoms or molecules are steadily growing in size and complexity and our ultracold molecule setup is no exception. This chapter explains the structure of experiment control, which is illustrated in figure 3.35. Furthermore the principle of absorption imaging and the analysis of image data is covered.

3.11.1. From Atticus to Cicero - operating complex machinery

The experiment control is based on a modified *Cicero Word Generator* program [216] and three *Atticus* servers. Cicero (running on the computer named *1860 Muenchen*) is the graphic interface for all digital and analog inputs as well as GPIB and RS232 commands. All variables and experiment timings for the sequence are selected in Cicero and communicated to the Atticus servers. Once the experimental cycle is started by running Cicero, the Atticus servers translate the commands into analog (13-bit $-10\,\mathrm{V}$ to $+10\,\mathrm{V}$) and digital ($0\,\mathrm{V}$ or $+5\,\mathrm{V}$ TTL) signals. Some of our analog signals use custom scales, which are implemented with *National Instruments* software to directly translate voltage inputs to more meaningful experimental values like frequencies for AOMs. The digital signals are used for electronic switches, shutters or triggers. For example, triggers are sent to the imaging PCs and the Raspberry Pi (see section 3.4.3), to capture pictures of atoms at the right time. The Atticus servers (*TSG*, *Fortuna* and *FC-Ingolstadt*) are placed at different positions in the lab and are connected to various hardware. We use a dedicated Atticus 'beatnote' sever for photoassociation laser frequencies. Secondly at the Atticus 'laser table' server, two *National Instruments* cards (analog PCI-6229 and digital PCI-6723 IO) communicate signals to the laser systems positioned in the laser room. The majority of controls is handled by the Atticus 'science table' server, which is connected to PCI cards, two translation stages, two microwaves and several motors. The hardware clocks of the servers are synced to a 20 kHz signal of one analog card to ensure tight timing.

The Aerotech translation stages are controlled via TCP/IP commands. The movement commands have to be sent in time-steps of the sequence control but first the stages have to perform a calibration drive to determine their position. In the sequence we can set a

motionprofile to minimize jerk (SCURVE100) before we give the stage a desired position. At the end of the sequence the stages get a 'move back'-command to get ready for the upcoming transport.

The microwaves and beatnotes have been integrated into Cicero and Atticus as a pseudo GPIB device. Meaning the USB connector of the evaluation boards of the microwaves and beatnote locks is thus interpreted as a fake GPIB. In order to distinguish multiple boards the serial number of the second microwave board has been changed. If Cicero detects two identical (ADF4159) devices it will just try to create a device with an ID that already exists and fail. Different commands in the GPIB time-steps have to set the starting frequency, power, span and time of the microwave signal. Once all parameters are set, a digital trigger instead of a serial command is sent to the board.

3.11.2. Collecting Images

All of the measured data in this thesis comes from absorption images of atomic clouds. This technique is used in all camera systems and can thus yield data from all vacuum chambers and most steps during the sequence.

The principle of absorption imaging relies on resonant light of wavelength λ_{img} passing through a dilute cloud of atoms. The attenuation of incident light along axis z with intensity $I_0(x, y)$ depends on the density of the atomic sample. For any local column density at point (x, y) one can calculate the remaining intensity of imaging light after the transmission with Lambert-Beer's law [10]:

$$I(x, y) = I_0(x, y) \cdot e^{-OD(x,y)} \tag{3.2}$$

The optical density describes the capability of atoms to absorb light and is related to the atomic cross section[1] σ_0 and the density of atoms $\tilde{n}(x, y)$ accumulating along a column in the imaging axis.

$$OD(x, y) = \sigma_0 \cdot \int \tilde{n}(x, y)dz \tag{3.3}$$

By recording three pictures on a single camera in quick succession, deviations in imaging light, dust and camera noise are detected together with the actual desired signal and can be eliminated. The first picture is a recording of the transmitted light (I_{abs}) through the cloud, while the second is detecting the incident light (I_0) without any atoms. The third image called the 'dark image' is made without imaging light nor atoms and simply contains stray light and camera noise (I_{dark}). A complete absorption picture is now composed of all three pictures by subtracting the second from the first and the camera noise from both pictures. The resulting column density can then be computed by applying Lambert-Beer's law.

$$\tilde{n}(x, y) = \int n(x, y, z)dz = -\frac{1}{\sigma_0}\ln\left[\frac{I_0 - I_{\text{dark}}}{I_{\text{abs}} - I_{\text{dark}}}\right] \tag{3.4}$$

[1] For a Clebsch-Gordon coefficient of 1 the atomic corss section is $\sigma_0 = 3 \cdot \frac{\lambda^2}{2\pi}$.

The camera control and configuration files for pixel scalings are done with *LabView*. The final composed image is displayed in a false colour picture within the *LabView* interface. It provides instant feedback to the experimenter and is very helpful for beam alignment or other adjustments in the experiment if no data evaluation is necessary. Figure 3.35 shows the assignment of the cameras to their imaging computers and vacuum chambers. For simultaneous imaging in the science chamber *Lokomotive* is deployed for Yb imaging, while the computer *KFC Uerdingen* is handling Rb images. Image data is saved on the local HDD but can be accessed and analysed from anywhere inside the network.

3.11.3. Analysing Images

During the setup of the experiment the way of measuring atoms numbers, cloud size, density and temperatures has changed considerably. In the beginning all theses parameters have been determined with old Matlab scripts with little documentation. Over time, all of the fits and data analysis were transferred to scripts in python notebooks.

The image from a camera can now be analysed by various python scripts running on the *Uefa* server. Calculated parameters like the number of atoms in a cloud are directly added into a database. Corresponding information from Atticus/Cicero such as time, date and runlog-path about the experiment cycle are previously written into the data table. They are then matched with the results from image data[2] on *Uefa* for documentation and to follow changing variables during a measurement. An automatic web-based data plotter[3] can read database entries and immediately plot them. Simple analysis functions can be implemented in the plotter, which for example directly fits temperatures or lifetimes to the selected data. For more complex image analysis dedicated python scrips are utilized. In the next section the basics for the evaluation of the collected images is discussed.

Measurements with atomic clouds are difficult to analyse if a high-density sample absorbs almost all imaging light. For high densities this is also challenging due to the dynamic range of the cameras. Therefore, images are usually taken shortly ($0.1 - 30\,\mathrm{ms}$) after a trap is turned off to reduce the peak density of the atomic cloud. The time in between turnoff and the first picture is called the 'time-of-flight' (TOF) because an atomic cloud can expand and fall freely until its picture is taken. This technique enables the measurement of the atom cloud in a two dimensional plane within the view of the camera.

Fitting Atomnumber and Temperature

The two major factors to determine the efficiency of each step in the preparation sequence are the atomnumber and the temperature. They indicate whether an excessive loss of atoms or accidental heating effect occurred. By optimising these values, a good phase space density can be achieved, which in turn is required for successfully photoassociation experiments.

[2] An additional program 'listen for Cicero' feeds runlog data to the image config .PAR file via the LabView program.

[3] This neat interface was setup by T. Franzen who used a python framework called Django.

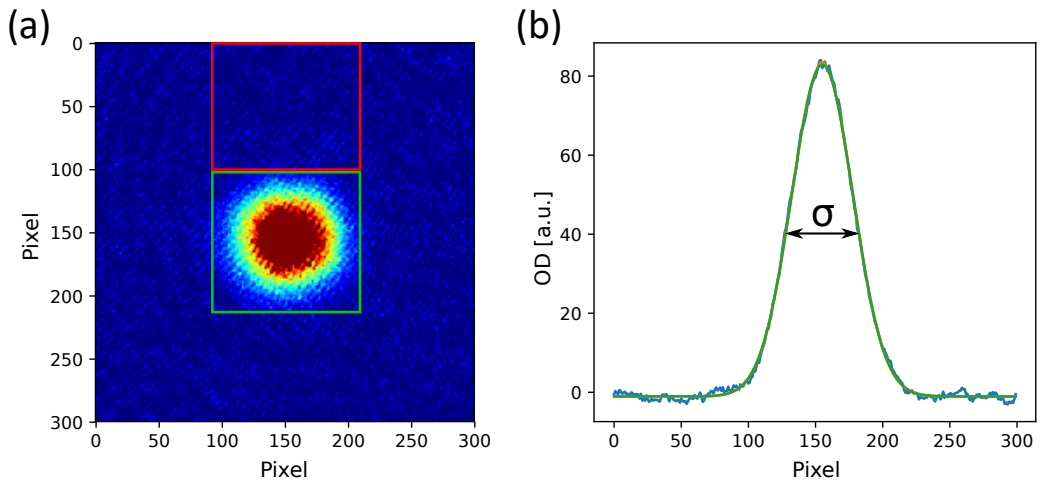

Figure 3.36.: (a) Typical absorption image of a time-of-flight expanded Rb cloud. This image is a defringed picture from the Apogee camera. In this example a thermal Rb sample was released from a crossed optical dipole trap. On the left the pixel-sum method with boxes is showcased and in segment (b) a Gaussian fit is presented.

The atomnumber can be determined in two ways. In the first approach we sum the density over all pixels in a region of interest and multiply with the pixelsize.

$$N = \frac{2\pi \cdot OD \cdot \text{Pixelsize}^2}{3 \cdot \lambda^2} \tag{3.5}$$

For a Stern-Gerlach experiment (see section 4.1.5) or the measurement of the Kapitza-Dirac effect (see section 4.3.1) it is practical to draw boxes around separated atomic clouds. In this case the pixel-sum inside a red control box without atoms is subtracted from the pixel-sum of a green box filled with atoms (see figure 3.36). By doing this, intensity variations impacting in the image quality can be removed from the pixel-sum.

In the second approach we fit a Gaussian density distribution to the sample along a selected axis. In figure 3.36 an example of a fit (green curve) for a thermal cloud of Rb atoms is shown. In addition to fitting an atomnumber this fit also allows us to gain knowledge of the position and width of the density profile. For a series of images with different times-of-flight this gives information about the temperature, trap frequency and even trap geometry for extremely cold clouds (BEC).

The temperature can be determined by looking at the ballistic expansion of the cloud and recording the Gaussian width $\sigma(t_{\text{tof}})$. A sample with temperature T will expand from it's initial size σ_0 according to the following formula [217].

$$\sigma(t_{\text{tof}}) = \sqrt{\sigma_0^2 + \frac{k_B T}{m} \cdot t_{\text{tof}}^2} \tag{3.6}$$

If the sample is cooled down to a BEC or a degenerate fermi gas, the radial expansion is no longer appropriate. The atoms will expand differently depending on the enclosure along each trap axis. A uniform temperature is not calculable and the concept of temperature

loses its meaning. However it is still possible to measure an aspect ratio between the axis to learn something about the trap shape and interaction strength between atoms [218].

For a case in between a quantum degenerate gas and a completely thermal cloud a bimodal density distribution has to be examined. Here the Gaussian fit is combined with a Thomas-Fermi fit [219] to calculate the temperature of the thermal part and the condensate fraction.

Defringing

Absorption imaging is susceptible to pictures with interference fringes in the light field. Since Labview is rather slow, it takes more than one second to take the next picture with a CCD camera. Any change in between the first two pictures with imaging light will be highlighted in the composed picture together with the atomic cloud. The reasons for bad image quality are usually instabilities of the imaging frequency, slight movements of the imaging beams or intensity and scattering of dust particles in the image path.

Images with fringes naturally hinder a correct analysis of the density profile in the picture. This can lead to miscalculated atomnumbers especially in the 'pixel-sum in a box'-approach. In an effort to eliminate fringes we use a post image processing technique [220]. The used algorithm is already described in detail in [1] and will thus not be further discussed here.

4.

Preparation of an ultracold mixture

This chapter describes the individual preparation and eventual mixing of ultracold rubidium (Rb) and ytterbium (Yb) atoms. Since the development of the preparation sequence and subsequent measurements were partly done together with T. Franzen, a similar preparation processes was already discussed in [1]. The chapter of this thesis builds on prior procedures and represents the progress that has since been made, as dense and cold mixture of both elements are the basis for further experiments like the photoassociation to molecules. Therefore a good part of the experimental work of this thesis was to establish a more efficient and stable preparation process, which can be implemented in a sequence in *Cicero* (see section 3.11). The present preparation sequence will be explained in three parts. The first two sections 4.1 and 4.2 deal with the simultaneous but spatially separated production of ultracold Rb and Yb atoms up to the creation of individual Bose-Einstein-condensates. Section 4.3 explains the utilization (loading, shaking and pulsing) of the optical lattice. The last section 4.4 discusses the techniques used to form a combined trap potential and Rb-Yb mixture.

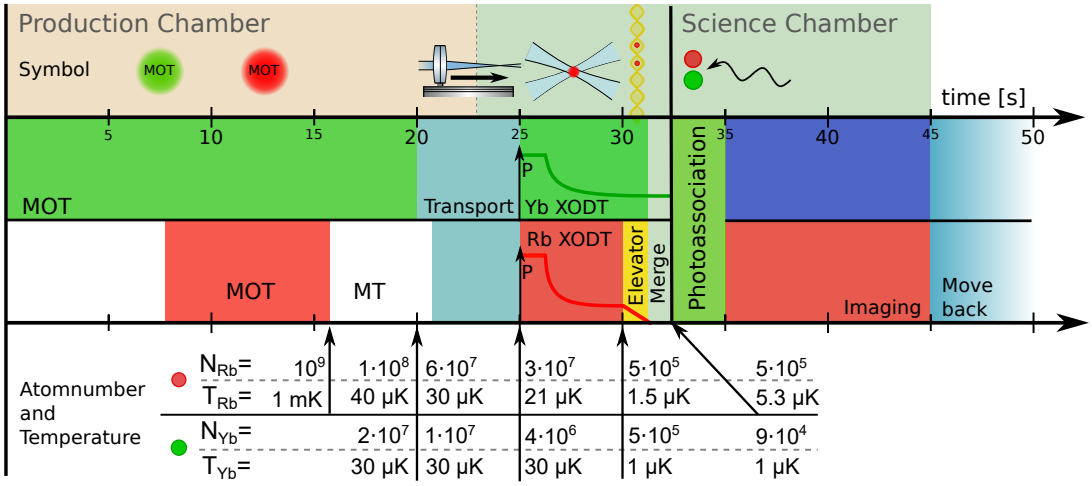

Figure 4.1.: Overview of the major steps during the preparation sequence of rubidium and ytterbium atoms and the following creation of an ultracold mixture. The process for each element is visualised with small symbols, graphs and experimental steps in a timeline over $\approx 50\,\mathrm{s}$. Key points are marked with arrows giving a momentary atomnumber and temperature.

Figure 4.1 gives a simplified overview of the major experimental steps. The general idea is to accumulate a large number of atoms in each production chamber, transport them to the science chamber using optical tweezers (ODTs) and finally create high phase space density samples in crossed optical dipole traps. While all of this can be performed separately for the two species, timing becomes crucial when merging both species in the combined trap.

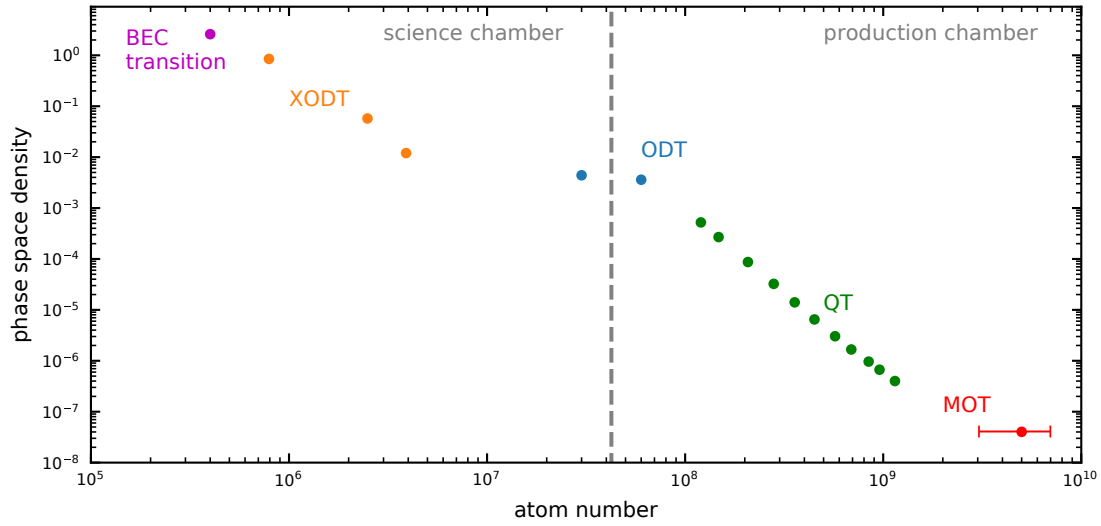

Figure 4.2.: Evolution of the phase space density and atomnumber of Rb during the preparation process inspired from [1].

4.1. Rubidium

The preparation of Rubidium atoms follows four consecutive steps. First a MOT is loaded from a Zeeman slower (section 4.1.1), and subsequently the atoms are transferred into a magnetic quadrupole trap for evaporation (section 4.1.2). Afterwards the atoms are loaded into an optical dipole trap (section 4.1.3), which transports the sample to the science chamber where a crossed ODT is formed with a folded beam. Finally in this trap the atoms can be evaporated to create a Bose-Einstein-Condensate (section 4.1.4).

Figure 4.2 illustrates the evolution of the phase space density and atomnumber of Rb during the preparation process. In the following sections, the experimental sequence and its key stages are described in detail.

4.1.1. The magneto optical trap

The origin of ^{87}Rb atoms in our experiment is the atomic oven and the attached Zeeman slower. In the slower[1], atoms are decelerated until they arrive in the production chamber. A magneto optical trap (MOT) can accumulate the slowed atoms to a vapor cloud of $\sim 5 \cdot 10^9$ atoms within 8 s. Cooling in the trap is realised with light driving the $^2S_{1/2} \rightarrow {}^2P_{3/2}$ ($|F = 2\rangle \rightarrow |F' = 3\rangle$) transition at 780.250 nm, also known as the D2 line of Rb. It has a linewidth of $\gamma = 2\pi \cdot 6.06$ MHz [126] and a Doppler temperature of 146 µK [190]. The actual temperature of atoms inside the loading stage of our bright MOT is estimated to be ≈ 1 mK.

A magnetic field gradient of 15 G/cm and a detuning of $-3\,\Gamma$ [2] is used during the

[1] Increasing field slower operated with 1-3mW and 18.5A. (Compensation coil -3A)
[2] (2x-181 MHz + 2x172 MHz) / 6 MHz = -3

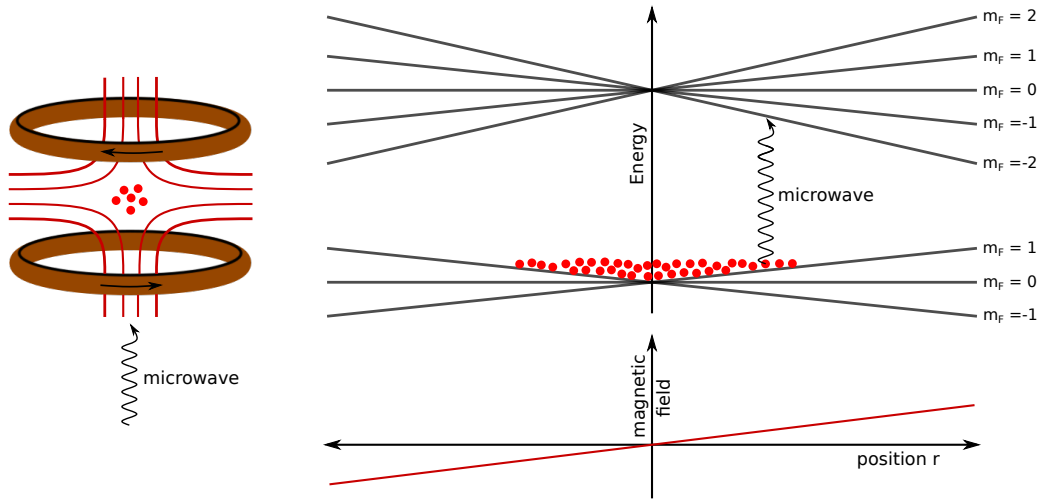

Figure 4.3.: Trapping and evaporative cooling of Rb in magnetic trap. A pair of Helmholtz coils generates a magnetic quadrupole field trapping Rb atoms in the center. Microwave radiation driving the $|F = 1, m_F = -1\rangle$ to $|F = 2, m_F = -2\rangle$ transition of Rb inside a magnetic trap is used to evaporate the trap.

loading period. Compensation fields in three orthogonal dimensions are needed to adjust the position of the MOT and compensate the slower magnetic field. After a fast switch-off of the atomic beam and slower, the MOT is transformed to a dark spot MOT [221]. The repump light in the MOT beams is extinguished and replaced by a doughnut shaped repumper beam via the dark spot laser (see section 3.3.3). This creates a dark region in the trap center. Atoms entering this area will not be returned into the cooling cycle and fall into the dark $|F = 1\rangle$ state via off resonant excitation. If they drift out of the dark region they will be returned to the MOT cycle and are exposed to the force towards the trap center. In the dark spot volume, the density can increase drastically because of reduced scattering rates of atoms in dark $|F = 1\rangle$ states. The atomic sample is further compressed with an increased magnetic field gradient of 44 G/cm in 30 ms and increasing the detuning to $-9\,\Gamma$ simultaneously. Thereby the temperature of the MOT is reduced to $\sim 100\,\mu$K by polarisation gradient cooling [34]. As a result the MOT size and temperature is reduced by about an order of magnitude. This effort is carried out in order to load a MOT with high phase space density into the quadrupole trap presented in the next section.

4.1.2. Magnetic trap and microwave evaporation

Since the MOT cannot reach temperatures low enough to efficiently load the optical tweezer an intermediate trap has to bridge this gap. The used magnetic quadrupole trap (Rb MT) [222] is the first conservative trap for Rb atoms in this sequence. In it dissipative cooling can no longer be applied and has to be replaced by evaporative cooling [223].

At the end of the MOT compression all laser light is switched off. Subsequently the magnetic field is exponentially ramped up from 44 G/cm to 290 G/cm in 1 s. We use the same coils that are used for the MOT field to create a simple quadrupole field. At the

end of the MOT phase the majority of the sample is in the $|F = 1\rangle$ manifold because of the dark region of the MOT. Atoms populating the $|F = 1, m_F = -1\rangle$ state are already held against gravity at the start of the magnetic field ramp and are thus not lost once the MOT light is extinguished. If they populate a different $|m_F\rangle$ state they are immediately lost since they are not in a trappable state. This leaves us with a pure single state sample of $1 \cdot 10^9$ atoms at 0.5 mK in the loaded magnetic trap. The increased temperature is attributed to the adiabatic compression and higher density in the MT.

Once the magnetic quadrupole field has reached its maximum evaporation can begin. In order to create a highly efficient evaporation process, one has to reduce the time in between collisions between Rb atoms. In the tightly confining potential of our MT the collision rate is increased, which leads to fast rethermalization and a shorter overall evaporation time [223].

We use a forced evaporation with a microwave (MW) signal driving the $|F = 1, m_F = -1\rangle$ to $|F = 2, m_F = -2\rangle$ transition (see chapter 3.10). Figure 4.3 shows how Rb atoms are transferred from the initially trapped to an anti-trapped state. Due to a sign swap in the g_F value between the $|F = 1\rangle$ and the $|F = 2\rangle$ manifold the negative $|m_F\rangle$ states in the $|F = 2\rangle$ state become anti-trapped states. This gives a distinct advantage compared to a previously employed rf-signal, which could only transfer atoms to the untrapped $|m_F = 0\rangle$ state as atoms in anti-trapped states actively leave the trap.

The evaporation starts at 120 MHz (6.715 GHz) detuning from the hyperfine resonance. In 3.2 s the detuning is linearly ramped towards the resonance until it stops at 20 MHz (6.810 GHz). The hottest atoms are removed from the sample leaving $1.2 \cdot 10^8$ atoms at 40 µK after a final holding step of 0.5 s. The development of the phase space density during this process can be seen in figure 4.2. We do not evaporate to even smaller temperatures for two reasons. First the optimal parameters for the highest space density after the transition into the optical tweezer determine the end conditions of the evaporation. These of course depend on the power of the tweezer beam and the decompression of the magnetic field during the turn-off of the magnetic trap. Secondly the nature of the trap design induces majorana spin flips [224] of atoms especially at low temperatures if they cross through the magnetic field zero. Of course this could be avoided with a different trap geometry like a clover-leaf configuration [225] or an additional repulsive laser beam as an optical plug [226] but would not significantly improve the loading efficiency of the optical trap.

It is important to note that the smallest amount of light with a frequency near the atomic resonance from the laser systems disturbs the evaporation and thus needs to be properly blocked from the vacuum chamber. Only the optical tweezer beam is turned on to 6 W during the evaporation process. Since it is far detuned from any Rb resonance it has a low scattering rate and thus does not heat the sample. However it can trap hot atoms in the $|F = 2, m_F = -2\rangle$ state in its optic dipole potential overlapping the magnetic trap. To avoid this, a relatively low initial laser power is used before the decompression of the magnetic trap.

In the decompression the magnetic field is ramped down exponentially in 1 s to a low field value, which is suitable to conserve the state of the atoms. Finally the compensation fields are used as they align the center of the fading MT to the focus of the optical tweezer

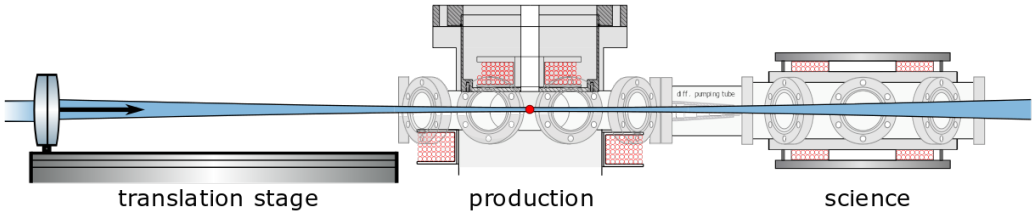

Figure 4.4.: Movement of focus and atoms in the optical tweezer by translation of the lens mounted on the translation stage. The travel distance of $\sim 450\,\mathrm{mm}$ is traversed in 3.3 s for Rb and 5.5 s for Yb

beam.

4.1.3. Optical tweezer and transport of atoms

The optical dipole trap, also called optical tweezer, is utilized to trap and transport atoms over a large distance ($\sim 450\,\mathrm{mm}$) into the science vacuum chamber.

During the decompression of the magnetic trap the power of the tweezer is linearly increased to 16 W. In this experimental step the transfer of the atoms from the MT to the optical trap is realised. Atoms are adiabatically released and expand from the potential of the magnetic trap and are captured by the increasing optical potential of the far detuned laser beam. We are able to load $6 \cdot 10^7$ atoms at 30 µK into the tweezer, which translates to a loading efficiency of 50 % and additional cooling.

Once the transfer is completed the Rb atoms stay in this optical trap - or a modified version of it - for the majority of the remaining sequence. This demands a long lifetime and minimal heating due to off resonant photon scattering for these type of traps. For the Rb tweezer we determine a lifetime[3] of 30(1) s in the production and 45 s in the science chamber, indicating that the lifetimes are pressure limited consistent with the pressure gauge reading of the ion pump controllers.

After a small hold step of 0.1 s, the focus position of the laser beam is shifted by moving the lens on the translation stage. The trap is moved along the beam axis over a distance of 441.5 mm in 2.7 s. In figure 4.4 the movement of the atomic cloud following the beam focus is indicated. The movement profile is characterised by a linearly changing acceleration and a constant third derivative of position also known as jerk. Typical maximum values for the Rb transport are[4]

$$v_{\max} = 0.33\,\mathrm{m/s}\,, \quad |a_{\max}| = 0.5\,\mathrm{m/s^2} \quad \text{and} \quad |j_{\max}| = 0.75\,\mathrm{m/s^3} \tag{4.1}$$

The maximum acceleration, which is experimentally determined to avoid unnecessary atom loss is chosen. For larger values of $|a|$ we observe decreasing atom numbers during

[3]Here the lifetime is defined to be the hold time until the atomnumber in the trap is reduced to $1/e$ of the initial number.

[4]The Yb transport values are slightly smaller compared to theses values since the Yb tweezer has less axial trap frequency.

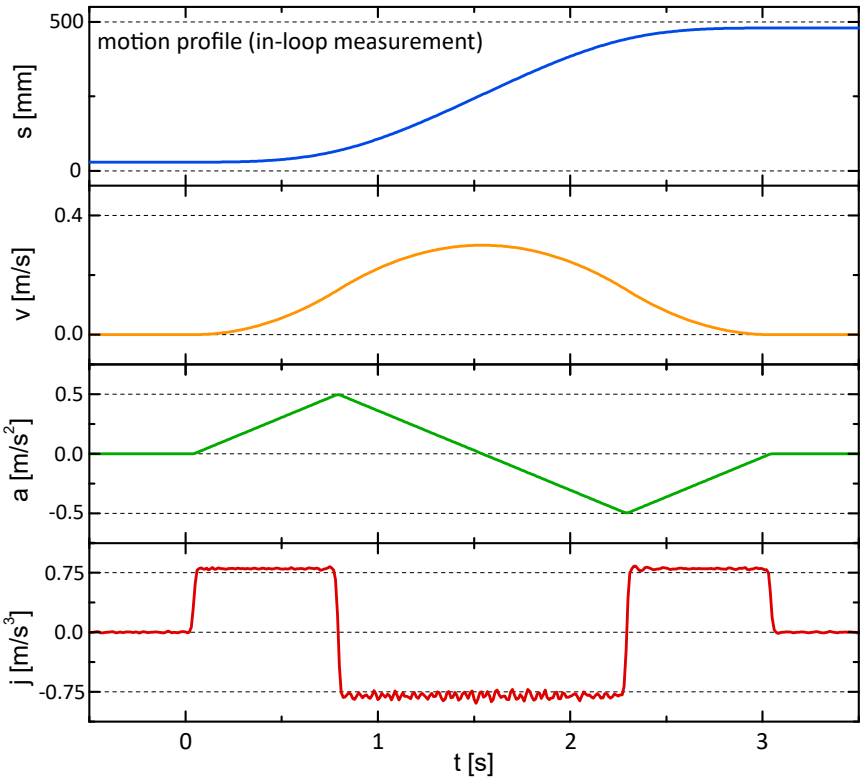

Figure 4.5.: Motion profile of the air-bearing translation stage (*Aerotech ABL1500*). Typical values over time for the optical transport of Rb atoms are shown in subplots from travel distance s in [mm] to the jerk j in $[\frac{m}{s^2}]$.

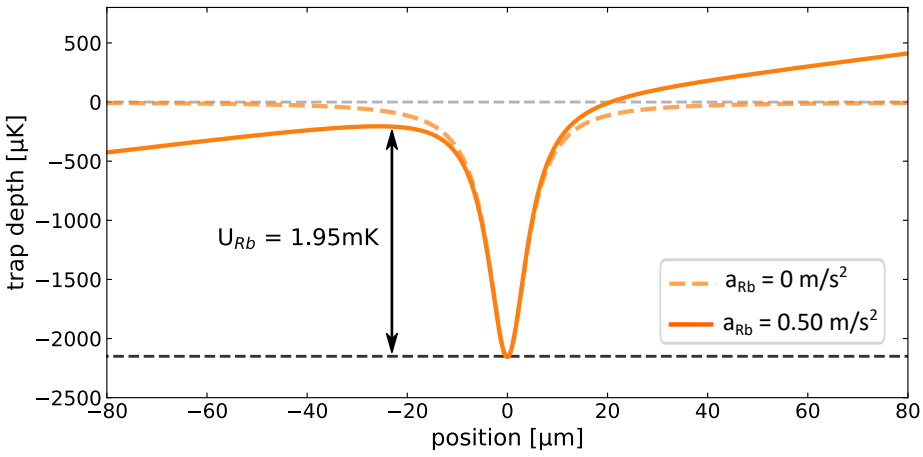

Figure 4.6.: Tilt of the optical potential under the maximum acceleration of $|a_{\max}| = 0.5\,\mathrm{m/s^2}$ during the transport of Rb atoms. The effective trap depth is reduced by 0.25 mK to 1.95 mK.

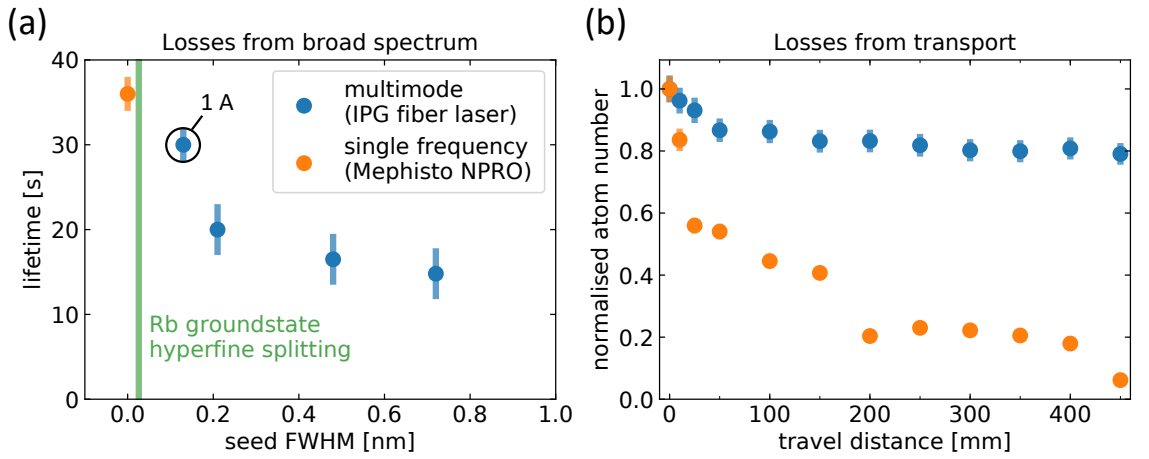

Figure 4.7.: Transport of Rb atoms over long distances and lifetime in optical dipole traps (appeared in [1], [227]) depend on the spectral characteristics of the laser beam. The multimode fiberlaser (IPG) with short coherence length (a) shortens the lifetime of the trap if the spectral width increases but (b) is able to transport atoms over a large distance of 450 mm. The seed FWHM changes for different laser currents (1 A, see figure 3.20). For a narrow linewidth Mephisto seed, the transport suffers from atom loss (b) due to the formation of a disrupting lattice from vacuum window reflections.

the transport due to the small axial trap frequency of $\omega_z = 2\pi \cdot 4\,\mathrm{Hz}$. Comparing this observation with figure 4.7 and figure 4.5 we suspect that the initial jerk of our motion leads to the largest atom loss as it starts to shake the atoms in the harmonic trapping potential. Hot atoms also leave the trap due to a tilting of the trap potential under acceleration as illustrated in figure 4.6. Here the effective trap depth is reduced by 0.25 mK to 1.95 mK. In figure 4.7 the quality of transport for different distances is shown. We compared different seed lasers for our trap laser, because we found a strong influence of different laser bandwidths impacting our transport performance. Due to interference effects originating from reflections from vacuum windows the formation of a disrupting parasitic lattice emerges especially for a single frequency laser. We suspect the formation of small standing waves in the optical potential along the transport axis to be the cause of heating effects during the axial movement of the trap. Therefore the Nd:Yag *NPRO (non-planar ring oscillator) Innolight Mephisto* seed with narrow linewidth of FWHM $<$ 1 kHz was tested unsuccessfully for a long distance transport. Compared with a multimode fiberlaser, the *IPG* PYL-20M-LP with FWHM $>$ 0.1 nm, with short coherence length ($\sim$ 2 mm) as a seed, transport was achieved with far less heating effects and atom losses.

With the right choice of the seed laser (IPG) the resulting loss during transport is eventually dominated by the pressure in both and in between the vacuum chambers and matches with the observed trap lifetime (30 s) without motion in the Rb preparation vacuum chamber. After a completed transport $3 \cdot 10^7$ atoms at 21 µK arrive in the science chamber.

4.1.4. Crossed optical dipole trap and evaporation to a BEC

The first milestone in this experiment was the creation of a ^{87}Rb BEC. Bose-Einstein condensation is realised by transforming the single beam transport ODT into a crossed ODT and performing further evaporation.

As presented in chapter 3.9.1, the optical potential of the XODT is formed by folding the tweezer beam to overlap with itself. The folding beam is introduced by flipping the motorized flip-mirror in 0.5 s. Afterwards a cubic function is used to ramp up the beam in 0.2 s to full power[5]. At the same time the tweezer power is linearly reduced to 10 W, which of course also reduces the maximum power of the folded beam. Now the trap is converted into a dimple trap and introduces a strong axial confinement to the atoms, while in the transport beam alone the confinement along the axial direction is only weak. Thus, an attempt to evaporate a single beam trap would be unsuccessfull as the already low collision rate decreases rapidly with a reduced confinement. In the crossed ODT however the increased trap depth and confinement at the intersection point of both beams allows for an efficient evaporation process [228]. In figure 4.8 the simulated trap at this stage is shown. The tweezer beam with higher intensity is plotted along the x-axis, while the crossing beam is intersecting at an angle of 45°.

The atomic sample is subsequently evaporated by reducing the tweezer beam power, which follows the exponential function in equation 4.2. Since the crossing beam is derived from the initial beam it is not possible to control each beam intensity independently.

$$P(t) = P_0 \cdot \left(1 + \frac{t}{\tau}\right)^{-3.5} \tag{4.2}$$

In equation (4.2) P_0 is the initial power of the Rb tweezer. The time constant τ and the exponent -3.5 determine the time and shape of the ramp. The ramp is designed to keep the ratio of trap depth and thermal energy $\eta = \frac{U}{k_B T}$ constant [229]. This is desirable because forced evaporation in a crossed optical dipole trap is only effective if the number of colliding pairs of atoms with enough energy to leave the trap is large enough and the trap depth is not reduced faster than the thermal energy with time [230]. It should be noted, that the derivation of the ramp function is not accurate for low powers due to the effects of gravity which are not taken into account. The duration of the evaporation depends on the desired final temperature of the sample. For the purpose of creating a BEC the ramp takes 6 s. After a final hold time of 0.5 s, to reach equilibrium temperature within the cloud, the sample is imaged as displayed in figure 4.9. The ensemble of atoms transitions from a thermal distribution to an almost pure BEC for different trap depths/laser powers. We are thus able to routinely produce BECs with $\sim 2.5 \cdot 10^5$ atoms with no discernible thermal fraction with lifetimes of up to[6] 10 s.

An effective evaporative cooling however turned out to be only possible for very well controlled conditions. Due to the special spectral characteristics of the trap light the

[5] This is measured to be about 40% of the tweezer power.

[6] The lifetime depends on the frequency shift of the XODT AOM as it changes the strength of the multimode beating of the trap.

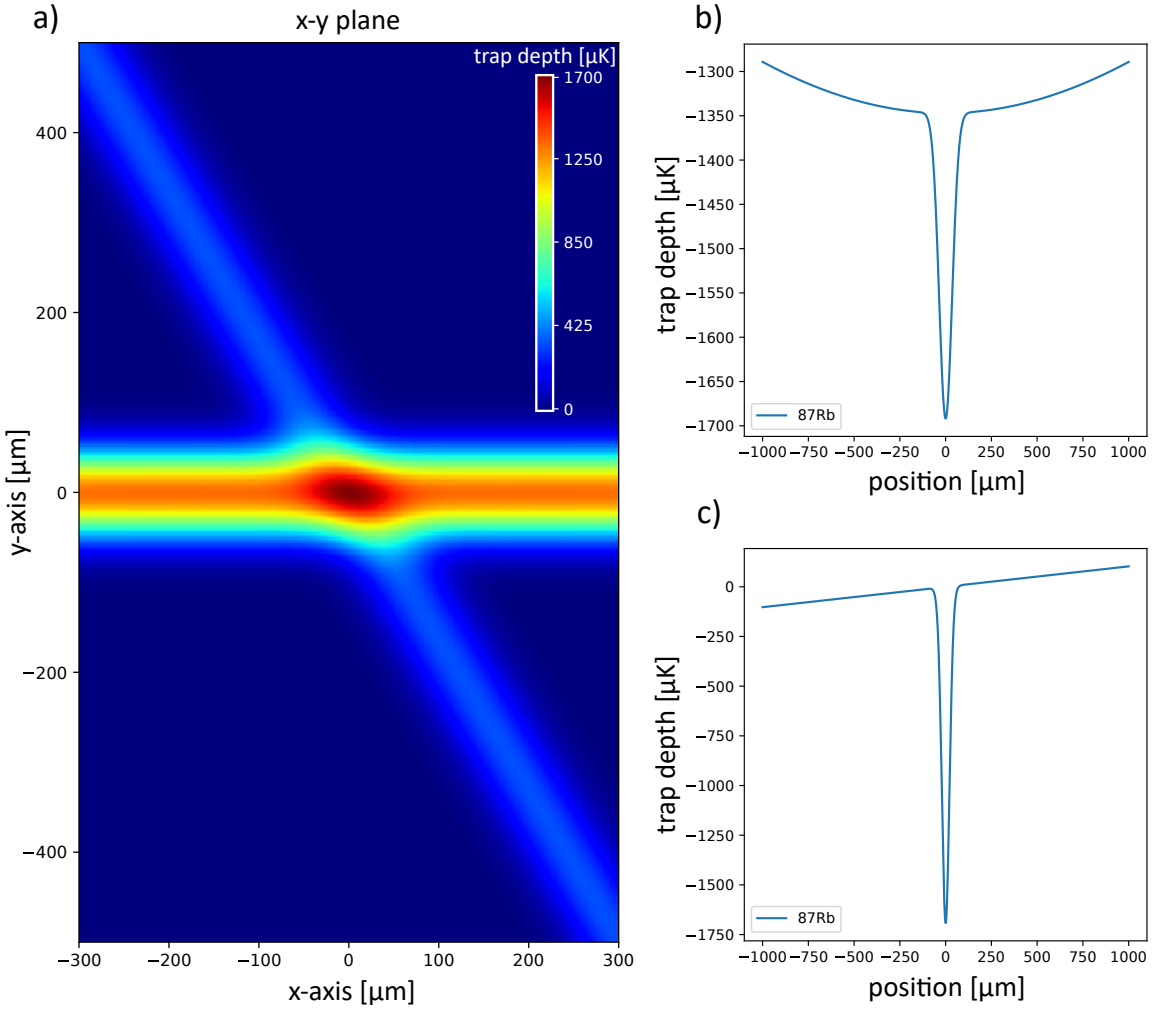

Figure 4.8.: Simulation of the trapping potential for the laser configuration of the crossed ODT for Rubidium. In a) the intensities of the lasers are plotted on the x-y horizontal plane. Graph b) shows the trapping potential along the axis (y-axis) of the higher intensity ODT beam and visualises the dimple potential due to the crossing of both beams. Graph c) displays the trapping potential along the vertical axis showcasing the influence of gravity.

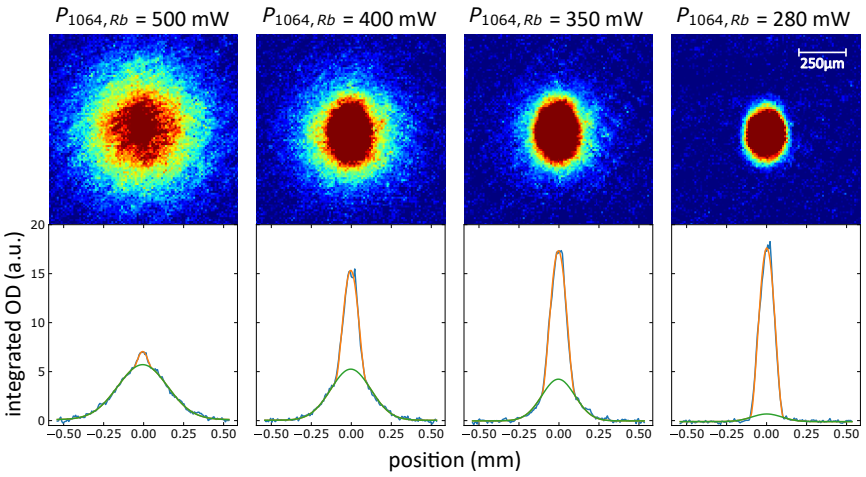

Figure 4.9.: Evaporation of a thermal cloud of ^{87}Rb atoms (on the left) inside a crossed optical dipole trap is shown at different laser powers with false colour absorption images. The bottom row presents the optical density profiles with bimodal fits. The green curve represents the thermal Gaussian distribution, while the total sum is drawn in orange. At the end of the evaporation $2.5 \cdot 10^5 \pm 0.1 \cdot 10^5$ atoms form a BEC with no discernible thermal fraction.

frequencies and polarisation of both XODT beams could not be chosen arbitrarily. In previous sections the multimode features of the tweezer beam have been mentioned and play a vital role again as atoms are heated out of the XODT by intermodal beats. This beating effect between modes is especially harmful because we use the same laser source for both beams. It occurs at every frequency shift $f_{\text{shift}} = f_{\text{beating}} + n \cdot 4\,\text{MHz}$ between the two laser beams and matches with the mode spacing of the multimode IPG fiber laser[7]. In figure 4.10 the results of evaporative cooling with different frequency differences between the two laser beams are shown. As a result the AOM frequency controlling the folded beam was adjusted in between the red destructive regions and the polarisations of the beams are set orthogonally to each other to further reduce the beating effect.

4.1.5. Hyperfine state manipulaton via microwave

The ability to change the hyperfine and Zeeman states of Rb opens up more possibilities for RbYb molecule pairing. The manipulation of these states is realised with the science microwave which was presented in chapter 3.10. Due to the preparation in the magnetic trap most Rb atoms are in the $|F = 1, m_F = -1\rangle$ state. Magnetic bias fields in both vacuum chambers try to conserve the purity of the sample inside the optical traps. However it is very challenging to control the magnetic field in between the chambers during the 45 cm transport. Therefore we observe a small population of atoms in the $|F = 1, m_F = 0\rangle$ state after the evaporation in Stern-Gerlach type experiments.

[7] This is the free spectral range of the fiber laser cavity.

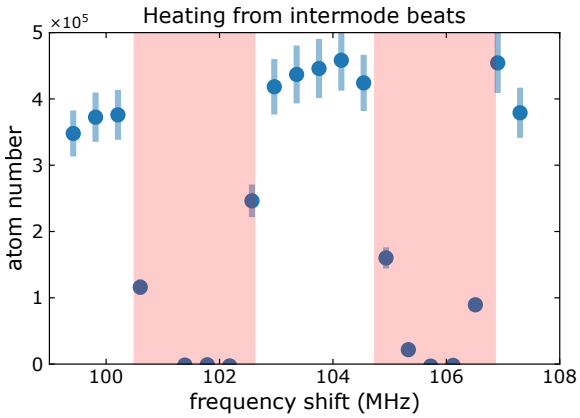

Figure 4.10.: Evaporative cooling with different frequency shifts between the trap lasers results in heating and eventually atom loss due to beating of the multimode spectrum. Knowledge of the 4 MHz mode spacing is used to bypass the red marked areas. Graph is taken from [1].

Rabi pulse and Landau-Zener sweep

Either microwave pulses creating Rabi oscillations [231] or Landau-Zener sweeps [232] can be used to manipulate the Zeeman and hyperfine state of Rb atoms. In practice both of them are short procedures that can be added anywhere in the sequence but are usually employed in the final stages just before photoassociation experiments[8].

Rabi pulses are short (~ 0.1 ms) bursts of microwave signals, which couple two ground state hyperfine levels on resonance. For different pulse durations the state population of those states oscillates with the Rabi frequency Ω_R.

$$\Omega_R = \frac{2\mu_B}{\hbar} \langle F', m_{F'} | \hat{B} \cdot J | F, m_F \rangle \tag{4.3}$$

Here $\hat{B}$ the microwave magnetic field couples to J the electron spin operator [233]. By way of example figure 4.11 shows a measured Rabi oscillation between the initial state $|F = 1, m_F = -1\rangle$ and $|F = 2, m_F = -2\rangle$. With $\Omega_R = 6$ kHz it is the strongest observed coupling and fastest Rabi oscillation between two states in our experiment.

While this method is probably the simplest to generate all kinds of state populations it also has a disadvantage. It is very sensitive to the magnetic background and with it the resonance condition. Changing magnetic fields in the system have a direct impact on the Zeeman splitting, which tunes the microwave out of resonance and impacts the Rabi frequency.

Landau-Zener sweeps[9] [234] are less susceptible to a changing environment in the experiment and are thus the preferred method. There are two versions of possible sweeps. The first is a sweep of the microwave frequency across the resonance frequency. The second is the variation of the magnetic field to indirectly sweep across the transition. The avoided

[8] The microwave signal does not effect Yb atoms.
[9] also known as the rapid adiabatic passage (RAP)

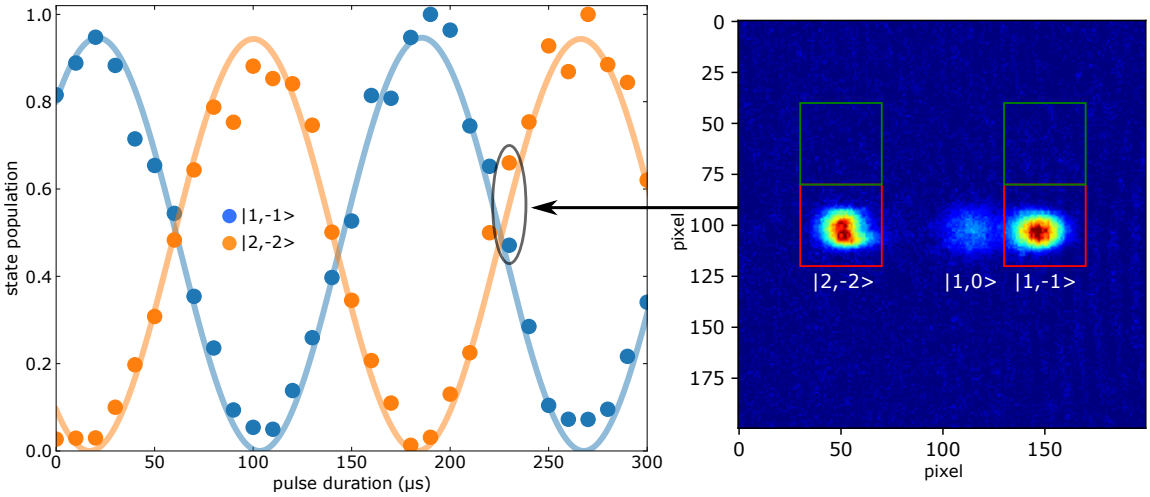

Figure 4.11.: Rabi oscillation between the initial hyperfine state $|F = 1, m_F = -1\rangle$ and $|F = 2, m_F = -2\rangle$ with Rabi frequency $\Omega_R = 6\,\mathrm{kHz}$. The oscillation is measured with Rabi pulses of different lenghts and a Stern-Gerlach type experiment to analyze the state distribution. The inset on the right shows a typical absorption image for one pulse duration and the areas used to calculate the pixelsum of both m_F states.

crossing between the states is induced by the microwave signal. If the ramp is slow enough ($\sim$ ms) the sweep traverses the crossing. Figure 4.12 shows a sketch of a Landau-Zener sweep adapted from [1]. Atoms in the initial state $|1\rangle$ will adiabatically follow into state $|2\rangle$ at the crossing with probability [235]

$$P = 1 - e^{-2\pi\Gamma} \quad \text{with} \quad \Gamma = \frac{|\langle 1|\, V\, |2\rangle|^2}{\hbar \frac{dE}{dt}} = \frac{\Omega_R^2/4}{\hbar \frac{dE}{dt}} \tag{4.4}$$

Here V is a time-dependent perturbation (here a microwave) in the system that creates the avoided crossing. The distance between the adiabatic states at the avoided crossing is Ω_R and describes the strength of the coupling. The probability for a complete transfer of all atoms to a different state is highest for with a small slew rate $\frac{dE}{dt}$ of the ramp and a high Rabi frequency Ω_R.

In the experiment we are able to perform complete transfer by applying the second sweep version. Here the sweep is performed for a sweep range of ΔB (with a typical value of $\sim 0.1\,\mathrm{G}$) and $t_{\mathrm{sweep}} \sim 20\,\mathrm{ms}$ and is optimized for an efficient but fast transfer, while the microwave signal is kept at constant frequency. This method is easier to operate, as it is easier for us to ramp magnetic fields compared to the microwave frequency. Varying magnetic background fields are much smaller than ΔB and do not disturb this process.

Stern-Gerlach

Stern-Gerlach experiments [236] are known to deflect particles with magnetic moment by applying a magnetic field gradient ∇B. To resolve the Zeeman states of our Rb atoms we perform a similar experiment and image separated clouds as shown on the right side of

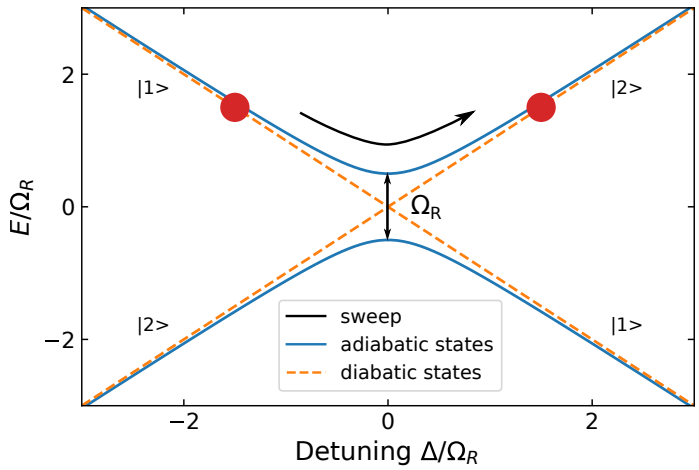

Figure 4.12.: Illustration of a Landau-Zener sweep (or rapid adiabatic passage) adapted from [1]. Adiabatically sweeping the detuning across the resonance frequency between state $|1\rangle$ and state $|2\rangle$ can transfer atoms into a different state by use of an avoided crossing.

figure 4.11. In order to detect the atoms, they are optically pumped to the F=2 state by an imaging repump pulse after the Stern-Gerlach experiment. We can distinguish between $|F = 1\rangle$ and $|F = 2\rangle$ atoms by simply not applying the repump pulse as atoms in the $|F = 1\rangle$ state will not get imaged.

In order to detect the state distribution the experiment is performed during the *time-of-flight* step in the experimental sequence. During free fall the atoms are exposed to an inhomogeneous field in the form of a magnetic field gradient and are deflected by a force

$$F = m_F g_F \mu_B \nabla B \tag{4.5}$$

depending on their m_F state and gyromagnetic ratio g_F. Due to a sign change of g_F between $|F = 1\rangle$ and $|F = 2\rangle$ we get an opposing deflection for equal m_F Zeeman states.

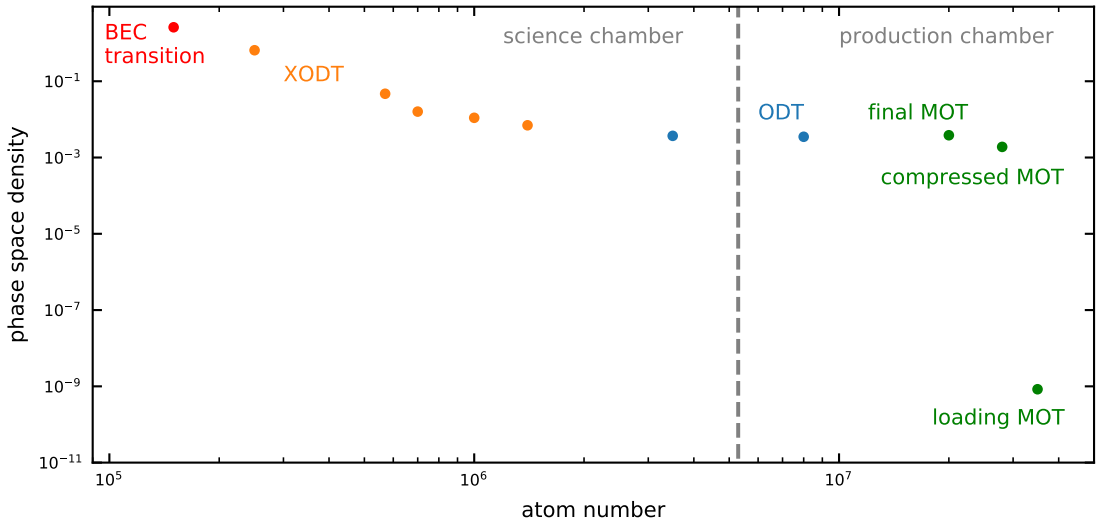

Figure 4.13.: Evolution of the phase space density and atomnumber of Yb during the preparation process.

4.2. Ytterbium

The preparation of Ytterbium atoms follows three consecutive steps. First of all, atoms coming from a Zeeman slower are loaded into a MOT (section 4.2.1), which is carefully positioned in the focus of an optical dipole trap. Afterwards the atoms are transferred into this optical trap and transported into the science chamber (section 4.2.2). Finally a crossed optical dipole trap (XODT) is created with an additional laser beam, which is evaporated to form a Bose-Einstein-Condensate (section 4.2.3). Figure 4.13 illustrates the development of the phase space density and atomnumber of Yb during the preparation process. In the following sections, the experimental sequence and its key stages are described in detail.

4.2.1. Yb MOT

The Yb MOT is loaded from an atomic oven and an attached Zeeman slower. This setup follows the same principle as the Rb MOT but is able to reach higher phase space density by utilizing ytterbium's narrow intercombination transition at 556 nm for laser cooling. Due to a vanishing magnetic moment in the $^1S_0$ ground state of Yb it is not possible to operate a magnetic trap as a tool. As a result the Yb MOT needs to reach lower temperatures without evaporation and be provided with a high position-stability to be directly loaded into an optical dipole trap. The preparation of the Yb MOT thus turns out to be a simple loading and compression process, followed by a complex vertical position stabilisation which will be presented here.

In order to accumulate a large number of atoms at low temperatures, the MOT is operated at the narrow linewidth $^1S_0 \rightarrow {}^3P_1$ at 556 nm transition. This intercombination line has a linewidth of $\Gamma = 2\pi \cdot 182\,\mathrm{kHz}$ and Doppler temperature of 4.4 µK [106]. The

Zeeman slower however makes use of the $^1S_0 \rightarrow {}^1P_1$ transition at 399 nm with much higher scattering rate due to a linewidth of $\Gamma = 2\pi \cdot 29\,\mathrm{MHz}$ (Doppler temperature 0.69 mK). In segment (a) of figure 4.14 the loading MOT is depicted with a temperature of 120 µK. While this is an order of magnitude colder than the Rb MOT, its disadvantages are long loading times ($\approx 20\,\mathrm{s}$) and a low capture velocity. Though the time for the entire preparation is shortened by the omission of a magnetic trap.

In contrast to a Rb-type MOT, the Yb MOT is much more sensitive to the intensity distribution, laser detuning and alignment of the MOT beams as the transition is much more narrow. Especially the amount of light in the vertical axis has a high influence on the density and position of the MOT during the initial loading and subsequent compression step, which will become important in the next section. For an optimised loading rate and low susceptibility to the vertical position during compression, the vertical intensity was chosen to be 2/3 of both horizontal beams, which are of equal intensity[1].

We use a detuning of $-10\,\Gamma$ and a magnetic field gradient of 3 G/cm during the loading period. Two horizontal magnetic field compensation coils are used to position the atom cloud[2]. This is an essential tool since the slower light introduces a force pushing the atoms away from the trap center. Even for detuned slower light, this scattering force prohibits the loading process unless a compensation field along the slower axis is present[3]. At the end of the MOT loading cycle the slower is switched off together with its compensation field in 0.4 s. Finally we are able to collect $3 \cdot 10^7$ ^{170}Yb atoms in 20 s during the first phase of the Yb MOT. The loading rate for other bosonic isotopes scales with their natural abundance[4].

In the next steps we compress and then cool the cloud to prepare the transfer into the optical tweezer. First the MOT is compressed by a magnetic field ramp from 3 G/cm to 19 G/cm in 0.1 s. Although this causes heating and some atom loss it is important to match the density distribution to the size of the trap region of the optical trap. Afterwards the temperature of the sample is reduced to 30 µK by a linear ramp of the intensity. The light is dimmed from $90\,I_{\mathrm{sat}}$ to $0.5\,I_{\mathrm{sat}}$ in 0.1 s while the laser detuning remains constant. In the center frame of figure 4.14 the MOT has now visibly dropped to the bottom of the trap as indicated by the grey dashed line. This effect can be observed in narrow linewidth MOTs as the influence of gravity plays an important role for low intensities [237][197]. The 'gravitational sag' appears if the gravitational force can be compared to the radiation pressure force of the upward vertical MOT beam[5]. The displacement from the trap center z_0 changes the detuning due to the Zeeman shift in the magnetic field. The trap thermodynamics are thus dictated by the balance of gravity and the radiation pressure of the upward MOT beam with a new effective detuning $\Delta - \mu d B_z z_0$ [237] such

[1] While this ratio is not relevant to find a Yb MOT at the intercombination line, proper MOT and Slower adjustment can be vital to meet the phase space density conditions for a BEC

[2] Vertical position shift is can be realised with an adjustment of one of the MOT coils but is more often used as a tool to adjust the MOT frequency detuning as this slowly drifts with the cavity.

[3] We use the slower compensation coil with 3A and a slower current of $\sim 9.5A$ depending on the intensity of the laser beam.

[4] Fermionic isotopes were not tested during this thesis.

[5] For ^{170}Yb atoms the ratio between gravitational force $F_g = mg$ and maximum optical force $F_{\mathrm{rad}} = \frac{\hbar k \Gamma}{2}$ is $R = \frac{F_{\mathrm{rad}}}{F_g} = 478$.

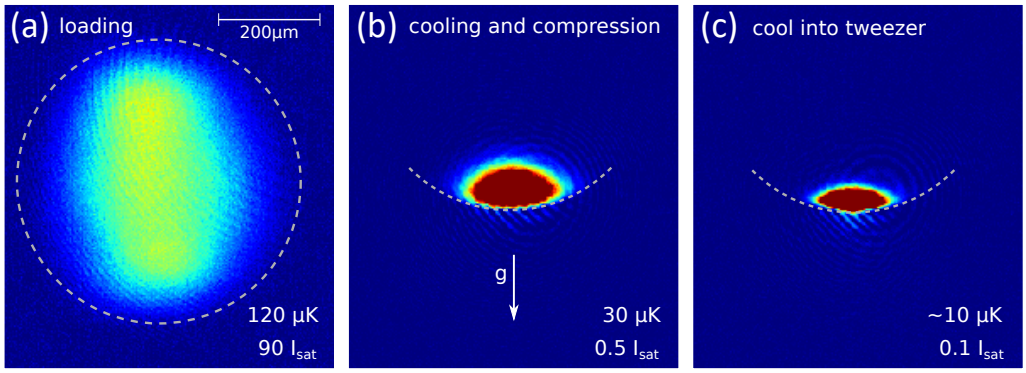

Figure 4.14.: Absorption images of Yb atoms at three different MOT stages. In segment (a) the MOT is loaded at high intensity and low magnetic gradient to form a low density cloud filling the entire trap volume. In segment (b) this MOT is then compressed and cooled by reducing the intensity. (c) Under the influence of gravity atoms sink to the bottom of the trap - indicated with the gray lines - before they get loaded into the optical tweezer.

that

$$\frac{\Delta_{\text{eff}}}{\Gamma} = -\frac{\sqrt{Rs - s' - 1}}{2} \tag{4.6}$$

with the ratio between gravitational force and radiation force R, saturation parameter s and linewidth Γ. While the initial detuning Δ is kept constant in our experimental control, it is still possible to suffer from small changes due to cavity drifts and lock imprecision (see section 3.4.3). For different detunings of our MOT light the cloud moves linearly with a slope of $\frac{dz_0}{d\Delta} = 223 \pm 4 \, \frac{\mu\text{m}}{2\pi \cdot \text{MHz}}$.

In conclusion the vertical position of the center of mass of the Yb cloud depends on the intensity (saturation parameter s) and frequency of the MOT light (detuing to atomic line Δ). This dependence makes it more difficult to repeatedly achieve a reasonable overlap between MOT and the optical tweezer for a successful transfer into the optical trap and forced us to implement the active position stabilisation. The following step thus contains the vertical position correction realised with the Rasberry Pi, which is already covered in section 3.4.3. We take an image with the Pi camera, calculate the needed frequency correction, apply it and take a second picture to verify the change in the MOT position. This process takes 0.6 s and is an important part of the cycle.

The last timestep in the MOT is something we refer to as the 'cool into tweezer' step. It is the transition into the optical trap, in which the intensity of the MOT beams is linearly reduced until extinguished in 0.3 s. Since the position of the atoms depends on the intensity, this step introduces an inevitable but small drift in MOT position. During this ramp the cloud of atoms is cooled down to $\sim 10\,\mu\text{K}$ at $0.1\,\text{I}_{\text{sat}}$ (see segment (c) in figure 4.14). In the absence of the optical trap and even lower intensities the atoms drop out of the MOT once the gravitational force exceeds the radiation pressure force.

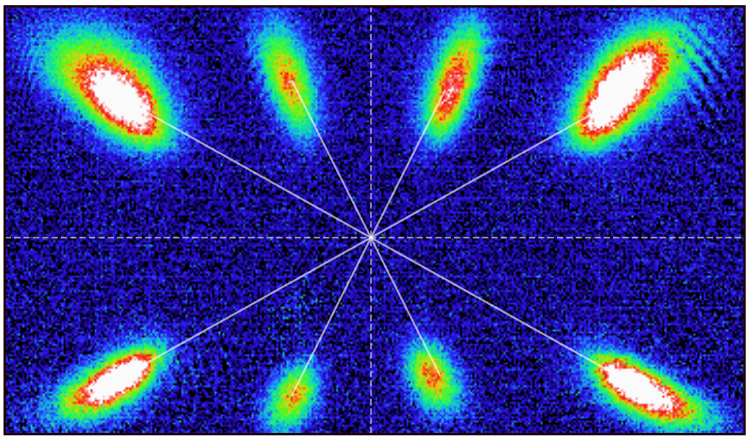

Figure 4.15.: Absorption image of eight fragments of a momentum crystal, that are formed after a frequency sweep across the atomic resonance of a Yb MOT. The white lines guide the eye from each split momentum package to their origin, the center of the MOT.

Stumbled upon: Usually the Yb MOT, like many others[6], is operated with red detuned light. For narrow linewidth MOTs an interesting phenomenon, illustrated in figure 4.15, can be observed if one switches to blue detuned light after accumulating a cold atom cloud [237]. The atoms previously compressed in the MOT form a momentum crystal, whose fragments in momentum space are positioned like corners of a cube, which are repelled from the trap center.

[6]There are molecule MOTs, which make an exception.

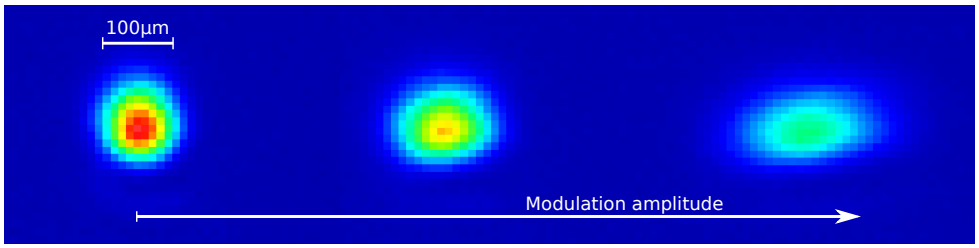

Figure 4.16.: Time-averaged beamshape of the Yb tweezer with increasing modulation amplitude. The focus is recorded with a CCD (*ABS UK-1117*) camera to visualise the beam quality and increasingly elliptic form.

4.2.2. Tweezer and transport

The optical tweezer for Yb is used to trap and transport atoms into the science chamber. The movement of atoms and the challenges it involves are already covered in the Rb transport chapter 4.1.3 and is thus not touched again. In fact the loading process is causing more difficulties in the case of Yb and will therefore be emphasised here.

The optical tweezer is able to trap many Yb atoms from the compressed MOT if the spatial overlap of both trapping potentials is well aligned. The pancake shape of the density distribution on the bottom of the cold Yb MOT however does not match well with a standard Gaussian laser beam. In order to adapt to this mismatch, the tweezer beam can be modulated with an AOM, as previously explained in chapter 3.4.5. The modulation increases the effective horizontal beam size and enables us to form an effectively elliptic beam for a better fit with the atom cloud[7]. In figure 4.16 the focus of the beam is recorded with a CCD (*ABS UK-1117*) camera to visualise the time-averaged beamshape for different modulation amplitudes. The initial beamwaist diameter of 40 µm can be adapted to the diameter of the cloud (estimated to be $\sim 100\,\mu m$) and is optimized to the atomnumber in the tweezer.

The tweezer power is set to a maximum power of 19 W during the complete MOT sequence. The axial trap frequency of the optical trap could not be measured as it is rather small at a calculated frequency of 2 Hz. We find no negative impact on the preparation in the MOT and favour a constant power during the majority of sequence steps to minimize thermal lensing effects (in the tweezer setup). In figure 4.17 the atomnumber in the optical trap for different modulation amplitudes is shown. With a stabilised MOT position and an adapted beam shape a transfer efficiency of 50% is reached. For a well performing MOT atomnumbers of $1.0 \cdot 10^7$ could be attained. However it should be noted that errors - due to frequency fluctuations - in the MOT position can still occur and are the major instability of the Yb preparation process. They are mainly corrected using the position stabilization (see section 3.4.3) but are still a nuisance in the search of weak molecule transitions.

Furthermore, the lifetime of the Yb tweezer in the production chamber is found to be only $15-20\,s$ limited by the vacuum pressure. The high variation in multiple measurements

[7] Modulation settings are -5V to +5V at the driver input. Usually 1 V at 3.5 Vpp with a frequency of 10 kHz is selected.

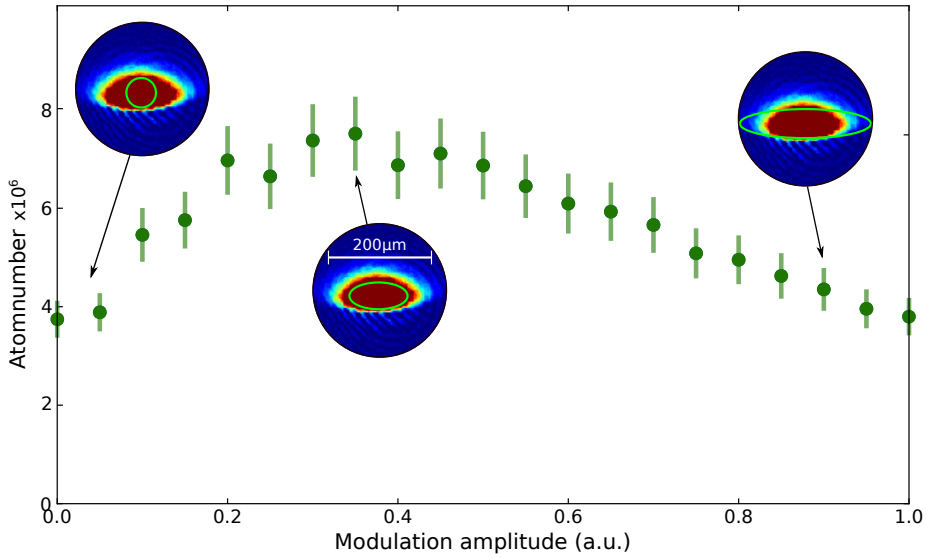

Figure 4.17.: Yb atomnumber after transfer from the compressed MOT into the optical tweezer. For different modulation amplitudes the overlap between the density distribution of the cold MOT and the laser beam influences the transfer efficiency as visualised for three examples.

over a long time is attributed to a change of pressure in the chamber. The limiting factor is the atomic oven, which is set to high temperatures for a sufficient atom flux of ^{170}Yb with an abundance of only 3%[8].

After the MOT light is completely extinguished the optical trap is held for 0.1 s. In this time the modulation is linearly decreased to zero to tighten the trap and prepare for the movement of the tweezer. The transport time is longer compared to Rb since the axial trap frequency in the transporting optical beam is about half for Yb atoms at equal intensities. As shown in figure 4.18 the effective trap depth for Yb under maximum acceleration is reduced by 70 µK to 130 µK. The atoms are moved for 5.5 s across a distance of 439 mm until about $4 \cdot 10^6$ atoms arrive in the science chamber[9].

Sidenote: Astigmatism and impurities in the laser beam have been an ongoing topic in the long distance transport of atoms. Especially in the case of Yb a time-consuming search for a recurring deterioration of the beam quality thwarted our transport. Eventually after the replacement of lenses and an AOM a stable setup was found to be working for months which will need to be rechecked in case of declining performance.

4.2.3. Crossed optical dipole trap evaporation to a BEC

The final phase for Yb is the evaporation in a crossed optical dipole trap (XODT). The combination of trap lasers has changed several times during this thesis work. In this

[8]Refilling the oven brings oxidised Yb into the vacuum chamber, which is hard to pump. Thus multiple TiSub firings are recommended to bring the pressure down to increase the tweezer lifetime.

[9]Thermal lensing effects lead to a difference in travel distances compared to the actual distance between the center of vacuum chambers. Loading position 27mm to final position 466mm.

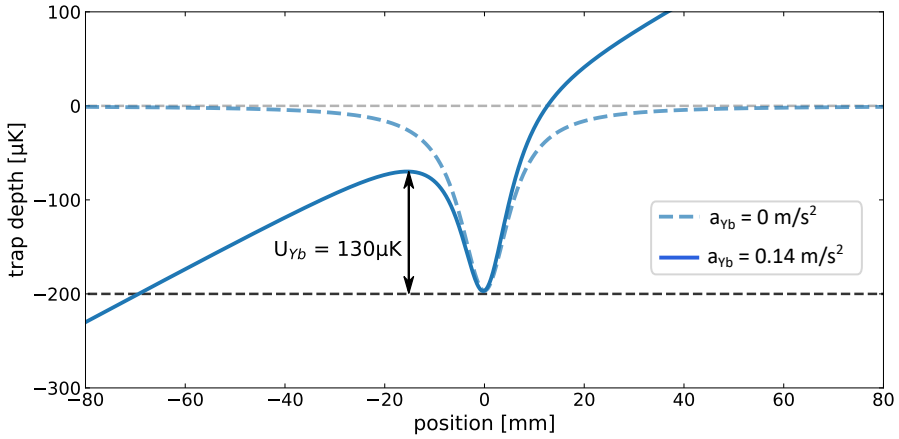

Figure 4.18.: Tilt of the optical potential under the maximum acceleration of $|a_{\max}| = 0.14\,\mathrm{m/s^2}$ during the transport of Yb atoms. The effective trap depth is reduced by 70 µK to 130 µK.

section two different configurations are presented. First data for the evaporation to an almost pure BEC in a trap formed with both optical tweezers is introduced. Afterwards the current system including the newly developed high power fiber laser from chapter 3.7 will be explained.

The evaporation of Yb in a crossing of both tweezer beams serves as a proof of concept and is realised in the absence of Rb atoms. This method cannot be used in the creation of an ultracold mixture, because Rb atoms loaded in the Rb tweezer, which is utilized as the crossing beam, would heat Yb out of the trap. Before the crossing is formed the focus of the Rb tweezer beam is already positioned in the science chamber. Next the Yb tweezer beam focus is moved to the same position. In the first step the atoms need to be collected from the wings of the potential into the dimple trap. This is realised by a linear ramp of the Yb tweezer power to 6 W in 3 s, while the Rb tweezer power is unchanged at 16 W. During this ramp the atom number drops to $1 \cdot 10^6$ but a high density of atoms in the trap center leads to a efficient evaporation. The ramp functions used in the following evaporation used the same exponential function as described in chapter 4.1.4. Both tweezers are ramped down proportionally to each other in about 10 s depending of course on the final power. Due to the smaller scattering length of $64a_0$ in ^{170}Yb and the lower trap depths compared to Rb the evaporation needs more time for thermalisation. A final hold step of 0.5 s is added to reach an equilibrium temperature within the cloud. In figure 4.19 the absorption pictures show a phase transition to a BEC, where we obtain $3.6(2) \cdot 10^4$ BEC atoms with no discernible thermal fraction. It is generally more difficult to create a pure BEC for Yb as the preparation offers less phase space density in the MOT compared to the MT and thus provides less atoms at the onset of the evaporation in crossed optical dipole traps compared to Rb.

With the introduction of the newly developed high power fiber laser presented in chapter 3.7 the crossing beam was constructed with this new laser source replacing a setup similar

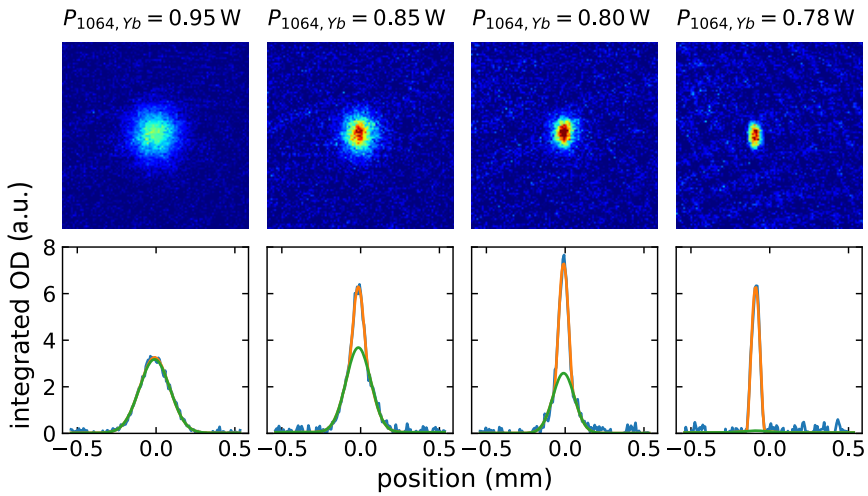

Figure 4.19.: Evaporation of a thermal cloud of ^{170}Yb atoms (on the left) inside a crossed optical dipole trap is shown at different powers with false colour absorption images. The bottom row presents the optical density profiles with bimodal fits. The green curve represents the thermal Gaussian while the total sum is depicted in orange. At the end of the evaporation $3.6(2) \cdot 10^4$ atoms form a BEC with a no discernible thermal fraction.

to the Rb crossing 'folding-beam-method'. The upsides of an independent laser for the crossing - compared to the reuse of the existing laser beam as done for Rb - are independent power ramps and most importantly no struggle with multimode beats. Consequently we are able to handle the evaporation in the crossed trap differently. Initially the crossing beam is ramped up to 9 W when the optical tweezer starts moving towards the center of the science chamber. We observe no excess heating or high loss of atoms as the atoms are confined into the crossing with the stationary optical trap. Next the Yb tweezer beam is ramped down in order to bring atoms from the wings of the potential into the dimple trap. Both traps can be evaporated to 0.8 W (tweezer beam) and 0.6 W (crossing beam) in 5 s. This results in $3 \cdot 10^5$ atoms at 0.3 µK with a lifetime of 16.1 ± 2.4 s. It is important to note that this evaporation is deliberately faster than a ramp that is optimised to create a BEC[10]. In fact it is optimised to the Yb phase space density in a mixture with Rb atoms and has to work in a complex merging sequence which will be explained in the following chapter.

4.3. Optical lattice

The optical lattices in our experimental apparatus (chapter 3.5) are used as an atom elevator (chapter 3.9.2) and the final trap potential for molecule production (chapter 4.4.4).

This chapter explains how shaking and pulsing of an optical lattice can help with the calibration of its depth. Moreover the momentum distribution of a Rb BEC is revealed by adiabatic loading and sudden release from a 2D lattice.

[10]With parameters optimised for condensation, small BECs could be produced

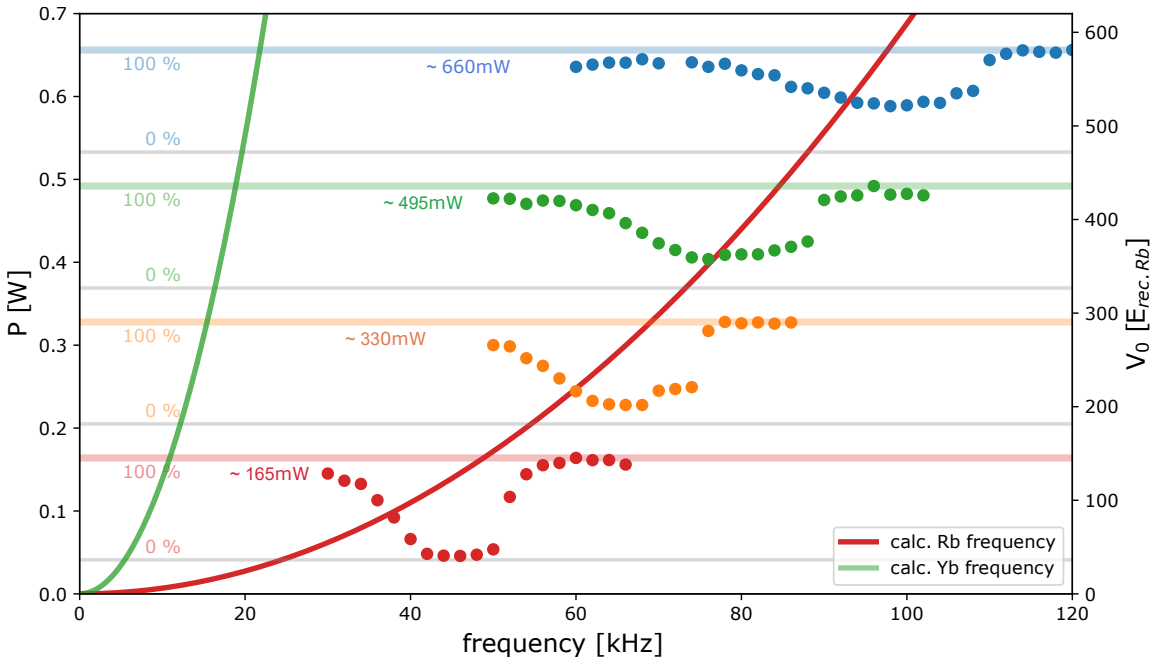

Figure 4.20.: Determination of the trapping frequency and depth of a 1D lattice by a modulation of the lattice depths with loaded Rb atoms at different beam powers (indicated with different colours). If the modulation frequency is close to the resonance frequency of the potential the trap is depleted, indicated by the signal drop from 100% close to 0%. The calculated trap frequency for Rb (and Yb) as the solid red line (green line) is in good agreement with the measured data.

4.3.1. Shaking and pulsing of a 1D lattice

For precise manipulation and control of atoms in optical lattices the potential depth $V_0[E_r]$ is the most crucial experimental parameter. It determines how strongly atoms are confined and how large tunneling rates are.

The first method used to find out more about the lattice depth is by 'shaking' it via amplitude modulation. Here we start by loading Rb atoms into a one dimensional standing light wave. Afterwards the trap light intensity is modulated with a frequency generator and the occurring atom loss is measured. If the trap is amplitude modulated close to twice the frequency of the trapping potential almost all atoms are heated out of the trap. The value of the trap frequency

$$\omega_{\mathrm{lat}} = 2\frac{\sqrt{V_0 E_r}}{\hbar} \tag{4.7}$$

can be related to the potential depth V_0 for a given beam power and waist. Figure 4.20 displays the experimental data for four different beam powers, which are in good agreement with the calculated trap frequency. While this method is easy to realise experimentally, it does not give very precise values for the lattice depth since the resonances are a couple of kHz wide. A more complex but also more precise technique consists of pulsing of the lattice beam.

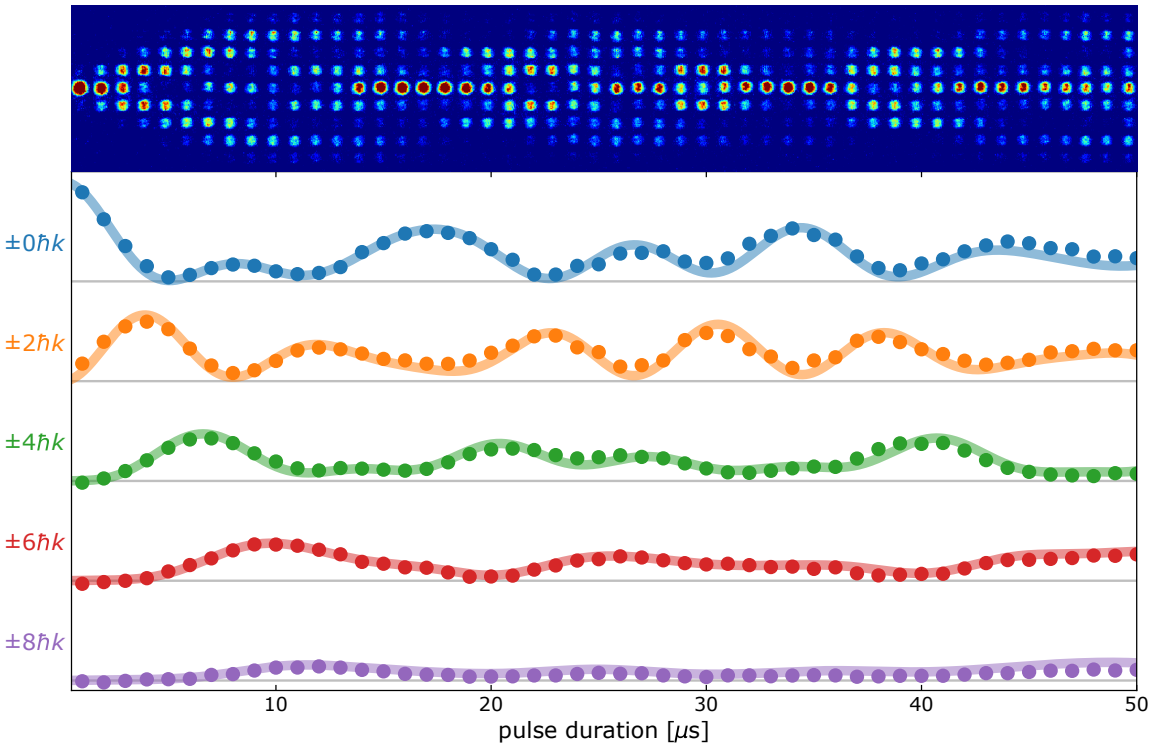

Figure 4.21.: Kapitza-Dirac scattering of a Rb BEC for different pulse length in a 1D optical lattice. On top the absorption pictures of the momentum distribution pattern evolve with increasing pulse duration. The data points for the population of each momentum package and solution of the numerical simulation of 4.8 with 77 E_r as solid lines is displayed below.

Kapitza-Dirac scattering

When slow particles interact with a standing light wave for a short amount of time, interference effects between the particles will occur. This effect is called Kapitza-Dirac scattering and describes the diffraction of electrons or atoms acting like matter-waves from the optical lattice working as a grating [238][239]. Slow particles and a short duration imply that ultracold atoms with negligible kinetic energy have little time for momentum transfer from photons of a pulsed optical lattice. During this short interaction a pattern in momentum space forms as atoms experience momentum transfers of $\pm 2n\hbar k$ from two-photon scattering events.

Figure 4.21 shows such a pattern with Rb atoms after different pulse lengths τ of a 1D lattice with unknown lattice depth. Previously a Rb BEC was prepared in and released from a XODT. After the atoms experience momentum transfer along the lattice axis by the pulsed lattice shortly after their release, they fall during a 30 ms TOF and are imaged as separate $\pm 2n\hbar k$ packages. The population of atoms P_n with different momenta $\pm\hbar k$ is recorded as a function of pulse duration. As depicted in figure 4.21 this data can be used to calibrate the lattice depth in E_r with the help of numerical solutions.

The solution for the evolution of the wavefunction of a BEC inside the standing wave

in this section follows [240]. The problem at hand can be described by the transformation of the time-dependent Schrödinger equation into a set of differential equations with amplitudes $c_n(t)$ for each diffraction order.

$$i\frac{\mathrm{d}c_n}{\mathrm{d}t} = \frac{\alpha n^2}{\tau}c_n + \frac{\beta}{4\tau}(c_{n-1} + 2c_n + c_{n+1}) \text{ with } \alpha = (\mathrm{E}_r^{(n)}/\hbar)\tau,\ \beta = (\mathrm{V}_{\mathrm{lat}}/\hbar)\tau \quad (4.8)$$

The atoms with the highest populated order $P_n = |c_n|^2$ already give a first estimate for the lattice depth. For this cut-off $n = \sqrt{\beta/\alpha} = \sqrt{s/4}$ the potential energy is completely converted into kinetic energy, giving $s = V_0/\mathrm{E}_r = 64$ as the minimum depth for a pattern with $n = 4$. The numerical integration of equation 4.8 gives a best fit for a lattice depth of $\sim 77\,\mathrm{E}_r$ and starts to diverge compared to the data-points for values $\pm 3\,\mathrm{E}_r$. This gives us relatively precise information of the depth of a single lattice beam and can be repeated for all three lattice axis. For a high fidelity calibration of the lattice depth a method with multiple pulses can achieve even more accurate measurements [241].

While this exemplary analysis was carried out with a deep lattice and long pulses of up to 50 µs, more shallow lattices can be evaluated in the Raman-Nath regime. This regime can be applied if the motion of atoms during the light pulse can be neglected and the interaction time is small compared to the harmonic oscillation period ($\tau\omega_{\mathrm{lat}} << 1$). In this case the αn^2 term can be neglected and equation 4.8 can be approximated to

$$c_n(t) = (-i)^n \mathrm{e}^{-i\beta t/2\tau} J_n(\beta t/2\tau) \quad (4.9)$$

with the Bessel function of the first kind J_n. It yields a simple expression for the population $P_n = J_n^2(\beta/2)$ [240].

4.3.2. Loading and release of a ^{87}Rb-BEC

Quite the contrary to the treatment with lattice pulsing is the adiabatic loading of a BEC in to an optical lattice. It is desirable to keep the many body ground state of a condensate which is prepared in the XODT. Any heating effects during transfer or inside the optical lattice would destroy the state and affect further experiments. Even for thermal atom clouds an adiabatic ramp into the lattice potential is important to prevent unnecessary loss of phase space density. For this to work the lattice potential has to be increased slowly with respect to the band structure of the lattice and many-body dynamics for enhanced confinement [166][242].

If changed to fast, higher energy bands will be populated and the adiabaticity depends on the level spacing. For the start of the ramp where $\mathrm{V}_0 \leqslant \mathrm{E}_r$ the condition from [243]

$$\frac{\mathrm{d}}{\mathrm{d}t}\frac{V_0}{E_r} << 32\sqrt{2}E_r/\hbar \sim 0.5 \cdot \mu s^{-1} \quad (4.10)$$

results in a recommended change below $0.5\,V_0/E_{\mathrm{rec}}$ per µs. After this initial phase a larger level spacing allows more aggressive and even linear ramps with a typical duration on the order of ms. Note that this criterion only considers the adiabacity of a single atom. Especially in the superfluid state, where atoms are not localised to a lattice site,

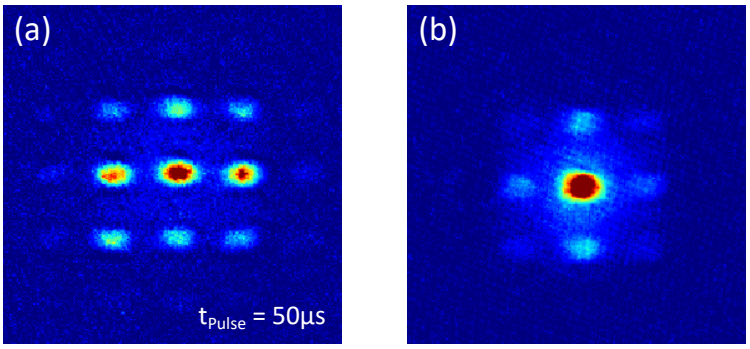

Figure 4.22.: Difference between (a) the pulsed two dimensional lattice ($t_{\mathrm{Pulse}} = 50\,\mu\mathrm{s}$) resulting in Kapitza-Dirac scattering and (b) the sudden release of a Rb BEC from a 2D lattice revealing an interference pattern.

this timescale is non-adiabatic with respect to atom-atom interactions. When it comes to many-body dynamic considerations about the non-adiabaticity time scales of many ms are required to be completely adiabatic [244]. The position of an atom offset to the trap center for example induces tunneling to balance out the chemical potential for increasing lattice depth. The time frame for this redistribution to achieve the correct Thomas-Fermi-shape in a changing potential limits the ramp speed.

Finally the quality of the ramp can be checked experimentally by abruptly releasing the atoms from the lattice trap. In figure 4.22 two different methods for the demonstration of a 2D lattice[1] are shown. In segment (a), the trap is simply pulsed for a short time and creates Kapitza-Dirac scattering in two dimensions. The other segment (b) however shows the momentum distribution of a Rb BEC released from the 2D lattice. The total wavefunction describing every atom in the BEC evolves during the trap release. It can be described by waves with equal phase from each lattice site, which interfere with each other during the time-of-flight and form an interference pattern. If the condensate would be loaded non-adiabatically the atoms would start to populate higher energy bands and eventually just expand as an ordinary thermal cloud if the BEC is dissolved. For this thermal distribution, wave-packets without phase relation are confined to individual lattice sites and thus do not interfere during expansion. This is already slightly visible as the circular thermal background on the right side of figure 4.22.

4.4. Mixture in a combined trap

Up until now the individual preparation of each atom species has been presented. We have cooled both Rb and Yb atom clouds to quantum degeneracy in the science chamber in their own experiment cycle. The next big challenge is to load both species in a combined trap to create an ultracold atom mixture. To this day mixtures of alkali and alkali-earth-like atoms have been studied in various two-species combinations [95], [97]–[99], [245]–[247]. Strategies like sympathetic cooling [248] and bichromatic optical dipole traps (BODT) [249] have been

[1] vertical: Lattice 1 horizontal: Lattice 3

used to achieve quantum degenerate mixtures in order to circumvent the issue of different temperatures in optical traps originating from different trap depths due to the unequal polarizabilities of different atomic species. For all dual species experiments the choice of the wavelength combination for BODTs is dictated by these polarizabilities, the availability of lasers and the optical access of the vacuum system. The RbYb mixtures created in this thesis are restricted to single wavelength traps, but an upgrade to a bichromatic trap is currently under way as will be discussed in chapter 7.2.

In our case the use of distinctive production chambers for either species is a great benefit. It allows us to run the sequence for Rb and Yb at the same time. However in order to get the correct timing of the final steps which create the mixture, the Yb sequence has to start several seconds earlier to load enough atoms. Figure 4.1 shows a timeline of simultaneous loading of both MOTs, the magnetic trap for Rb and the transport in optical tweezers. As the predecessor experiment of this apparatus has shown [14], the preparation in a single vacuum chamber is unpractical. For instance the loading of the intercombination line MOT would be impossible during the evaporation of the MT since we have to apply correction fields to balance the strong magnetic fields coming from the Rb production chamber although it is about one meter away. On the other hand the setup restricts us to the necessity of long range transport.

After transport into the science chamber, the tweezer beams for Rb and Yb are adjusted to have a small vertical offset to avoid a crossing. Attempts to evaporate a mixture in a crossed optical dipole trap at 1064 nm have been confirmed to be impractical. For Rb atoms the trap depth of such a trap is always about ten times deeper than for Yb. Experiments have shown that Yb atoms are completely removed from an evaporated XODT in the presence of hot Rb atoms since they cool much slower with decreasing potential depth. As a result we create two crossed optical dipole traps in different horizontal planes for independent evaporation. The following sections present the resulting detour to get both types of atoms mixed together. In order to get an overview of this relatively complex mixing sequence, a simplistic side-view illustration is shown in figure 4.23. The description in this chapter will follow it's segments a) through d) and eventually give results for the mixture in the combined final trap. For a more detailed look, the experimental steps with their most important parameters are again presented in figure 4.24.

4.4.1. Synchronized evaporation

Segment (a) starts with the synchronized evaporation of Rb and Yb. The evaporation in both crossed optical dipole traps is performed at the same time. Since the thermalisation of Yb is slower the evaporation takes 4.6 s to reach a power of 1 W in the tweezer beam, while the Rb evaporation finishes 0.9 s earlier at 1 W. This time is conveniently used to load and transport Rb atoms into the final trap in segments (b)-(d). The end of the evaporation of both species sets the starting conditions for the mixing sequence. Commonly used ramps result in the values presented in table 4.1. Other final powers combined with different durations can be used to tune the temperatures and atomnumber ratios of the final mixture.

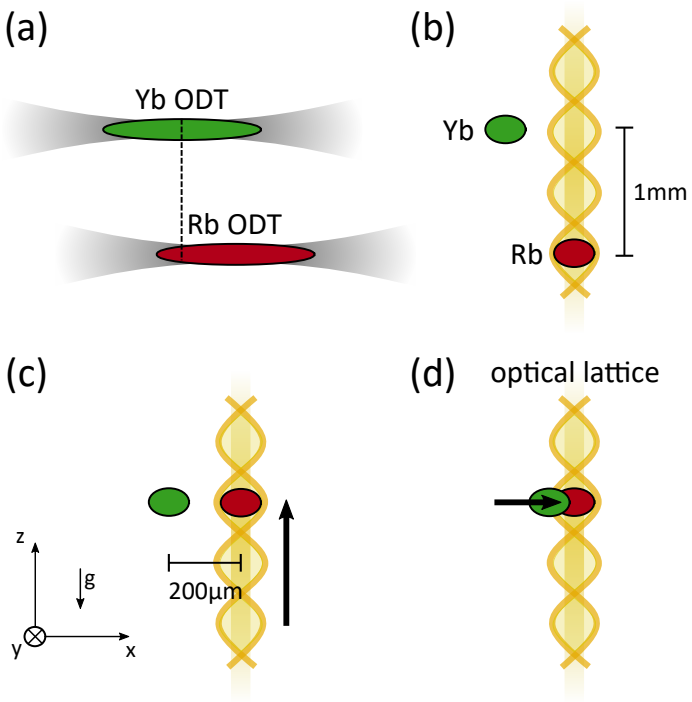

Figure 4.23.: Schematic representation of the sequence used to prepare a Rb-Yb mixture, where Rb is shown in red and Yb is indicated in green. The vertical (1D) optical lattice is depicted as a (yellow) standing light wave, while each tweezer beam at 1064 nm is indicated with a Gaussian beam profile. All sizes and distances are exaggerated. First the Rb and Yb tweezers arrive at different heights and horizontal positions in the science chamber indicated with the dashed line (a). Secondly both species have been evaporated in their respective XODTs and the optical lattice is ramped up (b). The XODT laser beams are not shown for better visibility. Next the Rb sample is transferred to and elevated in the optical lattice covering a vertical gap of 0.87 mm (c) and is merged/mixed together with the Yb sample by shifting the Yb XODT horizontally over a distance of 0.2 mm (d).

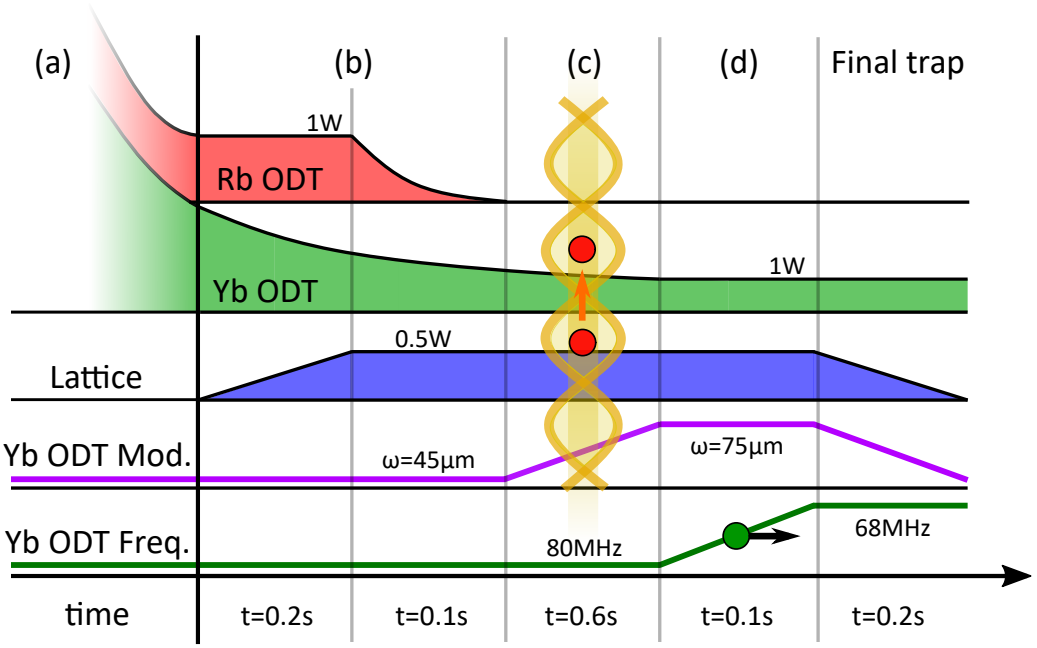

Figure 4.24.: Schematic diagram of the experimental steps in a sequence used to prepare a mixture of Rb and Yb. Steps (a) to (d) are identical with figure 4.23. Beam powers of Rb ODT, Yb ODT and lattice elevator beam are illustrated across steps (a) to (d). Additionally the modulation of the Yb ODT beam and the horizontal shift of Yb via the Yb Tweezer AOM frequency is shown. In the final trap both atomic clouds are overlapped and a thermal mixture is created.

Table 4.1.: Starting values before the mixing sequence.

	Rb	Yb
Power P in Tweezer/Crossing	1 W/0.4 W	1 W/0.7 W
Atomnumber N	$5.5 \cdot 10^5$	$5 \cdot 10^5$
Temperature T	0.35 µK	1 µK

4.4.2. Lattice elevator loading and transport

Segment (b) and (c) describe the loading and vertical transport of Rb atoms in a one dimensional optical lattice. This so called 'lattice elevator' can store and move atoms inside the antinodes of a standing wave as explained in chapter 3.9.2. It is important that the trap center for the Yb XODT is not too close to the optical lattice axis since Yb atoms would be heated and moved by the potential. In segment (a) of figure 4.23, a lateral displacement between both foci is indicated. This offset of ~ 200 µm becomes more obvious in segment (b), where the optical lattice does not intersect with the Yb cloud.

For transport the lattice beam - vertically aligned to the Rb cloud - is first ramped up to ~ 500 mW in 0.2 s. Afterwards the XODT for Rb is ramped down and eventually fully extinguished in 0.1 s. At this point the transfer is completed and the Rb sample is spread over multiple lattice sites. Assuming an initial Rb cloud size of $s_0 \approx 10$ µm from fits of TOF experiments we can expect to fill at least ten 1D lattice sites. It is then elevated over a distance of $z = 0.87$ mm in 0.4 s to arrive in the horizontal plane of the Yb XODT [1].

The motion profile has a constant acceleration of 20 mm/s^2, a maximum velocity of 20 mm/s as the stage controller does allow for a constant jerk trajectory. In contrast to the motion in a single beam ODT the movement profile does not lead to noticeable heating or atom loss due to the high vertical trap frequency and depth of the lattice wells. Towards the end of the transport the strong lattice potential protects Rb atoms from the Yb XODT trap potential when they arrive at the position of the Yb XODT. Even though much lower lattice powers would be sufficient to hold Rb atoms against gravity and transport them to the Yb-level, we want to prevent Rb atoms from traveling along the Yb XODT beam and subsequently ending up in the Yb crossing. However it is important to note that at high densities Rb suffers from substantial three-body losses during the elevation and wait time in segment (d). This effect is weakened by using higher temperatures (larger Rb ODT powers in (a)) and a slightly defocussed Rb tweezer during the transition into the lattice to fill more lattice sites. Nevertheless, in figure 4.25 we can see a heating effect depending on the power of the optical lattice beam. Eventually $5 \cdot 10^5$ atoms at 1.5 µK are transported at the end of segment (c). Figure 4.25 also shows how sensitive the final Rb atomnumber in the mixture is to the calibration of the travel distance.

[1] The positions in the LabView program are 61.30 mm to 62.17 mm

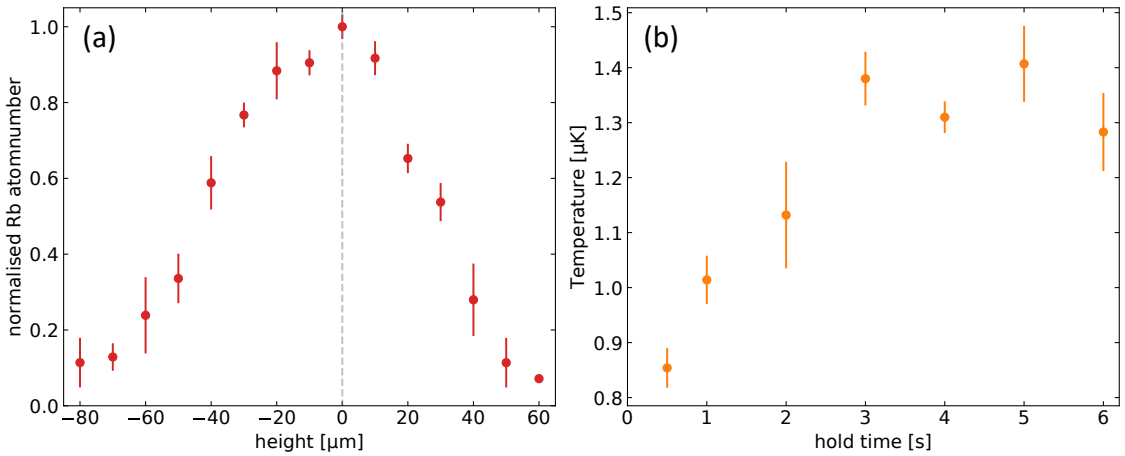

Figure 4.25.: (a) Sensitivity of the final number of Rb atoms in the mixture on the end position of the vertical movement in the lattice elevator. (b) Heating of Rb atoms in the one dimensional optical lattice which is used for vertical transport.

4.4.3. Merging sequence

During the penultimate step shown in segment (d) the Yb atoms get shifted $\sim 200\,\mu m$ horizontally towards Rb in the optical lattice by applying a frequency shift (80 MHz $\rightarrow$ 68 MHz) to the Yb Tweezer AOM. For this segment to work the timing and parameters of previous power ramps is crucial since they determine the temperature and atom number of Rb and Yb. The parameters resulting from this segment are the latest set of values used in the experiment for the detection of 1-photon and 2-photon PA-lines (see chapter 5 and chapter 6) and are sub-optimal in creating a mixture with equal number of atoms. It is however favourable to use unequal atom numbers for our photoassociation experiments close to the atomic threshold of an atomic $(^2S_{\frac{1}{2}}+^3P_1)$ asymptote. In this case a larger Yb atom number is required to still observe a photoassociation signal due to the off resonant scattering of PA photons with Yb atoms (see chapter 5).

In the next 0.1 s after segment (c), Yb follows the changing Yb tweezer potential as the laser beam is moving towards the Rb position along the crossing beam. Combining the traps should be realised adiabatically by matching their trap shapes and depths as depicted in figure 4.26. The values used in this simulation are chosen for illustration purposes and may deviate from the real experiment. Although being measured, the power, the position and especially the beam waists in the foci for all beams can differ for example due to sleight misalignment. Since even small deviations in beam waists for example change the evolution of the potential curves, this simulation has to be viewed with caution. To obtain a depth similar to the lattice potential the laser beams for the Yb trap are ramped down to 1 W and 0.7 W respectively. As an additional tool we can increase the Yb ODT size from 45 µm to 75 µm by modulating the associated AOM frequency in an effort to match it with the lattice trap shape. This is carried out during the vertical movement of Rb and adds an additional evaporation step for Yb atoms. As visualised in figure 4.26, horizontal

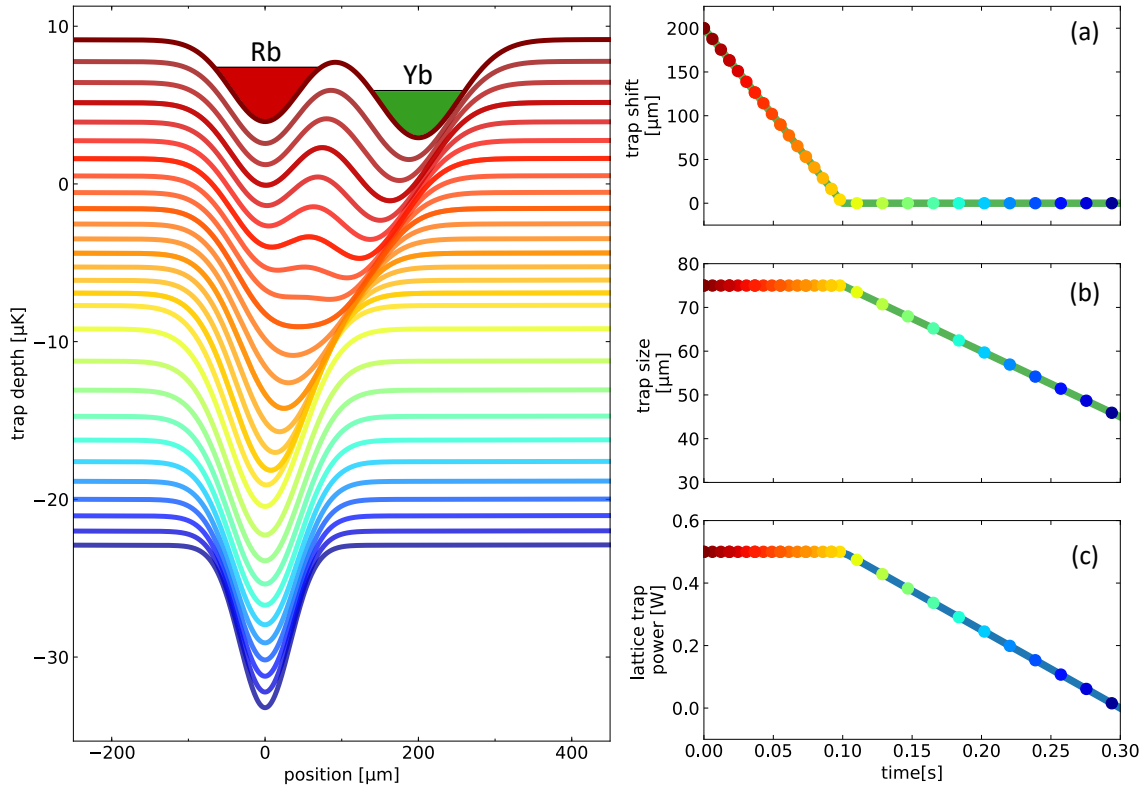

Figure 4.26.: Simulated trapping potential for Yb during the merging step (d) - is plotted along the axis of Yb XODT beam, depicted in the left image. Potentials at different times/positions are colour-coded and are vertically shifted for better visibility. For each curve the trap center is shifted by the trap shift (see segment (b)). The three subplots (colours are identical to potential curves) show the development of the Yb ODT (a) trap shift, (b) trap size and (c) the lattice laser power over 0.3 s. The first 0.1 s of horizontal shifting is followed by 0.2 s, in which the lattice potential and trap size of the ODT beam are reduced to form the final trap. This simulation is adapted from existing code [1] but describes a new sequence design.

translation of Yb is leading to a merge into a combined trap potential of a crossed ODT and an optical lattice. From here on, two possible final traps can be prepared to enable photoassociation experiments in a mixture.

The first one is already included in figure 4.26, in which the lattice power is reduced to zero in 0.2 s, while the final XODT beam powers remain at 1 W/0.7 W. At the same time the beam size of the Yb ODT is reduced to 45 µm to increase the density in the trap. The resulting potential is strong enough to mitigate gravitational sag of Yb, which would reduce the overlap with the Rb cloud. This simple XODT was used in the first photoassociation experiments of this thesis including the search for photoassociation lines [1], [20]. PA experiments in more complex final optical traps - optical lattices - build on the described sequence.

To load the atoms into an optical lattice the XODT beam power is reduced to zero in 0.2 s, while the remaining two beams needed for a three dimensional (3D) optical lattice are ramped up. In this trap the gravitational sag can be neglected due to the strong vertical confinement in standing wave. The 3D optical lattice is equipped with a power stabilisation for every lattice beam allowing for stable conditions for PA measurements in a 3D optical lattice (see section 5.5). A comparison of both traps is discussed in the following chapter.

4.4.4. Final combined trap

The final trap is the crucial starting point for all experiments performed with our machine. The density of atoms and the trapping potential is vital for the successful creation of molecules.

XODT

In this section the mixture in the first trap design, the crossed optical dipole trap, is discussed. As already mentioned the final trap depth in any monochromatic optical trap at 1064 nm is about ten times larger for Rb than for Yb. Together with the preceding three-body collisions in the 1D lattice potential it is generally hard to obtain cold Rb, meaning anything close to $\sim 0.4\,\mu K$, the temperature of Yb in segment (a) of figure 4.27. However, observing interactions between ^{170}Yb and ^{87}Rb isotopes is non trivial because of the small scattering length of $a_{\mathrm{RbYb}} = -11\,a_0$. The timescales for collisions and a measurable thermalisation is thus to be expected to take several seconds. Fortunately, this plays to our advantage because we are thus able to prepare a larger Rb atom number at higher temperature ($T_{\mathrm{Rb}} = 5.3\,\mu K$ in table 4.2) without immediately heating Yb out of the trapping potential.

Nevertheless, some measurements of the temperatures and lifetimes in the combined trap clearly indicate a RbYb mixture. The first signs of contact between 'cold' Yb and 'hot' Rb can be proven by temperature measurements with the time-of-flight method. After holding the final trap for 6 s, the temperature of Yb atoms in a mixture with Rb has increased compared to a measurement without Rb shown by segment (a) in figure 4.27. For a small amount of Rb atoms ($N_{\mathrm{Rb}} \sim \frac{1}{3} N_{\mathrm{Yb}}$) a lower temperature has been measured in a mixture

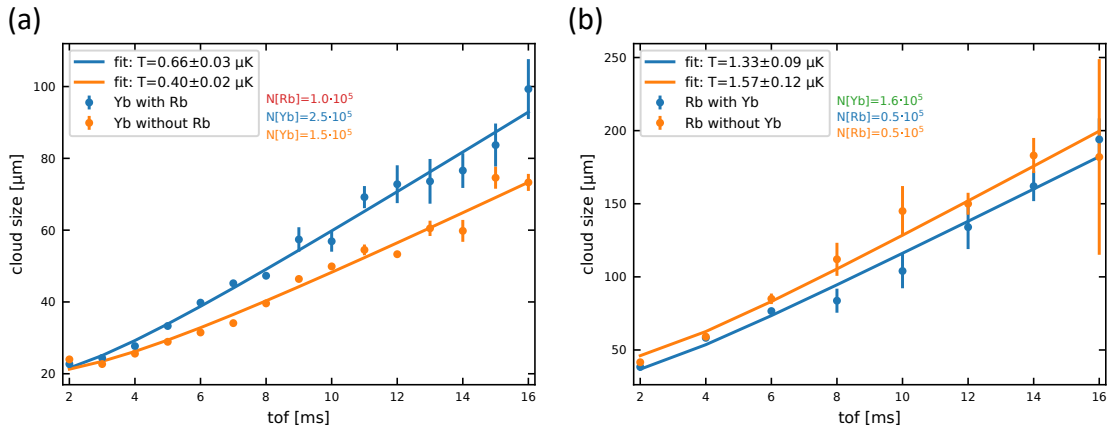

Figure 4.27.: Time-of-flight measurement of the temperature of (a) Rb and (b) Yb in the mixture. (a) It can be seen that Yb experiences heating in the presence of Rb with a temperature increasing from $0.40 \pm 0.02\,\mu\text{K}$ to $0.66 \pm 0.03\,\mu\text{K}$. (b) In contrast Rb is cooled down during the same time from $1.76 \pm 0.10\,\mu\text{K}$ to $1.22 \pm 0.09\,\mu\text{K}$ due to collisions with cold Yb atoms.

with Yb, compared to a measurement without Yb atoms after the same hold time shown by segment (b) in figure 4.27.

Another indicator for interactions of overlapping atom clouds are changing atom numbers and lifetimes due to collisions. If the trap depth becomes to shallow, Yb atoms receiving energy in a collision with Rb leave the trap and do not contribute to the thermalisation process. This effect can be observed as a loss of Yb atoms from the trap. Depending on the density of Rb and the quasi-adiabaticity of the merging process explained in 4.4.3, joining Rb and Yb in the trapping potential has a large effect on the initial Yb atom loss. The thermalisation process thus already starts $\approx 0.2\,\text{s}$ earlier than the measurements shown in figure 4.27 and 4.29. While this is not relevant for the temperature measurement (after 6 s), increasing the Rb density can reduce the Yb atom number until no Yb atoms remain in the mixture. If the density distributions of both species have less overlap this effects is weaker but is obviously an obstacle for observing photoassociation.

For measurements in the XODT, the differences in gravitational sag between both types of atoms can have significant influence on the overlap of the atomic clouds. On the left in figure 4.28 the normalized density distributions of Rb and Yb inside the XODT trap potential are plotted. For experiments in this final trap a difference in sag of 3.3 µm is calculated, negligible compared to the Rb cloud size of 53(6) µm (Yb cloud size of 13.4(3) µm), thus maintaining good overlap between both species. While this mismatch is still sufficiently small, the increasing sag of Yb in a more shallow trap does not only prevent sympathetic cooling but also reduces the photoassociation rate and the amount of molecules that can be created (see section 5.5). As a result, gravity limits the temperature for photoassociation experiments for this trap. Typically prepared atom numbers, temperatures, densities, PSDs and trap frequencies are summarized in table 4.2.

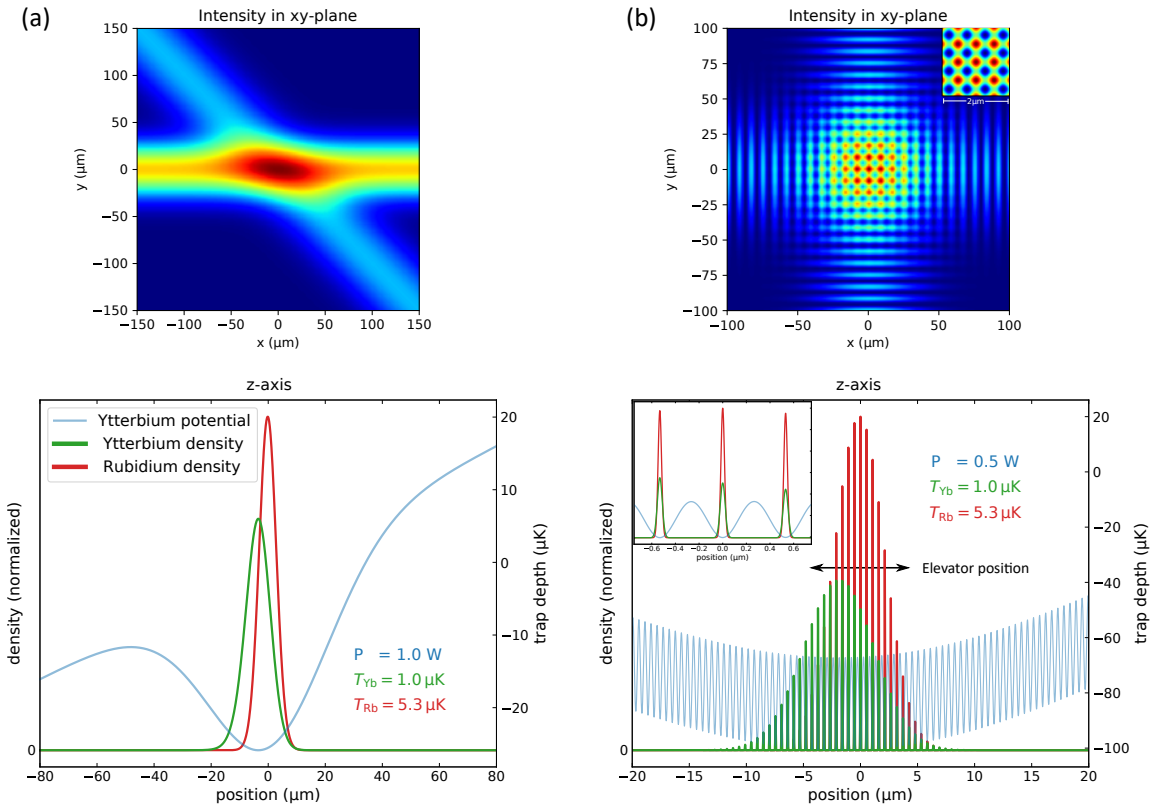

Figure 4.28.: Difference in gravitational sag between a XODT and a 3D lattice. Segment (a) shows the intensity of the presented XODT and the calculated density distributions for Rb and Yb for the given potential along the vertical axis that similarly appeared in [1]. The offset of 3.3 µm between the curves is the difference in gravitational sag. Segment (b) shows the same graphs for the 3D lattice trap design, in which the potential created by a standing light wave prevents gravitational sag and the offset of the Rb envelope can be compensated for by the final position of the vertical lattice elevator. The inset illustrates an improved overlap between the density distributions.

Table 4.2.: Typical values for the crossed optical dipole trap.

	Rb	Yb
Atomnumber N	$5 \cdot 10^5$	$9 \cdot 10^4$
Temperature T	5.3 µK	1 µK
Peak density n	$\approx 10^{13}\,\mathrm{cm}^{-3}$	$\approx 10^{12}\,\mathrm{cm}^{-3}$
PSD	$\approx 10^{-1}$	$\approx 10^{-2}$
calc. Trapfrequency ω	$2\pi \cdot [390\,\mathrm{Hz}, 930\,\mathrm{Hz}, 1000\,\mathrm{Hz}]$	$2\pi \cdot [90\,\mathrm{Hz}, 210\,\mathrm{Hz}, 225\,\mathrm{Hz}]$

3D Lattice

A 3D lattice is alternative final trap, whose application for photoassociation is presented in section 5.5. This trap design changes the behaviour of atoms due to the much more confining potential. For deep lattices, like the simulated one in segment (b) in figure 4.28, Rb atoms are restricted to single lattice sites as the tunneling matrix element becomes extremely small[2]. As already mentioned, the gravitational sag can be avoided by the potential of the vertical lattice beam. Therefore the quality of the density overlap can be adjusted as it depends on the positioning of Rb during the merge step (see figure 4.28).

We are able to load both atomic species into a 3D optical lattice and study their lifetimes. In figure 4.29 one can see that they appear to be shorter compared to the bulk trap lifetimes and need to be fitted with a two component exponential decay. The fast component can arguably be attributed to an incomplete thermalisation process after the lattice ramp, which influences the measurement. The impact on lifetimes within the 3D lattice compared between mixtures and single species populations have not been measured within the scope of this thesis. First photoassociation measurements in a 3D optical lattice are presented in chapter 5.

The expected benefit of PA experiments in the 3D lattice trap compared to the XODT are increasing PA rates because of higher peak densities[3] and trap frequencies. These and other typical trap values in the experiment are summarized in table 4.3. A disadvantage of the trap however are leftover atoms without a reaction partner in their potential well, which of course can not be exited into molecules. Another issue is the potential loss of the atoms due to collisions in deep lattices with many atoms in one lattice site. As a solution, the ideal filling of each lattice site should contain only one Rb and one Yb atom. For this reason we selected the isotopes ^{87}Rb and ^{170}Yb. A combination of these isotopes energetically favours a ^{87}Rb-^{170}Yb atom pairing instead of a ^{87}Rb-^{87}Rb or ^{170}Yb-^{170}Yb pairing occupying a lattice site, when in a mixed Mott insulator state, see section 2.7.2. In a superfluid state during the ramp up of an optical lattice, shallow lattice wells allow the redistribution of atoms with the increased tunneling term J. In the ideal case of an

[2] $10^{-12}\,\mathrm{E_{Rb,rec}}$ for Yb and $10^{-29}\,\mathrm{E_{Rb,rec}}$ for Rb

[3] The calculated peak density values were estimated based on a measured initial could diameter of $\sim 15\,\mu\mathrm{m}$ from tof measurements and an average number of atoms per lattice site.

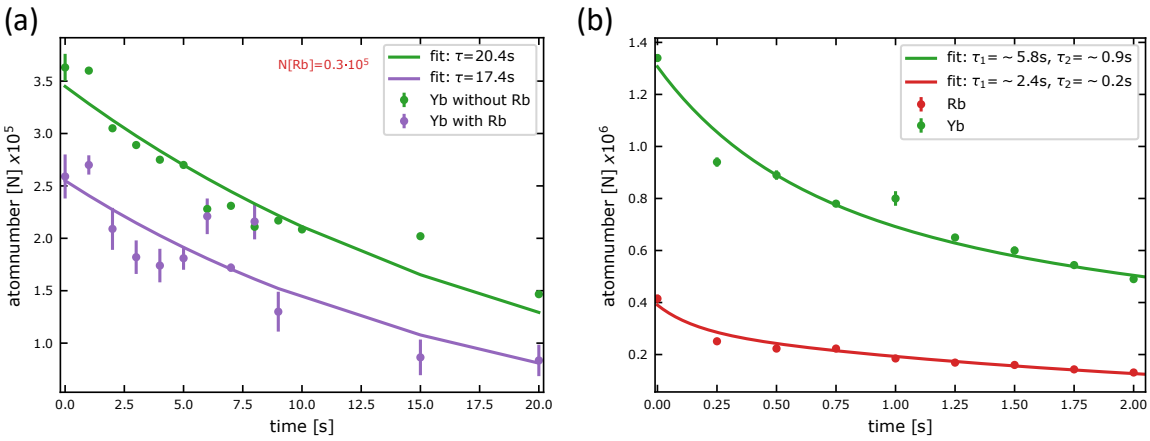

Figure 4.29.: Lifetimes of atoms in each final trap design. Segment (a) shows the lifetime of Yb and Rb in a mixture in the XODT. In segment (b) the shorter lifetimes of Rb and Yb in the 3D lattice trap are fit with a two-component decay.

adiabatically loaded lattice from a quantum degenerate mixture, the desired pairing is forced by the higher on site interaction energy U of different combinations like Rb-Rb or Yb-Yb pairs and will be realised via tunneling.

Another advantage of PA experiments in optical lattices is the discreteness of states within each lattice site. Instead of a thermal continuum inside a XODT, atoms can now be excited from well defined energies, which results in stronger and narrower PA lines [250]. This is especially useful for the association to bound molecular states with 2 photons with the STIRAP technique which is explained in chapter 7.3.2. In conclusion the 3D lattice trap is the ideal candidate for upcoming molecule experiments presented in the outlook (Chapter 7) of this thesis.

Table 4.3.: Typical values for the 3D optical lattice.

	Rb	Yb
Atomnumber N	$4.3 \cdot 10^5$	$1.6 \cdot 10^5$
Temperature T	$\sim 6\,\mu K$	$\sim 12\,\mu K$
Peak density n	$\approx 10^{16}\,cm^{-3}$	$\approx 10^{15}\,cm^{-3}$
calc. Trapfrequency ω	$2\pi \cdot [120\,kHz, 120\,kHz, 120\,kHz]$	$2\pi \cdot [26\,kHz, 26\,kHz, 26\,kHz]$

5.

1-Photon-Photoassociation

5.1. Introduction

The experiments with mixtures of Rb and Yb presented in this chapter are results from spectroscopy close to the $^1S_0 \rightarrow {}^3P_1$ intercombination line of Yb. In these measurements one photon with frequency ν_L and the collision of a Rb atom and a Yb atom is necessary to probe transitions to the excited molecular potential. Results from this and the successive chapter have been published in [20]. The process of interest can be described by

$$\mathrm{Rb} + \mathrm{Yb} + \nu_L \rightarrow [\mathrm{RbYb}]^* \tag{5.1}$$

For a resonant transition into the least bound states of a molecular potential, only a small detuning of a few GHz to the atomic line is needed. This directs our interest to the long range part of molecule potentials with large internuclear distances. Figure 5.1 shows ab initio calculations of the molecular potential curves of the relevant lowest electronic states that we want to explore [18]. Since the theoretical calculations for potential curves [16]–[18] concerning the $^3P_{0,1,2}$ states in Yb differ and lack the support of experimental data to become more accurate it is impossible to accurately predict energies for photoassociation resonances. This initiated the upcoming detailed search for resonances in the not well understood molecular Π-state manifold connecting to the atomic $^2S_{\frac{1}{2}}+{}^3P_1$ asymptote.

5.2. Photoassociation on the Yb intercombination line versus the D1 line of Rb

Previous work done with one photon PA of RbYb molecules was conducted on the $^2\Pi_{\frac{1}{2}}$ excited molecular state and in a preceding experimental machine [11], [14], [102]. This state corresponds to the atomic $^2P_{\frac{1}{2}} + {}^1S_0$ channel close to the Rb D1 line. Spectroscopy measurements for this potential have been carried out down to the $\Delta v' = 28$ vibrational level[1] at $E_\mathrm{b} = h \cdot 2.2\,\mathrm{THz}$ binding energy [14]. Here the dipole transition is mainly determined by Rb, which gives the molecular spectrum the characteristics of its hyperfine splitting. However with increasing binding energy of bound molecular levels the internuclear distance shrinks and the properties of their individual constituents changes as their

[1] $\Delta v'$ implies that the vibrational levels are counted starting from the least bound vibrational level.

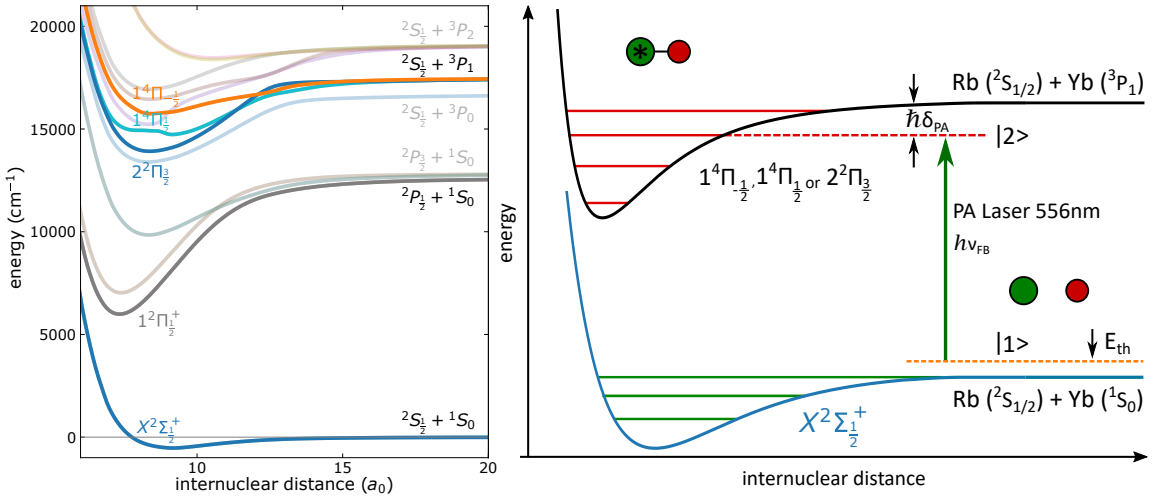

Figure 5.1.: The left graph shows the energy potential curves of a RbYb molecule taken from [18] previously also presented in [1]. The colored curves represent the relevant ground and exited state potentials for photoassociation close to the intercombination line of Yb. On the right sketch (not to scale) an arbitrary excited state is selected to visualise the investigation of weakly bound exited states with a red detuned PA laser.

electron clouds get distorted. This effect has been measured as a reduction of the hyperfine splitting, showcasing the transition to a stronger bound molecule [19].

The advantage of PA close to the strong Rb D1 line, compared to the weaker Yb intercombination line, are larger photoassociation rates, which makes the search for resonances and mapping of the potential curve easier. A drawback of these transitions are rather broad line widths and therefore imprecision in the exact determination of binding energies of molecular levels. Spectroscopy along the [Rb] $5s\,^2S_{\frac{1}{2}}$ + [Yb] $6s\,6p\,^3P_1$-asymptote corresponding to the atomic intercombination line of Yb allows higher resolution because it is about 30 times narrower. Moreover it enables measurements relatively close to the atomic threshold due to a lower scattering rate by off-resonant excitation of the atomic transition. When it comes to finding unknown resonances however this route suggests the necessity of a more detailed and extensive search for a molecular signal.

For this reason it is recommended to look at available information from theory and experiment on RbYb [16]–[18], [140] and the similar alkali–closed-shell dimer RbSr [251][22] before we start to scan for lines. Both molecules share some characteristics due to their similar electronic structure. Experimental results with photoassociation of RbSr at the intercombination line [252][26][95] confirm our suspicion of weak and narrow lines. Furthermore, theoretical considerations of the transition dipole moments (TDM) predict small transition strengths for our undertaking. Molecular states close to the spin-forbidden atomic transition at the $^3P_1$ asymptote are predicted to be hard to observe [18][22]. This means a small step size and good signal to noise ratio is essential if one wants to detect a loss-signal in the atom number as a sign for the excitation into a molecular state. As a consequence the 1-photon spectroscopy measurements demand a high shot to shot stability

of the photoassociation laser and high consistency of the preparation of diatomic mixtures.

A prediction from theory, on where to start to look for a molecule signal would be ideal. Unfortunately the complexity of alkali–closed-shell combinations in molecules is not helpful in this regard. This is already obvious from the theoretical predictions discussed in chapter 2.3.2, where substantial differences for the dissociation energy and the equilibrium internuclear distance of the ground state occur. Nevertheless there are valuable contributions from theorists that predict excited potential energy curves without experimental data [18], [140]. The excited molecular states connecting to the asymptote are ${}^{(2S+1)}\Lambda_\Omega = 1^4\Pi_{\frac{1}{2}}$, $1^4\Pi_{-\frac{1}{2}}$, $2^2\Pi_{\frac{3}{2}}$ in the short range (Hund's terms) and $(n)\Omega = (5)\frac{1}{2}$, $(1)-\frac{1}{2}$, $(2)\frac{3}{2}$ in the long range potential [18]. The set of short-range states have doublet ($^2\Pi$) or quartet ($^4\Pi$) form and split into multiple states if spin-orbit coupling is included. In our attempt to look for the least bound states in such potentials, the long range parts are of particular interest. In this case the C_6 long range interaction coefficient is needed to describe the potential curve for low binding energies[2]. Porsev et al. calculated a C_6 value for each $|\Omega|$ quantum number for the ${}^2\mathrm{S}_{\frac{1}{2}}+{}^3\mathrm{P}_1$ asymptote [140], which are given in table 5.1 together with values for the ground state and the other excited ${}^2\mathrm{P}_{\frac{1}{2}}+{}^1\mathrm{S}_0$ state.

	Rb + Yb	$\|\Omega\|$	Experiment	Theory [140]
ground state	${}^2\mathrm{S}_{\frac{1}{2}}$ + ${}^1\mathrm{S}_0$	1/2	2837(13) [15]	2837(57)
Rb asymptote	${}^2\mathrm{P}_{\frac{1}{2}}$ + ${}^1\mathrm{S}_0$	1/2	5684(94) [11]	7607(114)
Yb asymptote	${}^2\mathrm{S}_{\frac{1}{2}}$ + ${}^3\mathrm{P}_1$	1/2	?	3955(160)
		3/2	?	4460(180)

Table 5.1.: C_6 coefficients for potential curves of molecular states of the RbYb molecule.

The available experimental values for C_6 coefficients (see table 5.1) come from an improved Leroy Bernstein fit [142] to experimental data taken by our group by photoassociation near the D1-line of Rb. While the values are in very good agreement for the ground state, there is a 33% mismatch for the ${}^2\mathrm{P}_{\frac{1}{2}}+{}^1\mathrm{S}_0$ state. Porsev et al. states that this may result from a neglected C_8 term, indicating that this mismatch is a model dependent issue that can change the value and uncertainty of the C_6 coefficient [140]. A third way of achieving C_6 values would be to fit a C_6/r^6 power law to the tail of the potential curves offered by ab initio multi-reference perturbation theory calculations [18]. But since these potential curves are not reliable enough for the long range case $< 30\,a_0$ this method does not yield valuable C_6 and C_8 coefficients.

Finally the C_6 coefficient gives us an impression of the density of states but not their accurate energy. In his work Franzen predicted five to six transitions within $h\cdot 10\,\mathrm{GHz}$ from dissociation threshold [1]. For more detail, theory would have to predict not only the total number of states in an ab initio potential but also the distance of the last bound state from the dissociation threshold with high accuracy. This energy gap is called the fractional part

[2]Typically C_8 coefficients are also included in high precision calculations of long range potentials.

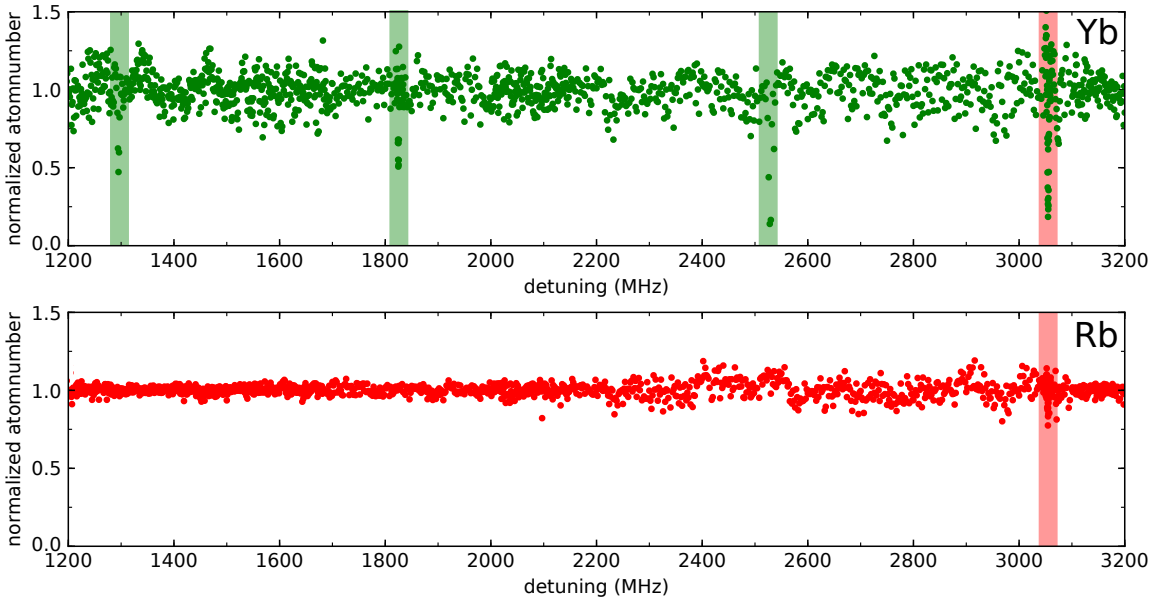

Figure 5.2.: Normalized ^{170}Yb and ^{87}Rb atomnumber for PA detunings of 1.2 GHz to 3.2 GHz. The vertical green lines show Yb_2 transitions, while the red line highlights the only observed pair of RbYb* molecule lines.

of level index ν_D (see section 2.3.3), which is unknown and impossible to predict without experimental data. Fortunately once the first energy levels are measured, a provisional value for ν_D can be derived from the Leroy Bernstein formula [142]. With more than one found transition the search for the next bound state is then limited to a smaller energy region. This will accelerate the search for the next PA lines, until the molecule potential curve can not only be described by its long range part and thus deviates from the Leroy Bernstein model (see section 2.3.3).

5.3. Search for excited Molecules at the $^2S_{\frac{1}{2}}+^3P_1$ asymptote

The light used to couple the scattering state and a vibrational level in the excited molecular potential is generated with the laser system presented in chapter 3.8. But before the search for the signal of excited RbYb molecules begins, some calibrations have to be completed. First the laser (PA) beam needs to be adjusted to hit both atomic clouds. This is realized by shining in nanowatts of light resonant with the atomic line[1] of Yb. The amount of Yb loss affirms the correct beam adjustment for Yb but not necessarily for Rb. The final trap thus needs to be prepared with little difference in gravitational sag to secure overlap of both species. Thermalisation measurements in this context are definitely helpful to confirm interactions of Rb and Yb atoms but can still be misleading in case of partial could overlap. Moreover trap configurations are difficult to compare due to very low thermalisation rates.

In the span of this thesis and the thesis of T. Franzen [20] a frequency range of 0.1 GHz to

[1] or later with Yb_2 transitions

11 GHz except the detuning between 3.2 GHz and 3.7 GHz was scanned within the XODT. The beam intensity and time of illumination (PA time) depended on the scattering rate from the nearby atomic resonance and limited the measurements to a minimal detuning of ~ 100 MHz from the atomic resonance before the confidence in resolving a molecular signal amongst a quickly decaying atom number became to small. Because of this relation the intensity and PA time was adapted throughout the entire search. Typical intensities ranged from $1-3$ mW and the PA time was increased from 0.5 s at $100\,\text{MHz}-400\,\text{MHz}$ to 2 s for larger detunings. In an effort to cover all frequencies in a reasonable timescale, the light was typically[2] swept across 1 MHz during the PA time per cycle. Figure 5.2 shows the accumulated data for the search range from 1.2 GHz to 3.2 GHz. Each data point for the normalised atomnumber of Rb and Yb is a measurement at different PA detuning. It is important to mention that the Rb atomnumber was typically five times the Yb number, which increases the availability of reaction partners for Yb and makes a detection in the Yb signal more likely. In general the observable signal loss in such data has three possible reasons. The first and most common explanation is a technical issue in the experimental machine after which data is discarded and remeasured. The second is a homonuclear photoassociation transition and the third is the RbYb* excitation that we are looking for.

Let us start with the second case. During the hunt for a molecular line in RbYb several Yb_2 and no Rb_2 transitions have been measured. These lines are thoroughly analysed in [1] and are thus only presented here as table 5.2 for completeness. Even if these lines are not our primary goal, they give us great insight in the sensitivity of our experiment. We find that the available sensitivity to detect any molecule line is limited by the shot to shot stability of the atom numbers in our mixture. Any fluctuation in the experimental cycle is effectively a barrier for the detection of very weak lines with our search method. With it we should be able to observe transitions with PA rate constants of up to $K_{\text{PA}} \gtrsim 2\cdot 10^{-14}\,\text{cm}^3/\text{s}$ [20]. Of course there are several ways to increase this sensitivity. For example one can use smaller steps in frequency or average over multiple measurements. However the preparation of ultracold mixtures in 3D optical lattices appears to be the more attractive option to increase the PA rate constant and will be discussed in chapter 5.5.

[2] For large detunings > 3 GHz the PA time was increased in exchange for a larger sweep range eg. 4 MHz to save time.

Δ_ν	detuning [MHz]	Takahashi [253], [254]	Theory [254]
-9	-34(2)	-	-31.0
-10	-60(2)	-	-57.3
-11	-103(2)	-	-99.9
-12	-169(2)	-	-166.1
-13	-269(2)	-268(3)	-265.4
-14	-416(2)	-413(3)	-410.4
-15	-620(2)	-619(3)	-616.6
-16	-908(2)	-906(3)	-903.9
-17	-1297(2)	-	-1296.9
-18	-1827(2)	-	-1826.5
-19	-2531(2)	-	-2525
-20	-	-	-3428
-21	-4662(2)	-	-4616
-22	-6215(2)	-	-
-23	-8202(2)	-	-
-24	-10720(2)	-	-

Table 5.2.: Yb_2 (YbYb*) lines found during the search for RbYb* signals. The label Δ_ν numerates the bound levels starting from dissociation threshold. The detuning in our experiment is compared to the values published by the Takahashi group and theoretical predictions.

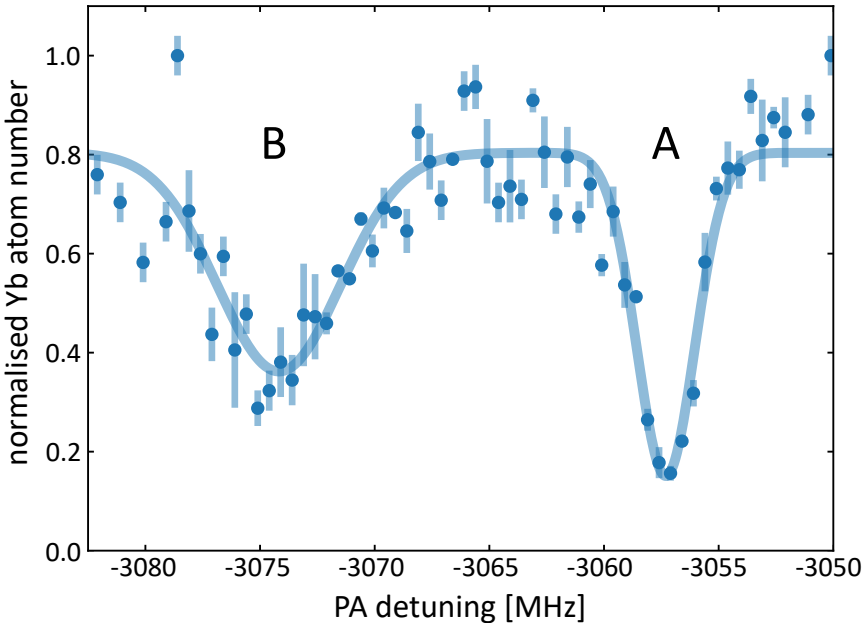

Figure 5.3.: Signal loss observed in the normalised Yb atomnumber as a function of the PA laser detuning in MHz. Two free-bound photoassociation lines (A) and (B) are fit with Gaussian curves to guide the eye.

5.4. A single pair of photoassociation lines

At last one molecular signal was found around 3.06 GHz. Figure 5.3 shows the observed loss feature in Yb, which vanishes in the absence of Rb. The depicted signal is a pair of lines that correspond to two related electronically excited molecular states that are close to each other with a distance of about 17 MHz. This discovery was an eagerly anticipated milestone in the development of this experiment. In the following subchapters, a detailed investigation of the characteristics of the observed line pair, recorded in the crossed optical dipole trap, is launched.

5.4.1. Zeeman shift

Before we start with the study of the Zeeman effect on our PA lines, a magnetic field calibration is performed. For this, the PA fiber laser was locked to an arbitrary offset frequency[1] because it cannot be locked to the atomic resonance without additional AOMs. Then the PA diode laser system was beatnote locked to the fiber laser, adjusted to the atomic resonance and used to observe the Zeeman splitting in atomic Yb. For different coil currents installed around the science chamber the well known atomic shift of 2.1 MHz/G can help to determine the magnetic field inside the chamber[2]. Additionally a technical offset of 2.1 MHz (resulting from our initial guess of the Yb MOT laser frequency) of the unshifted $m_j = 0$ component visible in figure 5.4 was detected and used to calibrate the

[1] 4 GHz in this case.
[2] The magnetic field was also measured with microwave transitions in Rb to verify this result.

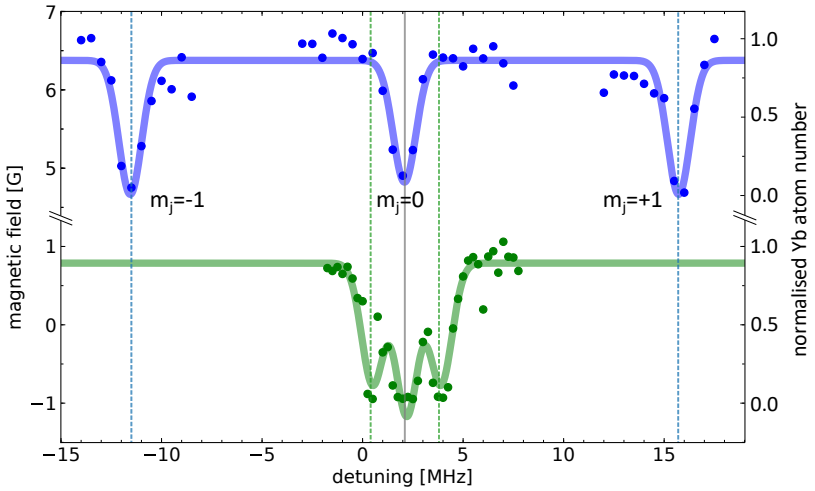

Figure 5.4.: Atomic line reference and Zeeman splitting of the m_j components of the $^3P_1$ state of atomic Yb at magnetic fields of 0.8 G (green) and 6.5 G (blue). These measurements show Yb atom loss for different detunings of the PA laser to the atomic line and are used for the calibration of the magnetic field and PA detuning.

PA detuning from atomic resonance.

Similar to the Zeeman shift on atomic lines, the observed molecular lines shift when a magnetic field is applied. The polarisation of light is undefined in this measurement meaning that all three π, σ_+ and σ_- components could contribute. In the left of figure 5.5 the spectrum was recorded with several field strengths and fit with a double Gaussian curve. The centers for both peaks labeled A and B are connected with a linear fit leading to an observed a shift of $-0.11(3)$ MHz/G for peak A and $-0.42(3)$ MHz/G for peak B. Both shifts are quite small and need some interpretation. At first the Zeeman shift of the atomic ground states needs to be accounted for. Yb atoms are prepared in the non magnetic ground state which obviously does not contribute any shift. Rb atoms on the other hand are prepared in the $|F = 1 > |m_F = -1 >$ state, which is shifting with 0.7 MHz/G [126]. If one adds this value, peak A indicates a Zeeman shift of the excited molecular state at 0.59(3) MHz/G and peak B a shift of 0.28(3) MHz/G. This is also illustrated on the right side of figure 5.5.

With the fit of the Zeeman shift and the calibration of our PA frequency, the location of the resonances at zero fields can be calculated. The energy levels of the exited molecule potential without Zeeman shift, are at $-3057.5(3)$ MHz (A) and $-3074.3(3)$ MHz (B). Both peaks remain split but are close to each other with a distance of about 17 MHz.

Another observed effect of larger magnetic fields is the line broadening visible in figure 5.5. Both peaks appear to have quite similar broadening with 0.4(2) MHz/G (A) and 0.5(2) MHz/G (B). These values have to be treated carefully as the fits give a relatively large error and for a field of 29.1 G peak B could not be detected. For low field (0.81 G) peak A is stronger and more narrow than peak B with a FWHM of 3.0(3) MHz compared to 6.3(7) MHz.

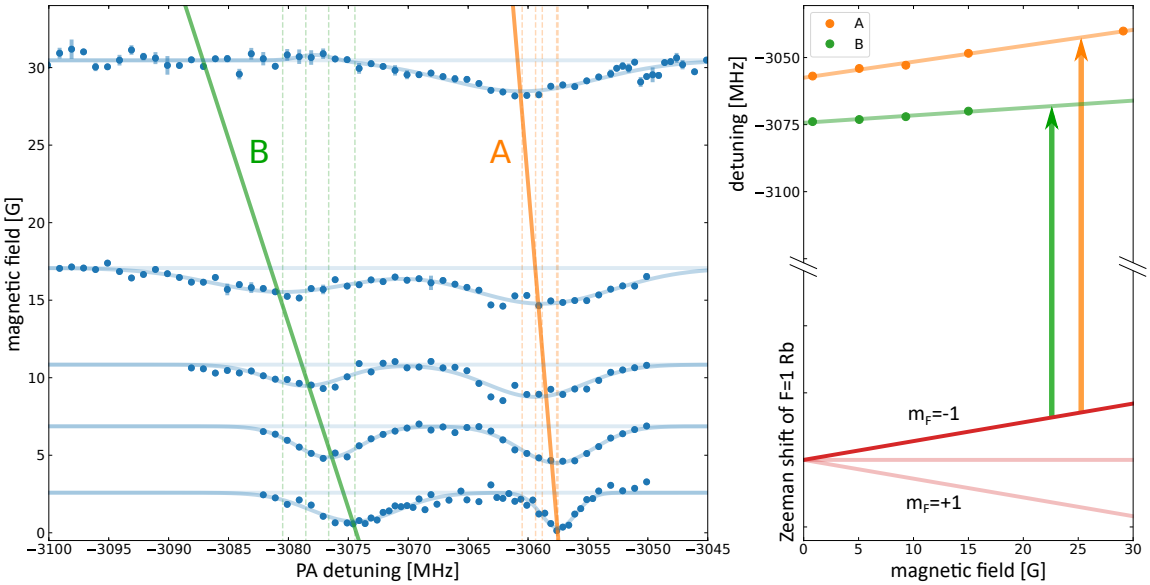

Figure 5.5.: Zeeman shift of the observed excited molecular states of RbYb. On the left the spectrum was recorded with several field strengths and fit with a double Gaussian curve. The centers for both peaks labeled A and B are connected with a linear fit leading to a shift of 0.59(3) MHz/G for peak A and 0.28(3) MHz/G for peak B, when the atomic shift of $|F = 1, m_F = -1\rangle$ Rb, displayed on the right side, is accounted.

5.4.2. Light shift

The influence of the trap light and photoassociation light shifts the position of the photoassociation line via the AC stark effect. In figure 5.6 the center frequency of peak A is analysed for different trap powers in the crossed optical dipole trap. We find that the trap laser intensity has a small but measurable influence of $-0.14(1)$ MHz/W on the excitation energy of the transition. The width of the line is at least an order of magnitude larger than this shift, which produces large uncertainties in the center position of our fit. Since the calibration of the PA detuning was done in the same trap the shift due to the different polaizabilities of the Yb ground ($^1S_0$) and excited ($^3P_1$) state is already accounted for. Nevertheless it is important to gather knowledge about the strength of this shift for other trap powers or experiments in the optical lattice.

It is important to note, that a sample prepared in larger trap power in this setup is at higher temperature. Therefore a thermal shift for each power had to be included in the calculation for the light shift.

5.4.3. Thermal shift

For the calculation of the thermal shift, the temperatures of each atomic species is determined with time-of-flight (TOF) measurements. The thermal energy in a quantum gas mixture shifts the scattering state and can be calculated with

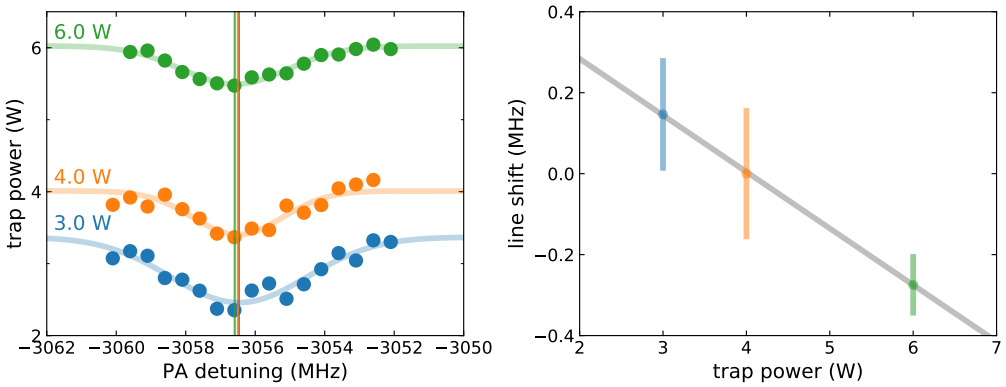

Figure 5.6.: The light shift for different trap powers of the XODT is determined with a gaussian fit. The center position is marked with vertical lines and plotted as a line shift against the trap power with a linear fit on the right graph. Note that the values have been compensated for the thermal shift.

$$E_{\text{thermal}} = \frac{3}{2}\mu k_B \left(\frac{T_{\text{Rb}}}{m_{\text{Rb}}} + \frac{T_{\text{Yb}}}{m_{\text{Yb}}} \right) \tag{5.2}$$

Since typical temperatures in the crossed optical trap are $T_{\text{Rb}} = 5\,\mu\text{K}$ and $T_{\text{Yb}} = 1\,\mu\text{K}$, the shift calculated with equation 5.2 can be estimated to be around $E_{\text{th}} = h \cdot 0.1\,\text{MHz}$. This is the mean shift for a Maxwell-Boltzmann distributed energy. The thermal spread of the collision energy of reaction partners changes the frequency needed for association effectively broadening the scattering state. In theory the reduction of the sample temperature should thus narrow the linewidth, due to the reduced collisional energy and corresponding light shift. This effect however has not yet been properly observed experimentally because it is much smaller than the observed linewidths of the detected line pair, which in the order of MHz. Another reason for this is the high temperature of Rb and large off-resonant scattering rate of Yb. Although some improvements in temperature and density have been made since the presented work in [1] to enhance the PA rates discussed in section 5.4.5, a preparation of Rb at lower temperature at a balanced trap depth would be of great advantage. For a more detailed discussion see chapter 7.

5.4.4. Attempts at interpretation and line assignment

In the following we will try to interpret the the nature of the observed excited molecular states of RbYb. Their energy levels (accounting for the shifts analysed in subsection 5.4.1 for the Zeeman shift, in 5.4.2 for the light shift and in 5.4.3 for the thermal shift) are at $-3057.2(3)\,\text{MHz}$ (A) and $-3074.3(3)\,\text{MHz}$ (B). The remaining task is to explain the observed Zeeman shifts and the zero field line splitting of 17 MHz of the doublet in figure 5.3 with a theoretical picture.

The binding energy associated with the discovered transitions is very small ($E_{\text{b}} = 0.1\,\text{cm}^{-1}$), resulting in the formation of a large and weakly bound molecule. The wave function of the discovered molecular state stretches to large internuclear distances and has

the classical outer turning point at $\approx 45\,a_0$, according to a toy model solver presented in chapter 5.4.6. Thus, it seems reasonable to initially treat the molecular state like an atomic state, especially for the Rb atom as the transition dipole moment is mainly determined by the atomic Yb transition.

After excitation, the molecule is close to the atomic $^3P_1$ level of Yb, which shifts with $m_j \cdot 2.1\,\mathrm{MHz/G}$ in an external magnetic field (see figure 5.4). Since there is no experimental selection (e.g. by polarisation of the light field) of a single excited m_j state of Yb we would expect a Zeeman splitting into three lines corresponding to excited $m_j = 0, \pm 1$ with increasing external magnetic field. The inability to resolve a state due to line broadening could be a possibility for a missing line in our spectrum. However, in addition to that the observed shifts in figure 5.5 are too small compared to the atomic 2.1 MHz/G shift and are thus unlikely to originate from the atomic Yb structure. Furthermore any combination of the atomic Yb shift and the atomic Rb shift of 0.7 MHz/G cannot explain the shift of peak B. As a consequence we have to leave the atomic picture and instead account for the interactions between the weakly bound atoms. Different ideas trying to explain the limited available data will be discussed in the following segments.

Selecting Hund's cases

The different coupling regimes, where certain angular momenta predominate over all other terms, are expressed in Hund's cases (see chapter 2.3.1). Their application to our problem has already been attempted by T. Franzen [1]. Nevertheless finding a case to go by is vital to proceed with the interpretation of spectroscopic data and is thus repeated and extended here. Since both atoms contribute angular momentum the choice of a single Hund's case is not easy and might lead to an intermediate state. In order to select a Hund's case, which offers the best description of the molecule, the dominant energy term in the coupling between atoms has to be found. There is electrostatic coupling E, spin-orbit (SO) coupling A and rotational coupling B.

The spin-orbit (SO) coupling describes the coupling between the atomic electron orbital angular momentum $\hat{l}$ and spin $\hat{s}$. It splits the atomic Yb ^3P_j manifold into its three fine-structure components and is also the reason for the energy difference of the molecular potential energy curves corresponding to different $j_{\mathrm{Yb}} = 0, 1, 2$. For the Rb(^{2}S) + Yb(^{3}P) system $\hat{l}_{\mathrm{Yb}}$ couples to spin $\hat{s}_{\mathrm{Yb}}$ and in a second term $\hat{l}_{\mathrm{Yb}}$ couples to spin $\hat{s}_{\mathrm{Rb}}$ for short internuclear distances. For our molecule, spin-orbit coupling dominates the other terms with the spin-orbit coupling constants (SOCCs giving the energy difference between fine structure levels) $a_{\mathrm{Yb}} = 807\,\mathrm{cm}^{-1}$ and $a_{\mathrm{Rb}} = 524\,\mathrm{cm}^{-1}$ [105]. Therefore we end up in either Hund's case (c) or (e), because these cases describe situations where the spin orbit coupling is larger than the coupling to the internuclear axis. Previous PA experiments at the D1 line of Rb were fortunate in this regard since only Rb contributed to the angular momentum and the observed line splitting in the spectrum could simply be explained with Hund's case (e) [11]. In our case the selection is slightly more difficult due to less data and the fact that Yb as well as Rb contributes angular momentum.

In order to decide between case (c) and (e) the rotational and electrostatic coupling

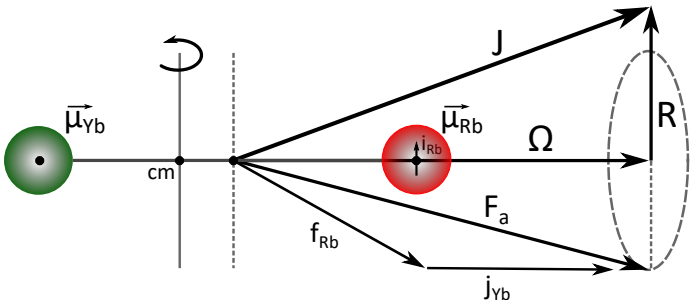

Figure 5.7.: Modified Hund's case (c) angular momentum coupling for RbYb*.

strengths have to be compared. The electrostatic coupling E is the interaction of the orbital motion of electrons with the electrostatic field of the nuclei giving rise to a coupling to the internuclear axis. If the electrostatic coupling dominates over the rotational energy, Hund's case (c) is suggested and vice-versa case (e) is the better representation for the opposite case where the rotational energy dominates over the electrostatic coupling. This comparison however is non trivial and in the worst case of equal energies suggests a transition between both cases. For the rotational coupling we estimate $B \approx 5 \cdot 10^{-4}\,\mathrm{cm}^{-1}$ using formula 2.23, with the classical outer turning point of approximately $45\,a_0$. Acquiring an estimate for the electrostatic interaction energy is much more complicated. In [255] it is suggested to compare the energy difference between the closest potential curve with different Λ. For us this would be a Σ potential (either $1^4\Sigma_{3/2}$, $1^4\Sigma_{1/2}$ or $3^2\Sigma_{1/2}$) coming from the $^3P_2$ atomic asymptote calculated in [18]. In order to estimate the energy difference originating from the electrostatic interaction spin-orbit-free potential curves (without spin-orbit coupling) have to be used for both potentials [105]. In this case both curves have identical energy for a large separation of the nuclei. The approach here is to make an approximation by taking the expectation value at the outer turning point of each potential curve with the same multiplicity and subtract both values. The difference between the two potential curves at this internuclear distance can be estimated to $|E| \approx 0.02\,\mathrm{cm}^{-1}$ yielding also an estimate for the electrostatic coupling [1]. However it should be noted that the relevant spin-orbit coupling between the states may be far more complicated, since the coupling itself is not perturbative across the whole state especially for the short range part. The ratio of rotational to electrostatic energy needed to be allowed to approximate the situation with a single Hund's case coupling mechanism is unclear. Anyhow the estimates suggest then we are on the case (c) side on the crossover to case (e), (described in the appendix A.1). While this result leans towards the type (c) coupling, which is described in the following subsection, this approach could still be incorrect and in theory requires a full quantum chemistry calculation.

Applying Hund's case (c)

Since the estimated coupling strengths suggest Hund's case (c), let us start an attempt to explain the Zeeman shift and doublet structure of our lines with a modified version of its coupling method (see fig. 5.7). The application of our molecule to Hund's case (c)

slightly differs from the simple theoretical picture given in section 2.3.1. Therefore I will first explain the coupling, leading to the modified scheme in figure 5.7. The general rule here is to consider the mentioned couplings in an order of decreasing strength.

Starting with the dominating spin-orbit coupling, the orbital angular momentum and spin of each atom will couple to form j_{Rb} and j_{Yb}. In the case of ^{170}Yb we do not have to be concerned with hyperfine coupling because it has no nuclear spin. ^{87}Rb however has a nuclear spin of $i_{\mathrm{Rb}} = \frac{3}{2}$, which we now need to deal with. Our excited molecule is bound with $\approx 3\,\mathrm{GHz} = 0.1\,\mathrm{cm}^{-1}$, which is already smaller than the Rb hyperfine splitting of $6.8\,\mathrm{GHz} \approx 0.2\,\mathrm{cm}^{-1}$. The electrostatic energy or effective anisotropy with $|E| \approx 0.02\,\mathrm{cm}^{-1}$ is presumably about an order of magnitude smaller [1]. While this is not a lot, and could potentially lead to a complicated intermediate coupling, we couple the nuclear spin i_{Rb} to j_{Rb} leading to a treatment of f_{Rb} rather than j_{Rb}.

So far we replaced L and S from section 2.3.1 with j_{Yb} and f_{Rb} (already deviating from the pure Hunds case (c) as discussed in chapter 2.3.1). In analogy to case (c) we then couple the atomic angular momenta f_{Rb} and j_{Yb} to form F_a instead of J_a since a nuclear spin is involved. The projection of F_a onto the internuclear axis Ω_F and the rotational angular momentum R eventually form the total angular momentum J. Since Ω_F is also the projection of J, the values of J can only be equal or larger than Ω_F. The states can now be described with $|\Omega, J\rangle$ and split up with their M_J components in a magnetic field.

From now on we can determine which molecular states are possible with the atomic state preparation of Rb and Yb. The angular momentum of atomic Yb in the $^3\mathrm{P}_1$, $|j = 1, m_j = 0\rangle$ state is $j_{\mathrm{Yb}} = 1$ and the total angular momentum of atomic Rb prepared in the $^2\mathrm{S}_{1/2}$, $|f = 1, m_f = -1\rangle$ state is $f_{\mathrm{Rb}} = 1$. Their combined angular momenta can be $F_a = 0, 1, 2$ and thus create states with $|\Omega_F| = 0, 1, 2$. With this we can attempt to find states whose Zeeman shift and line splitting at zero field matches with the experimental data. The possible combinations are summarized in table 5.3.

Ω_F	J	E_{rot} [MHz]	$\frac{E_Z(B)}{\mu_B B}$
0	0	0	0
0	1	31	0
0	2	92	0
1	1	15	$1/4 \cdot M_J$
1	2	77	$1/12 \cdot M_J$
2	2	31	$1/3 \cdot M_J$

Table 5.3.: Possible combinations of quantum numbers in case (c) coupling for the given atomic state preparation. The rotational energy E_{rot} and a Zeeman shift coefficient calculated with equations 5.5 and 5.3 are included.

First the energy shift of M_J states in a magnetic field can be calculated with [256]

$$E_Z(B) = \mu_B M_J g_{F_a} \frac{{\Omega_F}^2}{J(J+1)} B \tag{5.3}$$

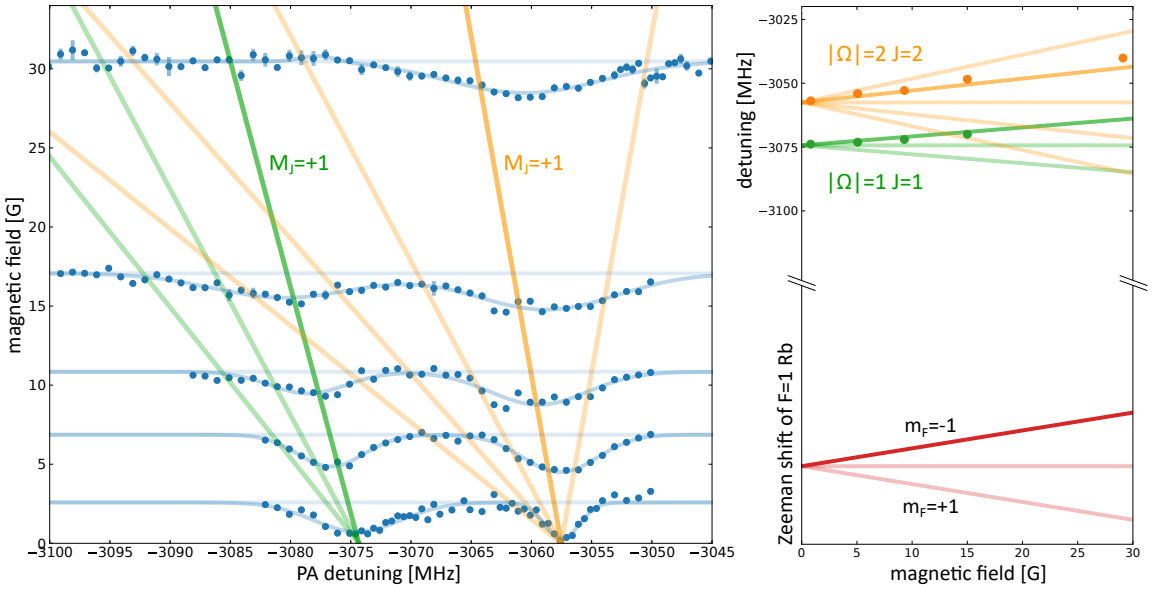

Figure 5.8.: Zeeman shifts of the molecular states $|\Omega = 1, J = 1\rangle$ and $|\Omega = 2, J = 2\rangle$ incorporated into the experimental data. This approach is also described in [1].

Analog to the atomic g_J Landé factor [257] the molecular equivalent is given by

$$\begin{aligned} g_{Fa} &= g_{f_{\mathrm{Rb}}} \frac{F_a(F_a+1) - j_{\mathrm{Yb}}(j_{\mathrm{Yb}}+1) + f_{\mathrm{Rb}}(f_{\mathrm{Rb}}+1)}{2F_a(F_a+1)} \\ &+ g_{j_{\mathrm{Yb}}} \frac{F_a(F_a+1) + j_{\mathrm{Yb}}(j_{\mathrm{Yb}}+1) - f_{\mathrm{Rb}}(f_{\mathrm{Rb}}+1)}{2F_a(F_a+1)} \\ &= \frac{1}{2} \quad \text{for both} \quad F_a = 1,\, 2 \end{aligned} \tag{5.4}$$

This attempt to explain the Zeeman shifts was also discussed in [1]. Since we observed a shift for both lines (A,B) it is reasonable to rule out a $|\Omega_F| = 0$ state, as it would not shift in a magnetic field, leaving only $|\Omega_F| = 1, 2$ states. Following formula 5.3, we should find an increasing shift for higher Ω_F or lower J. The higher energy state possesses the larger shift. Considering both states with equal Ω_F would imply that the higher lying state needs a larger J quantum number but thereby will have a smaller Zeeman shift, if no other relevant shift is present. This contradiction and the fact that we see a zero field splitting indicates that the states are of different Ω_F.

The rotational energy of a molecule is given by [167]

$$E_{\mathrm{rot}} = B_\nu \cdot \left(J(J+1) - {\Omega_F}^2\right) \tag{5.5}$$

with B_ν as the rotational constant. The observed splitting is $\sim$ 17 MHz. Choosing $|\Omega = 1, J = 1\rangle$ for the energetically lower and $|\Omega = 2, J = 2\rangle$ for the higher state with the estimated B_ν value of $\sim$ 15 MHz corresponding to the classical outer turning point at 45 a_0 leads to a comparable splitting. For the first part this splitting can be constructed with the set of quantum numbers and available states in our modified Hund's case (c).

Using the same states and plotting their Zeeman shifts on top of our data gives the splitting visible in figure 5.8. The highlighted $|M_J = +1\rangle$ Zeeman states are closest to the observed shift. In the first instance one would expect the molecule to appear in the $|M_J = -1\rangle$ state analog to the clean atomic preparation of Rb in the $|m_F = -1\rangle$ state. But we find a change in sign of the magnetic quantum numbers. The swap from negative to positive sign is due to the Landé factor switching signs in equation 5.4. Furthermore the state assignment raises another question because no $\Omega = 0$ state was found. Possible reasons for missing lines like this one might be predissociation of this state, that leads to a strong line broadening, which is further discussed in chapters 5.4.6 and 5.4.7.

Inclusion of angular momentum decoupling in a magnetic field

As an extension to the application of Hund's case c) we will include the decoupling of angular momenta in an external field in the following. This treatment is analogous to the Breit-Rabi formula which describes the hyperfine splitting and magnetic field shift of atoms in magnetic fields of intermediate strength [257]. In this approach the observed zero field splitting is treated analogously to the zero-field hyperfine splitting of an atom. The energy shift in an external magnetic field is then calculated by assuming that at zero magnetic field j_{Yb} couples to f_{Rb} while at large field j_{Yb} and f_{Rb} couple independently to the magnetic field.

The classic derivation of the Breit-Rabi formula describes the hyperfine coupling of nuclear spin $\vec{i}$ and total angular momentum $\vec{j}$ and the interaction Hamiltonian H_B, which for example can be found in [257]. Let us now assume that a coupling between the atomic total angular momentum $\vec{j}_{\mathrm{Yb}}$ and $\vec{f}_{\mathrm{Rb}}$ can be treated analog to the atomic hyperfine Hamiltonian

$$H_{\mathrm{mol}} = A_{\mathrm{mol}} \frac{\vec{j}_{\mathrm{Yb}} \cdot \vec{f}_{\mathrm{Rb}}}{\hbar^2} \tag{5.6}$$

with a coupling constant A_{mol}, which is here interpreted as the observed zero field splitting. In order to calculate the energies of states in a magnetic field corresponding to the Hamiltonian $H_{\mathrm{mol}} + H_B$ a complex matrix M has to be constructed and evaluated for its eigenvalues λ_i. Assuming that only Rb in $f = 1$ with $m_f = +1, 0, -1$ and Yb in $j = 1$ with $m_j = +1, 0, -1$ are possible states that have to be included we already get a $[9\,\mathrm{x}\,9]$ matrix. Its diagonal elements Λ are the only elements that involve a simple sum of terms originating independently from H_{mol} and H_B with

$$\Lambda = \Lambda_1 + \Lambda_2 \tag{5.7}$$

and

$$\begin{aligned} \Lambda_1 &= \langle f\, m_f; j\, m_j |\, H_{\mathrm{mol}}\, | f\, m_f; j\, m_j \rangle = A_{\mathrm{mol}} \cdot m_f m_j \\ \Lambda_2 &= \langle f\, m_f; j\, m_j |\, H_B^{(\mathrm{mol})}\, | f\, m_f; j\, m_j \rangle = g_f m_f \mu_B B + g_j m_j \mu_B B \end{aligned} \tag{5.8}$$

It should be noted that Λ_2 is the term from the interaction Hamiltonian that describes the Zeeman energy for large magnetic fields. This energy is the atomic Zeeman shift from

section 5.4.4, which does not fit to our data. Therefore we can assume that we are not in a regime of large but instead in a regime of intermediate magnetic fields.

The off-diagonal elements however involve more complicated terms. The entire list of terms necessary to construct the matrix M in equation 5.10 involving the components a to x is

$$
\begin{aligned}
a &= \langle f\,(m_f-1); j\,(m_j+1)|\,H_{\mathrm{mol}}\,|f\,m_f; j\,m_j\rangle \\
b &= \langle f\,(m_f+1); j\,(m_j-1)|\,H_{\mathrm{mol}}\,|f\,m_f; j\,m_j\rangle \\
c &= \langle f\,(m_f-1); j\,m_j|\,H_{\mathrm{mol}}\,|f\,m_f; j\,m_j\rangle \\
d &= \langle f\,(m_f+1); j\,m_j|\,H_{\mathrm{mol}}\,|f\,m_f; j\,m_j\rangle \\
e &= \langle f\,m_f; j\,(m_j-1)|\,H_{\mathrm{mol}}\,|f\,m_f; j\,m_j\rangle \\
f &= \langle f\,m_f; j\,(m_j+1)|\,H_{\mathrm{mol}}\,|f\,m_f; j\,m_j\rangle \\
g &= \langle f\,(m_f-1); j\,(m_j-1)|\,H_{\mathrm{mol}}\,|f\,m_f; j\,m_j\rangle \\
h &= \langle f\,(m_f+1); j\,(m_j+1)|\,H_{\mathrm{mol}}\,|f\,m_f; j\,m_j\rangle \\
i &= \langle f\,(m_f-2); j\,m_j|\,H_{\mathrm{mol}}\,|f\,m_f; j\,m_j\rangle \\
j &= \langle f\,(m_f+2); j\,m_j|\,H_{\mathrm{mol}}\,|f\,m_f; j\,m_j\rangle \\
k &= \langle f\,m_f; j\,(m_j-2)|\,H_{\mathrm{mol}}\,|f\,m_f; j\,m_j\rangle \\
l &= \langle f\,m_f; j\,(m_j+2)|\,H_{\mathrm{mol}}\,|f\,m_f; j\,m_j\rangle \\
m &= \langle f\,(m_f-2); j\,(m_j-2)|\,H_{\mathrm{mol}}\,|f\,m_f; j\,m_j\rangle \\
n &= \langle f\,(m_f+2); j\,(m_j+2)|\,H_{\mathrm{mol}}\,|f\,m_f; j\,m_j\rangle \\
o &= \langle f\,(m_f-2); j\,(m_j+2)|\,H_{\mathrm{mol}}\,|f\,m_f; j\,m_j\rangle \\
p &= \langle f\,(m_f+2); j\,(m_j-2)|\,H_{\mathrm{mol}}\,|f\,m_f; j\,m_j\rangle \\
q &= \langle f\,(m_f-2); j\,(m_j-1)|\,H_{\mathrm{mol}}\,|f\,m_f; j\,m_j\rangle \\
r &= \langle f\,(m_f-2); j\,(m_j+1)|\,H_{\mathrm{mol}}\,|f\,m_f; j\,m_j\rangle \\
s &= \langle f\,(m_f+2); j\,(m_j-1)|\,H_{\mathrm{mol}}\,|f\,m_f; j\,m_j\rangle \\
t &= \langle f\,(m_f+2); j\,(m_j+1)|\,H_{\mathrm{mol}}\,|f\,m_f; j\,m_j\rangle \\
u &= \langle f\,(m_f-1); j\,(m_j-2)|\,H_{\mathrm{mol}}\,|f\,m_f; j\,m_j\rangle \\
v &= \langle f\,(m_f+1); j\,(m_j-2)|\,H_{\mathrm{mol}}\,|f\,m_f; j\,m_j\rangle \\
w &= \langle f\,(m_f-1); j\,(m_j+2)|\,H_{\mathrm{mol}}\,|f\,m_f; j\,m_j\rangle \\
x &= \langle f\,(m_f+1); j\,(m_j+2)|\,H_{\mathrm{mol}}\,|f\,m_f; j\,m_j\rangle
\end{aligned}
\tag{5.9}
$$

Obviously, it is also non-trivial to determine all eigenvalues λ_i with $i = 9$ of such a matrix. The eigenvalues give formulas with magnetic field dependence and thus describe the Zeeman shift of all 9 possible molecular states with the respective $|m_{f_{\mathrm{Rb}}}, m_{j_{\mathrm{Yb}}}\rangle$ combination. Since we prepare our Rb sample in the atomic $|F = 1, m_f = -1\rangle$ state, 6 of these molecular states (the ones with $|m_{f_{\mathrm{Rb}}} = +1, 0\rangle$) are irrelevant for our Zeeman shift analysis but contribute to the calculated energy of the 3 relevant $|F = 1, m_f = -1\rangle + |J = 1, m_j = +1, 0, -1\rangle$ combinations with Yb. Furthermore, deciding which eigenvalue corresponds to a specific state is also not an easy task, given the fact that only two 1-photon-PA lines have been detected.

$$M = \begin{pmatrix} \Lambda & e & k & c & g & u & i & q & m \\ f & \Lambda & e & a & c & g & r & i & q \\ l & f & \Lambda & w & a & c & o & r & i \\ d & b & v & \Lambda & e & k & c & g & u \\ h & d & b & f & \Lambda & e & a & c & g \\ x & h & d & l & f & \Lambda & w & a & c \\ j & s & p & d & b & v & \Lambda & e & k \\ t & j & s & h & d & b & f & \Lambda & e \\ n & t & j & x & h & d & l & f & \Lambda \end{pmatrix} \tag{5.10}$$

Finally, the observed zero field splitting in our 1-photon-PA spectrum has to be interpreted as a 'hyperfine-type' splitting analog to the atomic Breit-Rabi model, which is typically expressed with $\Delta E_{\mathrm{mol}} \propto A_{\mathrm{mol}}$. All in all, this approach involves a complicated matrix calculation which was not solved in the scope of this thesis. Moreover it is reasonable to assume that it is insufficient to explain the complex molecular interaction. Therefore it remains unclear if it can help to explain the Zeeman shift of the observed 1-photon-PA lines.

Dipole-dipole interaction energy of magnetic moments

Assuming that the long range dipole-dipole interactions between Rb and Yb has to be taken into account is yet another approach to explain the observed photoassociation zero line splitting. When using the intercombination line for PA, Yb as well as Rb possess a magnetic dipole moment in the excited molecular state[3]. The Rb spin is connected to a magnetic moment $\vec{\mu}_{\mathrm{Rb}}$ that could interact with Yb, which now also has a magnetic moment $\vec{\mu}_{\mathrm{Yb}}$ since it is in the $^3\mathrm{P}_1$ state. The strength of the interaction is determined by the orientation of total angular momentum m_j. Additionally we also have the nuclear spin contributing to the total magnetic moment of the Rb atom. In table 5.4 the known quantum numbers and states that are involved are summarized.

	atomic state	nuclear spin i	electron spin s	angular momentum l
Rb	$^2\mathrm{S}_{1/2}$	$\frac{3}{2}$	$\frac{1}{2}$	0
Yb	$^3\mathrm{P}_1$	0	1	1

Table 5.4.: States and quantum numbers for Rb and Yb for PA at the Yb intercombination line.

The magnetic moments for Rb and Yb are thus

$$\vec{\mu}_{\mathrm{Rb}} = -g_s\mu_B\vec{s}_{\mathrm{Rb}} + g_N\mu_N\vec{i}_{\mathrm{Rb}} \quad \text{and} \quad \mu_{\mathrm{Yb}} = -g_l\mu_B\vec{l}_{\mathrm{Yb}} - g_s\mu_B\vec{s}_{\mathrm{Yb}} \tag{5.11}$$

[3]Previously the distance dependence of hyperfine interactions between alkali-metal atoms and closed-shell atoms has been observed [19], [25]. In earlier photoassociation experiments with RbYb at the D1 line a PA-line splitting into m_R components was attributed to a coupling of the Rb spin to the internuclear rotation. In this case the Yb atom does not posses a magnetic moment in the ground state [11].

with $g_s \approx 2$ and $g_l = 1$. The nuclear magnetic moment μ_N for ^{87}Rb is significantly smaller compared to μ_B and can thus be neglected [131].

$$|\vec{\mu}_1| = |\vec{\mu}_{\mathrm{Rb}}| \approx -\vec{\mu}_B \quad \text{and} \quad |\vec{\mu}_2| = |\vec{\mu}_{\mathrm{Yb}}| \approx -\frac{3}{2}\vec{\mu}_B \tag{5.12}$$

The classical expression for the dipole-dipole interaction energy of the magnetic moments of atom 1 and 2 is

$$\hat{H}_{\mathrm{dip}} = \frac{\mu_0}{4\pi}\left(\frac{\vec{\mu_1}\cdot\vec{\mu_2}}{r^3} - \frac{3(\vec{\mu_1}\cdot r)(\vec{\mu_2}\cdot r)}{r^5}\right) = A\left(\frac{\vec{e}_1\vec{e}_2}{r^3} - \frac{3(\vec{e}_1\cdot r)(\vec{e}_2\cdot r)}{r^5}\right) \tag{5.13}$$

The magnitude of the dipole-dipole interaction A/r^3 at the classical outer turning point $r = 45a_0$ can thus be estimated to $4.8 \cdot 10^{-5}\,\mathrm{cm}^{-1}$ corresponding to an energy of a couple MHz. This simple estimate shows that long range dipole-dipole interactions can be the reason for the observed zero line splitting.

However, to be more accurate we have to use a more refined Hamiltonian. In their book J. Brown and A. Carrington [131] present the coupling cases of dipolar interaction terms between nuclei and spin components[4]. According to Gonzalez et. al. [258] the dipolar interaction Hamiltonian between the magnetic moments of two atoms that we are essentially interested in can be written as

$$\hat{H}_{\mathrm{dip}} = -\sqrt{6}(\mu_0/4\pi)r^{-3}T^2(\hat{\mu}_1, \hat{\mu}_2)T^2(\boldsymbol{u}_R) \tag{5.14}$$

Here $\boldsymbol{u}_R$ is the unit vector conjugate to the orbital angular momentum and the second rank tensors T^2 describe the angular dependence of the interactions in a spherical coordinate system such as

$$T^2_q(\boldsymbol{C}) = C^2_q(\theta, \phi)(r^{-3}) \tag{5.15}$$

with $C^2_q = \sqrt{4\pi/5}Y^2_q(\theta, \phi)$ as the Racah-normalised spherical harmonic of order 2 depending on the polar angle ϕ of the molecule's internuclear axis and the azimuthal angle θ [259]. In the appendix of their paper they also give the matrix elements of the dipole interaction in the ls-coupled atomic basis set. Using their formula for the dipole-dipole potential matrix elements for possible atomic basis sets and a internuclear spacing of $\sim 45\,a_0$ again suggests energy splittings in the MHz regime. For different basis sets the value can vary from almost zero splitting to about 12 MHz. This also suggests that dipolar coupling could be the reason for the observed zero field splitting. Unfortunately, the Hamiltonian, including spin-orbit coupling, hyperfine, Zeeman, rotational, and dipole-dipole contributions based on the model in [258] can only be written using atomic basis sets because the molecular basis is unknown. Afterwards the Hamiltonian has to be diagonalized to yield more useful results.

A recent python module for the calculation of diatomic molecules from Blackmore et. al. [259] could be a valuable tool to perform the diagonalization or transformation to a

[4] $\hat{H}_{\mathrm{dip}} = -\sqrt{6}g_1g_2\mu_N^2(\mu_0/4\pi)T^2(\boldsymbol{C})\cdot T^2(\boldsymbol{I}_1, \boldsymbol{I}_2)$ [nuclear-nuclear]
$\hat{H}_{\mathrm{dip}} = -\sqrt{6}g_s^2\mu_B^2(\mu_0/4\pi)T^2(\boldsymbol{C})\cdot T^2(\boldsymbol{S}_1, \boldsymbol{S}_2)$ [spin-spin]
$\hat{H}_{\mathrm{dip}} = +\sqrt{6}g_S g_N\mu_B\mu_N(\mu_0/4\pi)T^2(\boldsymbol{C})\cdot T^2(\boldsymbol{S}, \boldsymbol{I})$ [spin-nuclear] (page 561)

molecular basis and furthermore calculate the rotational and hyperfine structure of RbYb molecules. However it has to be fed with information about the RbYb molecule and needs to be extended to be capable of dealing with electronically exited Π states instead of $^1\Sigma$ ground states.

Ω-doubling

In heavy heteronuclear molecules such as RbYb, Ω-doubling is a level splitting effect, which creates sublevels of every rotational level J for Ω values with opposite sign and can theoretically be another reason for the observed zero field splitting. The magnitude of this effect however is typically small, in the range of kHz and is used for the electron EDM search [260]. We can try to calculate this effect to judge when this effect becomes relevant. For Ω-doubling calculations of heteronuclear diatomic molecules the energy spacing between $\pm\Omega$ $^2\Pi_{3/2}$ levels[5] is on the order of

$$\Delta E_\Omega = B(B/a_{so})(B/\Delta E_e)(J-1/2)(J+1/2)(J+3/2) \tag{5.16}$$

,with ΔE_e as the spacing between electronic levels and a_{so} as the spin-orbit coupling constant [260]. In our case with $\Delta E_e \approx 0.02\,\mathrm{cm}^{-1}$, $B \approx 5 \cdot 10^{-4}\,\mathrm{cm}^{-1}$ and $a_{so} \approx 10^2\,\mathrm{cm}^{-1}$ this splitting can be estimated to be around $\Delta E_\Omega = 1 \cdot 10^{-10}\,\mathrm{cm}^{-1} \approx 10^{-6}\,\mathrm{MHz}$. If this is the case a doublet resulting from Ω-doubling can be ruled out. Furthermore, this splitting seems unlikely because the observed lines should behave similarly in a magnetic field coming from the same $|\Omega|$ quantum number [261].

Conclusion

All in all, neither approach that I have presented leads to an entirely conclusive interpretation of the observed 1-photon-PA doublet. This can be attributed to the first mentioned intermediate state problem in section 5.4.4, where neither of Hund's cases is clearly selected and no good quantum numbers exist. While Hund's case (c) in subsection 5.4.4, the decoupling interpretation in subsection 5.4.4 and the dipole-dipole interaction of magnetic moments in subsection 5.4.4 offer possible partial explanations to the observed zero field splitting, no approach has fully explained the Zeeman shift of both lines.

To solve this puzzle, the experimental approach would be to perform additional measurements to gather more spectroscopic data. Preparing different atomic states for Rb or Yb and subsequent 1-photon-PA spectroscopy together with a Zeeman analysis would be ideal to learn about more about the affect of the initial atomic quantum numbers on the discovered molecular states. First attempts to prepare Rb atoms in the $f = 2, m_f = -2$ state using a Landau-Zener sweep (see section 4.1.5) with a microwave at 6.8 GHz have already been performed. The state preparation however was not perfect meaning that about 10% of Rb atoms remained in the $f = 1$ state. The subsequent 1-photon-PA measurements across the frequency range of the discovered doublet are depicted in figure 5.9. Further spectroscopy within a range of ±100 MHz around the located PA signal (with Rb

[5] $^2\Pi_{1/2}$ levels are around the same magnitude

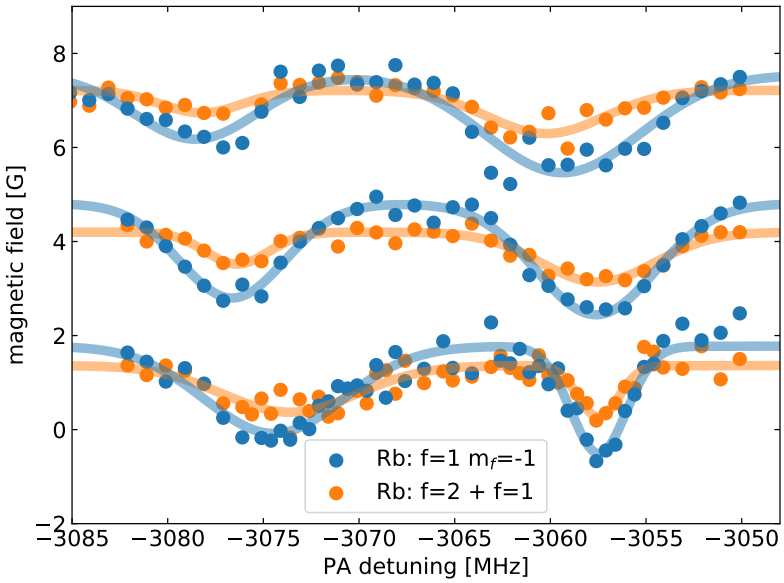

Figure 5.9.: Attempt to probe Rb in the $f = 2$ state (orange) with 1-photon-PA spectroscopy in a quantum gas mixture with Yb in increasing magnetic field compared to the already presented spectroscopy, where Rb only occupies the $f = 1, m_f = -1$ state.

in $f = 1, m_f = -1$) was also conducted but did not result in any additional molecular signals. Therefore the present interpretation of the orange curve in figure 5.9 is that we do not see any significant difference in the observed molecular excitation for Rb in the $f = 2, m_f = -2$ state. The zero field splitting, Zeeman shift and linewidth remains equal (within error bars) compared to the previously shown blue curve, where we prepared Rb purely in the $f = 1, m_f = -1$ state. However we can not rule out that the signal (orange) originates from a mixture of states ($f = 2, m_f = -2$ and $f = 1, m_f = -1$) and actually only corresponds to the Rb atoms remaining in the $f = 1, m_f = -1$ state. Improved state preparation and spectroscopy have to confirm this assumption in the future.

Another idea to learn more about our lines is to change the combination of isotopes in the quantum gas mixture. A different reduced mass can for example change the rotational energy (5.5) and thus affect the zero field splitting.

Of course finding more undiscovered 1-photon-PA lines aside from the 3 GHz signal would be the preferred information on the electronically excited molecular potential. In order to find more, the photoassociation rate, which is presented in the next section 5.4.5, needs to be increased.

5.4.5. Photoassociation rate

The photoassociation rate $K_{\mathrm{PA}}(I)$ of a molecular transition can be determined experimentally by measuring the atom loss of both reaction partners as a function if interaction time. If the PA laser is on resonance with an excited state the loss will increase due to the formation of molecules, which can no longer be detected. Figure 5.10 shows measurements off and on resonance with the 3057 MHz (A) line for a Rb-Yb mixture in the XODT. As a comparison earlier results, published in [20] and reported in [1], are included in segment (b). The results of this thesis are shown in segment (a). Since the photoassociation rate depends on the light intensity I all PA rate measurements within this thesis - independent of the final trap - are performed with 0.8 mW to be comparable. The temperatures in the mixture were $T_{\mathrm{Rb}} = 5\,\mu\mathrm{K}$ and $T_{\mathrm{Yb}} = 1\,\mu\mathrm{K}$, which gives an effective temperature of $T_{\mathrm{eff}} = 3.6\,\mu\mathrm{K}$. The assumed densities are calculated peak values taken from table 4.2 and are on the order of $10^{13}\,\mathrm{cm}^{-3}$ for Rb and $10^{12}\,\mathrm{cm}^{-3}$ for Yb.

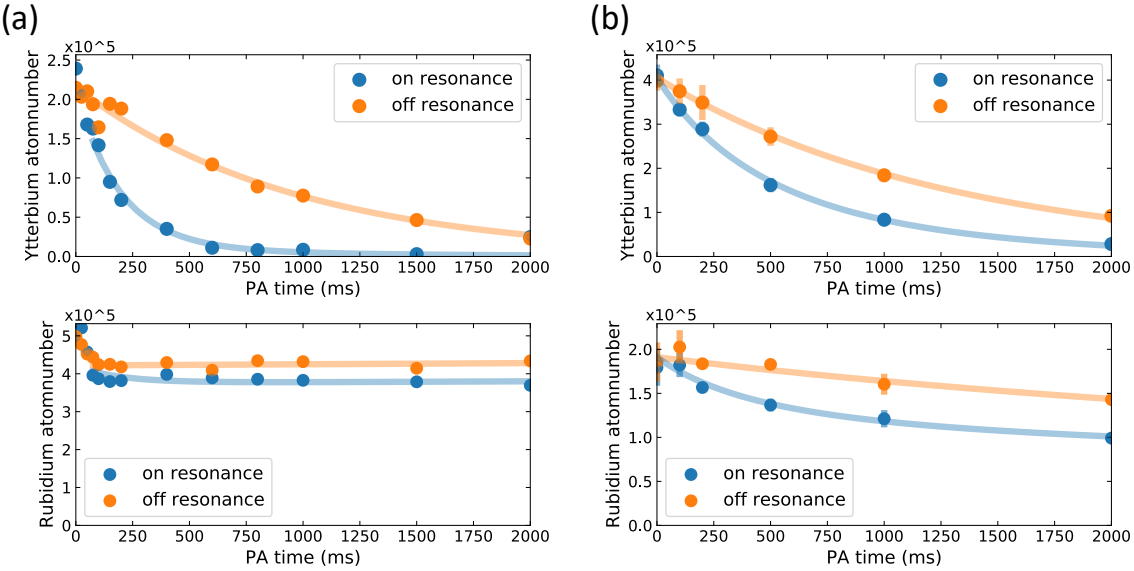

Figure 5.10.: (a) Measurement (from this thesis) of the Yb and Rb atomnumber decay in the crossed optical dipole trap over a PA time of 2 s. The loss rate on (blue) and off (orange) resonance with the 3057 MHz transition is fit with a rate equation model. With it the photoassociation rate $K_{\mathrm{PA}}(I)$ of this molecular transition can be determined. In comparison, segment (b) depicts the previously published [20] measurement of the photoassociation rate that is reported in [1].

Since the Yb loss - caused by scattering near the atomic line - is fairly strong, we observe a continuous loss over time even while measuring off resonance. The elapsed time until the Yb atom number becomes difficult to measure sets our available time-frame to detect the PA rate. In this case (segment (a) of figure 5.10), on resonance, the atom number of Yb has dropped below $\sim 1 \cdot 10^4$ atoms after 2 s. Choosing higher PA laser intensities to boost our PA rate is not feasible because we would simply enhance the off-resonant scattering and close our time window even further. Furthermore we unfortunately observe an unfinished

thermalisation process of Rb during the first $\sim 100\,\mathrm{ms}$ in this measurement. We use the rate equations 5.17 and 5.18 and find numerical solutions to fit the photoassociation rate K_{PA} and the atom loss rates K_{Rb} and K_{Yb}.

$$\dot{n}_{Rb} = -n_{Rb} \cdot K_{Rb} - n_{Rb} \cdot n_{Yb} \cdot K_{PA} \tag{5.17}$$

$$\dot{n}_{Yb} = -n_{Yb} \cdot K_{Yb} - n_{Rb} \cdot n_{Yb} \cdot K_{PA} \tag{5.18}$$

The time dependent thermalisation loss component of Rb however was not implemented in the coupled differential equations and thus does not appear in the fit. Therefore the fit begins after the first 100 ms visible in segment (a) in figure 5.10. After the initial thermal Rb loss, the Yb loss rate constant of $K_{\mathrm{Yb}} = 0.7\,\mathrm{s}^{-1}$ is much larger than the negligible value determined for the Rb loss rate K_{Rb}. Since three-body losses have not been observed they are not included in the rate equation model. Since we drive the transition close to the Yb intercombination line let us assume that any Yb atom is available to be associated to a molecule. The possibility to actually create a molecule thus depends on the availability of a nearby Rb atom. Hence our PA rate depends on the average Rb density. We finally obtain a photoassociation rate of $K_{\text{PA-XODT}} = 5(2) \cdot 10^{-13}\,\mathrm{cm}^3/\mathrm{s}$. This term describes the PA rate per Rb density and per Yb atomnumber. The value is about one order of magnitude larger than the number reported in [1] and exceeds the theoretical expectations of $\approx 10^{-16}\,\mathrm{cm}^3/\mathrm{s}$ for the largest rate coefficient in RbSr [22]. The amount of molecules created is illustrated by the difference between the on- and off-resonance curves in figure 5.10. The molecule production rate is $5.8(1.8)\,\frac{1}{\mathrm{s}}$ per Yb atom or $2.4(0.8)\,\frac{1}{\mathrm{s}}$ per Rb Atom.

The increased PA rate, as compared to the value reported in [1], was achieved with several improvements of the experiment. First of all, a simplified, faster and more effective merge sequence (see chapter 4.4) is able to achieve better conditions for 1-photon-PA. Furthermore the overlap of the Rb sample with the Yb sample was optimized and adjusted via the 1D vertical lattice position to achieve an improved overlap of both peak densities. As a result the temperatures of both species are lower than in the previously produced $^{87}\mathrm{Rb}^{170}\mathrm{Yb}$ mixtures in [1]. Additionally, the ratio between Rb atomnumber and Yb atomnumber was altered by changing the powers of the trap lasers in the preparation process. At the moment we prepare about two Rb atoms for every Yb atom in the mixture. In conclusion, this gives us a higher sensitivity in the Yb loss signal since it is now easier for every Yb atom to find a reaction partner in the much denser Rb sample. Finally the PA laser beam was also readjusted to intersect with the peak density of the mixture. Of course, the previously measured PA rates near the D1 line of Rb are still several magnitudes larger [14]. Nonetheless, the improved PA rate persuaded us to repeat our search for additional 1-photon-PA lines from $1\,\mathrm{GHz} - 2\,\mathrm{GHz}$ in hopes to find previously undetected lines which was unfortunately again unsuccessful.

Finally the theoretical value for the saturation of the PA rate with increased laser intensity is not observable under our experimental conditions. In order to reach the value of $K_{\mathrm{sat}} = 10^{-10}\,\mathrm{cm}^3/\mathrm{s}$ discussed in chapter 2.5.1, we would need approximately 550 mW

of power, which is neither possible due to off-resonant scattering on the atomic line nor available from our laser system.

5.4.6. Line strength

Eventually the discovery of a comparably strong one photon transition during the extensive search over 10 GHz begs the question:

'why did we not find more lines ?'

This question mainly asks for the free-bound Franck Condon factors (FCFs) of neighbouring transitions, the number of transitions within the measured range and the detectable PA rate of the experiment. Let us start with the expected sensitivity of $K_{\mathrm{PA}} \gtrsim 2 \cdot 10^{-14}\,\mathrm{cm}^3/\mathrm{s}$ [20]. All signals below this threshold remain undetected with the search method presented in chapter 5.3. The number of states within a given energy range can be calculated by the LeRoy-Bernstein formula for a theoretical C_6 value. As already mentioned in the beginning of this chapter we expect five to six transitions within the first 10 GHz without knowing the exact binding energies.

In order to calculate their line strength and whether or not they should have been detected, we have to determine the free-bound Franck Condon factors with a model potential. Since we do not have an accurate potential energy curve for the electronically excited state at long range we have to build our own Hamiltonian with a Lennard-Jones type potential. We use the theoretical coefficient $C_6 = 4466\,E_H\,{a_0}^6$ for $|\Omega| = \frac{3}{2}$ from [140] and try to fit a nominal C_{12} value with the information of the single observed binding energy[6]. For the ground state we reuse the potential presented in Münchow's work [262][7]. Here we utilize the first unbound vibrational wavefunction of the ground state with a free energy matching the thermal energy shift of ~ 0.1 MHz. For different thermal shifts the corresponding scattering wavefunction has a negligible influence on the relative FCFs between different transitions. The vibrational wavefunctions of the excited eigenstates in our self-built Lennard-Jones type potential (with $C_6 = 4466\,E_H\,{a_0}^6$ and C_{12} extracted from our single binding energy fit) can then be compared to the scattering wavefunction of the ground state potential. If the maxima of their lobes lie close to each other, especially around the Condon point, the probability to drive a transition is higher. This is referred to as the estimated overlap of the wavefunctions within our self-built potential. The free-bound Franck Condon factors are equal to the squared overlap integral of the scattering and excited state vibrational wavefunction.

$$f_{FC} = |\langle \psi_{sc} | \psi_{vib} \rangle|^2 \tag{5.19}$$

Although this method inherently possesses a large inaccuracy we get an impression of line strengths of the neighbouring transitions for different vibrational energy levels. Since

[6] This was previously done in [1] and is now revised with similar values, in this case $C_{12} = 2.54{\cdot}10^9\,E_H\,{a_0}^{12}$ was used. Due to the $\frac{1}{r^6}$ dependence of the potential energy, the difference in outer turning point between the two values of $|\Omega|$ is very small around $1\,a_0$.

[7] In this case we use $C_6 = 2837$, $C_8 = 4.6 \cdot 10^5$, $C_{12} = 1.4 \cdot 10^{10}$.

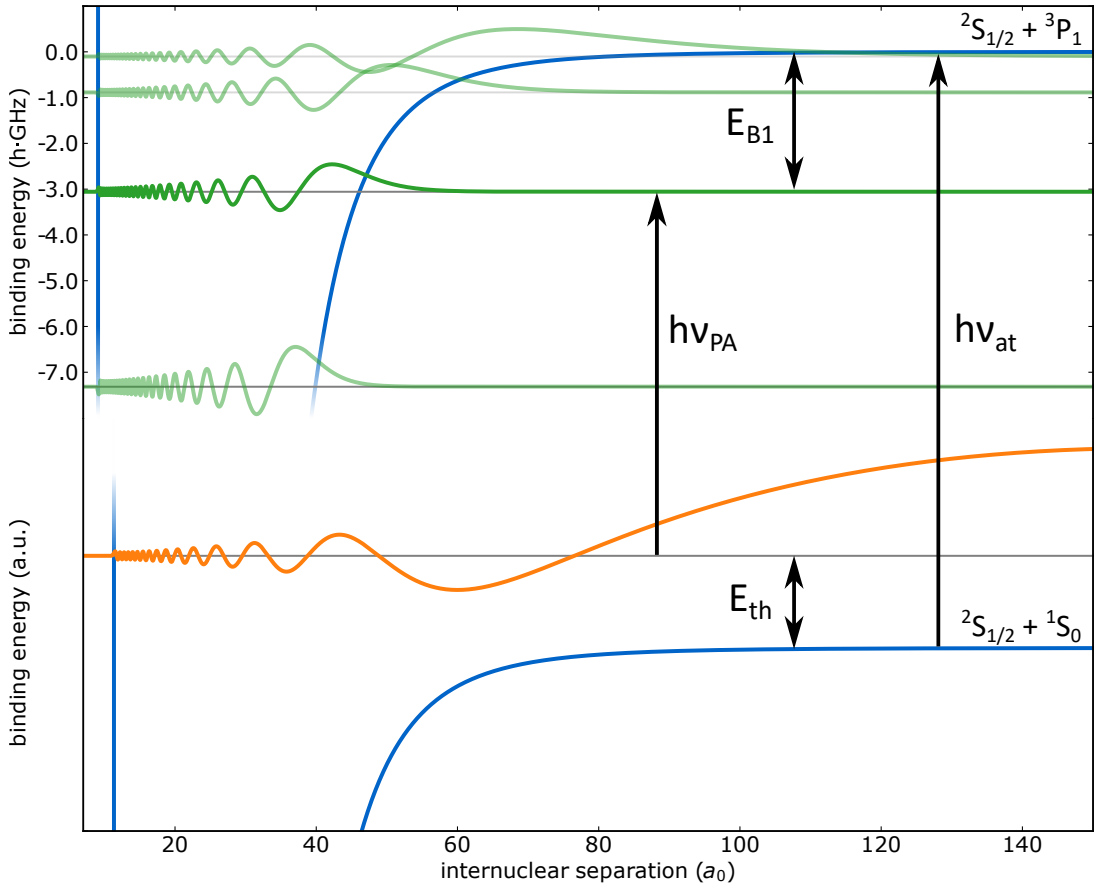

Figure 5.11.: Excited and ground state energy curves calculated with Lennard-Jones type potentials. The ground state scattering function is plotted with exaggerated offset to the ground state potential to showcase the thermal energy.

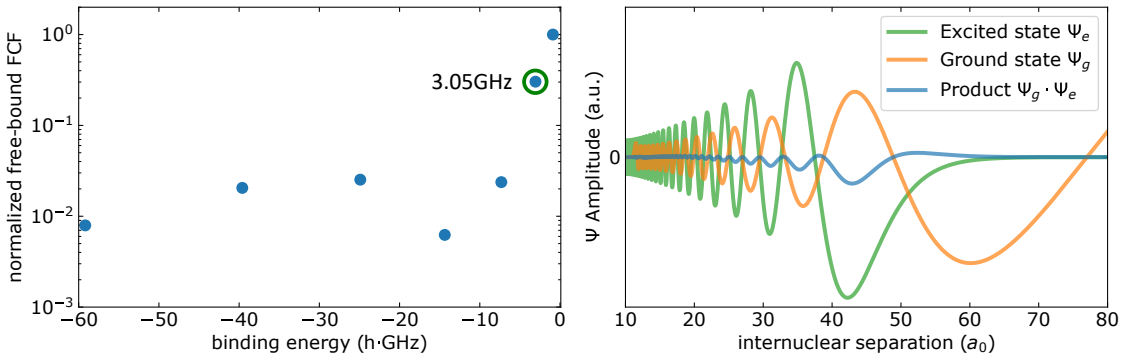

Figure 5.12.: Normalized free-bound Franck Condon factors calculated from wavefunction overlaps. The green encircled value belongs to the observed transition found at −3 GHz binding energy. On the right side its ground state (orange) and excited state (green) wavefunctions are adjusted to zero. The integral over the square of the product shown in blue is then the FCF. The ground state wavefunction and the product of both wavefunctions are scaled for display purposes (Ψ_g by a factor of 50 and $\Psi_g \cdot \Psi_e$ by a factor of 2000).

the accuracy of the used C_6 value is specified with an error of $\pm 180\, E_H\, {a_0}^6$ in [140] the real potential energy curve can be different. For example a sightly different C_6 that only deviates by $\pm 10\, E_H\, {a_0}^6$ from the proposed value will shift the 1-photon-PA transition at 3 GHz by about ± 300 MHz if the coefficient C_{12} remains unchanged. In figure 5.11 and figure 5.12 the extracted wavefunctions and normalized free-bound Franck Condon factors are plotted. The more deeply bound states have FCFs that are an order of magnitude smaller compared to the state we found and are thus harder to detect. The two most weakly bound states above our resonance are estimated to be around PA detunings of ~ 900 MHz and ~ 100 MHz. They have larger FCFs but are both located next to Yb_2 lines found at 908(2) MHz and 103(2) MHz (see table 5.2). If we got unlucky and as it happens have transition very close to Yb_2 lines it is exceedingly difficult to detect a much weaker molecule transition. This at least offers a possible explanation to the question asked in the beginning of this section.

There are some ideas on how to increase the line strengths to molecular vibrational levels near forbidden optical atomic transitions. Experiments with Yb_2 resonances utilizing a secondary light field close to a resonance have shown the possibility to manipulate the scattering wavefunction [263]. If this approach is adaptable to diatomic RbYb molecules, a small wavefunction overlap could be enhanced for weakly bound states. Finally it should be noted that the theoretical work in [18] suggests that, for states which are much more deeply bound down at the THz level, photoassociation rates could increase again. The predicted mechanism for this is the mixing of molecular states, which enhances the dipole matrix moment [22]. However it is unlikely that this effect outweighs the decrease in the FCFs due to increasingly different wavefunctions for shorter internuclear separation. Nevertheless if one can precisely calculate the binding energies of more states in the excited potential, with the support of more experimental data, other states could end up as valuable candidates for the production of ground state molecules.

5.4.7. Linewidth

The linewidths at a small magnetic field below 1 Gauss - obtained from the Zeeman effect measurements presented earlier - are approximately 3.0(3) MHz and 6.3(7) MHz for line A and B respectively. Following this, it is safe to assume that at zero magnetic field both widths are still more than a magnitude larger than the atomic linewidth width of $2\pi \cdot 182$ kHz. On one hand a plausible explanation for this difference could be an unresolved magnetic field splitting of multiple lines (for small fields $B << 1$ G this can be ruled out). On the other hand this hypothesis is inconsistent with the observed Zeeman shifts and the attempted interpretation of molecular states and line assignment of Hund's case (c) in section 5.4.4. In addition the width of peak B appears to stay unaffected at small fields, making this explanation more unlikely. Another possible reasons for linewidth broadening is the laser intensity of the PA laser. In figure 5.13 the FWHMs of the line at 3057 MHz (Peak A) for different PA powers at equal magnetic field are shown. Unfortunately the line was not observable with less than 0.2 mW PA power and the maximum available output power of the fiber laser was limited to 1 mW at the atoms, which leads to

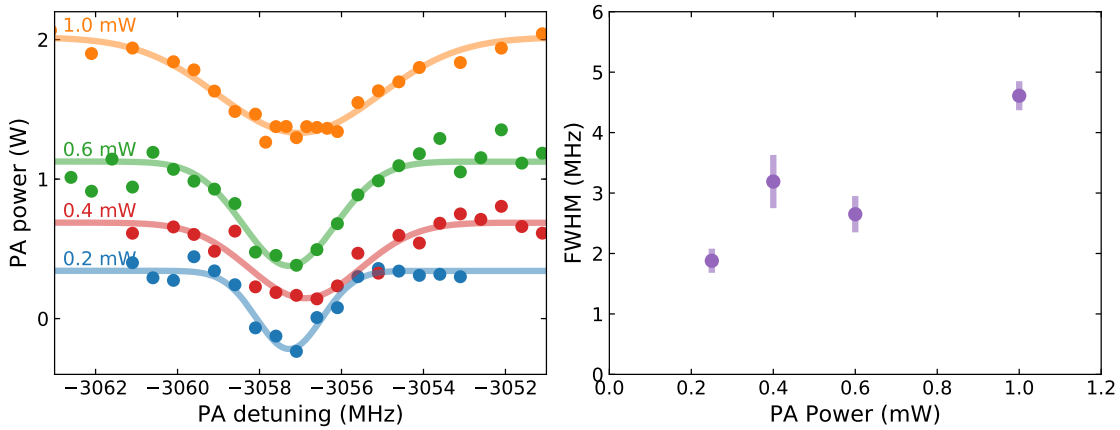

Figure 5.13.: Linewidth of the molecule line at 3057 MHz (Peak A). (a) shows spectroscopic lines for various PA powers. (b) the linewidth as a function of laser power for four different PA laser powers is determined with Gaussian fits.

a restricted measurement with large error. Therefore a saturation broadening of the PA line with increasing intensity can only be speculated on, as its analysis needs more reliable data. Nevertheless saturation broadening could not explain the large residual width around 2 MHz at low intensities. Additionally this data does not resolve any identifiable line shift resulting from the PA laser.

The same phenomenon of a linewidth at zero field that is significantly larger than the linewidth of the corresponding atomic transition is also reported in photoassociation experiments at an intercombination line with RbSr molecules [264]. However, sub MHz linewidths of PA resonances at the intercombination line with homonuclear Yb_2 close to the atomic value were found [264]. The Yb_2 resonances presented in [1] range from 1 MHz − 5 MHz but are likely saturation broadened since they were found during the search for a much weaker RbYb molecule signal. This leads to the assumptions that the combination of the ^{3}P level of Yb (or Sr) with Rb or a (less likely) strong coupling from the excited to a vibrational ground state may be the reason for the broadening of such PA lines. Therefore radiative decay and possible interactions between molecular states are discussed in the following.

Radiative decay

One possible reason for a broad linewidth is a strong radiative decay to the electronic ground state [264]. If the excited state has a strong coupling to a vibrational ground state, a rapid decay to tightly bound molecular levels could produce the observed linewidth. This theory is supported by the increased transition dipole matrix element to deeply bound levels, calculated by Shundalau and Minko [18]. Figure 5.14 shows how the dipole moments for electronic molecular $(N)\Omega$ states evolve with the internulcear separation. For large separation and thus transitions to weakly bound states the TDMs are close to the atomic values due to weak interactions and their atomic selection rules. In contrast to the decrease for the single state at the Rb D1 line at short distances, the three other state's electronic

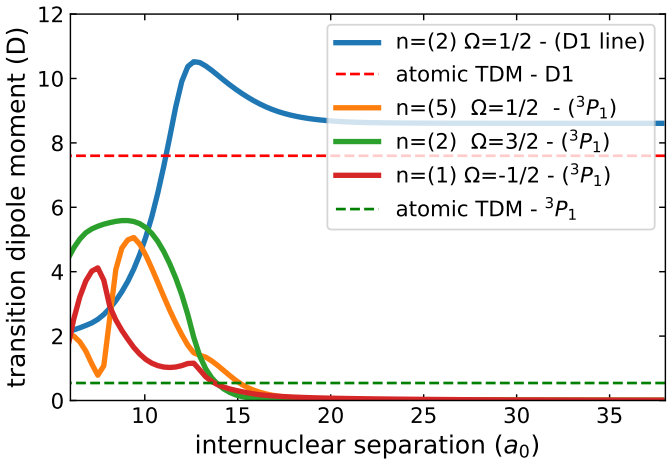

Figure 5.14.: Transition dipole moments for transitions from the $n = (1)\ \Omega = 1/2$ molecular ground state to selected molecular excited states for short internuclear separation $< 20\,a_0$, as calculated by Shundalau and Minko [18]. In contrast to the decrease of the dipole moment for the excited molecular state $n = (2)\ \Omega = 1/2$ close to the Rb D1 line at small internuclear separation, the three other excited molecular levels (corresponding to the $^3\mathrm{P}_1$ intercombination line of Yb) state's electronic component increases due to state mixing, which removes the spin-forbidden nature of the transition. (This graph was also used in [1].)

component corresponding to the $^3\mathrm{P}_1$ Yb line increase. This results from state mixing, which removes the spin-forbidden nature of the Yb transition [22] if a Rb atom is nearby. Now the magnitude of this effect has to overpower the diminishing Franck-Condon factor for transitions to deeply bound states in order to verify this idea. In the work of T. Franzen the expected matrix elements value for all possible Π states $(\frac{1}{2}, \frac{3}{2}, -\frac{1}{2})$ were estimated with the potential energy curves and TDMs from Shundalau and Minko [18]. The result is an increase of less than 10% of the atomic dipole moment, which would rule out the radiative decay mechanism as a cause [1].

Non-radiative decay

The other possible cause is a non-radiactive decay mechanism. In the $^3\mathrm{P}$ manifold the molecular states associated with the atomic $^3\mathrm{P}_0$ and $^3\mathrm{P}_2$ levels are energetically close to the $^3\mathrm{P}_1$ state. For the RbYb molecule these triplet levels correspond to even more molecular potentials: $^2\Pi_{1/2}$ for the $^2\mathrm{S}_{\frac{1}{2}} +^3 \mathrm{P}_0$ and $^2\Sigma_{1/2}$, $^4\Pi_{3/2}$, $^4\Pi_{5/2}$, $^4\Sigma_{1/2}$, $^4\Sigma_{3/2}$ for the $^2\mathrm{S}_{\frac{1}{2}} +^3 \mathrm{P}_2$ asymptote. Since the single molecular level associated with the $^3\mathrm{P}_0$ state is the energetically lowest of all, predissociation from a bound $^3\mathrm{P}_1$ state into an unbound $^3\mathrm{P}_0$ state is possible, as depicted in figure 5.15. If the energy of the vibrational state in our excited potential is close to this unbound state the molecule can change states and subsequently break apart. External factors like collisions with other atoms and molecules or magnetic fields can also induce predissociation. Introducing Zeeman mixing between

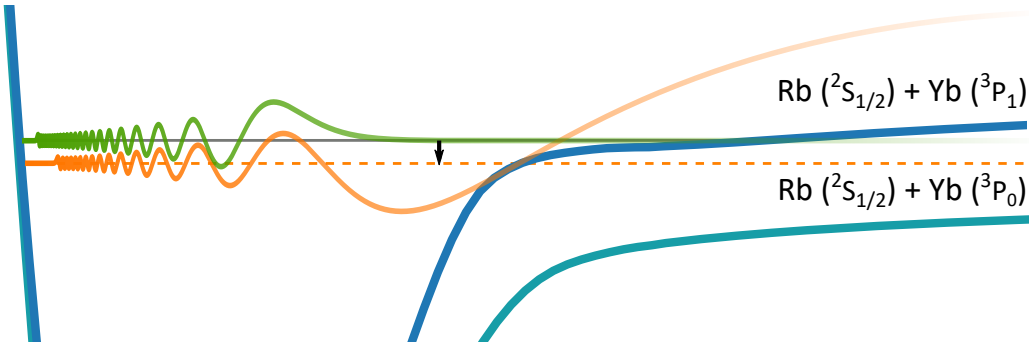

Figure 5.15.: Sketch of the predissociation process from a bound state inside the $^2S_{\frac{1}{2}} + {}^3P_1$ molecular potential (green) into an unbound state (orange) of the $^2S_{\frac{1}{2}} + {}^3P_0$ potential. If the bound state is close to a unbound level the molecule can swap states into the unbound state associated with the $^2S_{\frac{1}{2}} + {}^3P_0$ molecular potential as indicated by the black arrow.

^3P states, analog to the doubly forbidden clock transition in Yb [265], could explain the linewidth broadening with increasing magnetic field strength.

Non-radiative decay mechanisms have also been discussed by Mukherjee, Frye and Hutson, in the analysis of possible Feshbach resonances at the ^3P manifold [105]. They investigated the magnetoassociation of RbYb molecules at the $^3P_2$ threshold and found a strong decay that would result in lifetimes of a few microseconds at most. Additionally magnetic field dependent interactions in LiYb show that the decay width depends on the magnetic field (at around 100 G), inducing finite lifetimes due to inelastic collisional effects [266]. The mixing of molecular states in such molecules involves complex calculations exceeding this thesis, but if this behaviour is transferable to $^3P_1$ levels the broad linewidth could be explained.

5.5. Photoassociation in a optical lattices

After the extensive treatment and interpretation of data taken in the crossed optical dipole trap, in this chapter, I will present the first results on 1-photon-PA in optical lattices. The 1-photon-PA in optical lattices is the starting point for improved photoassociation measurements and hopefully the first ground state RbYb molecules in future experiments.

5.5.1. Preparation in optical lattices

In order to confirm the functionality of the new optical lattice trap (see chapter 4.4.4), the same PA lines needed to be remeasured. Therefore, the preparation in various optical lattice configurations is realised in the last time step of the merging sequence presented in chapter 4.4.3. As already mentioned the mixture in a combined XODT trap can be transferred into an optical lattice by ramping down the beam powers of both Yb ODTs within $t = 0.2\,\mathrm{s}$. Here one can choose between creating a 1D, 2D or 3D optical lattice trap by selecting to ramp up only one or more corresponding laser beams. In the simplest case, the 1D optical lattice, the vertical lattice beam can be kept on after the vertical Rb transport to turn it into the final mixture trap after the Yb ODTs are extinguished. To create a 2D (3D) optical lattice one (both) of the other horizontal lattice beams has (have) to be ramped up during the time t.

All of these configurations are of course possible with different power ratios between the lattice beams. As a reminder, in a effort to match the lattice depth of each beam the beams are all derived from identical fiber ports and collimation optics and all focussed to $\approx 100\,\mu\mathrm{m}$ beam waists. However, preliminary investigation of the individual lattice depths of each beam via the lattice pulsing method described in chapter 4.3 resulted in different depths for equal beam intensities. These differences can be attributed to slight (focus) miss-alignment with respect to the intersecting point of all lattice beams. Furthermore the data presented in this chapter is taken without a lattice beam power stabilisation, which caused a slow shift in the power distribution between lattice beams due to a rotation of the polarisation of the lattice laser (section 3.5) and as a result made a proper realignment impossible. However, by now the experiment is updated with a power stabilisation an can thus be properly adjusted in the future (with the developed lattice depth measurements in chapter 4.3).

5.5.2. 1-photon-PA in optical lattices

As a start, the 1-photon-PA signals were detected in all three 1D, 2D and 3D configurations by scanning over the known PA detunings analog to the measurements in the bulk trap. It should also be noted that the pair of resonances did not change significantly in center frequency or even vanish due to a different trap environment or laser light source (see chapter 3.5).

The main result of this chapter are the PA rates on resonance with the 3057 MHz (A) line for a Rb-Yb mixture in a 2D and 3D optical lattice[1]. In figure 5.16 the atom loss on and

[1] In a 1D lattice configuration the signal was not strong enough.

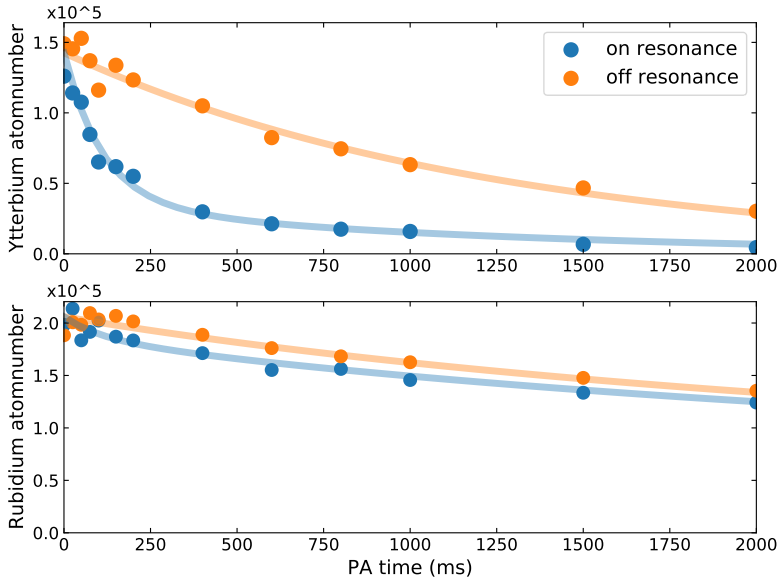

Figure 5.16.: Measurement of the Yb and Rb atomnumber decay in the 2D optical lattice trap over a PA time of 2 s. The loss rate on (blue) and off (orange) resonance with the 3057 MHz transition is fit with the rate equation model in section 5.4.5. The lattice increases the PA rate but shows signs of saturation in the Yb loss signal after 250 ms, resembling an off resonant Yb loss.

off resonance with the 3057 MHz line in the 2D optical lattice is shown, while figure 5.17 shows the same measurement in a 3D optical lattice. The PA light intensities (0.8 mW) in both are chosen to be equal to the previous measurement in the bulk trap (see section 5.4.5) to be able to compare the measurements and analyse the differences in PA rates. We see a fast initial loss of Yb atoms in the first 250 ms if the PA laser is on resonance. Afterwards the reduction in Yb atom number is equal to the off-resonant scattering loss from PA light.

In contrast to a conventional bulk trap, spectroscopy in optical lattices gives us some advantages. Most of them will be discussed extensively in the next section 5.5.3, since experiments in the new trap are in the early stages, but some possible benefits, supported by the results in the PA rate measurements, are already addressed here. An optical lattice with high intensities can restrict Rb and Yb atoms to localised lattice sites. Of course this confinement depends on the number of intersecting lattice beams (1D, 2D or 3D). The resulting potential provides a larger density overlap and increases the probability for photoassociation. The density calculation of a 3D optical lattice in figure 4.28 in section 4.4.4 clearly shows the improvement compared to the density overlap in a conventional bulk trap, which suffers from gravitational sag. As a result we expect an increased PA rate compared to the values obtained in the bulk trap. Moreover it can suppresses recoil shifts and Doppler broadening and thus simplifies the interpretation of PA line shapes [250].

If the lattice site however is only occupied by a single atomic species or even a single

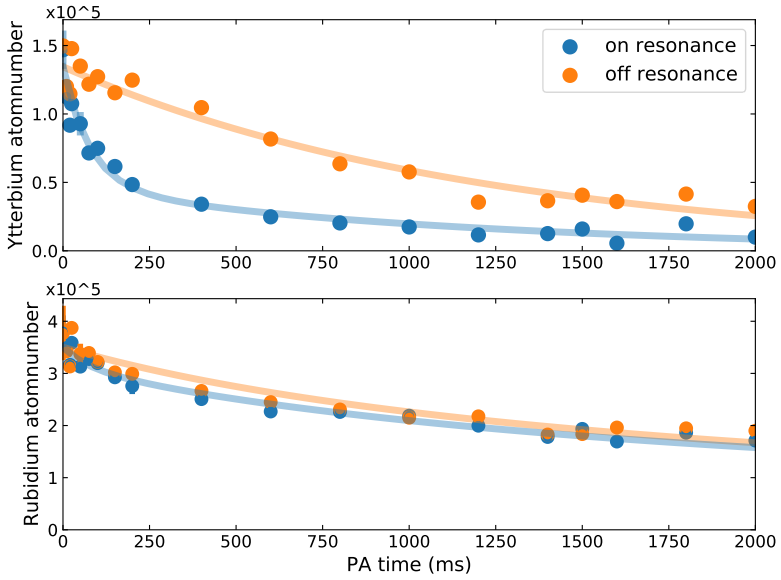

Figure 5.17.: Measurement of the Yb and Rb atomnumber decay in the 3D optical lattice trap over a PA time of 2 s. The loss rate on (blue) and off (orange) resonance with the 3057 MHz transition is fit with the rate equation model in section 5.4.5. The lattice increases the PA rate but shows signs of saturation in the Yb loss signal after 250 ms, resembling an off resonant Yb loss.

atom no heterogeneous molecule process is possible. From TOF measurements we can assume cloud diameters of $d_0 \approx 50\,\mu m$ in the 3D optical lattice. With the lattice spacing of $a = 532\,nm$ a rough estimate of the average lattice filling is below one atom per site for either atomic species (0.5 atoms per site for Rb and 0.2 atoms per site for Yb). The calculated lattice depth for a 3D optical lattice with a power of 0.5 W per beam is $V_{lat,Yb} = 84\,E_{Yb,rec}$ corresponding to a lattice frequency of $\omega_{Yb} = 19\,kHz$ and $V_{lat,Rb} = 443\,E_{Rb,rec}$ corresponding to a lattice frequency of $\omega_{Rb} = 85\,kHz$. Due to the lattice band structure the energy levels for Yb atoms in a harmonic potential are only well separated up to the 5th energy band, while the lattice is much deeper for Rb atoms. As a reminder, atoms with higher energy and temperature can populate higher bands and are thus able to freely move through the potential. In table 5.5 the lattice bands are calculated in units of kHz and µK to be comparable to temperature measurements[2].

As already stated in chapter 4.4.4, a TOF measurement indicated higher temperatures of $T_{Rb} \approx 6\,\mu K$ and $T_{Yb} \approx 12\,\mu K$ in the 3D optical lattice compared to the XODT. It should be noted that atoms in a lattice populate discrete (n) energy levels and the enegry is not continuously distributed. Furthermore, we assume an instantaneous trap release and thus the accuracy of the size and the temperature measurement is limited by the speed at which all three lattice AOMs are switched off. Due to the large trapping frequencies in the

[2]In order to calculate the energy bands in Hz you divide the lattice recoil energy with Planck's constant and to convert to Kelvin you divide with the Boltzmann constant

quantum number n	0	1	2	3	4	5	6	unit
Energy bands for Yb	9.3	22.8	43.5	59.1	74	83.9 - 87.4	89.8 - 98.5	[kHz]
	9	26	42	57	70	~ 80	~ 95	[E_{rec}]
	0.4	1.1	2.1	2.8	3.5	3.8 - 4.0	4.7 - 5.1	[µK]
Energy bands for Rb	42.5	125.6	206.6	285.6	362.6	435.5	506.4	[kHz]
	21	62	102	141	179	215	250	[E_{rec}]
	2.0	6.0	9.9	13.7	17.4	20.9	24.3	[µK]

Table 5.5.: Calculated energy bands in kHz, E_{rec} and µK in the trap potential of the 3D optical lattice.

optical lattice the switch off might not be completely diabatic. As a consequence the given temperature is a lower bound of the average temperature of atoms. Remember that the data presented here is taken without a lattice power stabilisation (which was only recently introduced). We can see from table 5.5 that it is reasonable to assume that we have a population of several lattice bands (two for Rb and at least six for Yb) because the lowest energy band values of the calculation are below the measured temperature. Especially for Yb atoms we have to assume that a high fraction of atoms is not localised to single lattice sites (above the first six bands). This population spread is not an ideal condition for efficient PA experiments, as it would be beneficial to only populate the ground state of the lattice in order to prepare all atoms with a discrete energy. Future upgrades to the machine are proposed in the next section (5.5.3) of this chapter and will have to improve on this thermal distribution and instead load BECs of Rb and Yb into the optical lattice.

As already mentioned, the largest difference between the atom loss observed in the XODT in figure 5.10 and in the lattices (2D and 3D) in figures 5.16 and 5.17 is the faster initial loss of Yb atoms in the first 250 ms and afterwards slow decrease in Yb atom number in the lattice traps. This phenomenon can be explained by a low lattice filling. For Yb atoms that find no reaction partner the loss rate has to be equal to the off resonant scattering loss if we are not operating in the Lamb-Dicke regime. The Lamb-Dicke regime is reached when $\eta^2(2n+1) \ll 1$, or rather when the coupling of Yb atoms to the off-resonant transition is sufficiently suppressed by the energy structure of the optical lattice. The Lamb-Dicke parameter η for Yb in our 3D lattice trap for example can be calculated to $\eta = 0.45$. Therefore only for atoms with the motional quantum number $n = 0$ the condition is somewhat fulfilled and for higher states $n > 0$ we are clearly not in the Lamb-Dicke regime.

In an effort to prevent 'lonely' Yb atoms, the density of Rb atoms in all presented measurements (XODT and 3D Lattice) compared to [20] is intentionally prepared higher. This unfortunately hinders the detection of the transition in Rb for these measurements. In fact the difference between on and off resonance is hardly visible in the Rb data. However if the densities are prepared the over way around the transition will also be visible in the Rb atom number.

Eventually the same rate equations 5.17 and 5.18 are used to determine PA rates of $K_{\text{PA-2D}} = 8.5(1.3) \cdot 10^{-13}\,\text{cm}^3/\text{s}$ and $K_{\text{PA-3D}} = 1.0(2) \cdot 10^{-12}\,\text{cm}^3/\text{s}$, which show an increase by a factor of ≈ 2 compared to the XODT (section 5.4.5). These values have to be viewed in the context of the mean density in the trap. To put the values into context, Naidon and Julienne [267] have investigated photoassociation resonances of alkaline-earth-metal atoms in optical lattices with different dimensions. While they claim that 2D and 3D lattices can be used to increase the spectroscopic resolution by an order of magnitude, the regime where this effect is observable could not be reached in our experiment due to the current mixture temperatures. Furthermore their calculations with ^{88}Sr (also an element with a narrow intercombination line for PA spectroscopy), motivated by experimental results in [268], show that the precise strength of a PA line (or on-resonance rates) between 2D and 3D lattices are very comparable at equal temperatures.

Finally both values show a successful doubling of the PA rate compared to the bulk trap, but do not necessarily facilitate the detection of much weaker resonances. Nonetheless it is a first step in the direction towards ground state molecules and gives motivation to prepare a mixed Mott Insulator of Rb and Yb to further enhance our PA rate as discussed in the next subsection.

5.5.3. Mott Insulator with an optical lattice

Modern cold molecule experiments utilize molecule formation in optical lattice traps [269][270] and demonstrate novel methods to observe interesting quantum many-body effects via photoassociation [271]. For example the before mentioned high resolution PA of Sr_2 molecules in a lattice allows doppler and recoil free spectroscopy [268] with linewidths of Raman transitions of only about 0.1 kHz [272].

Up until now, the advantages of the 3D optical lattice trap in our apparatus have not been fully exploited. The first photoassociation measurements in section 5.5 showed an increasing PA rate but have been performed with thermal samples and Yb atoms in a non confinement-dominated regime. Therefore we have not yet made use of the enhanced local density of a single lattice site nor its energy structure. The next main goal is to further improve PA rates by starting the photoassociation process with atoms occupying the ground state of the lattice. Achieving this goal will provide even greater spectroscopic precision and as discussed in the outlook in section 7.3.2 may open up the possibility to produce molecules with free-bound STIRAP.

As stated above, photoassociation in 3D optical lattices enhances the efficiency to create RbYb molecules [273]. In this regard, it is recommended to prepare our mixture in a deep lattice regime with a high density allowing to create a Mott insulator (MI) state. The feasibility of MI states for our atomic species is proven by previous results in [274] for Yb and [176] for Rb. Dual Mott insulators have also already shown interesting interactions between bosons and fermions [275]. A dual Mott insulator in our specific alkali - closed-shell (rare earth) atom combination however has not been achieved yet. Using the upgrades and proposals described in the outlook (see chapter 7), the idea is to load a dual species BEC with high phase space density in an 3D optical lattice in order to create a dual Mott

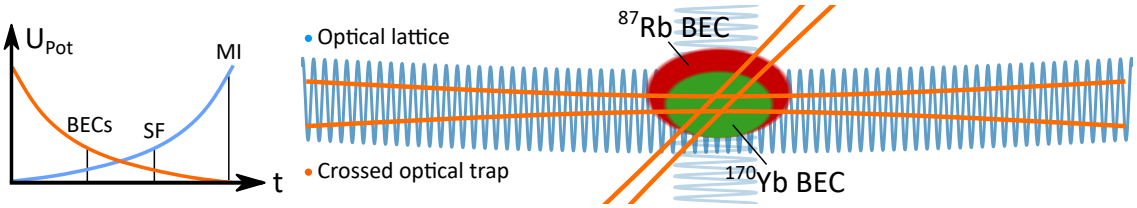

Figure 5.18.: Sketch of the transfer of a dual species BEC with ^{87}Rb and ^{170}Rb into a 3D lattice trap (the sample and beam sizes are not to scale). The dual BEC is loaded into a optical lattice by reducing the trapping potential of the crossed optical trap and increasing the optical lattice potential. At low lattice depth the mixture is in a superfluid (SF) state until it transitions to a Mott insulator (MI) state.

insulator (MI) state.

Let us assume that we are able to produce a dual species BEC with ^{87}Rb and ^{170}Rb (for example in a bichromatic optical trap, see chapter 7.2). This dual BEC then needs to be loaded into a 3D lattice without heating up either species. Therefore the lattice potential needs to be carefully ramped up, while the preparation trap is ramped down. Figure 5.18 shows a sketch of the transfer process but specific power ramps and the transfer time are hard to predict as they depend on the BEC lifetimes and the configuration of the trap that initially holds the samples. Ideally this transition is adiabatic, meaning that the trap depth remains constant for the whole transition process. For this reason the 3D lattice at 1064 nm needs to be power stabilised and properly adjusted to provide the same lattice depth in every beam axis.

In the theory chapter 2.7.2, the behaviour of atoms in this quantum phase in a 3D optical lattice is already discussed in detail. As a reminder, Rb and Yb samples each have different lattice depths at which they turn from a superfluid (SF) state to a Mott insulator state. Since Rb atoms experience a larger lattice depth at equal laser powers, Rb will reach the MI state at a lattice depth, where Yb atoms are not yet localized to single lattice sites. It should be noted that there is also a spatial dependence of the lattice depth due to the Rayleigh length of the lattice beams. Therefore doubly occupied sites with one Yb and one Rb atom corresponding to a Mott insulator state in the center of the trap can be surrounded by a Yb superfluid state, while the Rb Mott insulator extends to larger diameters.

5.5.4. Molecules in a Mott insulator

In principle our ideal molecule experiment starts with exactly one Rb atom and one Yb atom inside each optical lattice site. This would yield a very good atomic wavefunction overlap and the optimal condition for photoassociation and effective molecule production. As the calculation presented in figure 2.15 predicts, this specific pairing is energetically favourable for the isotope combination for the work presented in this thesis. For other combinations of isotopes, the use of Feshbach resonances is necessary to tune the scattering lengths such that a good atomic wave function overlap is warranted. Of course the ideal

preparation is practically impossible because vacancies in the form of empty lattice sites and defects, like two atoms of the same species in a lattice site, still have to be expected. Nevertheless a two-species MI in an optical lattice is a significant improvement compared to the bulk trap. It has already been proposed and demonstrated for RbK [276] that controlling two-species Mott-insulator phases in an optical lattice is a possible approach to form an array of dipolar molecules [277].

Another great benefit of atoms prepared in the lowest energy state in an optical lattice instead of a bulk trap is the prevention of collisions such as two- and three-body loss processes. Even at high densities there is no collisional broadening as it would occur in mixtures in bulk traps. Once molecules are produced (via 2-photon-PA) avoiding collisions is again helpful as they would otherwise strongly limit the lifetime of ground state molecules. Furthermore, the state selective production of molecules in optical lattices has already been achieved [278]. It is thus possible to control the internal rovibronic state of molecules formed inside an optical lattice. Therefore, on optical lattice offers the highest effectiveness for molecule production and is the ideal trap design on the quest for ground state RbYb molecules. Afterwards it might even be possible to create a molecular BEC of RbYb by dynamically melting a Mott insulator [273].

5.6. Summary and Outlook

Here the results of the first intercombination line 1-photon photoassociation of RbYb [20] are summarized. Two most likely connected transitions at $-3057.2(3)$ MHz and $-3074.3(3)$ MHz have been found. Their binding energies have been determined by evaluation and calculation of all relevant shifts, including the Zeeman shift, light shift and thermal shift. However, the assignment of the excited molecular states is challenging. Several attempts at the interpretation of the detected line pair are presented in this thesis but neither approach leads to an entirely conclusive solution explaining the Zeeman shifts and zero field splitting. Due to the limited information available, an investigation towards the localisation of transitions with Rb prepared in the $f = 2$ state or a different m_f state via microwave preparation of Rb has already started. Data about a possible line splitting and shifts in magnetic fields of other excited molecular states might allow a proper state assignment.

Furthermore the line strength and width of a single molecular state at the $^3P_1$ asymptote has been discussed. Compared to the first results obtained in [1] we could increase the PA rate by one order of magnitude in the XODT. We find an additional increase by a factor of 2 in the photoassociation rate from $K_{\text{PA-XODT}} = 5(2) \cdot 10^{-13}\,\text{cm}^3/\text{s}$ in a crossed optical dipole trap to $K_{\text{PA-2D}} = 8.5(1.3) \cdot 10^{-13}\,\text{cm}^3/\text{s}$ in a 2D and $K_{\text{PA-3D}} = 1.0(2) \cdot 10^{-12}\,\text{cm}^3/\text{s}$ in a 3D optical lattice. The quest of finding more deeply bound states (with FCFs estimated to be much smaller) is still limited by the sensitivity of our experiment. In the future, experiments with lower temperature and higher density in a mixed Mott Insulator state in the 3D lattice trap could increase the PA rate even more to make these weak transitions accessible and thus lead to important information about the excited state potential or

allow a proper molecular state assignment. However we expect to have already found the strongest line as additional signals have not been observed over the course of multiple scans across a 10 GHz range. Furthermore, a potential weakly bound state (with a larger transition matrix element for the free-bound transition) below 100 MHz detuning from the atomic resonance is inaccessible with our spectroscopy.

The detected line may nonetheless prove very useful if we can achieve high Rabi frequencies with this free-bound transition by enhancing the PA rate with dual BECs or Mott Insulator states. In the upcoming chapter the currently obtained Rabi frequencies, which are essential for the prospective production of weakly bound ground state molecules via STIRAP (see chapter 7.3.2), are determined with 2-photon photoassociation spectroscopy. If the attempt to utilise the excited molecule potentials connected to the Yb $^3P_1$ asymptote does not result in efficient STIRAP to the ground state potential, one can always revert back to the $^2\Pi_{\frac{1}{2}}$ exited molecular state at the Rb D1 asymptote [11], [14], [102].

6.

2-Photon-Photoassociation

6.1. Introduction to the RbYb ground state

After the discovery of a transition to the excited molecular state via 1-photon spectroscopy, we can use this state as a gate into the ground state potential. As the name suggests, 2-photon photoassociation (2-photon-PA) involves two photons. While the first one couples the scattering state of free atoms to a vibrational state of the electronically excited potential, the newly added second photon can connect this state to bound states in the ground state potential. For more thorough discussion refer to theory section 2.6. The spectroscopic results presented in this chapter are published in [20] and are also discussed in [1].

As illustrated in figure 6.1, the first photon is called ν_{FB} 'free-bound' and the second is named ν_{BB} 'bound-bound'. In our case the ground state is composed of the atomic $^2\mathrm{S}_{1/2}$ state of Rb and the $^1\mathrm{S}_0$ state of Yb. Since the sole angular momentum is contributed from the Rb atom, the molecular state is a $^2\Sigma^+_{1/2}$ state in the short range and $\Omega = \frac{1}{2}$ in the long range description of Hunds case (c) (see chapter 2.3.2).

With 2-photon spectroscopy one can learn a lot about the RbYb molecule as the detection of bound vibrational states allows a mapping of the $^2\Sigma^+_{1/2}$ potential energy curve. Moreover the position of vibrational states close to the threshold is important for the calculation of Feshbach resonances. In the preceding works of F. Münchow [13] and C. Bruni [14] seven levels with a binding energy of up to $E_B = h \cdot 58.5\,\mathrm{GHz}$ have already been observed. This achievement is a result of 2-photon PA close to the D1 line of Rb and lead to an accurate determination of the s-wave scattering lengths for all isotope combinations of RbYb [15]. Although a pathway via the different $^2\Pi_{1/2}$ excited potential was utilized, the results can still be used for 2-photon PA close to the intercombination line of Yb as presented here since both methods share the same ground state potential. Furthermore the experimental data allowed calculations to model the rovibrational levels, the number of bound states $N = 66$, the potential depth $D_e = 787(18)\,\mathrm{cm}^{-1}$ and most importantly the $C_6 = 2837 E_h {a_0}^6$ and $C_8 = 4.6 \cdot 10^5 E_h {a_0}^8$ values[1] [15]. All this information is of great advantage for us, as it practically hands us the transition frequencies for our second PA photon on a silver platter. The predicted binding energies from Borkowski et all. [15] for the vibrational levels of a RbYb molecule using the isotopes ^{87}Rb and ^{170}Yb used in this thesis are given in table 6.1.

[1] $E_h = 2R_y = \frac{\hbar^2}{m_e {a_0}^2}$ is the Hartree-Energy, a physical constant in atomic units that is used as a unit of energy.

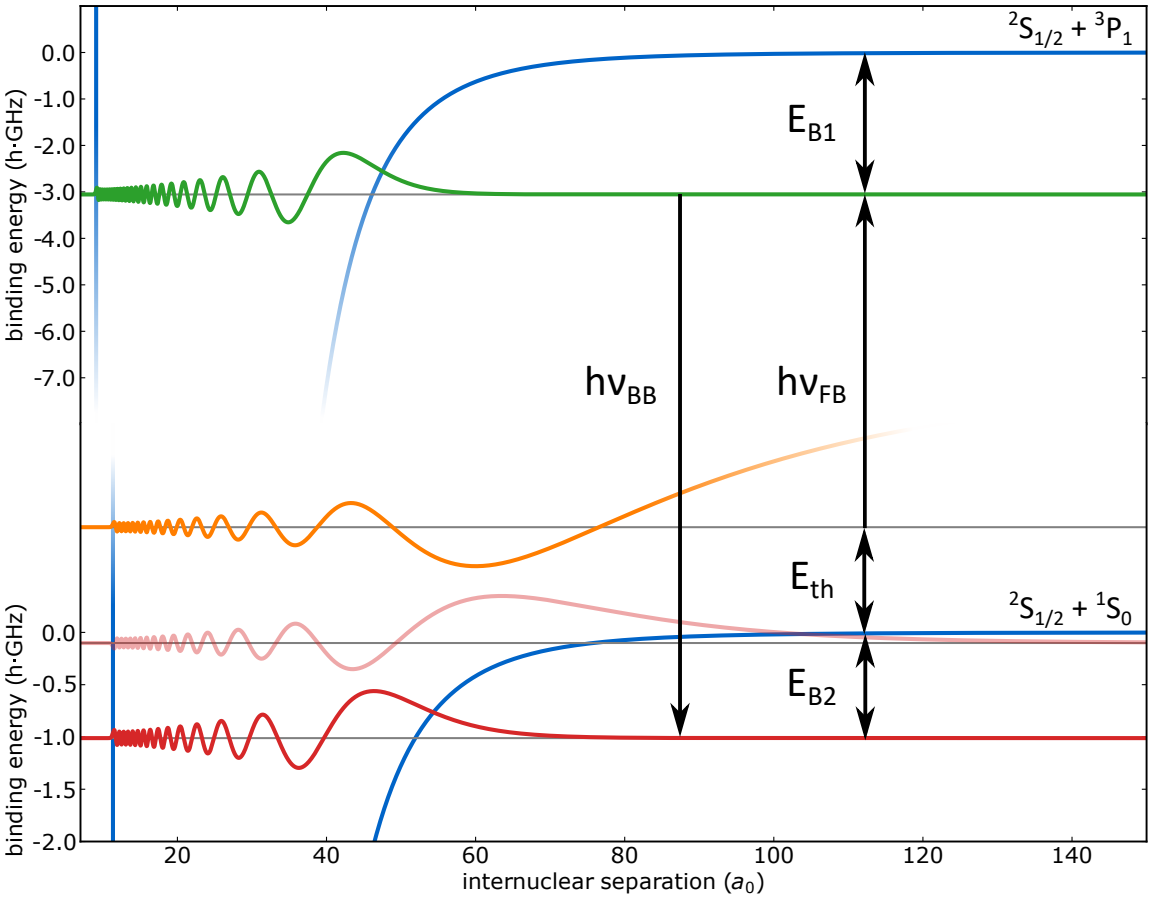

Figure 6.1.: Scheme for the 2-photon photoassociation at the intercombination line of Yb. The relevant wavefunctions of the scattering state (orange), the electronically excited state (green) and the vibrational ground state (red) are connected to their respective potential curve (blue). The energy of the scattering state is exaggerated for clarity. The frequencies required to conduct 2-photon-PA are affected by the thermal energy of the atoms E_{th}, the binding energy E_{B1} of the excited state and the binding energy E_{B2} of the ground state.

The data for those binding energies mostly relies on 2-photon-PA with a different isotope combination, namely: ^{87}Rb and ^{176}Yb in a dual-species MOT [279] and a few transitions with other isotopes to obtain the mass scaling. Thus the energies have been adjusted with Born-Oppenheimer mass scaling presented in chapter 2.3.3, which is reported to be remarkably accurate due to the high mass of the molecule [280].

$\Delta\nu'$	ν	binding energy F=1	binding energy F=2	hyperfine splitting
-1	65	−0.103 GHz	−0.103 GHz	0.2 MHz
-2	64	−1.019 GHz	−1.017 GHz	1.1 MHz
-3	63	−3.675 GHz	−3.673 GHz	2.5 MHz
-4	62	−9.018 GHz	−9.013 GHz	4.5 MHz
-5	61	−17.997 GHz	−17.990 GHz	7.2 MHz
-6	60	−31.564 GHz	−31.554 GHz	10.5 MHz
-7	59	−50.665 GHz	−50.650 GHz	14.4 MHz

Table 6.1.: Binding energies and hyperfine splitting for the ground state potential of the ^{87}Rb^{170}Yb molecule from [15][281].

6.2. 2-photon-photoassociation with the intercombination line

The 2-photon-PA experiments are carried out in the crossed optical dipole trap in a similar way as described in the previous chapter. While the ν_{FB} 'free-bound' photon is identical with the one used for the 1-photon-PA, the second ν_{BB} 'bound-bound' photon can be superimposed from the same fiber laser source. All results appearing in this chapter are thus achieved with photons originating from the same source with a frequency close to the $^1\mathrm{S}_0 \rightarrow {}^3\mathrm{P}_1$ intercombination line of Yb and we can therefore we assume the light to be coherent and any frequency uncertainty caused by the laser or its stabilisation to be identical. While this perfect coherence is not necessary for the spectroscopy of the two least bound levels shown in figure 6.2, it is important for the dark resonance spectroscopy visible in figure 6.3. 2-photon-PA experiments along the D1 Rb line were performed with a separate unlocked diode laser and a wavemeter for detuning measurements with an uncertainty of to $10 - 100$ MHz [279]. Therefore an improved resolution and accuracy of the spectroscopy can be expected from new investigation presented here.

As already mentioned the search for a two-photon resonance was far less time consuming than the search for a one-photon line. The free-bound laser was set to the −3057 MHz resonance ($\delta_{\mathrm{FB}} = 0$), while the bound-bound laser detuning δ_{BB} was scanned across the predicted binding energies in table 6.1. Both laser beams are switched on simultaneously and run continuously for $t_{\mathrm{PA}} = 1$ s. For the least bound level $\Delta\nu' = -1$ at 102 MHz an AOM was used to produce the necessary detuning. EOM sidebands were necessary to access the second bound vibrational level $\Delta\nu' = -2$ at 1011 MHz. Having the first (free-bound) PA-laser on resonance results in the typical Yb atom loss that was previously discussed in

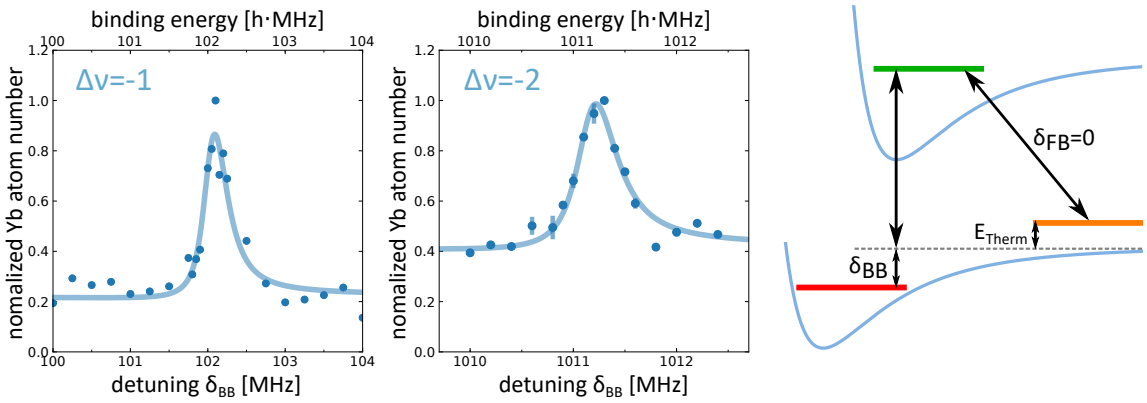

Figure 6.2.: Spectroscopy of the $\Delta\nu' = -1$ and $\Delta\nu' = -2$ states of the RbYb ground state potential by 2-photon-PA. The level scheme on the right illustrates the spectroscopy method, in which the bound-bound laser is scanned while the free-bound laser is kept on resonance. The data is fit with formula 2.39, which was integrated over the Boltzmann distribution, leading to the distortion to higher binding energies.

chapter 5. In figure 6.2 scans with peaks of 'returning' Yb atomnumbers can be observed, when the (bound-bound) second PA-photon is set to the correct δ_{BB} detuning. This signal is known as a 'loss-of-loss signal', where a revival of the detected atomnumber implies that atoms remain in the scattering state. As explained in theory section 2.6 the second laser thus successfully prevents the transition to the electronically excited state of the first photon. Both signals have been fit with formula 2.39 and integrated over the Boltzmann distribution creating the slight distortion due to thermal broadening of the collisional state. In contrast to [1] the data presented in figure 6.2 results from multiple measurements to increase the accuracy of the fit. The fit curves for $\Delta\nu' = -1$ and $\Delta\nu' = -2$ including this thermal component shown in figure 6.2 are centered at 101.97(1) MHz and 1011.09(1) MHz respectively. The associated linewidths determined with a Lorentzian fit are 0.17(2) MHz and 0.23(2) MHz. Their linewidths are thus an order of magnitude smaller than the ones for the 1-photon-PA transition. Unfortunately more vibrational levels in the ground state could not be accessed. The next levels $\Delta\nu' = -3$ and $\Delta\nu' = -4$ have predicted binding energies of 3.67 GHz and 9.02 GHz.

6.3. Shifts

In analogy to the 1-photon-PA line in the previous chapter, the 2-photon-PA resonance is shifted by similar effects. This chapter discusses all relevant line shifts influencing the binding energies of the observed bound states.

6.3.1. Zeeman shift

The Zeeman shift of both states was determined by measuring the same lines for multiple magnetic fields, similar to the procedure in subsection 5.4.1. The shift was very small with

less then 0.1 MHz/G [1], which indicates that the least bound states in the ground state potential shift similar to the scattering state. Therefore it is reasonable to assign these least bound states with $|F = 1, m_F = -1\rangle$ to atomic Rb character in a magnetic field (i.e. $\mu_{\mathrm{RbYb}} = \mu_{\mathrm{Rb}}$). Furthermore no neighbouring transitions with a different magnetic moment were found, which suggests that the bound-bound laser does not couple any Rb Zeeman or hyperfine states. For more deeply bound molecular states the electron cloud of Yb would come closer to the Rb atom due to shorter internuclear distances, which for the excited molecular state was found to reduce the hyperfine splitting compared to the atomic values [19].

6.3.2. Light shift

Since the scattering state and the detected bound states have almost the same polarizability at trapping wavelength, the light shifts from trapping light should cancel to a great extent. Only for deeply bound ground state molecules a significant change in polarizability is to be expected [282]. Therefore the light shift should not produce a relevant influence on shallow binding energies for the bound states. In contrast to the analysis of the shift for the electronically excited state in subsection 5.4.2, no measurements were undertaken in this case.

6.3.3. Thermal shift

Our scattering state $|1\rangle$ is thermally distributed, which means that some collisional partners need less energy to be associated to excited molecules or are energetically further away from a bound state in the ground state potential. Under the same trap conditions presented in section 4.4.4 the thermal shift can thus be assumed to be -0.2 MHz according to the value determined for 1-photon-PA in 5.4.3. Here this shift is already included in the fit curve.

In figure 6.2 this effect becomes visible as it produces a broadening of the expected side of the line and offsets the center of the line compared to a Lorentzian fit. It is only remotely noticeable in the shape of figure 6.3 in the upcoming section but nevertheless hinders the determination of the lifetime of the dark state. Furthermore a thermal distribution is always a challenge to overcome, since it is desirable and more effective to perform STIRAP (see chapter 7) from clearly defined energies, ideally of course with mixed BECs and/or a Mott Insulator (see section 5.5.3).

6.4. Dark resonances

After the location of the 2-photon-PA lines, the 2nd photon was tuned to resonance, i.e. $\delta_{\mathrm{BB}} = 0$. Now the spectroscopy process can be inverted by scanning the first laser across the 1-photon-PA resonance at -3057 MHz. The resulting signals for both bound-bound resonances is presented in figure 6.3. In contrast to 1-photon-PA spectroscopy, where the second laser is missing, we observe a sharp peak in the center if both lasers are on resonance. The same observations have for example been made with LiYb [283], RbCs [159], CsYb

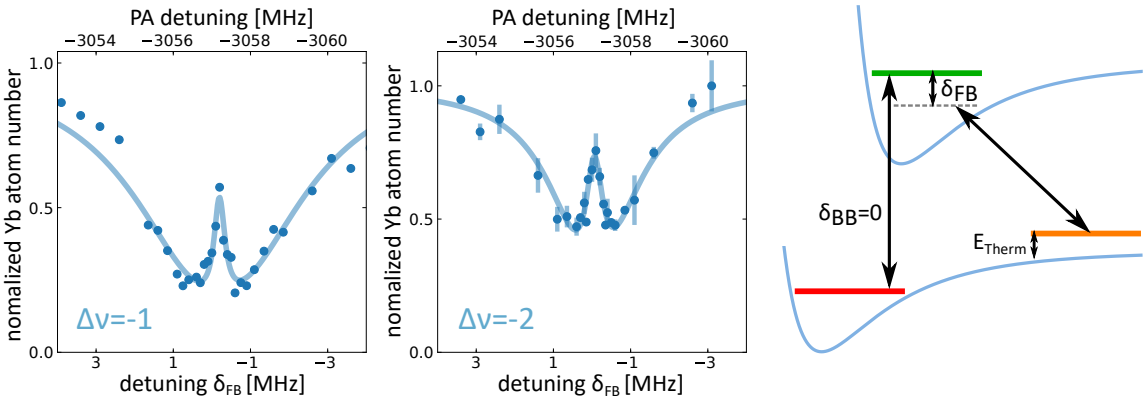

Figure 6.3.: Dark resonance spectroscopy of the 3057 MHz 1-photon-PA transition to the RbYb excited state potential via 2-photon-PA. For this 2-photon spectroscopy method, dark resonances can be observed if the free-bound laser is scanned while the bound-bound laser is kept on resonance with the respective ground state level. The data is fit with equation 2.39, which is again integrated over the Boltzmann distribution. (Published in [20] and also presented in [1].)

[96], NaK [284] or Rb_2 molecules [285] in a BEC. The findings can be explained by the theory of electromagnetically induced transparency (EIT) [157] and dark state spectroscopy discussed in chapter 2.6. The dark state is a superposition of states that does not couple to the electronically excited state due to the destructive interference of the probability amplitudes for different paths. Here these two states are the scattering state and the molecular ground state. Since the bound states in the ground state potential have a comparatively long lifetime the 'transparent' peak in the center prevents the population of the dark state. For increasing intensity of the bound-bound laser this peak will at first broaden [285] and than split the PA line into an Autler-Townes pair, according to the light shift picture [286]. This effect was not observed for either of the states because of the limited available light intensity and regardless would have been prevented by off resonant scattering.

Nevertheless some results can be collected from fits performed with equation 2.39. Since we work in a thermal mixture we have to average over a Maxwell-Boltzmann distribution. We then make an educated guess for the parameters in the equation and subsequently perform a curve fit resulting in the solid line in figure 6.3. The dark resonance fit gives sharp peaks with widths for both dark resonance peaks of 0.20(5) MHz ($\Delta\nu' = -1$) and 0.20(7) MHz ($\Delta\nu' = -2$). The width depends on finite temperature effects and the ratio between the Rabi frequencies Ω_{FB} and Ω_{BB}. For smaller Ω_{BB} and larger Ω_{FB} the width decreases and vise versa. The depth of the peaks is affected by the effective linewidth Γ_{eff}, which includes the decoherence of the dark state. For complete coherence, $\Gamma_{eff} = 0$, the electronically excited state would be completely dark raising the normalised Yb atomnumber to one if both free-bound and bound-bound light fields are on resonance. The coherence times for both dark states are thus $\frac{1}{\Gamma_{eff}} \approx 5\,\mu s$. In the case of partial coherence the depth and thus 'darkness' of the state is reduced and vanishes if both free-bound and

bound-bound light fields are incoherent. Moreover, for both lines we do not fully deplete the Yb atom number with the first photon due to a small free-bound Franck-Condon factor. Furthermore the fit enables us to determine and compare both Rabi frequencies Ω_{FB} and Ω_{BB}. Without dark resonances these frequencies can be determined from the Autler-Townes splitting but a great advantage of dark resonance spectroscopy is the evaluation of both Rabi frequencies with a single scan of the free-bound detuning δ_{FB}. For both dark resonances the fit yields free-bound Rabi frequencies of $\Omega_{\mathrm{FB}} \approx 2\pi \cdot 1\,\mathrm{kHz}$ and bound-bound Rabi frequencies of $\Omega_{\mathrm{BB}} \approx 2\pi \cdot 1\,\mathrm{MHz}$. The interpretation of this result is discussed in the following section and in the outlook in chapter 7 of this thesis.

6.5. Franck-Condon factors and Rabi frequencies

In this section the relevance of Franck-Condon factors and the Rabi frequencies, Ω_{FB} and Ω_{BB} presented in section 6.4, in the context of molecule production is discussed.

Unfortunately the electronically excited state of a molecule is generally very short lived[1], while a bound level in the electronic ground state has a much longer lifetime. Considering our ambition to produce deeply bound ground state molecules, a rapid transfer to a stable bound state is preferred before excited molecules have time to split up again or decay into unknown bound states. Franck-Condon factors (f_{FC}) and Rabi frequencies Ω_{FB}, Ω_{BB} between states are a great measure for the strength or rather the rapidness of transitions. It is important to notice that the f_{FC} is purely a property of the transition, while the Rabi frequency also depends on the intensity of the driving laser field. Usually large Franck-Condon factors (or Rabi frequencies) are desired to drive transitions either really fast or to have more margin of error in driving rapid adiabatic passages (RAP). Furthermore Rabi frequencies with comparable values for the first and second photon transition would be interesting for STIRAP applications, where the undesirable fast decay of the excited state is circumvented entirely (see section 7). Regrettably for the observed transitions STIRAP would be more than challenging as the reported Rabi frequencies are three orders in magnitude apart. The crucial aspect here is the low Rabi frequency of the free-bound transition.

Here, an attempt at the estimation of Franck-Condon factors for the bound-bound transition with the help of the Rabi frequencies from dark state spectroscopy is shown. In the theory chapter 6.5, atom-photon interaction and Ω_0 the atomic Rabi frequency are already explained. For Ω_0 the atomic Rabi frequency with the natural linewidth γ_{at} and the atomic saturation intensity I_{sat} of the Yb intercombination line is used.

$$\Omega_0 = \gamma_{\mathrm{at}}\sqrt{\frac{I_{PA}}{2I_{\mathrm{sat}}}} \qquad \text{, with} \quad I_{\mathrm{sat}} = \frac{\hbar\omega_{\mathrm{at}}{}^3\gamma_{\mathrm{at}}}{12\pi c^2} \tag{6.1}$$

Since the populated states in our PA experiments are among the least bound, we assume that their transition dipole moments are still close to the atomic value (see 5.4.6). It is thus reasonable to estimate the Franck-Condon factors with the used photoassociation intensity

[1] For metastable states lifetimes can be larger.

I_{PA}, Ω_0 and bound-bound Rabi frequency Ω_{BB} determined with the fit in the dark state spectroscopy[2]. With a free-bound laser intensity of $I_{\mathrm{PA}} = 26\,\mathrm{W/cm^2}$ and bound-bound laser intensities of $5\,\mathrm{W/cm^2}$ for the $\Delta\nu' = -1$ state and $1\,\mathrm{W/cm^2}$ for the $\Delta\nu' = -2$ state, respectively.

$$f_{FC} = \left(\frac{\Omega_{\mathrm{BB}}}{\Omega_0}\right)^2 = \frac{{\Omega_{\mathrm{BB}}}^2}{{\gamma_{\mathrm{at}}}^2}\frac{2I_{\mathrm{sat}}}{I_{\mathrm{PA}}} \tag{6.2}$$

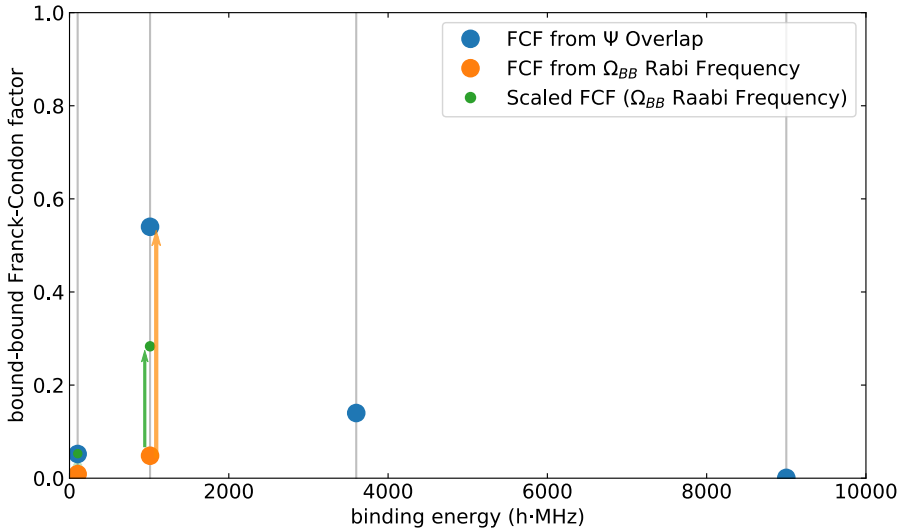

Figure 6.4.: Franck-Condon factors (f_{FC}) determined with equation 6.2 and the wavefunction overlap analog to the method presented in chapter 5. The orange points indicate the lowest estimate for values determined from Rabi frequencies via experimental dark state spectroscopy. The orange arrow represents a possibly underestimated value due to PA beam misalignment. The green points and arrow indicate a possible scaling of the experimental f_{FC} values. The blue markers are values obtained from wavefunction overlaps, which have to be viewed with caution.

In figure 6.4 the f_{FC} values determined with equation 6.2 and the wavefunction overlap along the lines of the method presented in figure 5.12 are presented. The numbers calculated from Ω_{BB} are to be regarded as estimates of lower bounds as they rely on the assumption that the PA beam perfectly intersects with the atom mixture. For any misalignment the effectively used intensity is lower and we might thus induce the same Rabi frequency with less light, making the f_{FC} value larger (indicated by orange arrow). The green points and arrow indicate a possible scaling of this underestimation based on the f_{FC} value corresponding to the least bound vibrational level obtained via the wavefunction overlap. Unfortunately we obtain a miss match of factor of two between both experimentally observed 2-photon-PA transitions. The values obtained from wavefunction

[2]The PA intensity was determined with a measured beamwaist of $1/e^2$ radius 110 µm.

overlap have to be treated with even more caution since the states and wavefunctions fitted using the model electronically excited potential are not very reliable. Especially the short range potential and the number of bound states are unknown and have a large influence on the f_{FC} values. Nevertheless the tendency of both first states agree in both approaches. Furthermore, for the modeled long range part the maximum f_{FC} is predicted between the $\Delta\nu' = -2$ and $\Delta\nu' = -3$ state. This results from the specific shapes of the ground and electronically excited potentials. The width of the potential at the energy in which we fit our wavefunctions is the deciding aspect for large wavefunction overlaps. In between the binding energies of $\Delta\nu' = -2$ and $\Delta\nu' = -3$ the outer turning points at the long range tail of the excited potential have the same internuclear separation as the ground state potential and thus the possibility to get a large f_{FC} is highest for these states.

6.6. Summary and future prospects

We presented the results of 2-photon spectroscopy via the previously discovered free-bound transition at $-3\,\mathrm{GHz}$. The two least bound ground states, corresponding to the preparation of Rb in the $f = 1$ hyperfine state, have been measured with high accuracy. The binding energies are $E_\mathrm{B}(\Delta\nu' = -1) = h \cdot 101.9(1)\,\mathrm{MHz}$ and $E_\mathrm{B}(\Delta\nu' = -2) = h \cdot 1011.1(1)\,\mathrm{MHz}$. The determined values are remarkably close to the predictions from theory [15] (see table 6.1) regarding the large experimental errors[1] of previous measurements with the D1 line underlying the theoretical model.

The lines have been observed with two different methods. First the bound-bound laser is scanned, while the free-bound laser is kept on resonance in order to find a returning atomic signal. In the subsequent dark state spectroscopy this configuration is inverted and thereby creates a sharp peak in the center of the 1-photon-PA line due to the induced dark state. With a fit of the particular (EIT) line shape the Rabi frequencies Ω_FB and Ω_BB can be extracted and give us estimates for the Franck-Condon factors of the observed transitions.

Sadly not more than two lines could be observed but with more data the ground state potential energy curve could be optimized further. Moreover the hyperfine splitting in the ground state is expected to be observable with our resolution, but up until now transitions corresponding to Rb in the $f = 2$ hyperfine state were not detected. It is possible that we first need to find a free-bound transition for Rb prepared in $f = 2$ in the electronically excited potential. On the other hand a similar experiment with an alkali-earthalkali combination Rb + Sr has shown 2-photon PA with the bound levels in the excited state and in the ground state corresponding to different hyperfine states [252]. Due to the requirement to bridge the hyperfine splitting in our system, a part of the search for such transitions needs to be done with an additional laser system for the fiber laser detuning methods employed in this chapter.

Eventually the exact determination of the hyperfine splitting is relevant for possible Feshbach resonances. The hyperfine coupling represents the interaction between nuclear

[1] The errors ranged from 7 to 257 MHz

spin and the electron spin density at the nucleus, which is a main coupling mechanism for Feshbach resonances between alkali and closed-shell atoms and therefore of great interest for future RbYb experiments [25].

7.

Quest for the absolute ground state

Looking back at the results of our photoassociation measurements in chapters 5 and 6, the experiment would benefit from several upgrades. First, the optical trap configurations and the status of the thermal quantum gas mixtures presented in chapter 4 need to be improved to achieve a higher density of atoms as discussed in the first two sections 7.1 and 7.2. The proposals contain the implementation of a bichromatic optical trap, an adventurous idea to scrap an entire vacuum chamber and include more moderate changes that are already under construction. Furthermore, the different paths towards vibrationally excited ground state molecules are then discussed in chapter 7.3 and the ultimate goal of production absolute ground state molecules is covered in chapter 7.4.

7.1. Improving conditions for 1-photon PA near the intercombination line

During the analysis of the PA data in chapters 5 and 6, off resonant scattering from the atomic transition was a recurring issue, which prevented us to use long illumination times with PA light. In fact the amount of Yb loss is currently the limiting factor for the hunt of weak molecular lines. With the current experiment design and resulting densities, we are most likely unable to detect more 1-photon photoassociation signals close to the atomic threshold. Therefore an obvious measure is to prepare more atoms to raise the density after evaporation in the final trap. Ideally we strive for large Rb and Yb BECs in order to prevent thermal spread.

In the following I present plans and ideas on how to improve the current status. First let us start to look at the issues of long range transport. For example, when we transfer cooled and compressed Yb atoms from the MOT into a single beam ODT we lose the confinement along the tweezer axis and about 50 % of atoms. On top of that the transport itself loses at least 50 % of the atomnumber mostly due to the lifetime of the trap. In total that amounts to about an order of magnitude in atom loss.

In his thesis Franzen [1] already proposed an improved transport via an optical lattice. A fast transport (in tens of ms) with high efficiency was already demonstrated with a moving lattice, which is generated by the interference of a Bessel and a weakly focused Gaussian laser beam for Cesium in [287]. In contrast to the small 1 mm gap in our vertical lattice transport, the long distance transport (45 cm) can be realised by controlling the AOM fre-

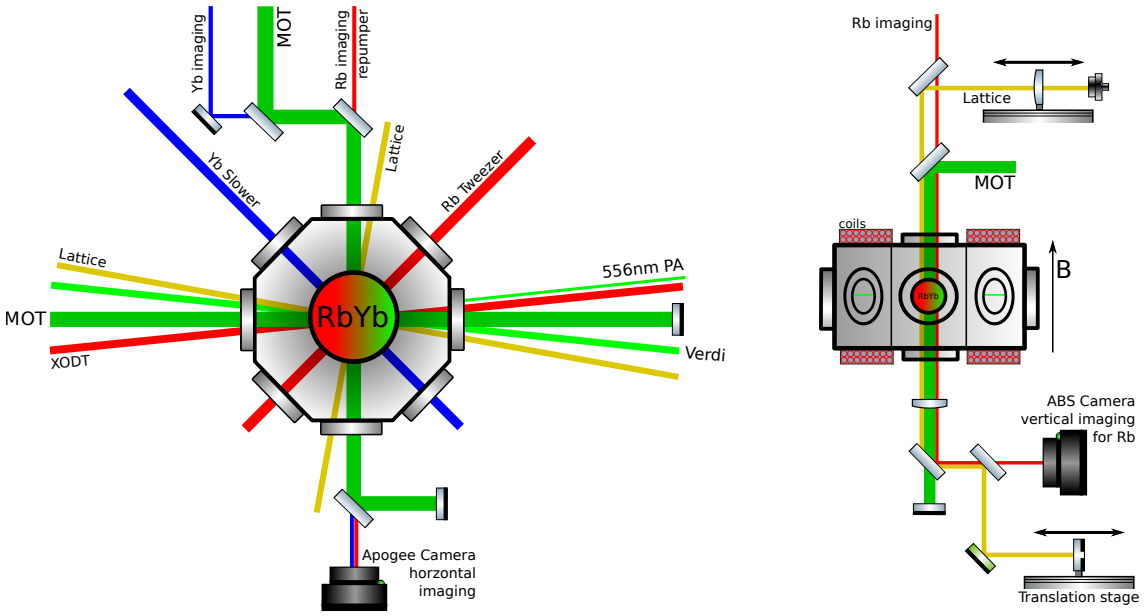

Figure 7.1.: Schematic illustration for a proposal of a 'simplified' experiment setup. By scraping the Yb production chamber and introducing a two-chamber setup, the transport of Yb is not needed anymore. The reconfiguration however would move the Yb MOT into the science chamber, which limits to optical access depicted by the newly arranged optical lattice beams.

quencies of both beams. The existing translation stage can then be used to follow the atoms with the laser focus of the tightly focused beam. Unfortunately, a narrow linewidth laser source is needed to create an optical lattice. Our homebuilt fiber amplifier currently used for the Yb tweezer has a broad linewidth adopted by its IPG seed laser (see. chapter 3.4.4) and would have to be replaced. The newly build fiber laser from chapter 3.28 shows that we might be able to build a suitable narrow linewidth laser but SBS suppression with multiple amplification stages was not yet attempted by ourselves. As a reminder the interference from vacuum windows for a narrow spectrum laser previously create unwanted parasitic lattices, which was a suspected reason for unsuccessful Rb transport. If the transport is however done on purpose with a much stronger lattice this effect might be negligible. Since this tweezer update already proposes a major reconstruction with uncertain outcome, we might as well pitch other drastic ideas.

Since most of the data in this thesis originates from Yb atoms at around 10 µK, which is a temperature that has been possible to reach with the Yb intercombination line MOT alone, the question of redundancy of three chambers and the requirement to transport Yb has to be asked. Loading an Yb MOT in the science chamber and overlapping it with a crossed ODT with Rb is practically feasible. In the search for 1-photon PA resonances a Yb MOT could maybe even be loaded continuously because the signal can be observed in the Rb atomnumber just as well. In this case the illumination time with PA light is limited by the lifetime of the Rb tweezer (30 s) or collisions with Yb atoms. A continuously

loaded MOT however probably has to be compressed as it is orders of magnitude less dense depending on the laser detuning and magnetic field gradient. Luckily the feasibility of this approach can be tested with the newly discovered 1-photon-PA resonance. Even in the present three chamber setup, Rb could be transferred from the Rb ODT into the Yb ODT and subsequently transported from the science chamber into the Yb production chamber. Since the Yb ODT is already adjusted to the compressed Yb MOT only the PA laser setup has to be moved to the Yb production chamber. Furthermore it is even possible to introduce a crossed ODT in the Yb production chamber for additional tests but of course takes more time and effort. Moreover if the overlap of both traps turns out to be the bottleneck, we can still load the Yb MOT into the same (crossed) ODT. Of course to realise the two chamber idea, the complete vacuum system needs to be reconfigured. The lattice beams and the imaging system would need to be rebuilt around the new MOT setup. In figure 7.1 the alternative design proposal is depicted.

Finally the optical access has historically proven to limit advances in the previous experiment operating with a single chamber. The same issue has provoked many research groups to use vacuum chamber glass cells [288] instead of a metal chamber for their next generation experiment, allowing them to use quantum gas microscopes for the single site detection of molecules [289]–[291].

Arguments that speak against this approach are fairly technical and include the vacuum pressure, which would definitely be worse if the Yb Zeeman slower with oven is directly attached to the science chamber. Furthermore the chamber would possibly need regular service due to window changes opposite of the slower depending on the performance of the newly developed capillary oven in chapter 3.1.1. Another proposal for loading of a Yb MOT without the Zeeman slower is a 2D MOT design in a dual MOT scheme utilizing the principle $^1S_0 \rightarrow {}^1P_1$ transition [292]. In this compact alternative method, atoms are transversely cooled from a dispenser and guided into the 3D MOT region as a collimated atom beam with an additional pushing laser beam.

On a shorter timescale, small and more realistic changes are currently included in the Yb section of the experiment. First a new slower laser - the DL Pro from Toptica with 100 mW - replaces the old laser system running at the $^1S_0 \rightarrow {}^1P_1$ transition. It offers more power to increase the available slowing intensity, which can boost the Yb MOT loading rate. Secondly the capillary oven introduced in chapter 3.1.1 is replacing the old design and hopefully provides a guided beam of atoms to further increase the Yb loading rate and elongates the time to the next oven refilling. The last idea to improve the final density of Yb atoms is the balanced trap, which is introduced in the following section.

7.2. Balanced optical dipole traps

The main issue, limiting the phase-space density of the diatomic mixture in the combined trap, is the large discrepancy in potential depth between the two atomic species. The XODT at 1064 nm produces a trap depth for Rb that is about ten times deeper compared to Yb, making it practically impossible[1] to evaporate both species to degeneracy at the same time. However, since high densities and ultracold temperatures are necessary for the advanced manipulation of molecules the implementation of a balanced trap would help us to increase the density and thus improve the sensitivity to undiscovered PA lines by enhancing PA rates and in addition reduce thermal influence to facilitate two-photon transitions laying the basis for STIRAP (see chapter 7.3.2). Furthermore, it could be the starting point for a mixed MOTT insulator in a 3D optical lattice, which was already presented in chapter 5.5.3.

7.2.1. Bichromatic traps

One possibility to balance the trap depth for Yb and Rb would be a bichromatic trap [12]. It is based on lasers with different wavelengths and uses the different wavelength-dependent atomic polarizabilities to combine attractive and repulsive optical potentials. From figure 2.10 we know the polarizabilities for Rb and Yb and have multiple possibilities to choose a wavelength for an additional 'balancing' laser.

Easily available laser sources are at 532 nm and 790 nm, while a third option at 420 nm is on the expensive side. The first possibility at 532 nm is easily accessible by frequency doubling of 1064 nm light. It is far detuned from all relevant atomic transitions of both species and thus has only negligible scattering issues. Furthermore, lots of power is available (in our case up to 10 W via a VERDI laser), which can be used to deepen the potential for Yb and raise it for Rb. The laser system presented in chapter 3.6 is already available in our lab and was constructed towards the end of my thesis. Up until now it was not added into the experimental sequence but is coarsely aligned on top of the existing XODT.

In the animated GIF in figure 7.2 an implementation into the experimental cycle is simulated. Its start shows the final trap configuration in the XODT presented in 4.4.4. In its evolution the intensity of the 532 nm balancing beam is increased up to 4 W. While this ramp evaporates Rb, it also increases the trap depth for Yb. Ideally the intensity of the 1064 nm XODT has to be reduced during this step to keep the potential depth constant for Yb and thus prevent heating.

Similar approaches with bichromatic traps in heteronuclear molecule experiments have successfully enabled evaporation to dual degeneracy with Cs and Yb [293] or with a degenerate Fermi-Bose mixture of Rb and Yb [100]. Furthermore, our research group already has some experience with Rb-Yb with a bichromatic trap design at 1064 nm and 532 nm and [12], [204]. While figure 7.2 presents the optical potential along a single ODT axis (x-axis) showcasing the principle to balance the potential depths for Rb and Yb, there

[1] Maybe tilting the trap for Rb with a very large magnetic gradient could be an exception but i would deem this as impractical.

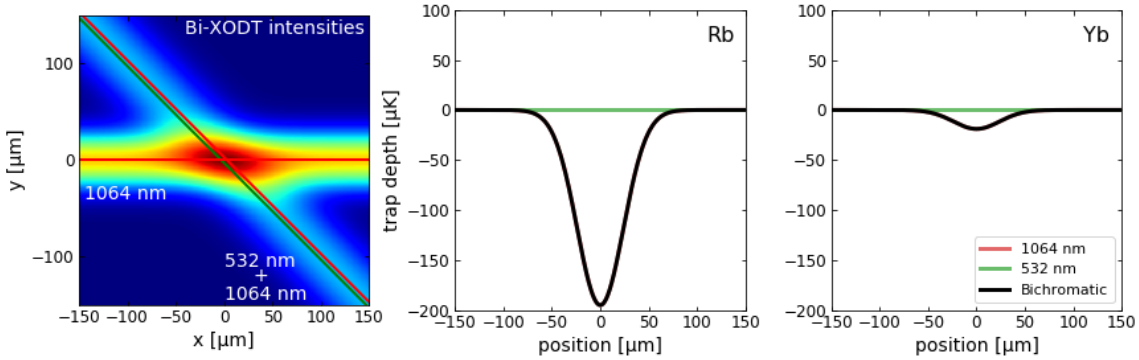

Figure 7.2.: Animation showing the balancing of a 1064 nm XODT using an additional 532 nm laser. The 2D plot on the left shows the trap geometry and light intensities, while the trap depths for Rb and Yb along the x-axis can be seen in the segments on the right. Initially, the first frame displays the final trap with a single wavelength 1064 nm configuration presented in 4.4.4 together with the corresponding trap depths for Rb and Yb. In the simulated sequence the intensity of an additional 532 nm beam is increased up to 4.25 W. The beam is aligned along the secondary XODT beam and has a beam waist of 40 µm. The reduction of the Rb potential depth and increasing Yb potential depth showcases the adaptation of the trap in one dimension.

are difficulties to overlap the light-fields at different wavelengths in all three dimensions. Focusing laser beams at 1064 nm and 532 nm to the same beam waists for example already leads to different Rayleigh lengths for the individual beams and results in a complex 3D optical potential that is very sensitive to the beam alignment and intensity ratio of the light fields. Furthermore, experiments in the old apparatus showed that the wavefront of a high intensity beam at 532 nm is easily distorted by AOM crystals and PBS cubes. This issue is hopefully solved with the power stabilisation via the rotating waveplate in chapter 3.6.

7.2.2. Monochromatic traps

Another option is to circumvent bichromatic traps altogether and create a much simpler monochromatic trap with equal or at least more comparable trap depths compared to the currently used 1064 nm ODTs. In order to find a better trap design let us revisit the scattering rates and optical trapping potentials for Rb and Yb shown in figure 7.3. The first possible candidate is light close to the tune-out wavelength of Rb at 790 nm [294], [295], which is located between the D1 and D2 line of Rb and thus offers great variability for the trap depth of spin-polarised Rb. On one hand only little ($\approx$ 100 mW) power is needed to create a considerable trap depth, as it is not far detuned, but on the other hand it has a large scattering rate for Rb, see segment (a) in figure 7.3. A laser system based on a diode laser system (plus a TA) was set up in [296] for this purpose, but has yet to be implemented in the experiment.

For light that is far detuned from atomic transitions the hyperfine structure and the

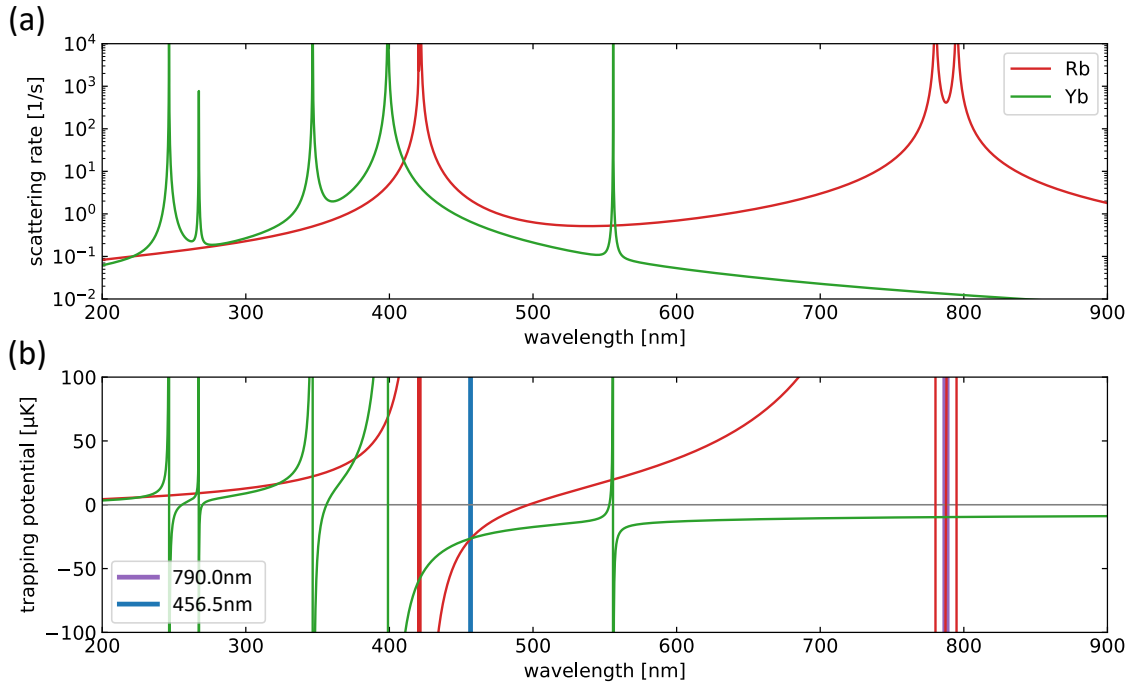

Figure 7.3.: (a) Scattering rate of Rb and Yb depending on the wavelength of the optical trap at an exemplary power of 1 W and in the center of a Gaussian beam with a beamwaist of 50 µm. (b) Optical trapping potential in μK at equal trap parameters for different wavelengths. For the highlighted wavelengths 790.0 nm and 456.5 nm the potential depths for Rb and Yb atoms are equal.

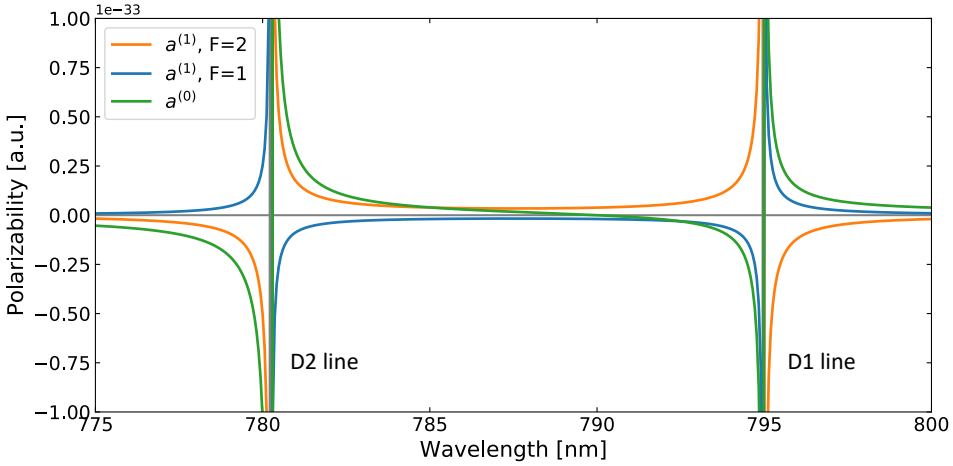

Figure 7.4.: The dynamic polarizabilitiy of ^{87}Rb in the $5^2S_{1/2}$ ground state (in $F = 1$ and $F = 2$) as a function of the wavelength of the driving light field. The scalar $a^{(0)}$ polarizability is independent of the hyperfine ground state, while the vector polarizabilities $a^{(1)}$ depend on F and the gyromagentic ratio g_F.

polarisation of the light field is irrelevant for the potential depth. Close to resonances however, the otherwise neglected vector and tensor polarizability contributing to the ac Stark shift have to be considered. Therefore all dipole allowed hyperfine transitions of Rb and their dipole matrix elements that couple to the light field have to be taken into account.

Following the theoretical work in [297] and experimental results of [294], [295] we can determine the (dynamic) polarizabilities and trapping potential of ^{87}Rb close to the tune-out wavelength around 790 nm. In figure 7.4 the scalar $a^{(0)}$ and vector polarizabilities $a^{(1)}$ of ^{87}Rb in the $5^2S_{1/2}$ ground state (in $F = 1$ and $F = 2$) are plotted as a function of the wavelength. Since we only consider building a trap for ground state Rb with a detuning much larger than the hyperfine splitting of Rb the tensor shift $a^{(2)}$ vanishes. Using the determined polarizabilities we can calculate the ac Stark shift following [294], [295]

$$V_{nFm_F}(\lambda) = -\left(\frac{1}{2}E_0\right)^2 \left[a^{(0)}(\lambda) + C\frac{m_F}{F}a^{(1)}(\lambda) - D\frac{3{m_F}^2 - F(F+1)}{2F(2F-1)}a^{(2)}(\lambda)\right] \tag{7.1}$$

with the parameters $C = \epsilon \cdot \cos(\theta_k)$ and $D = (3\cos^2\theta_p - 1)/2$. These values are functions of the polarisation of the trapping light, θ_k being the angle between B-field quantization axis and wave vector and θ_p being the angle between quantization axis and polarization vector. Here, ϵ is the degree of circular polarisation of the light field, where $\epsilon = 0$ is linear polarized light and $\epsilon = \pm 1$ the circular polarization σ^+ or σ^-. Figure 7.5 shows the resulting optical potential depth in µK for an exemplary σ^+-polarized laser beam with P = 100 mW and a beam waist of $\omega = 50$ µm that could be implemented in the experiment. The circular polarisation is selected to visualise the influence of the vector shift on the tune-out wavelength for the three possible Zeeman states $|m_F = -1, 0, +1\rangle$ of Rb in the $|F = 1\rangle$

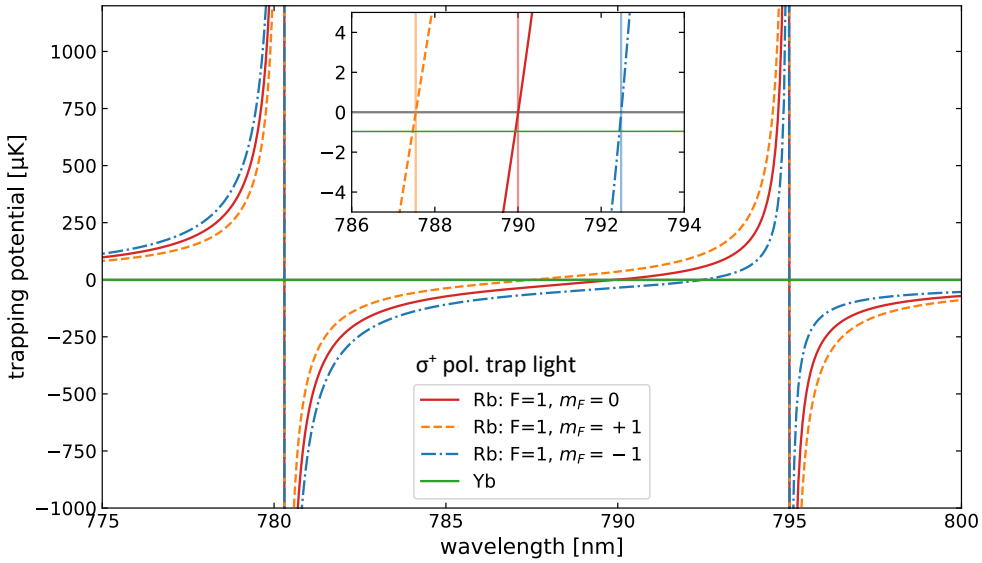

Figure 7.5.: The optical trapping potential as a function of wavelength of a σ^+ polarized light field with a power of 100 mW and a beam waist of 50 µm. In the inset the tune-out wavelength (zero potential) at 790 nm for Rb atoms in the $|F = 1, m_F = 0\rangle$ state is visible. For Rb atoms in the $|F = 1, m_F = \pm 1\rangle$ states this wavelength is shifted by the vector shift in equation 7.1.

ground state. For linearly polarized light only the scalar polarization has to be considered so that our tune-out wavelengths should be independent of the Zeeman m_F state. A much more involved calculation including relativistic configuration interactions and core polarization in [297] reveals that they are indeed close but not identical and calculates the tune-out wavelengths for all Rb hyperfine and Zeeman states much more accurately[2]. Furthermore it is possible to accurately determine the tune-out wavelength experimentally with a pulsed lattice and the evaluation of Kapitza-Dirac scattering [294], [295], see chapter 4.3.1.

The inset of figure 7.5 shows that the trap depth for Yb is equal to Rb around 790.0 nm but only at about 1 µK for a power of 100 mW and beam waist of 50 µm. As a result this trap can only be used as a monochromatic trap at very low mixture temperatures. It is however much more interesting as a 'balancing' bichromatic trap since small detunings from the tune-out wavelength can create large attractive or repulsive optical potentials for Rb. A similar approach can be repeated for the 420 nm tune-out wavelength for Rb [298] but is less suitable due to large scattering rates for Yb.

The second variant for a monochromatic trap would be a wavelength with equal trapping potential for Rb and Yb in a far detuned ODT at 456.5 nm, see segment (b) of figure 7.3. This option comes with convenient scattering rates for both atomic species and would thus enable a combined evaporation of a mixture in a joined crossed ODT. Compared to our 1064 nm ODTs at equal intensity the trap depth for Rb would be reduced by a factor of

[2]For ^{87}Rb $|F = 1, m_F = -1, +1\rangle$ the tune-out wavelength is calculated at 790.0182169 nm, while $|F = 1, m_F = 0\rangle$ is calculated to 790.0181259 nm [297]

3 but would increase by a factor of 3 for Yb. It is however not easy to generate high laser powers at this specific wavelength. There are some solutions that produce continuous wave light 456.5 nm with several Watts of output power [299], [300]. Here, a Nd:$GdVO_4$ crystal is pumped with a fiber-coupled laser diode array at 808 nm ([299]) or 880 nm ([300]). With intracavity frequency doubling with either an LBO ([299]) or BiB306(BiBO) ([300]) crystal, light at 456 nm is generated and coupled out of the resonator. A more low cost option is to use a laser diode at 455 nm. Such high power laser diodes (5 W) however are typically multimode with a linewidth of a couple of nm and run with multiple transverse modes [301]. To be applicable in our experiment this light would need to be coupled into a multimode fiber to be properly focused into the science chamber. Even if high intensities at this wavelength are impractical a crossed ODT at 456 nm would be a great addition to the experiment for pre-evaporated mixtures ($\approx 10\,\mu K$) prepared in 1064 nm traps.

7.3. Preparing vibrationally excited ground state molecules

Eventually one wants to use the complex and time-consuming experiment setup to find some interesting phenomena in molecule physics. We explored the molecular potentials in our 1-photon and 2-photon PA experiments to find ways to produce some molecules. There are different methods to build vibrationally excited ground state molecules from unbound atoms in a cold atom experiment. Some of them are explained in the following sections.

7.3.1. Guided decay

The trivial approach to associate molecules is to use a single photon photoassociation laser to the electronically excited state and then to simply wait. As described in the theory chapter 2.5 about 1-photon-PA, the molecules will either decay back into atom pairs or into ground states with high vibrational quantum numbers, which is more likely. The vibrational ground state though is not specified because a spontaneous decay process can lead to many levels. A channel with a comparably large Franck-Condon factor however can provide a predominant selection of decay into a single state. This method requiring only a single laser, a beneficial molecular structure and subsequent molecule detection was first presented in Cs_2 [83].

An extension of the idea is the use of a second laser (2-photon-PA), which guides the decay into the desired ground state by coupling the electronically excited state to a specific vibrational ground state. If both lasers are used, the first can pump molecules in the intermediate state and the second causes stimulated emission to dump them into the ground state. Unfortunately, stimulated emission pumping (SEP) remains inefficient and can theoretically transfer 50 % [302], experimentally only $\sim 10\,\%$, because of its incoherence and the decay of the intermediate state [84].

Now if both lasers are detuned to their respective resonances, Raman transitions can be used to produce molecules by using a virtual intermediate state. However the efficiency of the population transfer is limited due to the weak coupling affected by a small wave function overlap and spontaneous Raman scattering inducing decoherence. Luckily in the

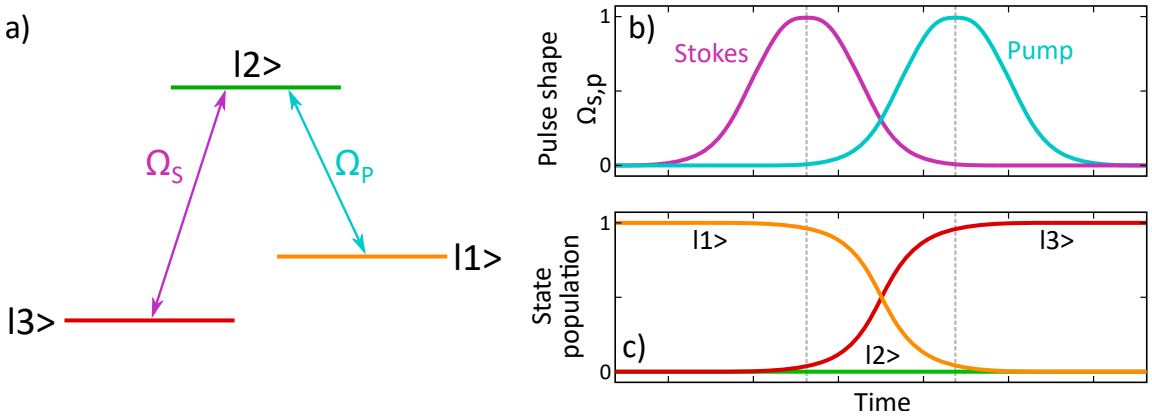

Figure 7.6.: A three-level Λ type scheme and the pulse sequence for a STIRAP process. In segment (a) the 'pump' ('Stokes') light field with Rabi frequency Ω_P (Ω_S) couples the states $|1\rangle$ and $|2\rangle$ ($|2\rangle$ and $|2\rangle$). Segment (b) shows the pulse sequence for the population transfer in (c) from state $|1\rangle$ to $|3\rangle$ over time.

case of forbidden transitions like the association to the ^3P_J manifold of Yb, off-resonant Raman scattering is reduced and has enabled the observation of Rabi oscillations between atomic and molecular states [303]. Therefore a pulse sequence with two-photon Raman transitions can be a possible tool to create RbYb molecules.

7.3.2. Free-bound STIRAP

This section follows the much more extensive description in [87]. As already mentioned the approach to gather ground state molecules via an intermediate excited state is inefficient because it is an incoherent process [85] and the involved decay prevents an efficient stimulated emission pumping process [84]. The transfer of molecules with a coherent process called stimulated Raman adiabatic passage (STIRAP) circumvents the necessity to populate an excited state and therefore increases the transfer efficiency [86][87]. This method already helped many ultracold molecule experiments to reach the rovibronic ground state, proving its high transfer efficiency and robustness, with Rb_2 [88], KRb [89], Cs_2 [90], RbCs [31], [91] and NaK molecules [54].

To help explaining the STIRAP technique, figure 7.6 shows a three level Λ-type system, a pulse sequence and the corresponding state population over time. The initial state $|1\rangle$ is coupled to the excited state $|2\rangle$ with a 'pump' laser expressed with the Rabi frequency Ω_P, while the final state $|3\rangle$ is coupled to $|2\rangle$ with a 'Stokes' laser with Rabi frequency Ω_S. The pulse sequence is counter-intuitive since the Stokes pulse is used before the pump pulse, which initially creates a coupling between unpopulated states. The reason for this sequential order is the creation of a dark state that will be explained now. The Hamiltonian for this system is [87]

$$\hat{H} = \frac{\hbar}{2}\begin{pmatrix} 0 & \Omega_P & 0 \\ \Omega_P & 2\Delta_P & \Omega_S \\ 0 & \Omega_S & 2\delta \end{pmatrix} \tag{7.2}$$

with Δ_P as the detuning of the pump laser and δ as the difference of the pump laser detuning to the Stokes laser detuning ($\delta = \Delta_P - \Delta_S$).

With both lasers on resonance the adiabatic eigenstates of the Hamiltonian are

$$\begin{aligned} |\, a^0 \,\rangle &= \cos\theta \quad |1\rangle \quad - \sin\theta \quad |3\rangle \\ |a^+\rangle &= \sin\theta\sin\phi \quad |1\rangle + \cos\phi \quad |2\rangle + \cos\theta\sin\phi \quad |3\rangle \\ |a^-\rangle &= \sin\theta\cos\phi \quad |1\rangle - \sin\phi \quad |2\rangle + \cos\theta\cos\phi \quad |3\rangle \end{aligned} \tag{7.3}$$

where θ and ϕ are defined as the mixing angles with

$$\tan\theta = \frac{\Omega_P}{\Omega_S}, \qquad \tan 2\phi = \frac{\sqrt{{\Omega_S}^2 + {\Omega_P}^2}}{\Delta_P} \tag{7.4}$$

and $|\, a^0 \,\rangle$ is the dark state that does not have any $|2\rangle$ excited state component. Exploiting this dark state makes full transfer (100 %) possible on timescales longer than its lifetime. The characteristic STIRAP pulse sequence starts by ramping up the Stokes Rabi frequency Ω_S. This triggers the adiabatic evolution of the eigenstates $|\, a^0 \,\rangle$,$|\, a^+ \,\rangle$ and $|\, a^- \,\rangle$, in which their degeneracy is removed and only the energy of the dark state remains constant. This corresponds to the Autler-Townes splitting of the levels $|3\rangle$ and $|2\rangle$. When the Stokes coupling is maximized the pump laser is introduced. Ramping up the Rabi frequency of the pump laser and simultaneously decreasing the Stokes field lets the state vector rotate in the $|1\rangle$ - $|3\rangle$ plane. This represents an adiabatic change of the mixing angle and prevents any state population in $|2\rangle$. The transfer is completed once the Stokes field is extinguished. Afterwards the pump Rabi frequency can be reduced to zero and the sequence is finished. This counter-intuitive sequence is robust to the pulse timing and fluctuating laser intensities compared to the pump and dump scheme, which is the inverted pulse sequence mentioned in the prior subsection[1].

The condition for efficient STIRAP given by [304]

$$\frac{{\Omega_P}^2 + {\Omega_S}^2}{\pi^2\gamma} \gg \frac{1}{\tau} \gg D \tag{7.5}$$

is the adiabatic development of the dark state, in which γ is the linewidth of the electronically excited state, τ is the sequence duration and D is the relative linewidth of the pump and Stokes lasers. A strong coupling between the states, meaning large Rabi frequencies[2] Ω_P and Ω_S, and a preferably small linewidth γ are essential for STIRAP. In order to confirm the production of molecules a STIRAP sequence can be reversed to detect atoms dissociating from molecules [306]. This procedure indirectly proves that molecules have been created in the first place.

It is much easier to use STIRAP on bound molecular states with previously associated Feshbach molecules instead of free atom pairs. However, magnetic Feshbach association

[1] In it molecules can be lost due to spontaneous emission and thus the pulse time needs to be shorter than the lifetime of the $|2\rangle$ in order to reach a maximum efficiency of 50 % [87]

[2] The derivation in [305] requires both Rabi frequencies to have similar peak values to make for an efficient transfer and thus have to be comparable.

[78], [80] of weakly bound ground state molecules composed of alkali atoms with closed shell atoms is extremely hard and so far only a few narrow resonances have been found for RbSr [26], CsYb [27] and LiYb [28] mixtures. For now magnetic Feshbach have only been proposed [25] and not yet detected in the RbYb system [14]. A detailed outlook on a possible use of magnetic Feshbach resonances in our experiment is already covered in [1].

In conclusion free-bound STIRAP could be the path required to produce RbYb ground state molecules. As discussed and measured in chapter 6.2, the coupling for free-bound transitions is about 10^3 times weaker due to the small Franck-Condon overlap with a scattering state. Therefore it is desirable to increase the free-bound coupling Ω_P as much as possible. Currently the Rabi frequencies measured in the experiment are on the order of kHz and thus too small due to the thermal distribution of the scattering state. Attempts to drive a STIRAP sequence under the present conditions would thus be ineffective unless Ω_P is on the order of MHz. In this regard it is favourable and maybe inevitable to work with the 1-photon-PA transition at the D1 line of Rb [14] as it offers a much larger free-bound coupling.

Nevertheless there already are advancements that we can use to generally increase the free-bound coupling and thus the effectiveness of free-bound STIRAP. If we are able to remove the thermal distribution by creating a dual BEC, the initial state would only be affected by mean field broadening and the free-bound Rabi frequency could be increased up to a factor of $\sqrt{N}$, with N being the number of BEC atoms, via Bose-enhancement [307]. This was already demonstrated with Sr atoms in a BEC [308]. Another idea has already been touched on in this thesis. The increased PA rate observed in the optical lattice in chapter 5.5 indicates that the preparation of a mixed Mott Insulator state in a 3D lattice trap discussed in chapter 5.5.3 has the potential further enhance our PA rate. Effectively ideal conditions for photoassociation are given if one Rb and one Yb atom are tightly confined in a optical lattice site. Successful production of Sr_2 molecules has shown that the confinement to lattice sites increases the wavefunction overlap and can even exceed the Rabi frequencies achieved with Bose-enhancement [30]. If free-bound STIRAP can be properly realized, an all optical production of ground state molecules with two independent STIRAP sequences and a total of four laser fields is possible [22] as indicated in figure 7.7. An all optical creation of Sr_2 molecules in the absolute ground state has recently been achieved with the combination of a photoassociation pulse followed by spontaneous decay into a weakly bound molecule and a subsequent STIRAP process [92].

7.4. The third photon - The next step towards absolute ground state molecules

The ultimate goal of this experiment is to produce molecules in the absolute ground state and make use of their magnetic and electric dipole moment. The absolute ground state means that the molecule has no vibrational or rotational energy and is thus also called the rovibronic ground state level. In order to utilize the STIRAP technique to transfer weakly bound molecules to this level, knowledge of deeply bound rovibrational levels of the ground

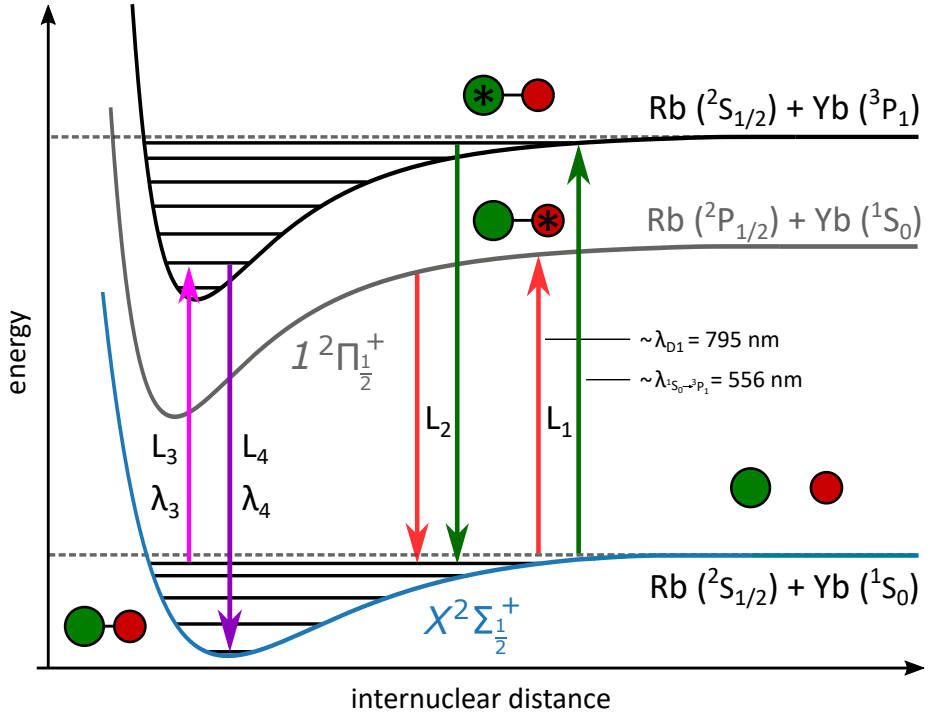

Figure 7.7.: Routes to the rovibronic molecular ground state in RbYb. Following the 1-photon and 2-photon spectroscopy along the electronically excited levels corresponding to the intercombination line of Yb and the D1 line of Rb and possible attempts at free-bound STIRAP with L_1 and L_2, molecules can be transferred to the rovibronic ground state with two additional laser fields L_3 and L_4. They can couple a weakly bound vibrational ground state to the absolute ground state via a deeply bound vibrational level in the excited state.

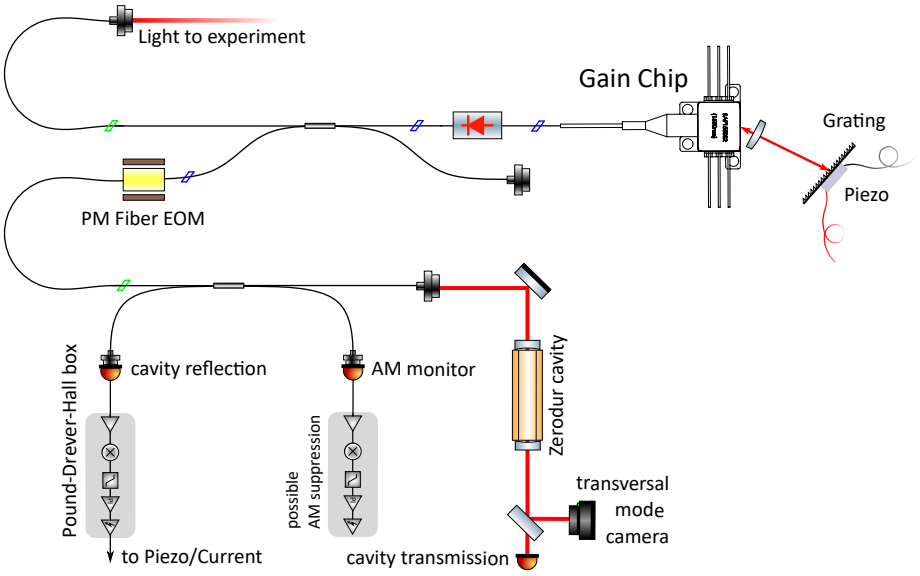

Figure 7.8.: Currently developed laser system at ≈ 1520 nm for the spectroscopy of deep lying states of the excited molecular potential.

and electronically exited state is needed. Unfortunately, the spectroscopy conducted at the $^2S_{1/2} + {}^3P_1$ channel has not led to a lot of data on energy levels of the associated excited potentials ($^4\Pi_{1/2}$,$^4\Pi_{-1/2}$,$^2\Pi_{3/2}$). There is much more data available on the excited $^2\Pi_{1/2}$ state down to the $\Delta v' = 28$ vibrational level from previous works [14]. Moreover, the line strengths observed in these transitions seem to be more suitable for attempts at free-bound STIRAP. The path along the excited potential connected to the Rb atom is therefore an attractive option because the way of creating weakly bound ground state molecules is irrelevant to the final STIRAP sequence. However, the developed spectroscopic technique and transitions we found in chapter 5.4 are far from useless. This high resolution and stability achieved on this resonance and the 2-photon transitions of chapter 6.2 can be used to search for proposed bound-bound transitions to deeply lying levels of excited molecular potentials [16]. As illustrated in figure 7.7 new lasers are eventually needed to probe these transitions around $\lambda_3 = 1.5\,\mu m$ and $\lambda_4 = 1.3\,\mu m$ [13], [309]. A started project for the first of them is presented in the following section.

A laser for the third photon

Gain chips in the infrared spectral region are commercially available as fiber coupled half butterfly packages. Cheap fiber optic communication parts produced around 1300 nm to 1600 nm, known as the Telecom bands, offer a lot of possibilities to build a laser system mostly consisting of fiber parts. Therefore we already started to develop a laser aimed at $\Lambda_{L3} \approx 1520\,nm$ to find and drive a transition to a deep lying level of the excited molecular potential [309]. The ECDL system displayed in figure 7.8 is based on a fiber coupled half butterfly gain chip (*Thorlabs SAF1550S2*) and an external grating. Similar to other comparable setups [310], [311] we plan to achieve a wide mode-hop-free tunability with a

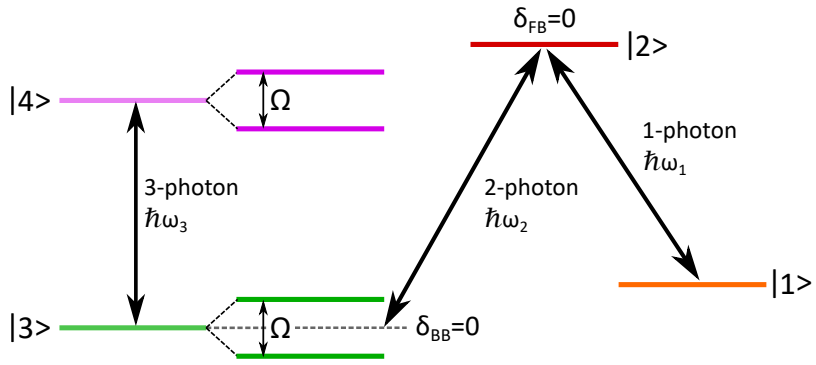

Figure 7.9.: Sketch of the 3-photon detection scheme for bound states ($|4\rangle$) in the electronically excited molecular potential. By using the 3rd photon laser the light shift on the molecular ground state $|3\rangle$ can be utilised to deplete the atomnumber signal that is achieved with 2-photon-PA on resonance with $\delta_{FB} = 0$ (between $|1\rangle$ and $|2\rangle$) and $\delta_{BB} = 0$ (between $|2\rangle$ and $|3\rangle$).

small linewidth. Together with a wideband fiber EOM a stabilisation to a high finesse cavity via a Pound-Drever-Hall lock should enable a laser scan on the range of GHz. Since the data acquired on deeper levels of the excited potential is non-existent, a precise prediction of the necessary laser frequency is not possible and requires extensive spectroscopy. In this regard a stable and sensitive 2-photon transition like the ones reported in chapter 6.2 is extremely helpful.

Detection scheme for low-lying rovibrational levels

The intended scheme to detect low lying rovibrational states in the electronically excited state of RbYb utilizes the 2-photon-PA technique described in chapter 6. In this case both 2-photon PA lasers are set on resonance with $\delta_{FB} = 0$ (between $|1\rangle$ and $|2\rangle$) and $\delta_{BB} = 0$ (between $|2\rangle$ and $|3\rangle$) leading to the population of a dark state (see section 6.4). As depicted in figure 7.9 the third photon (3-photon) can now be added during the PA time in the mixture. If the frequency of the third laser at 1.5 µm is close to an energy spacing $\hbar\omega_3$ between the utilized molecular ground state level $|3\rangle$ and an unknown electronically excited bound molecular level $|4\rangle$ the AC Stark effect will shift state $|3\rangle$ and thus perturbe the dark state. This will in turn influence the dark state signal. Since the dark state is very sensitive to perturbations, it will be affected even if the third laser is relatively far from an atomic resonance.

To maximise this loss effect it is recommended to produce a large AC Stark shift by using a high laser intensity of the 3rd-photon laser. Since the predicted bound states in the excited molecular potential are around 14 nm apart [309] the scan duration for such resonances highly depends on the frequency sweep range during the PA time. If bound states are detected they offer excellent information about the unexplored excited molecular potential and may be used to predict the location of the undiscovered 1-photon-PA transitions.

A.

Appendix

A.1. Hund's case (e)

Some efforts interpreting the situation with case (e) was put in by Franzen [1] but revealed some more inconclusiveness. Possible treatments with case (e) necessitate rotational quantum numbers $R > 0$ to avoid a violation of dipole selection rules. Even $R = 2$ needs to be assumed to achieve the desired Zeeman shift, without completely neglecting the atomic state preparation. For this we need an incoming channel already bringing $R > 0$ or a d-wave shape resonance behind a rotational barrier. The height of the rotational barrier[1] for ^{87}Rb + ^{170}Yb with a $C_6 = 4460\,E_h a_0{}^6$ is 53 µK for $R = 1$ and 274 µK for $R = 2$. Since our atoms should be restricted to s-wave scattering with a small negative scattering length and temperatures of 10 µK this approach seems very unlikely. Furthermore an $R = 2$ signal should definitely be smaller than the one for a smaller rotational quantum number. An $R = 0$ signal for example was not found. Nevertheless if a coupling like dipole-dipole interactions between an atomic basis and a molecular state providing a change in the rotational molecular quantum number ΔR exists, it is still possible to argue about this case. However in the 2-photon spectroscopy, we work in the same experimental conditions and with a $R = 0$ non rotational ground state potential level, which provides no reason to assume a excited state with rotational component. All in all, neither coupling approach leads to a conclusive interpretation of the doublet. This can be attributed to the previously mentioned intermediate state problem, where neither of Hund's cases is able to frame the situation properly. Angular coupling terms such as Coriolis type coupling could be one of the reasons for the imperfect descriptions. This effect is a coupling term that appears in the rotational Hamiltonian and arises from the interaction between the different Ω states of the molecule[2]. If the coupling strength is not negligible it could shift our molecule even more towards a crossover from case (c) to case (e) [312]. In an attempt to judge the relevance of Coriolis coupling we can consult Tomza who calculated a very small change in binding energy of $10^{-6}\,\mathrm{cm}^{-1}$ for SrYb states [313] and Barbé who dismisses this term for the ground state PECs of RbSr [151]. It is thus reasonable to assume that Coriolis-type coupling is not the reason for our intermediate coupling state.

[1] Calculated with $E_c(R) = \frac{1}{2}\left(\frac{R(R+1)}{3}\right)^{3/2} \cdot E_{\mathrm{vdW}}$, see [14].

[2] The discussed energy term is the perturbation operator $-2BJ.J_a$, which breaks the BO-approximation because it couples electronic states with a difference in Ω [312]

Bibliography

[1] T. Franzen, "A rbyb ultracold mixture machine - from chunks of metal to intercombination line photoassociation," Ph.D. dissertation, Heinrich-Heine-Universität Düsseldorf, 2023.

[2] R. V. Krems, "Cold controlled chemistry," *Physical Chemistry Chemical Physics*, vol. 10, pp. 4079–4092, 28 2008. DOI: 10.1039/B802322K.

[3] N Balakrishnan, "Perspective: Ultracold molecules and the dawn of cold controlled chemistry," *The Journal of chemical physics*, vol. 145, no. 15, p. 150 901, 2016.

[4] H. Son, J. J. Park, Y.-K. Lu, A. O. Jamison, T. Karman, and W. Ketterle, "Control of reactive collisions by quantum interference," *Science*, vol. 375, no. 6584, pp. 1006–1010, 2022. DOI: 10.1126/science.abl7257.

[5] J. Ye, S. Blatt, M. M. Boyd, *et al.*, "Precision measurement based on ultracold atoms and cold molecules," *AIP Conference Proceedings*, vol. 869, no. 1, pp. 80–91, 2006. DOI: 10.1063/1.2400637.

[6] D. DeMille, "Quantum computation with trapped polar molecules," *Phys. Rev. Lett.*, vol. 88, p. 067 901, 6 2002. DOI: 10.1103/PhysRevLett.88.067901.

[7] M. Karra, K. Sharma, B. Friedrich, S. Kais, and D. Herschbach, "Prospects for quantum computing with an array of ultracold polar paramagnetic molecules," *The Journal of chemical physics*, vol. 144, no. 9, p. 094 301, 2016.

[8] P. J. Ollitrault, A. Miessen, and I. Tavernelli, "Molecular quantum dynamics: A quantum computing perspective," *Accounts of Chemical Research*, vol. 54, no. 23, pp. 4229–4238, 2021, PMID: 34787398. DOI: 10.1021/acs.accounts.1c00514.

[9] A. Batär, "Erzeugung und Charakterisierung ultrakalter Rubidium-und Ytterbiumatome-auf dem weg zu einem gemischten quantengas," Ph.D. dissertation, Ph. D. thesis, Heinrich-Heine-Universität, Düsseldorf, 2005.

[10] S. Tassy, "Sympathetische Kühlung von Ytterbium mit Rubidium," Ph.D. dissertation, Ph. D. thesis, Heinrich-Heine-Universität, Düsseldorf, 2007.

[11] N. Nemitz, "Production and spectroscopy of ultracold YbRb* molecules," Ph.D. dissertation, Ph. D. thesis, Heinrich-Heine-Universität, Düsseldorf, 2008.

[12] F. Baumer, "Isotope dependent interactions in a mixture of ultracold atoms," Ph.D. dissertation, Ph. D. thesis, Heinrich-Heine-Universität, Düsseldorf, 2010.

[13] F. Münchow, "2-photon-photoassociation spectroscopy in a mixture of ytterbium and rubidium," Ph.D. dissertation, Heinrich-Heine-Universität Düsseldorf, 2012.

[14] C. Bruni, "Exploring strategies for the production of ultracold RbYb molecules in conservative traps," Ph.D. dissertation, Heinrich-Heine-Universität Düsseldorf, 2015.

[15] M. Borkowski, P. S. Zuchowski, R. Ciuryo, *et al.*, "Scattering lengths in isotopologues of the RbYb system," *Physical Review A*, vol. 88, p. 052 708, 5 2013. DOI: 10.1103/PhysRevA.88.052708.

[16] L. K. Sørensen, S. Knecht, T. Fleig, and C. M. Marian, "Four-component relativistic coupled cluster and configuration interaction calculations on the ground and excited states of the RbYb molecule," *The Journal of Physical Chemistry A*, vol. 113, no. 45, pp. 12 607–12 614, 2009.

[17] S. Tohme and M Korek, "Electronic structure and rovibrational calculation of the low-lying states of the RbYb molecule," *Chemical Physics*, vol. 410, pp. 37–44, 2013.

[18] M. Shundalau and A. Minko, "Ab initio multi-reference perturbation theory calculations of the ground and some excited electronic states of the RbYb molecule," *Computational and Theoretical Chemistry*, vol. 1103, pp. 11–16, 2017.

[19] C. Bruni and A. Görlitz, "Observation of hyperfine interaction in photoassociation spectra of ultracold RbYb," *Physical Review A*, vol. 94, p. 022 503, 2 2016. DOI: 10.1103/PhysRevA.94.022503.

[20] T. Franzen, B. Pollklesener, C. Sillus, and A. Görlitz, "Intercombination-line photoassociation spectroscopy of ^{87}Rb^{170}Yb," *Phys. Rev. A*, vol. 107, p. 023 114, 2 2023. DOI: 10.1103/PhysRevA.107.023114.

[21] S. Stellmer, B. Pasquiou, R. Grimm, and F. Schreck, "Creation of ultracold Sr_2 molecules in the electronic ground state," *Phys. Rev. Lett.*, vol. 109, p. 115 302, 11 2012. DOI: 10.1103/PhysRevLett.109.115302.

[22] A. Devolder, E. Luc-Koenig, O. Atabek, M. Desouter-Lecomte, and O. Dulieu, "Proposal for the formation of ultracold deeply bound RbSr dipolar molecules by all-optical methods," *Physical Review A*, vol. 98, no. 5, p. 053 411, 2018.

[23] D. Jaksch, C. Bruder, J. I. Cirac, C. W. Gardiner, and P. Zoller, "Cold bosonic atoms in optical lattices," *Phys. Rev. Lett.*, vol. 81, pp. 3108–3111, 15 1998. DOI: 10.1103/PhysRevLett.81.3108.

[24] M. Greiner, O. Mandel, T. Rom, *et al.*, "Quantum phase transition from a superfluid to a mott insulator in an ultracold gas of atoms," *Physica B: Condensed Matter*, vol. 329-333, pp. 11–12, 2003. DOI: https://doi.org/10.1016/S0921-4526(02)01872-0.

[25] D. A. Brue and J. M. Hutson, "Prospects of forming ultracold molecules in 2 Σ states by magnetoassociation of alkali-metal atoms with yb," *Physical Review A*, vol. 87, no. 5, p. 052 709, 2013.

[26] V. Barbé, A. Ciamei, B. Pasquiou, *et al.*, "Observation of Feshbach resonances between alkali and closed-shell atoms," *Nature Physics*, vol. 14, no. 9, pp. 881–884, 2018.

[27] T. Franzen, A. Guttridge, K. E. Wilson, *et al.*, "Observation of magnetic feshbach resonances between cs and ^{173}Yb," *Phys. Rev. Research*, vol. 4, p. 043 072, 4 2022. DOI: 10.1103/PhysRevResearch.4.043072.

[28] A. Green, H. Li, J. H. See Toh, *et al.*, "Feshbach resonances in p-wave three-body recombination within fermi-fermi mixtures of open-shell ^{6}Li and closed-shell ^{173}Yb atoms," *Phys. Rev. X*, vol. 10, p. 031 037, 3 2020. DOI: 10.1103/PhysRevX.10.031037.

[29] S. Stellmer, B. Pasquiou, R. Grimm, and F. Schreck, "Creation of ultracold sr-2 molecules in the electronic ground state," *Physical Review Letters*, vol. 109, no. 11, p. 115 302, Sep. 2012. DOI: 10.1103/PhysRevLett.109.115302.

[30] A. Ciamei, A. Bayerle, C.-C. Chen, B. Pasquiou, and F. Schreck, "Efficient production of long-lived ultracold Sr2 molecules," *Physical Review A*, vol. 96, no. 1, p. 013 406, 2017.

[31] P. K. Molony, P. D. Gregory, Z. Ji, *et al.*, "Creation of ultracold Rb 87 Cs 133 molecules in the rovibrational ground state," *Physical review letters*, vol. 113, no. 25, p. 255 301, 2014.

[32] W. Phillips and H. Metcalf, "Laser deceleration of an atomic beam," *Phys. Rev. Lett.*, vol. 48, p. 596, 1982.

[33] E. Raab, M Prentiss, A. Cable, S. Chu, and D. E. Pritchard, "Trapping of neutral sodium atoms with radiation pressure," *Physical review letters*, vol. 59, no. 23, p. 2631, 1987.

[34] J. Dalibard and C. Cohen-Tannoudji, "Laser cooling below the Doppler limit by polarization gradients: Simple theoretical models," *Journal of the Optical Society of America B: Optical Physics*, vol. 6, no. 11, pp. 2023–2045, Nov. 1989. DOI: 10.1364/JOSAB.6.002023.

[35] M. Kasevich and S. Chu, "Laser cooling below a photon recoil with three-level atoms," *Phys. Rev. Lett.*, vol. 69, p. 1741, 1992.

[36] K. Davis, "Evaporative cooling of sodium atoms," Ph.D. dissertation, Massachusetts Institute of Technology, 1995.

[37] K. B. Davis, M.-O. Mewes, M. R. Andrews, *et al.*, "Bose-Einstein condensation in a gas of sodium atoms," *Physical review letters*, vol. 75, no. 22, p. 3969, 1995.

[38] M. H. Anderson, J. R. Ensher, M. R. Matthews, C. E. Wieman, and E. A. Cornell, "Observation of Bose-Einstein condensation in a dilute atomic vapor," *Science*, vol. 269, no. 5221, pp. 198–201, 1995.

[39] B. DeMarco and D. S. Jin, "Onset of fermi degeneracy in a trapped atomic gas," *Science*, vol. 285, no. 5434, pp. 1703–1706, 1999. DOI: 10.1126/science.285.5434.1703.

[40] I. Bloch, J. Dalibard, and W. Zwerger, "Many-body physics with ultracold gases," *Reviews of modern physics*, vol. 80, no. 3, p. 885, 2008.

[41] O. Morsch and M. Oberthaler, "Dynamics of Bose-Einstein condensates in optical lattices," *Reviews of Modern Physics*, vol. 78, pp. 179–215, 1 Feb. 2006. DOI: 10.1103/RevModPhys.78.179.

[42] M. Greiner, O. Mandel, T. Esslinger, T. W. Hänsch, and I. Bloch, "Quantum phase transition from a superfluid to a Mott insulator in a gas of ultracold atoms," *Nature*, vol. 415, no. 6867, pp. 39–44, 2002.

[43] C. R. Cabrera, L. Tanzi, J. Sanz, *et al.*, "Quantum liquid droplets in a mixture of bose-einstein condensates," *Science*, vol. 359, no. 6373, pp. 301–304, 2018. DOI: 10.1126/science.aao5686.

[44] C. Ospelkaus, S. Ospelkaus, K. Sengstock, and K. Bongs, "Interaction-driven dynamics of k-40-rb-87 fermion-boson gas mixtures in the large-particle-number limit," *Physical Review Letters*, vol. 96, no. 2, p. 020 401, Jan. 2006.

[45] B. Bloom, T. Nicholson, J. Williams, *et al.*, "An optical lattice clock with accuracy and stability at the 10^{-18} level," *Nature*, vol. 506, no. 7486, pp. 71–75, 2014.

[46] R Wynands and S Weyers, "Atomic fountain clocks," *Metrologia*, vol. 42, no. 3, S64–S79, Jun. 2005. DOI: 10.1088/0026-1394/42/3/s08.

[47] J. B. Fixler, G. Foster, J. McGuirk, and M. Kasevich, "Atom interferometer measurement of the Newtonian constant of gravity," *Science*, vol. 315, no. 5808, pp. 74–77, 2007.

[48] G. Quéméner and P. S. Julienne, "Ultracold molecules under control!" *Chemical Reviews*, vol. 112, no. 9, pp. 4949–5011, 2012. DOI: 10.1021/cr300092g.

[49] T Lahaye, C Menotti, L Santos, M Lewenstein, and T Pfau, "The physics of dipolar bosonic quantum gases," *Reports on Progress in Physics*, vol. 72, no. 12, p. 126 401, 2009. DOI: 10.1088/0034-4885/72/12/126401.

[50] T. Chupp and M. Ramsey-Musolf, "Electric dipole moments: A global analysis," *Physical Review C*, vol. 91, no. 3, p. 035 502, 2015.

[51] J. Stuhler, A. Griesmaier, T. Koch, *et al.*, "Observation of dipole-dipole interaction in a degenerate quantum gas," *Physical Review Letters*, vol. 95, no. 15, p. 150 406, 2005.

[52] M. Lu, N. Q. Burdick, S. H. Youn, and B. L. Lev, "Strongly dipolar Bose-Einstein condensate of dysprosium," *Physical review letters*, vol. 107, no. 19, p. 190 401, 2011.

[53] M. Baranov, K Góral, L Santos, M Lewenstein, *et al.*, "Ultracold dipolar gases–a challenge for experiments and theory," *Physica Scripta*, vol. 2002, no. T102, p. 74, 2002.

[54] J. W. Park, S. A. Will, and M. W. Zwierlein, "Ultracold dipolar gas of fermionic Na23 K40 molecules in their absolute ground state," *Physical review letters*, vol. 114, no. 20, p. 205 302, 2015.

[55] M. Guo, B. Zhu, B. Lu, *et al.*, "Creation of an ultracold gas of ground-state dipolar Na 23 Rb 87 molecules," *Physical review letters*, vol. 116, no. 20, p. 205 303, 2016.

[56] A. Micheli, G. Brennen, and P. Zoller, "A toolbox for lattice-spin models with polar molecules," *Nature Physics*, vol. 2, no. 5, pp. 341–347, 2006.

[57] A. V. Gorshkov, S. R. Manmana, G. Chen, E. Demler, M. D. Lukin, and A. M. Rey, "Quantum magnetism with polar alkali-metal dimers," *Physical Review A*, vol. 84, no. 3, p. 033 619, 2011.

[58] J. Bardeen, L. N. Cooper, and J. R. Schrieffer, "Theory of superconductivity," *Phys. Rev.*, vol. 108, pp. 1175–1204, 5 1957. DOI: 10.1103/PhysRev.108.1175.

[59] S. Ospelkaus, K.-K. Ni, D. Wang, *et al.*, "Quantum-state controlled chemical reactions of ultracold potassium-rubidium molecules," *Science*, vol. 327, no. 5967, pp. 853–857, 2010. DOI: 10.1126/science.1184121.

[60] K. Matsuda, L. D. Marco, J.-R. Li, *et al.*, "Resonant collisional shielding of reactive molecules using electric fields," *Science*, vol. 370, no. 6522, pp. 1324–1327, 2020. DOI: 10.1126/science.abe7370.

[61] J. J. Hudson, D. M. Kara, I. J. Smallman, B. E. Sauer, M. R. Tarbutt, and E. A. Hinds, "Improved measurement of the shape of the electron," *Nature*, vol. 473, 7348 2011. DOI: 10.1038/nature10104.

[62] J. Baron, W. C. Campbell, D. DeMille, *et al.*, "Order of magnitude smaller limit on the electric dipole moment of the electron," *Science*, vol. 343, no. 6168, pp. 269–272, Jan. 2014. DOI: 10.1126/science.1248213.

[63] W. B. Cairncross, D. N. Gresh, M. Grau, *et al.*, "Precision measurement of the electron's electric dipole moment using trapped molecular ions," *Phys. Rev. Lett.*, vol. 119, p. 153 001, 15 2017. DOI: 10.1103/PhysRevLett.119.153001.

[64] J. Lim, J. R. Almond, M. A. Trigatzis, *et al.*, "Laser cooled ybf molecules for measuring the electron's electric dipole moment," *Phys. Rev. Lett.*, vol. 120, p. 123 201, 12 2018. DOI: 10.1103/PhysRevLett.120.123201.

[65] E. R. Hudson, H. J. Lewandowski, B. C. Sawyer, and J. Ye, "Cold molecule spectroscopy for constraining the evolution of the fine structure constant," *Physical Review Letters*, vol. 96, no. 14, p. 143 004, Apr. 2006.

[66] J. Kobayashi, A. Ogino, and Inouye, "Measurement of the variation of electron-to-proton mass ratio using ultracold molecules produced from laser-cooled atoms," *Nature Communications*, vol. 10, no. 3771, Aug. 2019. DOI: 10.1038/s41467-019-11761-1.

[67] M. Quintero-Pérez, T. E. Wall, S. Hoekstra, and H. L. Bethlem, "Preparation of an ultra-cold sample of ammonia molecules for precision measurements," *Journal of Molecular Spectroscopy*, vol. 300, pp. 112–115, 2014, Spectroscopic Tests of Fundamental Physics, ISSN: 0022-2852. DOI: https://doi.org/10.1016/j.jms.2014.03.018.

[68] T. N. C. for Physics, *Scientifc background on the nobel prize in physics 2022*, Nobel Prize Website, 2022. [Online]. Available: https://www.nobelprize.org/uploads/2022/10/advanced-physicsprize2022.pdf.

[69] P. D. Gregory, J. A. Blackmore, S. L. Bromley, J. M. Hutson, and S. L. Cornish, "Robust storage qubits in ultracold polar molecules," *Nature Physics*, vol. 17, no. 10, pp. 1149–1153, 2021.

[70] R. Sawant, J. A. Blackmore, P. D. Gregory, *et al.*, "Ultracold polar molecules as qudits," *New Journal of Physics*, vol. 22, no. 1, p. 013 027, 2020. DOI: 10.1088/1367-2630/ab60f4.

[71] L. D. Carr, D. DeMille, R. V. Krems, and J. Ye, "Cold and ultracold molecules: Science, technology and applications," *New Journal of Physics*, vol. 11, no. 5, p. 055 049, 2009.

[72] N. Fitch and M. Tarbutt, "Chapter three - laser-cooled molecules," in ser. Advances In Atomic, Molecular, and Optical Physics, vol. 70, Academic Press, 2021, pp. 157–262. DOI: https://doi.org/10.1016/bs.aamop.2021.04.003.

[73] S. Truppe, H. J. Williams, M. Hambach, *et al.*, "Laser cooling of a diatomic molecule," *Nature Physics*, vol. 13, 1173–1176, 12 2017. DOI: 10.1038/nphys4241.

[74] E. S. Shuman, J. F. Barry, and D. DeMille, "Laser cooling of a diatomic molecule," *Nature*, vol. 467, 820–823, 2010. DOI: 10.1038/nature09443.

[75] M. T. Hummon, M. Yeo, B. K. Stuhl, A. L. Collopy, Y. Xia, and J. Ye, "2d magneto-optical trapping of diatomic molecules," *Phys. Rev. Lett.*, vol. 110, p. 143 001, 14 2013. DOI: 10.1103/PhysRevLett.110.143001.

[76] I. Kozyryev, L. Baum, K. Matsuda, *et al.*, "Sisyphus laser cooling of a polyatomic molecule," *Phys. Rev. Lett.*, vol. 118, p. 173 201, 17 2017. DOI: 10.1103/PhysRevLett.118.173201.

[77] L. W. Cheuk, L. Anderegg, Y. Bao, *et al.*, "Observation of collisions between two ultracold ground-state caf molecules," *Phys. Rev. Lett.*, vol. 125, p. 043 401, 4 2020. DOI: 10.1103/PhysRevLett.125.043401.

[78] T. Köhler, K. Goral, and P. S. Julienne, "Production of cold molecules via magnetically tunable feshbach resonances," *Reviews Of Modern Physics*, vol. 78, no. 4, pp. 1311–1361, Oct. 2006.

[79] K. M. Jones, E. Tiesinga, P. D. Lett, and P. S. Julienne, "Ultracold photoassociation spectroscopy: Long-range molecules and atomic scattering," *Reviews of Modern Physics*, vol. 78, no. 2, p. 483, 2006.

[80] C. Chin, R. Grimm, P. Julienne, and E. Tiesinga, "Feshbach resonances in ultracold gases," *Reviews of Modern Physics*, vol. 82, no. 2, p. 1225, 2010.

[81] P. S. Żuchowski, J. Aldegunde, and J. M. Hutson, "Ultracold RbSr Molecules can be formed by Magnetoassociation," *Physical Review Letters*, vol. 105, p. 153 201, 15 2010. DOI: 10.1103/PhysRevLett.105.153201.

[82] B. Yang, M. D. Frye, A Guttridge, *et al.*, "Magnetic Feshbach resonances in ultracold collisions between Cs and Yb atoms," *Physical Review A*, vol. 100, no. 2, p. 022 704, 2019.

[83] A. Fioretti, D. Comparat, A. Crubellier, O. Dulieu, F. Masnou-Seeuws, and P. Pillet, "Formation of cold Cs_2 molecules through photoassociation," *Phys. Rev. Lett.*, vol. 80, pp. 4402–4405, 20 1998. DOI: 10.1103/PhysRevLett.80.4402.

[84] J. M. Sage, S. Sainis, T. Bergeman, and D. DeMille, "Optical production of ultracold polar molecules," *Phys. Rev. Lett.*, vol. 94, p. 203 001, 20 2005. DOI: 10.1103/PhysRevLett.94.203001.

[85] K. Bergmann, H. Theuer, and B. W. Shore, "Coherent population transfer among quantum states of atoms and molecules," *Reviews of Modern Physics*, vol. 70, pp. 1003–1025, 3 1998. DOI: 10.1103/RevModPhys.70.1003.

[86] J. Kuklinski, U Gaubatz, F. T. Hioe, and K Bergmann, "Adiabatic population transfer in a three-level system driven by delayed laser pulses," *Physical Review A*, vol. 40, no. 11, p. 6741, 1989.

[87] N. V. Vitanov, A. A. Rangelov, B. W. Shore, and K. Bergmann, "Stimulated raman adiabatic passage in physics, chemistry, and beyond," *Reviews of Modern Physics*, vol. 89, no. 1, p. 015 006, 2017.

[88] F. Lang, K. Winkler, C. Strauss, R. Grimm, and J. H. Denschlag, "Ultracold triplet molecules in the rovibrational ground state," *Phys. Rev. Lett.*, vol. 101, p. 133 005, 13 2008. DOI: 10.1103/PhysRevLett.101.133005.

[89] K. K. Ni, S. Ospelkaus, M. H. G. de Miranda, *et al.*, "A high phase-space-density gas of polar molecules," *Science*, vol. 322, no. 5899, 231, 2008. DOI: {10.1126/science.1163861}.

[90] J. G. Danzl, M. J. Mark, E. Haller, *et al.*, "An ultracold high-density sample of rovibronic ground-state molecules in an optical lattice," *Nature Physics*, vol. 6, no. 4, 265, 2010, ISSN: 1745-2473. DOI: {10.1038/NPHYS1533}.

[91] T. Takekoshi, L. Reichsöllner, A. Schindewolf, *et al.*, "Ultracold dense samples of dipolar RbCs molecules in the rovibrational and hyperfine ground state," *Physical review letters*, vol. 113, no. 20, p. 205 301, 2014.

[92] K. Leung, E Tiberi, B Iritani, I Majewska, R Moszynski, and T Zelevinsky, "Ultracold $^{88}Sr_2$ molecules in the absolute ground state," *New Journal of Physics*, vol. 23, no. 11, p. 115 002, 2021.

[93] Y. Takasu and Y. Takahashi, "Quantum degenerate gases of ytterbium atoms," *Journal of the Physical Society of Japan*, vol. 78, no. 1, p. 012 001, 2009. DOI: 10.1143/JPSJ.78.012001.

[94] T. Fukuhara, Y. Takasu, M. Kumakura, and Y. Takahashi, "Degenerate fermi gases of ytterbium," *Physical Review Letters*, vol. 98, p. 030 401, 3 2007. DOI: 10.1103/PhysRevLett.98.030401.

[95] A. Ciamei, J. Szczepkowski, A. Bayerle, *et al.*, "The RbSr $^2\Sigma^+$ ground state investigated via spectroscopy of hot and ultracold molecules," *Physical Chemistry Chemical Physics*, vol. 20, no. 41, pp. 26 221–26 240, 2018.

[96] A. Guttridge, M. D. Frye, B. Yang, J. M. Hutson, and S. L. Cornish, "Two-photon photoassociation spectroscopy of CsYb: Ground-state interaction potential and interspecies scattering lengths," *Physical Review A*, vol. 98, no. 2, p. 022 707, 2018.

[97] R. Roy, R. Shrestha, A. Green, *et al.*, "Photoassociative production of ultracold heteronuclear YbLi* molecules," *Physical Review A*, vol. 94, no. 3, p. 033 413, 2016.

[98] W. Dowd, R. J. Roy, R. K. Shrestha, *et al.*, "Magnetic field dependent interactions in an ultracold Li–Yb (3P2) mixture," *New Journal of Physics*, vol. 17, no. 5, p. 055 007, 2015.

[99] F. Schäfer, N. Mizukami, and Y. Takahashi, "Feshbach resonances of large-mass-imbalance er-li mixtures," *Phys. Rev. A*, vol. 105, p. 012 816, 1 2022. DOI: 10.1103/PhysRevA.105.012816.

[100] V. D. Vaidya, J Tiamsuphat, S. Rolston, and J. Porto, "Degenerate Bose-Fermi mixtures of rubidium and ytterbium," *Physical Review A*, vol. 92, no. 4, p. 043 604, 2015.

[101] F. Baumer, F. Münchow, A. Görlitz, S. E. Maxwell, P. S. Julienne, and E. Tiesinga, "Spatial separation in a thermal mixture of ultracold ^{174}Yb and ^{87}Rb atoms," *Physical Review A*, vol. 83, p. 040 702, 4 2011. DOI: 10.1103/PhysRevA.83.040702.

[102] N Nemitz, F Baumer, F Münchow, S Tassy, and A Görlitz, "Production of heteronuclear molecules in an electronically excited state by photoassociation in a mixture of ultracold Yb and Rb," *Physical Review A*, vol. 79, no. 6, p. 061 403, 2009.

[103] C. Bruni, F. Münchow, and A. Görlitz, "Optical Autler–Townes spectroscopy in a heteronuclear mixture of laser-cooled atoms," *Applied Physics B: Photophysics and Laser Chemistry*, vol. 123, no. 1, p. 6, 2017, ISSN: 1432-0649. DOI: 10.1007/s00340-016-6578-6.

[104] D. Menailava and M. Shundalau, "Optical cycle modelling for RbYb and CsYb molecules," *Journal of Applied Spectroscopy*, vol. 84, pp. 543–548, 2017. DOI: 10.1007/s10812-017-0508-1.

[105] B. Mukherjee, M. D. Frye, and J. M. Hutson, "Feshbach resonances and molecule formation in ultracold mixtures of rb and Yb(^3P) atoms," *Phys. Rev. A*, vol. 105, p. 023 306, 2 2022. DOI: 10.1103/PhysRevA.105.023306.

[106] S. Doerscher, "Creation of Ytterbium quantum gases with a compact 2D/3D MOT setup," Ph.D. dissertation, Universität Hamburg, 2013.

[107] I. V. Hertel and C.-P. Schulz, *Atome, Moleküle und optische Physik 2*. Springer Verlag, 2010.

[108] J. Dalibard, "Collisional dynamics of ultra-cold atomic gases," in *Bose-Einstein Condensation in Atomic Gases*, IOS Press, 1999, pp. 321–349.

[109] P. O. Schmidt, "Scattering properties of ultra-cold chromium atoms," Ph.D. dissertation, Universität Stuttgart, 2003.

[110] V. D. Vaidya, "Degenerate mixtures of rubidium and ytterbium for engineering open quantum states," Ph.D. dissertation, University of Maryland, 2015.

[111] J. Weiner, V. S. Bagnato, S. Zilio, and P. S. Julienne, "Experiments and theory in cold and ultracold collisions," *Rev. Mod. Phys.*, vol. 71, pp. 1–85, 1 1999. DOI: 10.1103/RevModPhys.71.1.

[112] P. K. Sørensen, "Three-body recombination in cold atomic gases," Ph.D. dissertation, 2013. DOI: 10.48550/ARXIV.1309.7545.

[113] P. F. Bedaque, E. Braaten, and H.-W. Hammer, "Three-body recombination in bose gases with large scattering length," *Phys. Rev. Lett.*, vol. 85, pp. 908–911, 5 2000. DOI: 10.1103/PhysRevLett.85.908.

[114] M. Kitagawa, K. Enomoto, K. Kasa, *et al.*, "Two-color photoassociation spectroscopy of ytterbium atoms and the precise determinations of s-wave scattering lengths," *Physical Review A*, vol. 77, p. 012 719, 1 2008. DOI: 10.1103/PhysRevA.77.012719.

[115] G. Gribakin and V. Flambaum, "Calculation of the scattering length in atomic collisions using the semiclassical approximation," *Physical Review A*, vol. 48, no. 1, p. 546, 1993.

[116] J. L. Bohn and P. S. Julienne, "Semianalytic theory of laser-assisted resonant cold collisions," *Phys. Rev. A*, vol. 60, pp. 414–425, 1 1999. DOI: 10.1103/PhysRevA.60.414.

[117] S. L. Cornish, N. R. Claussen, J. L. Roberts, E. A. Cornell, and C. E. Wieman, "Stable ^{85}Rb bose-einstein condensates with widely tunable interactions," *Phys. Rev. Lett.*, vol. 85, pp. 1795–1798, 9 2000. DOI: 10.1103/PhysRevLett.85.1795.

[118] S. Taie, Y. Takasu, S. Sugawa, *et al.*, "Realization of a SU(2) × SU(6) system of fermions in a cold atomic gas," *Phys. Rev. Lett.*, vol. 105, p. 190 401, 19 2010. DOI: 10.1103/PhysRevLett.105.190401.

[119] S. Sugawa, K. Inaba, S. Taie, R. Yamazaki, M. Yamashita, and Y. Takahashi, "Interaction and filling-induced quantum phases of dual mott insulators of bosons and fermions," *Nature Physics*, vol. 7, no. 8, pp. 642–648, 2011. DOI: 10.1038/nphys2028.

[120] R. Ciuryło, E. Tiesinga, and P. S. Julienne, "Optical tuning of the scattering length of cold alkaline-earth-metal atoms," *Phys. Rev. A*, vol. 71, p. 030 701, 3 2005. DOI: 10.1103/PhysRevA.71.030701.

[121] K Enomoto, K Kasa, M Kitagawa, and Y Takahashi, "Optical Feshbach resonance using the intercombination transition," *Physical Review Letters*, vol. 101, no. 20, p. 203 201, 2008.

[122] T. Fukuhara, S. Sugawa, and Y. Takahashi, "Bose-einstein condensation of an ytterbium isotope," *Physical Review A*, vol. 76, no. 5, 2007. DOI: 10.1103/physreva.76.051604.

[123] J. Söding, D. Guéry-Odelin, P. Desbiolles, F. Chevy, H. Inamori, and J. Dalibard, "Three-body decay of a rubidium bose–einstein condensate," *Applied Physics B*, vol. 69, no. 4, pp. 257–261, 1999. DOI: 10.1007/s003400050805.

[124] E. A. Burt, R. W. Ghrist, C. J. Myatt, M. J. Holland, E. A. Cornell, and C. E. Wieman, "Coherence, correlations, and collisions: What one learns about bose-einstein condensates from their decay," *Phys. Rev. Lett.*, vol. 79, pp. 337–340, 3 1997. DOI: 10.1103/PhysRevLett.79.337.

[125] J. R. de Laeter, J. K. Böhlke, P. D. Bièvre, *et al.*, "Atomic weights of the elements. Review 2000 (IUPAC technical report)," *Pure and Applied Chemistry*, vol. 75, no. 6, pp. 683–800, 2003. DOI: doi:10.1351/pac200375060683.

[126] D. A. Steck, *Rubidium 87 d line data*, accessed 30.05.2015, last revised 23 December 2010. [Online]. Available: http://steck.us/alkalidata/.

[127] L. Livi, "New quantum simulations with ultracold Ytterbium gases," Ph.D. dissertation, University of Florenz, 2017.

[128] M. Kitagawa, K. Enomoto, K. Kasa, *et al.*, "Two-color photoassociation spectroscopy of ytterbium atoms and the precise determinations of s-wave scattering lengths," *Phys. Rev. A*, vol. 77, p. 012 719, 1 2008. DOI: 10.1103/PhysRevA.77.012719.

[129] D. R. Lide, *Handbook of Chemistry and Physics*, 82nd edn. CRC Press, 2001.

[130] H. Lefebvre-Brion and R. Field, *The Spectra and Dynamics of Diatomic Molecules: Revised and Enlarged Edition*. Elsevier Science, 2004, ISBN: 9780080517506. [Online]. Available: https://books.google.co.uk/books?id=LwgHIo-NEccC.

[131] J. Brown and A. Carrington, *Rotational Spectroscopy of Diatomic Molecules*, ser. Cambridge Molecular Science. Cambridge University Press, 2003, ISBN: 9780521530781. [Online]. Available: https://books.google.co.uk/books?id=TU4eA7MoDrQC.

[132] G. Herzberg, *Molecular Spectra and Molecular Structure*. Van Nostrand Reinhold, 1950, vol. I. Spectra of Diatomic Molecules.

[133] B. Judd, *Angular Momentum Theory for Diatomic Molecules*. Elsevier Science, 2012, ISBN: 9780323159050. [Online]. Available: https://books.google.co.uk/books?id=0yprSc8ivl8C.

[134] P. W. Atkins and R. Friedman, *Molecular Quantum Mechanics an introduction to quantum chemistry*, 2nd ed. Oxford, 1983.

[135] F. Hund, "Concerning the importance of some appearances in the molecular spectra," *Zeitschrift für Physik*, vol. 36, p. 658, 1926.

[136] V Aquilanti, S Cavalli, and G Grossi, "Hund's cases for rotating diatomic molecules and for atomic collisions: Angular momentum coupling schemes and orbital alignment," *Zeitschrift für Physik D Atoms, Molecules and Clusters*, vol. 36, no. 3, pp. 215–219, 1996.

[137] F. Münchow, C. Bruni, M. Madalinski, and A. Görlitz, "Two-photon photoassociation spectroscopy of heteronuclear ybrb," *Physical Chemistry Chemical Physics*, vol. 13, no. 42, pp. 18 734–18 737, 2011.

[138] J. Tennyson, L. Lodi, L. K. McKemmish, and S. N. Yurchenko, "The ab initio calculation of spectra of open shell diatomic molecules," *Journal of Physics B: Atomic, Molecular and Optical Physics*, vol. 49, no. 10, p. 102 001, 2016.

[139] P. M. Morse, "Diatomic molecules according to the wave mechanics. ii. vibrational levels," *Phys. Rev.*, vol. 34, pp. 57–64, 1 1929. DOI: 10.1103/PhysRev.34.57.

[140] S. Porsev, M. Safronova, A Derevianko, and C. W. Clark, "Relativistic many-body calculations of van der waals coefficients for Yb-Li and Yb-Rb dimers," *Physical Review A*, vol. 89, no. 2, p. 022 703, 2014.

[141] J. E. Jones and S. Chapman, "On the determination of molecular fields.—i. from the variation of the viscosity of a gas with temperature," *Proceedings of the Royal Society of London. Series A, Containing Papers of a Mathematical and Physical Character*, vol. 106, no. 738, pp. 441–462, 1924. DOI: 10.1098/rspa.1924.0081.

[142] D. Comparat, "Improved leroy–bernstein near-dissociation expansion formula, and prospect for photoassociation spectroscopy," *Journal of Chemical Physics*, vol. 120, no. 3, pp. 1318–1329, 2004. DOI: 10.1063/1.1626539.

[143] R. J. LeRoy and R. B. Bernstein, "Dissociation energy and long-range potential of diatomic molecules from vibrational spacings of higher levels," *Journal of Chemical Physics*, vol. 52, no. 8, pp. 3869–3879, 1970. DOI: 10.1063/1.1673585.

[144] "Dissociation energies and long-range potentials of diatomic molecules from vibrational spacings: The halogens," *Journal of Molecular Spectroscopy*, vol. 37, no. 1, pp. 109–130, 1971, ISSN: 0022-2852. DOI: https://doi.org/10.1016/0022-2852(71)90046-4.

[145] S. Falke, E. Tiemann, and C. Lisdat, "Born-oppenheimer approximation for mass scaling of cold-collision properties," *Phys. Rev. A*, vol. 76, p. 012 724, 1 2007. DOI: 10.1103/PhysRevA.76.012724.

[146] J. J. Lutz and J. M. Hutson, "Deviations from born-oppenheimer mass scaling in spectroscopy and ultracold molecular physics," *Journal of Molecular Spectroscopy*, vol. 330, pp. 43–56, 2016, Potentiology and Spectroscopy in Honor of Robert Le Roy, ISSN: 0022-2852. DOI: https://doi.org/10.1016/j.jms.2016.08.007.

[147] C. Cohen-Tannoudji, J. Dupont-Roc, and G. Grynberg, *Atom-Photon Interactions*. New York: Wiley, 1992.

[148] M. Borkowski, R. Ciurylo, P. S. Julienne, S. Tojo, K. Enomoto, and Y. Takahashi, *Line shapes of optical feshbach resonances near the intercombination transition of bosonic ytterbium*, 2009. DOI: 10.48550/ARXIV.0905.0958.

[149] R. Napolitano, J. Weiner, C. J. Williams, and P. S. Julienne, "Line shapes of high resolution photoassociation spectra of optically cooled atoms," *Physical Review Letters*, vol. 73, no. 10, pp. 1352–1355, 1994. DOI: 10.1103/PhysRevLett.73.1352.

[150] J. L. Bohn and P. S. Julienne, "Semianalytic theory of laser-assisted resonant cold collisions," *Physical Review A*, vol. 60, no. 1, p. 414, 1999.

[151] V. Barbé, "Ultracold RbSr: Optical and magnetic spectroscopy, Feshbach resonances and molecular structure," Ph.D. dissertation, Universiteit van Amsterdam, 2018.

[152] R. González-Férez and C. P. Koch, "Enhancing photoassociation rates by nonresonant-light control of shape resonances," *Phys. Rev. A*, vol. 86, p. 063 420, 6 2012. DOI: 10.1103/PhysRevA.86.063420.

[153] J. L. Bohn and P. S. Julienne, "Semianalytic treatment of two-color photoassociation spectroscopy and control of cold atoms," *Physical Review A*, vol. 54, R4637–R4640, 6 1996. DOI: 10.1103/PhysRevA.54.R4637.

[154] W. McAlexander, E. Abraham, N. Ritchie, C. Williams, H. Stoof, and R. Hulet, "Precise atomic radiative lifetime via photoassociative spectroscopy of ultracold lithium," *Physical Review A*, vol. 51, no. 2, R871, 1995.

[155] S. H. Autler and C. H. Townes, "Stark effect in rapidly varying fields," *Phys. Rev.*, vol. 100, pp. 703–722, 2 1955. DOI: 10.1103/PhysRev.100.703.

[156] G. Alzetta, A. Gozzini, L. Moi, and G. Orriols, "An experimental method for the observation of r.f. transitions and laser beat resonances in oriented na vapour," *Il Nuovo Cimento B (1971-1996)*, vol. 36, 1 1976. DOI: 10.1007/BF02749417.

[157] S. E. Harris, J. Field, and A Imamoğlu, "Nonlinear optical processes using electromagnetically induced transparency," *Physical Review Letters*, vol. 64, no. 10, p. 1107, 1990.

[158] M. Fleischhauer, A. Imamoglu, and J. P. Marangos, "Electromagnetically induced transparency: Optics in coherent media," *Reviews of modern physics*, vol. 77, no. 2, p. 633, 2005.

[159] M. Debatin, T. Takekoshi, R. Rameshan, *et al.*, "Molecular spectroscopy for ground-state transfer of ultracold rbcs molecules," *Phys. Chem. Chem. Phys.*, vol. 13, pp. 18 926–18 935, 42 2011. DOI: 10.1039/C1CP21769K.

[160] R. Dumke, M Volk, T Müther, F Buchkremer, G Birkl, and W. Ertmer, "Micro-optical realization of arrays of selectively addressable dipole traps: A scalable configuration for quantum computation with atomic qubits," *Physical review letters*, vol. 89, p. 097 903, Sep. 2002. DOI: 10.1103/PhysRevLett.89.097903.

[161] D. Barredo, S. de Léséleuc, V. Lienhard, T. Lahaye, and A. Browaeys, "An atom-by-atom assembler of defect-free arbitrary two-dimensional atomic arrays," *Science*, vol. 354, no. 6315, pp. 1021–1023, 2016. DOI: 10.1126/science.aah3778.

[162] R. Grimm, M. Weidemüller, and Y. Ovchinnikov, "Optical dipole traps for neutral atoms," *Adv. at. mol. opt. phys*, vol. 42, no. 95, p. 130, 2000.

[163] H. Metcalf and P. van der Straten, "Cooling and trapping of neutral atoms," *Phys. Rep.*, vol. 244, p. 203, 1994.

[164] S. Chu, J. Bjorkholm, A. Ashkin, and A. Cable, "Experimental observation of optically trapped atoms," *Phys. Rev. Lett.*, vol. 57, p. 314, 1986.

[165] Y. Ralchenko, A. Kramida, J. Reader, and NIST ASD Team, *NIST Atomic Spectra Database (version 3.1.5)*. `http://physics.nist.gov/asd3`, Zugriff am 15.06., 2010.

[166] M. Greiner, "Ultracold quantum gases in three-dimensional optical lattice potentials," Ph.D. dissertation, Ludwig-Maximilians-Universität München, 2003.

[167] M. Weidemüller and C. Zimmermann, *Interaction in Ultracold Gases*. Wiley-VCH Verlag, 2003, pp. 291–319, ISBN: 3-527-40389-2.

[168] P. H., *Lecture notes in optical lattices*, 2019.

[169] G. H. Wannier, "The structure of electronic excitation levels in insulating crystals," *Phys. Rev.*, vol. 52, pp. 191–197, 3 1937. DOI: 10.1103/PhysRev.52.191.

[170] B. Neyenhuis, "Ultracold Polar KRb Molecules in Optical Lattices," Ph.D. dissertation, Brigham Young University, 2006.

[171] D. Jaksch, "Bose-Einstein Condensation and Applications," Ph.D. dissertation, LeopoldFranzens-Universität Innsbruck, 1999.

[172] E. Arimondo and S. Wimberger, "Tunneling of ultracold atoms in time-independent potentials," Apr. 2011. DOI: 10.1201/b10712-12.

[173] C.-L. Hung, "In Situ Probing Of Two-Dimensional Quantum Gases," Ph.D. dissertation, University of Chicago, 2011.

[174] F. Gerbier, "Quantum gases in optical lattices," Ph.D. dissertation, Collège de France, 2018.

[175] M. Moore and H. Sadeghpour, "Controlling two-species Mott-insulator phases in an optical lattice to form an array of dipolar molecules," *Physical Review A*, vol. 67, no. 4, p. 041 603, 2003.

[176] M. Greiner, O. Mandel, T. Esslinger, T. W. Hnsch, and I. Bloch, "Quantum phase transition from a superfluid to a mott insulator in a gas of ultracold atoms," *Nature*, vol. 415, p. 44, 2002.

[177] D. Jaksch, C. Bruder, J. I. Cirac, C. W. Gardiner, and P. Zoller, "Cold bosonic atoms in optical lattices," *Physical Review Letters*, vol. 81, no. 15, pp. 3108–3111, 1998. DOI: 10.1103/physrevlett.81.3108.

[178] I. B. Spielman, W. D. Phillips, and J. V. Porto, "Mott-insulator transition in a two-dimensional atomic bose gas," *Phys. Rev. Lett.*, vol. 98, p. 080 404, 8 2007. DOI: 10.1103/PhysRevLett.98.080404.

[179] W. S. Bakr, A. Peng, M. E. Tai, *et al.*, "Probing the superfluid to mott insulator transition at the single-atom level," *Science*, vol. 329, no. 5991, pp. 547–550, 2010. DOI: 10.1126/science.1192368.

[180] C. Castor, *Charakterisierung eines Yb-Kapillarofens*, Directed Study, Universität Düsseldorf, 2021.

[181] E. Staub, "Developing a High-Flux atomic beam source for Experiments with ultracold Strontium quantum gases," Ph.D. dissertation, University München, 2019.

[182] R. Senaratne, S. V. Rajagopal, Z. A. Geiger, K. M. Fujiwara, V. Lebedev, and D. M. Weld, "Effusive atomic oven nozzle design using an aligned microcapillary array," *Review of Scientific Instruments*, vol. 86, no. 2, p. 023 105, 2015, ISSN: 1089-7623. DOI: 10.1063/1.4907401.

[183] S. L. Kemp, K. L. Butler, R. Freytag, *et al.*, "Production and characterization of a dual species magneto-optical trap of cesium and ytterbium," *Review of Scientific Instruments*, vol. 87, no. 2, p. 023 105, 2016. DOI: 10.1063/1.4941719.

[184] H. Pauly, *Atom, Molecule and Cluster Beams I.* Springer Verlag, 2000.

[185] J. Huckans, W. Dubosclard, E. Maréchal, O. Gorceix, B. Laburthe-Tolra, and M. R. de Saint-Vincent, *Note on the reflectance of mirrors exposed to a strontium beam*, 2018. arXiv: 1802.08499 [physics.atom-ph].

[186] B. Pollklesener, *Setup of an optical lattice for rubidium and ytterbium*, Master Thesis, Universität Düsseldorf, 2014.

[187] K. Singer, S. Jochim, M. Mudrich, A. Mosk, and M. Weidemüller, "Low-cost mechanical shutter for light beams," *Review of Scientific Instruments*, vol. 73, no. 12, pp. 4402–4404, 2002. DOI: 10.1063/1.1520728.

[188] Johnson and Matthey, *Graphic from Website*, 2022. [Online]. Available: https://www.piezoproducts.de/produkte/aktoren-biegewandler/.

[189] P. B. W. Bowden I.R. Hill and P. Gill, "A high-performance, low-cost laser shutter using a piezoelectric cantilever actuator," *AIP*, 2016.

[190] H. J. Metcalf and P. Van der Straten, *Laser cooling and trapping*. Springer, 1999, ISBN: 0387987282, 9780387987286.

[191] X. Baillard, A. Gauguet, S. Bize, *et al.*, "Interference-filter-stabilized external-cavity diode lasers," *Optics Communications*, vol. 266, no. 2, pp. 609–613, 2006, ISSN: 0030-4018. DOI: https://doi.org/10.1016/j.optcom.2006.05.011.

[192] E. A. Khazanov, "Compensation of thermally induced polarisation distortions in Faraday isolators," *Quantum Electronics*, vol. 29, no. 1, pp. 59–64, 1999. DOI: 10.1070/qe1999v029n01abeh001412.

[193] N. Kostylev, E. Ivanov, M. E. Tobar, and J. J. McFerran, "Sub-doppler cooling of ytterbium with the 1s0–1p1 transition including 171yb (i=1/2)," *J. Opt. Soc. Am. B*, vol. 31, no. 7, pp. 1614–1620, 2014. DOI: 10.1364/JOSAB.31.001614.

[194] M. Gilowski, C. Schubert, M. Zaiser, *et al.*, "Narrow bandwidth interference filter-stabilized diode laser systems for the manipulation of neutral atoms," *Optics Communications*, vol. 280, no. 2, pp. 443–447, 2007, ISSN: 0030-4018. DOI: https://doi.org/10.1016/j.optcom.2007.08.043.

[195] B. Pollklesener, *Aufbau eines Lasersystems zur Laserkühlung von Ytterbium*, Bachelor Thesis, Universität Düsseldorf, 2014.

[196] T. Franzen, B. Pollklesener, and A. Görlitz, "A single-stage 1112 nm fiber amplifier with large gain for laser cooling of ytterbium," *Applied Physics B: Photophysics and Laser Chemistry*, vol. 124, no. 12, pp. 1–7, 2018.

[197] C. Sillus, T. Franzen, B. Pollklesener, and A. Görlitz, "Active position stabilization of an atomic cloud in a narrow-line magneto-optical trap using a Raspberry Pi," *Review of Scientific Instruments*, vol. 92, no. 3, p. 033 204, 2021. DOI: 10.1063/5.0040257.

[198] E. D. Black, "An introduction to pound–drever–hall laser frequency stabilization," *American Journal of Physics*, vol. 69, no. 1, pp. 79–87, 2001. DOI: 10.1119/1.1286663.

[199] W. Zhang, M. J. Martin, C. Benko, *et al.*, "Reduction of residual amplitude modulation to $1 \cdot 10^{-6}$ for frequency modulation and laser stabilization," *Optics Letters*, vol. 39, no. 7, pp. 1980–1983, 2014. DOI: 10.1364/OL.39.001980.

[200] R. Paschotta, D. C. Hanna, P. DeNatale, G. Modugno, M. Inguscio, and P. Laporta, "Power amplifier for 1083 nm using ytterbium doped fiber," *Opt. Commun.*, vol. 136, 1997.

[201] R. Roy, A. Green, R. Bowler, and S. Gupta, "Rapid cooling to quantum degeneracy in dynamically shaped atom traps," *Physical Review A*, vol. 93, p. 043 403, 4 2016. DOI: 10.1103/PhysRevA.93.043403.

[202] E. Ippen and R. Stolen, "Stimulated Brillouin scattering in optical fibers," *Applied Physics Letters*, vol. 21, no. 11, pp. 539–541, 1972. DOI: 10.1063/1.1654249.

[203] T. Kemmerling, *Setup of an Optical Lattice at 1064nm for Ultracold Rubidium Atoms*, Master Thesis, Universität Düsseldorf, 2019.

[204] S Tassy, N Nemitz, F Baumer, C Höhl, A Batär, and A Görlitz, "Sympathetic cooling in a mixture of diamagnetic and paramagnetic atoms," *Journal of Physics B: Atomic, Molecular and Optical Physics*, vol. 43, no. 20, p. 205 309, 2010. DOI: 10.1088/0953-4075/43/20/205309.

[205] M. N. Zervas and C. A. Codemard, "High power fiber lasers: A review," *IEEE Journal of Selected Topics in Quantum Electronics*, vol. 20, no. 5, pp. 219–241, 2014. DOI: 10.1109/JSTQE.2014.2321279.

[206] O. G. Okhotnikov, *Fiber lasers*. John Wiley & Sons, 2012.

[207] B. Upadhyaya, "Self-pulsing dynamics in yb-doped fiber lasers," in *Fiber Laser*, M. C. Paul, Ed., Rijeka: IntechOpen, 2016, ch. 1. DOI: 10.5772/62087.

[208] R. Niemann, *Photoassociation Spectroscopy at the Intercombination Line of Ytterbium*, Master Thesis, Universität Düsseldorf, 2019.

[209] S. Schiller, A. Görlitz, A. Nevsky, *et al.*, "Towards Neutral-atom Space Optical Clocks (SOC2): Development of high-performance transportable and breadboard optical clocks and advanced subsystems," in *2012 European Frequency and Time Forum*, 2012.

[210] J. F. Kelly and A. Gallagher, "Efficient electro-optic modulator for optical pumping of na beams," *Review of Scientific Instruments*, vol. 58, no. 4, pp. 563–566, 1987. DOI: 10.1063/1.1139269.

[211] A. Kallweit, *Aufbau eines Lasersystems bei 1112nm*, Bachelorarbeit, AG Görlitz, Universität Düsseldorf, 2010.

[212] D Jacob, E Mimoun, L. D. Sarlo, M Weitz, J Dalibard, and F Gerbier, "Production of sodium bose–einstein condensates in an optical dimple trap," *New Journal of Physics*, vol. 13, no. 6, p. 065 022, 2011. DOI: 10.1088/1367-2630/13/6/065022.

[213] F. Türck, *Microwave spectroscopy in an ultracold mixture of Yb and Rb atoms*, Master Thesis, Universität Düsseldorf, 2018.

[214] J. D. Kraus, *Antennas*, 2 Sub. McGraw-Hill Companies, 1988, ISBN: 0070354227,9780070354227.

[215] K. N. G. from New Zealand, *The Cantenna Waveguide*. [Online]. Available: http://www.wikarekare.org/Antenna/WaveguideCan.html.

[216] A. Keshet and W. Ketterle, "A distributed, graphical user interface based, computer control system for atomic physics experiments," *Review of Scientific Instruments*, vol. 84, no. 1, p. 015 105, 2013. DOI: 10.1063/1.4773536.

[217] W. Ketterle, D. Durfee, and D. Stamper-Kurn, "Making, probing and understanding Bose-Einstein condensates," in *Proceedings of the International School of Physics - Enrico Fermi*, M. Inguscio, S. Stringari, and C. Wieman, Eds., IOS Press, 1999, p. 67.

[218] M Zawada, R Abdoul, J Chwedeńczuk, *et al.*, "Free-fall expansion of finite-temperature bose–einstein condensed gas in the non-thomas–fermi regime," *Journal of Physics B: Atomic, Molecular and Optical Physics*, vol. 41, no. 24, p. 241 001, 2008. DOI: 10.1088/0953-4075/41/24/241001.

[219] J. Stajic, Q. Chen, and K. Levin, "Density profiles of strongly interacting trapped fermi gases," *Phys. Rev. Lett.*, vol. 94, p. 060 401, 6 2005. DOI: 10.1103/PhysRevLett.94.060401.

[220] C. F. Ockeloen, A. F. Tauschinsky, R. J. C. Spreeuw, and S. Whitlock, "Detection of small atom numbers through image processing," *Physical Review A*, vol. 82, p. 061 606, 6 2010. DOI: 10.1103/PhysRevA.82.061606.

[221] W. Ketterle, K. B. Davis, M. A. Joffe, A. Martin, and D. E. Pritchard, "High densities of cold atoms in a dark spontaneous-force optical trap," *Physical review letters*, vol. 70, no. 15, p. 2253, 1993.

[222] A. L. Migdall, J. V. Prodan, W. D. Phillips, T. H. Bergeman, and H. J. Metcalf, "First observation of magnetically trapped neutral atoms," *Physical Review Letters*, vol. 54, pp. 2596–2599, 24 1985. DOI: 10.1103/PhysRevLett.54.2596.

[223] W. Ketterle and N. V. Druten, "Evaporative cooling of trapped atoms," in ser. Advances In Atomic, Molecular, and Optical Physics, B. Bederson and H. Walther, Eds., vol. 37, Academic Press, 1996, pp. 181–236. DOI: https://doi.org/10.1016/S1049-250X(08)60101-9.

[224] D. M. Brink and C. V. Sukumar, "Majorana spin-flip transitions in a magnetic trap," *Phys. Rev. A*, vol. 74, p. 035 401, 3 2006. DOI: 10.1103/PhysRevA.74.035401. [Online]. Available: https://link.aps.org/doi/10.1103/PhysRevA.74.035401.

[225] M. Mewes, M. Andrews, N. V. Druten, D. Kurn, D. Durfee, and W. Ketterle, "Bose-Einstein Condensation in a Tightly Confining DC Magnetic Trap," *Phys. Rev. Lett.*, vol. 77, p. 416, 1996.

[226] R. Dubessy, K. Merloti, L. Longchambon, *et al.*, "Rubidium-87 bose-einstein condensate in an optically plugged quadrupole trap," *Phys. Rev. A*, vol. 85, p. 013 643, 1 2012. DOI: 10.1103/PhysRevA.85.013643.

[227] B. Pollklesener, T. Franzen, C. Sillus, and A. Görlitz, "A new apparatus for the production of ultracold mixtures of rb and yb," *Manuscript in preparation*, 2023.

[228] M. D. Barret, J. A. Sauer, and M. S. Chapman, "All-optical formation of an atomic bose-einstein condensate," *Phys. Rev. Lett.*, vol. 87, p. 010 404, 2001.

[229] K. M. O'Hara, M. E. Gehm, S. R. Granade, and J. E. Thomas, "Scaling laws for evaporative cooling in time-dependent optical traps," *Physical Review A*, vol. 64, p. 051 403, 5 2001. DOI: 10.1103/PhysRevA.64.051403.

[230] C. Adams, H. Lee, N. Davidson, M. Kasevich, and S. Chu, "Evaporative cooling in a crossed dipole trap," *Phys. Rev. Lett.*, vol. 74, p. 3577, 1995.

[231] I. I. Rabi, "Space quantization in a gyrating magnetic field," *Physical Review*, vol. 51, no. 8, p. 652, 1937.

[232] C. Zener and R. H. Fowler, "Non-adiabatic crossing of energy levels," *Proceedings of the Royal Society of London. Series A, Containing Papers of a Mathematical and Physical Character*, vol. 137, no. 833, pp. 696–702, 1932. DOI: 10.1098/rspa.1932.0165. eprint: https://royalsocietypublishing.org/doi/pdf/10.1098/rspa.1932.0165.

[233] B. Pascal A., "Coherent manipulation of ultracold atoms with microwave near-fields," Ph.D. dissertation, Max-Planck-Institut für Quantenoptik, 2010.

[234] M.-O. Mewes, M. Andrews, D. Kurn, D. Durfee, C. Townsend, and W. Ketterle, "Output coupler for bose-einstein condensed atoms," *Phys. Rev. Lett.*, vol. 78, pp. 582–585, 1997.

[235] J. R. Rubbmark, M. M. Kash, M. G. Littman, and D. Kleppner, "Dynamical effects at avoided level crossings: A study of the Landau-Zener effect using Rydberg atoms," *Physical Review A*, vol. 23, pp. 3107–3117, 6 1981. DOI: 10.1103/PhysRevA.23.3107.

[236] W. Gerlach and O. Stern, "Der experimentelle nachweis der richtungsquantelung im magnetfeld," German, *Zeitschrift für Physik*, vol. 9, no. 1, pp. 349–352, 1922, ISSN: 0044-3328. DOI: 10.1007/BF01326983.

[237] T. H. Loftus, T. Ido, M. M. Boyd, A. D. Ludlow, and J. Ye, "Narrow line cooling and momentum-space crystals," *Physical Review A*, vol. 70, p. 063 413, 6 2004. DOI: 10.1103/PhysRevA.70.063413.

[238] P. L. Kapitza and P. A. M. Dirac, "The reflection of electrons from standing light waves," *Mathematical Proceedings of the Cambridge Philosophical Society*, vol. 29, no. 2, 297–300, 1933. DOI: 10.1017/S0305004100011105.

[239] P. Gould, G. Ruff, and D. Pritchard, "Diffraction of atoms by light: The near–resonant kapitza–dirac effect," *Phys. Rev. Lett.*, vol. 56, p. 827, 1986.

[240] B. Gadway, D. Pertot, R. Reimann, M. G. Cohen, and D. Schneble, "Analysis of Kapitza-Dirac diffraction patterns beyond the Raman-Nath regime," *Optics Express*, vol. 17, no. 21, pp. 19 173–19 180, 2009. DOI: 10.1364/OE.17.019173.

[241] T. Zhou, K. Yang, Y. Zhai, *et al.*, "High precision calibration of optical lattice depth based on multiple pulses kapitza-dirac diffraction," *Opt. Express*, vol. 26, no. 13, pp. 16 726–16 735, 2018. DOI: 10.1364/OE.26.016726.

[242] J. Hecker Denschlag, J. Simsarian, H. Häffner, *et al.*, "A bose-einstein condensate in an optical lattice," English, *Journal of Physics B: Atomic, Molecular and Optical Physics*, vol. 35, no. 14, pp. 3095–3110, Jul. 2002, ISSN: 0953-4075. DOI: 10.1088/0953-4075/35/14/307.

[243] M. Ben Dahan, E. Peik, J. Reichel, Y. Castin, and C. Salomon, "Bloch oscillations of atoms in an optical potential," *Phys. Rev. Lett.*, vol. 76, pp. 4508–4511, 24 1996. DOI: 10.1103/PhysRevLett.76.4508.

[244] T. Gericke, F. Gerbier, A. Widera, S. Fölling, O. Mandel, and I. Bloch, "Adiabatic loading of a bose–einstein condensate in a 3d optical lattice," *Journal of Modern Optics*, vol. 54, no. 5, pp. 735–743, 2007. DOI: 10.1080/09500340600777730.

[245] H. Hara, Y. Takasu, Y. Yamaoka, J. M. Doyle, and Y. Takahashi, "Quantum degenerate mixtures of alkali and alkaline-earth-like atoms," *Phys. Rev. Lett.*, vol. 106, p. 205 304, 20 2011. DOI: 10.1103/PhysRevLett.106.205304.

[246] K. E. Wilson, A. Guttridge, J. Segal, and S. L. Cornish, "Quantum degenerate mixtures of Cs and Yb," *Physical Review A*, vol. 103, no. 3, p. 033 306, 2021.

[247] Z.-X. Ye, L.-Y. Xie, Z. Guo, *et al.*, "Double-degenerate bose-fermi mixture of strontium and lithium," *Phys. Rev. A*, vol. 102, p. 033 307, 3 2020. DOI: 10.1103/PhysRevA.102.033307.

[248] G. Modugno, G. Ferrari, G. Roati, R. J. Brecha, A. Simoni, and M. Inguscio, "Bose-Einstein condensation of potassium atoms by sympathetic cooling," *Science*, vol. 294, no. 5545, pp. 1320–1322, 2001, ISSN: 0036-8075. DOI: 10.1126/science.1066687.

[249] R. Onofrio and C. Presilla, "Ultracold atomic fermi–bose mixtures in bichromatic optical dipole traps: A novel route to study fermion superfluidity," *Journal of Statistical Physics*, vol. 115, no. 1, pp. 57–89, 2004.

[250] T. Zelevinsky, M. M. Boyd, A. D. Ludlow, *et al.*, "Narrow line photoassociation in an optical lattice," *Physical Review Letters*, vol. 96, p. 203 201, 20 2006. DOI: 10.1103/PhysRevLett.96.203201.

[251] P. S. Żuchowski, R. Guérout, and O. Dulieu, "Ground- and excited-state properties of the polar and paramagnetic RbSr molecule: A comparative study," *Physical Review A*, vol. 90, p. 012 507, 1 2014. DOI: 10.1103/PhysRevA.90.012507.

[252] A. Bayerle, "Ultracold strontium and rubidium: Mixtures, quantum gases and molecules," Ph.D. dissertation, Universiteit van Amsterdam, 2017.

[253] S. Tojo, M. Kitagawa, K. Enomoto, *et al.*, "High-resolution photoassociation spectroscopy of ultracold ytterbium atoms by using the intercombination transition," *Physical review letters*, vol. 96, no. 15, p. 153 201, 2006.

[254] M Borkowski, R Ciuryło, P. Julienne, S Tojo, K Enomoto, and Y Takahashi, "Line shapes of optical Feshbach resonances near the intercombination transition of bosonic ytterbium," *Physical Review A*, vol. 80, no. 1, p. 012 715, 2009.

[255] B. Bransden and C. Joachain, *Physics of Atoms and Molecules*. Pearson Education, 2003, ISBN: 9788177582796.

[256] Y. Takasu, Y. Saito, Y. Takahashi, M. Borkowski, R. Ciuryło, and P. S. Julienne, "Controlled production of subradiant states of a diatomic molecule in an optical lattice," *Physical review letters*, vol. 108, no. 17, p. 173 002, 2012.

[257] D. A. Steck, *Quantum and Atom Optics*. 2007, accessed 31.10.2022. [Online]. Available: http://steck.us/teaching.

[258] M. L. González-Martínez and J. M. Hutson, "Sympathetic cooling of fluorine atoms with ultracold atomic hydrogen," *Physical review A*, vol. 88, no. 5, p. 053 420, 2013.

[259] "Diatomic-py: A python module for calculating the rotational and hyperfine structure of 1 molecules," *Computer Physics Communications*, vol. 282, p. 108 512, 2023, ISSN: 0010-4655. DOI: https://doi.org/10.1016/j.cpc.2022.108512.

[260] D. Chubukov and L. Labzowsky, "Omega-doubling and a limit for the enhancement of the electron edm effect in diatomic molecules," *Physics Letters A*, vol. 378, no. 38, pp. 2857–2860, 2014, ISSN: 0375-9601. DOI: https://doi.org/10.1016/j.physleta.2014.07.043.

[261] B. Mukherjee and M. D. Frye, Personal communication.

[262] F. Münchow, "2-Photon-Photoassociation spectroscopy in a mixture of Ytterbium and Rubidium," Ph.D. dissertation, HHU Düsseldorf, 2012.

[263] K. Enomoto, K. Kasa, M. Kitagawa, and Y. Takahashi, "Optical feshbach resonance using the intercombination transition," *Phys. Rev. Lett.*, vol. 101, p. 203 201, 20 2008. DOI: 10.1103/PhysRevLett.101.203201.

[264] A. Ciamei, "Taming ultracold RbSr and Sr_2," Ph.D. dissertation, Universiteit van Amsterdam, 2018.

[265] N. Poli, Z. W. Barber, N. D. Lemke, *et al.*, "Frequency evaluation of the doubly forbidden $^1S_0 \rightarrow ^3P_0$ transition in bosonic ^{174}Yb," *Phys. Rev. A*, vol. 77, p. 050 501, 5 2008. DOI: 10.1103/PhysRevA.77.050501.

[266] W. Dowd, R. J. Roy, R. K. Shrestha, *et al.*, "Magnetic field dependent interactions in an ultracold li–yb(3p2) mixture," *New Journal of Physics*, vol. 17, no. 5, p. 055 007, 2015. DOI: 10.1088/1367-2630/17/5/055007.

[267] P. Naidon and P. S. Julienne, "Optical feshbach resonances of alkaline-earth-metal atoms in a one- or two-dimensional optical lattice," *Phys. Rev. A*, vol. 74, p. 062 713, 6 2006. DOI: 10.1103/PhysRevA.74.062713.

[268] T. Zelevinsky, M. M. Boyd, A. D. Ludlow, *et al.*, "Narrow line photoassociation in an optical lattice," *Phys. Rev. Lett.*, vol. 96, p. 203 201, 20 2006. DOI: 10.1103/PhysRevLett.96.203201.

[269] M. Tomza, F. Pawłowski, M. Jeziorska, C. P. Koch, and R. Moszynski, "Formation of ultracold sryb molecules in an optical lattice by photoassociation spectroscopy: Theoretical prospects," *Phys. Chem. Chem. Phys.*, vol. 13, pp. 18 893–18 904, 42 2011. DOI: 10.1039/C1CP21196J.

[270] D. Jaksch, V. Venturi, J. I. Cirac, C. J. Williams, and P. Zoller, "Creation of a molecular condensate by dynamically melting a mott insulator," *Phys. Rev. Lett.*, vol. 89, p. 040 402, 4 2002. DOI: 10.1103/PhysRevLett.89.040402.

[271] T. Tomita, S. Nakajima, I. Danshita, Y. Takasu, and Y. Takahashi, "Observation of the mott insulator to superfluid crossover of a driven-dissipative bose-hubbard system," *Science Advances*, vol. 3, no. 12, e1701513, 2017. DOI: 10.1126/sciadv.1701513.

[272] B. H. McGuyer, M McDonald, G. Z. Iwata, *et al.*, "High-precision spectroscopy of ultracold molecules in an optical lattice," *New Journal of Physics*, vol. 17, no. 5, p. 055 004, 2015. DOI: 10.1088/1367-2630/17/5/055004.

[273] D. Jaksch, V. Venturi, J. I. Cirac, C. J. Williams, and P. Zoller, "Creation of a molecular condensate by dynamically melting a mott insulator," *Phys. Rev. Lett.*, vol. 89, p. 040 402, 4 2002. DOI: 10.1103/PhysRevLett.89.040402.

[274] T. Fukuhara, S. Sugawa, M. Sugimoto, S. Taie, and Y. Takahashi, "Mott insulator of ultracold alkaline-earth-metal-like atoms," *Physical Review A*, vol. 79, no. 4, p. 041 604, 2009.

[275] S. Sugawa, K. Inaba, S. Taie, R. Yamazaki, M. Yamashita, and Y. Takahashi, "Interaction and filling-induced quantum phases of dual Mott insulators of bosons and fermions," *Nature Physics*, vol. 7, no. 8, pp. 642–648, 2011.

[276] A. Chotia, B. Neyenhuis, S. A. Moses, *et al.*, "Long-lived dipolar molecules and feshbach molecules in a 3d optical lattice," *Phys. Rev. Lett.*, vol. 108, p. 080 405, 8 2012. DOI: 10.1103/PhysRevLett.108.080405.

[277] M. G. Moore and H. R. Sadeghpour, "Controlling two-species mott-insulator phases in an optical lattice to form an array of dipolar molecules," *Phys. Rev. A*, vol. 67, p. 041 603, 4 2003. DOI: 10.1103/PhysRevA.67.041603.

[278] T. Rom, T. Best, O. Mandel, *et al.*, "State selective production of molecules in optical lattices," *Phys. Rev. Lett.*, vol. 93, p. 073 002, 7 2004. DOI: 10.1103/PhysRevLett.93.073002.

[279] F. Muenchow, C. Bruni, M. Madalinski, and A. Goerlitz, "Two-photon photoassociation spectroscopy of heteronuclear ybrb," *Physical Chemistry Chemical Physics*, vol. 13, no. 42, pp. 18 734–18 737, 2011. DOI: 10.1039/c1cp21219b.

[280] J. J. Lutz and J. M. Hutson, "Deviations from born-oppenheimer mass scaling in spectroscopy and ultracold molecular physics," *Journal of Molecular Spectroscopy*, vol. 330, pp. 43–56, 2016.

[281] M. Borkowski, Private communication.

[282] M. Deiß, B. Drews, J. H. Denschlag, N. Bouloufa-Maafa, R. Vexiau, and O. Dulieu, "Polarizability of ultracold molecules in the rovibrational ground state of," *New Journal of Physics*, vol. 17, no. 6, p. 065 019, 2015. DOI: 10.1088/1367-2630/17/6/065019.

[283] A. Green, J. H. See Toh, R. Roy, M. Li, S. Kotochigova, and S. Gupta, "Two-photon photoassociation spectroscopy of the $^2\Sigma^+$ yb li molecular ground state," *Phys. Rev. A*, vol. 99, p. 063 416, 6 2019. DOI: 10.1103/PhysRevA.99.063416.

[284] J. W. Park, S. A. Will, and M. W. Zwierlein, "Two-photon pathway to ultracold ground state molecules of 23na40k," *New Journal of Physics*, vol. 17, no. 7, p. 075 016, 2015.

[285] K. Winkler, G. Thalhammer, M. Theis, H. Ritsch, R. Grimm, and J. H. Denschlag, "Atom-molecule dark states in a bose-einstein condensate," *Phys. Rev. Lett.*, vol. 95, p. 063 202, 6 2005. DOI: 10.1103/PhysRevLett.95.063202.

[286] Y. N. Martinez de Escobar, P. G. Mickelson, P. Pellegrini, *et al.*, "Two-photon photoassociative spectroscopy of ultracold ^{88}Sr," *Phys. Rev. A*, vol. 78, p. 062 708, 6 2008. DOI: 10.1103/PhysRevA.78.062708.

[287] T. Klostermann, C. R. Cabrera, H. von Raven, *et al.*, "Fast long-distance transport of cold cesium atoms," *Phys. Rev. A*, vol. 105, p. 043 319, 4 2022. DOI: 10.1103/PhysRevA.105.043319.

[288] S. Brakhane, W. Alt, D. Meschede, C. Robens, G. Moon, and A. Alberti, "Ultra-low birefringence dodecagonal vacuum glass cell," *Review of Scientific Instruments*, vol. 86, no. 12, p. 126 108, 2015. DOI: 10.1063/1.4938281.

[289] A. Kerkmann, "A novel apparatus for quantum gas microscopy of lithium atoms," Ph.D. dissertation, Staats-und Universitätsbibliothek Hamburg Carl von Ossietzky, 2019.

[290] S. A. Moses, J. P. Covey, M. T. Miecnikowski, D. S. Jin, and J. Ye, "New frontiers for quantum gases of polar molecules," *Nature Physics*, vol. 13, no. 1, pp. 13–20, 2017.

[291] S. Kuhr, "Quantum-gas microscopes: A new tool for cold-atom quantum simulators," *National Science Review*, vol. 3, no. 2, pp. 170–172, 2016.

[292] S. Dörscher, A. Thobe, B. Hundt, *et al.*, "Creation of quantum-degenerate gases of ytterbium in a compact 2d-/3d-magneto-optical trap setup," *Review of Scientific Instruments*, vol. 84, no. 4, p. 043 109, 2013.

[293] K. E. Wilson, A. Guttridge, J. Segal, and S. L. Cornish, "Quantum degenerate mixtures of cs and yb," *Phys. Rev. A*, vol. 103, p. 033 306, 3 2021. DOI: 10.1103/PhysRevA.103.033306.

[294] F. Schmidt, D. Mayer, M. Hohmann, T. Lausch, F. Kindermann, and A. Widera, "Precision measurement of the ^{87}Rb tune-out wavelength in the hyperfine ground state $F = 1$ at 790 nm," *Phys. Rev. A*, vol. 93, p. 022 507, 2 2016. DOI: 10.1103/PhysRevA.93.022507.

[295] K. Wen, Z. Meng, L. Wang, *et al.*, "Experimental study of tune-out wavelengths for spin-dependent optical lattice in 87rb bose–einstein condensation," *J. Opt. Soc. Am. B*, vol. 38, no. 11, pp. 3269–3276, 2021. DOI: 10.1364/JOSAB.432448.

[296] B. Scheidler, *Aufbau eines diodenlasersystems bei 790nm zur manipulation von atomen in einer optischen dipolfalle*, Bachelor Thesis, Universität Düsseldorf, 2021.

[297] X. Wang, J. Jiang, L.-Y. Xie, D.-H. Zhang, and C.-Z. Dong, "Polarizabilities and tune-out wavelengths of the hyperfine ground states of ^{87,85}Rb," *Phys. Rev. A*, vol. 94, p. 052 510, 5 2016. DOI: 10.1103/PhysRevA.94.052510.

[298] C. Herold, V. Vaidya, X. Li, S. Rolston, J. Porto, and M. Safronova, "Precision measurement of transition matrix elements via light shift cancellation," *Physical review letters*, vol. 109, no. 24, p. 243 003, 2012.

[299] Y. Qi, Y. Bi, Y. Wang, *et al.*, "High power and efficient continuous wave 456 nm blue laser for laser display," *Proceedings of the International Quantum Electronics Conference and Conference on Lasers and Electro-Optics Pacific Rim 2011*, p. C415, 2011.

[300] "Highly efficient nd:gdvo4/bibo laser at 456nm under direct 880nm diode laser pumping," *Optics Communications*, vol. 282, no. 24, pp. 4793–4795, 2009, ISSN: 0030-4018. DOI: https://doi.org/10.1016/j.optcom.2009.09.045.

[301] R. L. GmbH, *Rlt455-5w-gop*, Roithner Website. [Online]. Available: http://www.roithner-laser.com/datasheets/ld_div/rlt455-5w-gop.pdf.

[302] N. Vitanov, M. Fleischhauer, B. Shore, and K. Bergmann, "Coherent manipulation of atoms molecules by sequential laser pulses," in ser. Advances In Atomic, Molecular, and Optical Physics, B. Bederson and H. Walther, Eds., vol. 46, Academic Press, 2001, pp. 55–190. DOI: https://doi.org/10.1016/S1049-250X(01)80063-X.

[303] M. Yan, B. J. DeSalvo, Y. Huang, P. Naidon, and T. C. Killian, "Rabi oscillations between atomic and molecular condensates driven with coherent one-color photoassociation," *Phys. Rev. Lett.*, vol. 111, p. 150 402, 15 2013. DOI: 10.1103/PhysRevLett.111.150402.

[304] K Aikawa, D Akamatsu, J Kobayashi, M Ueda, T Kishimoto, and S Inouye, "Toward the production of quantum degenerate bosonic polar molecules, 41k87rb," *New Journal of Physics*, vol. 11, no. 5, p. 055 035, 2009. DOI: 10.1088/1367-2630/11/5/055035.

[305] L. P. Yatsenko, V. I. Romanenko, B. W. Shore, and K. Bergmann, "Stimulated Raman adiabatic passage with partially coherent laser fields," *Physical Review A*, vol. 65, p. 043 409, 4 2002. DOI: 10.1103/PhysRevA.65.043409.

[306] S. Ospelkaus, A. Pe'er, K. Ni, *et al.*, "Efficient state transfer in an ultracold dense gas of heteronuclear molecules," *Nature Physics*, vol. 4, pp. 622–626, Jun. 2008. DOI: 10.1038/nphys997.

[307] M. Mackie, R. Kowalski, and J. Javanainen, "Bose-stimulated raman adiabatic passage in photoassociation," *Phys. Rev. Lett.*, vol. 84, pp. 3803–3806, 17 2000. DOI: 10.1103/PhysRevLett.84.3803.

[308] A. Ciamei, A. Bayerle, B. Pasquiou, and F. Schreck, "Observation of bose-enhanced photoassociation products," *Europhysics Letters*, vol. 119, no. 4, p. 46 001, 2017. DOI: 10.1209/0295-5075/119/46001.

[309] C. Castor, *A laser system for Molecular Spectroscopy of RbYb at 1500nm*, Master Thesis, Universität Düsseldorf, 2022.

[310] S. Bennetts, G. D. McDonald, K. S. Hardman, *et al.*, "External cavity diode lasers with 5khz linewidth and 200nm tuning range at 1.55 μm and methods for linewidth measurement," *Optics express*, vol. 22, no. 9, pp. 10 642–10 654, 2014.

[311] D. K. Shin, B. M. Henson, R. I. Khakimov, *et al.*, "Widely tunable, narrow linewidth external-cavity gain chip laser for spectroscopy between 1.0 - 1.1 µm," *Opt. Express*, vol. 24, no. 24, pp. 27 403–27 414, 2016. DOI: 10.1364/OE.24.027403.

[312] L Veseth, "Hund's coupling case (c) in diatomic molecules. i. theory," *Journal of Physics B: Atomic and Molecular Physics*, vol. 6, no. 8, p. 1473, 1973. DOI: 10.1088/0022-3700/6/8/025.

[313] M. Tomza, F. Pawłowski, M. Jeziorska, C. P. Koch, and R. Moszynski, "Formation of ultracold sryb molecules in an optical lattice by photoassociation spectroscopy: Theoretical prospects," *Phys. Chem. Chem. Phys.*, vol. 13, pp. 18 893–18 904, 42 2011. DOI: 10.1039/C1CP21196J.

Danksagung

Den letzten Teil dieser Arbeit möchte ich den Menschen widmen, die mich während meiner Zeit als Doktorand unterstützt, immer wieder motiviert und vor allem erheitert haben. Ohne sie wäre diese Arbeit nicht begonnen, und am wichtigsten, nicht vollendet worden.

- Zunächst möchte ich Axel Görlitz danken. Er hat mir ermöglicht in seiner Arbeitsgruppe meine ersten Schritte in der Experimentalphysik als Bachelorstudent und dann als Masterstudent zu machen. Sein Angebot am RbYb Molekülexperiment als Doktorand weiterzuarbeiten, bereue ich tatsächlich bis heute nicht. Denn wenn es mal nicht so läuft, wie es soll, ist seine Erfahrung und physikalische Intuition für pragmatische Problemlösung sehr hilfreich. Seine Bereitschaft zu hilfreichen Gesprächen und die aufflammende Begeisterung im Labor mitzuarbeiten, wenn er die Gelegenheit bekommt, befeuert regelmäßig die Hoffnung aller Team-Mitglieder/innen. Außerdem möchte ich mich für das sorgfältige Korrekturlesen dieser Arbeit bedanken.
- Ich danke Prof. Dr. Kollmannsberger für die freundliche Übernahme des Koreferates und ganz besonders für die zügige Fertigstellung des Gutachtens.
- Entscheidend für das Gelingen eines großen Forschungsprojekts ist das Team. Für die durchaus lange aber lustige Zeit an der RbYb Maschine möchte ich mich besonders bei Tobias Franzen und Christian Sillus bedanken. Um mich möglichst kurz zu fassen, ohne Tobias gäbe es das Experiment und mein physikalisches Verständnis dafür nicht. Sein immenses physikalisches Talent, seine große Ausdauer, Dinge öfter als dreimal zu erklären und die Fähigkeit, sehr lange Abende im Labor oder anderswo zu verbringen, ist schlichtweg bewundernswert. Christian danke ich für die Kameradschaft bei der Suche nach verloren gegangenen Atomen, Laserstrahlen, Locks und Linien, sowie seinen besonderen Sinn für Humor und Coolness. Außerdem danke ich Arne für die kompetente Übernahme des Experiments. Seine schnelle Auffassungsgabe und sein experimentelles Geschick wird das Experiment zweifelsfrei weiter bringen.
- Nun möchte ich mich bei einer Menge von Leuten bedanken, die ich während meiner Zeit an der Uni Düsseldorf kennen und schätzen gelernt habe. Vorneweg das Rydberg Team mit Christan Halter, Alexander Miethke und Apoorva Hegde, mit denen das Zusammensein in und außerhalb des Labors immer unterhaltsam war. Außerdem möchte ich mich bei meinen ehemaligen Kolleg/innen Fabian Türck, Torsten Kemmerling, Simone Veltum und Gregor Mura bedanken. Letzterer dafür, dass er mir gezeigt hat, wie ich meinen ersten Laser baue. Für ihre Fähigkeit, mich erfolgreich durch mein Studium und zeitweilig auf andere Gedanken zu bringen, danke ich zudem Michael Stumpf und Laurin Schnorr.

- Ein besonderer Dank geht wie immer an Ralf Stephan. Als begabter und stets bescheidener Techniker der Arbeitsgruppe gibt er nur ungern zu den Großteil des Labors selbst erbaut zu haben und auch noch in Stand zu halten. Er hat immer die Idee, auf die man selber nicht gekommen ist und kann, meiner Meinung nach, alle Herausforderungen und Geräte elektro-technischer Art lösen, bauen und reparieren. Vielen Dank für deine Hilfe!
- Meiner Familie möchte ich für die Unterstützung über die vielen Jahre meines Studiums hinweg danken.
- Zum Schluss möchte ich dir danken, Céline. Du bist besonders in Zeiten, in denen es mal nicht so läuft, meine wichtigste Stütze und gleichzeitig Rückzugsort. Ohne deine Motivation, Unterstützung und dein Verständnis wäre diese Arbeit und ich als Mensch nicht halb so gut gelungen.

Publications

The following scientific papers involving work within this thesis have been published:

Reference [196]:
T. Franzen, B. Pollklesener and A. Görlitz
A single-stage 1112 nm fiber amplifier with large gain for laser cooling of ytterbium. in Applied Physics B, 124(12):1–7, 2018.
The author participated in the setup and maintenance of the amplifier and performed the MOT measurements appearing in the publication.
Within this thesis the laser system is only briefly mentioned since it is thoroughly described in the thesis of its main author [1].

Reference [197]:
C.Sillus,T. Franzen, B. Pollklesener and A. Görlitz
Active position stabilization of an atomic cloud in a narrow-line magnetooptical trap using a Raspberry Pi. in Review of Scientific Instruments, 92(3):033204,2021.
The author participated in the development and characterisation of the system and performed measurements for the publication.
Section 3.4.3 in this work describes the system in condensed form without directly reproducing contents of the publication.

Reference [20]:
T. Franzen, B. Pollklesener, C.Sillus and A. Görlitz
Intercombination line photoassociation spectroscopy of 87Rb170Yb. in Phys. Rev. A 107, 023114 (2023)
The author participated in the development and maintenance of the laser systems, recorded data, joined in the analysis appearing in this publication and edited the manuscript.
Contents of this publication appear in chapters 5 and 6 of this thesis.

Reference [227]:
B. Pollklesener, T. Franzen, C.Sillus and A. Görlitz
A new apparatus for the production of ultracold mixtures of Rb and Yb [manuscript to be submitted]
The author led the development and optimisation of the presented experimental apparatus pioneered by T. Franzen and prepared the manuscript.

Eidesstattliche Erklärung

Hiermit versichere ich eidesstattlich, dass die vorliegende Dissertation eigenständig und ohne unzulässige Hilfe unter Beachtung der "Grundsätze zur Sicherung gute wissenschaftlicher Praxis an der Heinrich-Heine-Universität Düsseldorf" erstellt worden ist.

Düsseldorf, 10.08.2023
Ort, Datum

Bastian Pollklesener